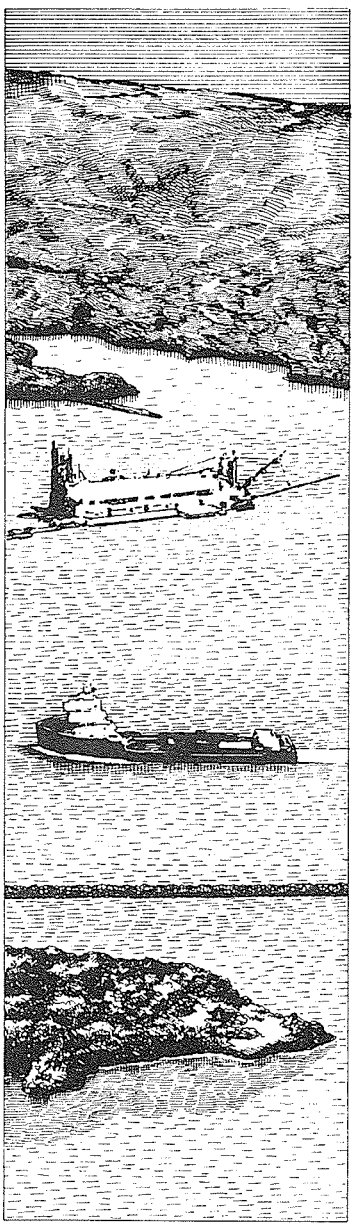

DREDGING RESEARCH PROGRAM

TECHNICAL REPORT DRP-92-6

ADCIRC: AN ADVANCED THREE-DIMENSIONAL CIRCULATION MODEL FOR SHELVES, COASTS, AND ESTUARIES

Report 1
THEORY AND METHODOLOGY OF ADCIRC-2DDI AND ADCIRC-3DL

by

R. A. Luettich, Jr.
Institute of Marine Sciences
University of North Carolina at Chapel Hill
Morehead City, North Carolina 27514

J. J. Westerink
Department of Civil Engineering
University of Notre Dame, Notre Dame, Indiana 46556

Norman W. Scheffner
Coastal Engineering Research Center
DEPARTMENT OF THE ARMY
Waterways Experiment Station, Corps of Engineers
3909 Halls Ferry Road, Vicksburg, Mississippi 39180-6199

November 1992

Report 1 of a Series

Prepared for DEPARTMENT OF THE ARMY
US Army Corps of Engineers
Washington, DC 20314-1000

Under Work Unit No. 32466

The Dredging Research Program (DRP) is a seven-year program of the US Army Corps of Engineers. DRP research is managed in these five technical areas:

Area 1 - Analysis of Dredged Material Placed in Open Water

Area 2 - Material Properties Related to Navigation and Dredging

Area 3 - Dredge Plant Equipment and Systems Processes

Area 4 - Vessel Positioning, Survey Controls, and Dredge Monitoring Systems

Area 5 - Management of Dredging Projects

US Army Corps
of Engineers
Waterways Experiment
Station

Dredging Research Program Report Summary

ADCIRC: An Advanced Three-Dimensional Circulation Model for Shelves, Coasts, and Estuaries; Report 1, Theory and Methodology of ADCIRC-2DDI and ADCIRC-3DL (TR DRP-92-6)

ISSUE: A unified and systematic methodology must be provided to use in the investigation of the dispersive or nondispersive characteristics of a site proposed for the disposal of dredged material in open water as well as to analyze existing disposal sites.

RESEARCH: ADCIRC (Advanced Three-Dimensional Circulation Model) was developed as a part of the Dredging Research Program (DRP) as a means of generating a database of harmonic constituents for tidal elevation and current at discrete locations along the east, west, and Gulf of Mexico coasts and to utilize tropical and extratropical global boundary conditions to compute frequency-indexed storm surge hydrographs along the US coasts. The database is being developed to provide site-specific hydrodynamic boundary conditions for use in analyzing the long-term stability of existing or proposed dredged material disposal sites.

SUMMARY: The report describes the theory, methodology, and verification of the finite element numerical model ADCIRC. The model was developed to produce long numerical simulations on the order of a year for very large computational domains: for example, the entire east coast of the United States. The model was designed for high computational efficiency and was tested extensively for both hydrodynamic accuracy and numerical stability. Results of the tests are included in the report.

AVAILABILITY OF REPORT: The report is available through the Interlibrary Loan Service from the US Army Engineer Waterways Experiment Station (WES) Library, telephone number (601) 634-2355. National Technical Information Service (NTIS) report numbers may be requested from WES Librarians.

To purchase a copy of the report, call NTIS at (703) 487-4780.

About the Authors: Dr. Norman W. Scheffner, Coastal Processes Branch of the Coastal Engineering Research Center's Research Division at the US Army Engineer Waterways Experiment Station, was the Principal Investigator for the DRP work unit. Dr. R. A. Luettich, Jr., Institute of Marine Sciences, University of North Carolina at Chapel Hill, and Dr. J. J. Westerink, Department of Civil Engineering, University of Notre Dame, assisted Dr. Scheffner in developing the modeling goals, concepts, and methodologies. Drs. Luettich and Westerink completed development and implementation of the model. For further information about the DRP, contact Mr. E. Clark McNair, Jr., Manager, DRP, at (601) 634-2070.

November 1992

REPORT DOCUMENTATION PAGE

Form Approved
OMB No. 0704-0188

1. AGENCY USE ONLY *(Leave blank)*	2. REPORT DATE	3. REPORT TYPE AND DATES COVERED
	November 1992	Report 1 of a series

4. TITLE AND SUBTITLE
ADCIRC: An Advanced Three-Dimensional Circulation Model for Shelves, Coasts, and Estuaries; Report 1, Theory and Methodology of ADCIRC-2DDI and ADCIRC-3DL

5. FUNDING NUMBERS
WU No. 32466

6. AUTHOR(S)
R. A. Luettich, Jr., J. J. Westerink,
Norman W. Scheffner

7. PERFORMING ORGANIZATION NAME(S) AND ADDRESS(ES)
See reverse.

8. PERFORMING ORGANIZATION REPORT NUMBER
Technical Report
DRP-92-6

9. SPONSORING/MONITORING AGENCY NAME(S) AND ADDRESS(ES)
US Army Corps of Engineers
Washington, DC 20314-1000

10. SPONSORING/MONITORING AGENCY REPORT NUMBER

11. SUPPLEMENTARY NOTES
Available from National Technical Information Service, 5285 Port Royal Road, Springfield, VA 22161.

12a. DISTRIBUTION/AVAILABILITY STATEMENT
Approved for public release; distribution is unlimited.

12b. DISTRIBUTION CODE

13. ABSTRACT *(Maximum 200 words)*

This report describes the theory, methodology, and verification of the ADCIRC (ADvanced CIRCulation) finite element numerical models. ADCIRC-2DDI is a two-dimensional, depth-integrated hydrodynamic model. ADCIRC-3DL is a three-dimensional model that couples the external mode solution generated by ADCIRC-2DDI to a locally one-dimensional internal mode solution. The numerical internal mode solution can be obtained using either velocity or stress as the dependent variable.

ADCIRC has been developed to simulate hydrodynamic circulation along shelves, coasts, and within estuaries. To allow long numerical simulations (on the order of a year) over very large computational domains (for example, the entire east coast of the United States), ADCIRC has been designed to have high computational efficiency and has been tested extensively for both hydrodynamic accuracy and numerical stability. The results of these tests are included in this report.

14. SUBJECT TERMS
See reverse

15. NUMBER OF PAGES
141

16. PRICE CODE

17. SECURITY CLASSIFICATION OF REPORT	18. SECURITY CLASSIFICATION OF THIS PAGE	19. SECURITY CLASSIFICATION OF ABSTRACT	20. LIMITATION OF ABSTRACT
UNCLASSIFIED	UNCLASSIFIED		

7. (Continued)

University of North Carolina at Chapel Hill, Morehead City, NC 27514

University of Notre Dame, Notre Dame, IN 46556

USAE Waterways Experiment Station, Coastal Engineering Research Center, 3909 Halls Ferry Road, Vicksburg, MS 39180-6199

14. (Continued)

Bottom stress
Circulation model
Direct stress solution
Finite element method
Hydrodynamic model
Numerical model
Three-dimensional model
Two-dimensional model

PREFACE

The work described in this report was authorized and funded under Work Unit No. 32466, "Numerical Simulation Techniques for Evaluating Long-Term Fate and Stability of Dredged Material Disposed in Open Water," of Technical Area 1 (TA1), "Analysis of Dredged Material Placed in Open Water," of the Dredging Research Program (DRP), sponsored by Headquarters, US Army Corps of Engineers (HQUSACE). Messrs. Robert Campbell and John Lockhart, Jr., DRP Chief and TA1 Technical Monitor from HQUSACE, respectively. Mr. E. Clark McNair, Jr., Coastal Engineering Research Center (CERC), US Army Engineer Waterways Experiment Station (WES), was DRP Program Manager (PM) and Dr. Lyndell Z. Hales, CERC, was Assistant PM. Dr. Nicholas C. Kraus, Senior Scientist, Research Division (RD), CERC, was the Technical Manager of the DRP TA1 and Dr. Norman W. Scheffner, Coastal Processes Branch (CPB), RD, CERC, is the Principal Investigator of Work Unit No. 32466. The numerical modeling goals, concepts, and methodologies were developed by Drs. Norman W. Scheffner, Richard A. Luettich, Jr., and Joannes J. Westerink. Development and implementation of the model were completed by Drs. Luettich and Westerink.

This study was performed and the report prepared over the period of 19 July 1988 through 30 September 1990. Dr. Scheffner was under the administrative supervision of Dr. James R. Houston, Director, CERC; Mr. Charles C. Calhoun, Jr., Assistant Director, CERC; Mr. H. Lee Butler, Chief, RD, CERC; and Mr. Bruce A. Ebersole, Chief, CPB, RD, CERC. Ms. Janean C. Shirley, Information Technology Laboratory, WES, edited the final report.

At the time of publication of this report, Director of WES was Dr. Robert W. Whalin. Commander was COL Leonard G. Hassell, EN.

Additional information on this report can be obtained from Mr. E. Clark McNair, Jr., DRP Program Manager, at (601)634-2070 or Dr. Norman W. Scheffner, Principal Investigator, at (601)634-3220.

CONTENTS

LIST OF TABLES

LIST OF FIGURES

CONVERSION FACTORS, NON–SI TO SI (METRIC) UNITS OF MEASUREMENT

Non–SI units of measurement used in this report can be converted to SI (metric) units as follows:

Multiply	By	To Obtain
degrees	0.01745329	radians
feet	0.3048	meters

SUMMARY

This report describes the theory, methodology, and verification of the finite element numerical model ADCIRC, an ADvanced three–dimensional CIRCulation model developed for the specific purpose of generating long time periods of hydrodynamic circulation along shelves, coasts, and within estuaries. The intent of the model is to produce long numerical simulations (on the order of a year) for very large computational domains (for example the entire east coast of the US). Therefore, the model was designed for high computational efficiency and was tested extensively for both hydrodynamic accuracy and numerical stability. The results of these tests are included in this report.

The ADCIRC model was developed by the Dredging Research Program (a) to provide a means of generating a database of harmonic constituents for tidal elevation and current at discrete locations along the east, west, and Gulf of Mexico coasts, and (b) to utilize tropical and extratropical global boundary conditions to compute frequency indexed storm surge hydrographs along the US coasts. The database of storm and tidal surface elevation and current data is being developed to provide site–specific hydrodynamic boundary conditions for use in analyzing the long–term stability of existing or proposed dredge material disposal sites.

The overall intent of the DRP work unit is to provide a unified and systematic methodology for investigating the dispersive or nondispersive characteristics of a disposal site. These goals can be realized through the use of hydrodynamic, sediment transport, and bathymetry change models. The ADCIRC model provides the tidal– and storm–related hydrodynamic forcings necessary for site–specific site designation.

ADCIRC: AN ADVANCED THREE-DIMENSIONAL CIRCULATION MODEL FOR SHELVES, COASTS, AND ESTUARIES

THEORY AND METHODOLOGY

PART I: INTRODUCTION

1. Interest in developing a more accurate technique for predicting sea surface elevation and circulation in coastal areas has been spurred on by concerns relating to navigation, shoreline flooding, pollutant transport, and sediment transport. A model for computing the important features of circulation patterns driven by tides, wind, atmospheric pressure gradients, and ocean currents must be broad in scope and size. To simplify seaward boundary conditions, yet include important flow details, the model must encompass large domains while providing a high degree of resolution in high–gradient regions as well as in nearshore areas. This means that the model should allow for the simultaneous solution of flow in continental shelf regions, coastal areas, and in estuarine systems. The model should solve the three–dimensional conservation equations [thereby resolving the vertical profile of horizontal velocity] instead of the widely used depth–integrated conservation equations. This is necessary since it is impossible to assume a relationship between bottom stress and depth–averaged velocity that is generally valid for stratified flows, Ekman layers, and wind–driven circulation in enclosed or semi–enclosed basins or in cases where wave orbital velocities or suspended sediment concentration gradients are significant near the bottom. Furthermore, it is impossible to assume values for momentum dispersion coefficients, which are inherent in depth–integrated solutions, that are generally valid in complex flows.

2. The requirements of very large domains, a high degree of horizontal resolution in portions of the domain, and the resolution of rapidly varying vertical profiles of horizontal velocity place strenuous demands on even the largest supercomputers. The goal in the development of ADCIRC (ADvanced three–dimensional CIRCulation model) has been to bring together algorithms that are highly flexible, accurate, and extremely efficient. These issues are closely interrelated and have been emphasized in the selection of discretization techniques. The algorithms that comprise ADCIRC allow for an effective minimization in the required number of

degrees of freedom for a desired level of accuracy, show good stability characteristics, generate no spurious artificial modes, have minimal inherent artificial numerical damping, efficiently separate the partial differential equations into small systems of algebraic equations with time–independent matrices, and are capable of running months to years of simulation while providing detailed intra–tidal computations.

3. The framework within which ADCIRC has been developed is a coupled external mode – internal mode approach. This technique has proven to be successful in past three–dimensional models and can significantly reduce the cost of three–dimensional hydrostatic circulation computations. The governing equations and the basic concept behind mode splitting are discussed in detail in Part II. The external mode solution, which uses the well–known depth–integrated or shallow–water equations, is discussed in Part III. Key features of the external mode solution include the use of a generalized wave–continuity equation (GWCE) formulation and numerical discretizations using the finite element (FE) method in space and the finite difference (FD) method in time. Results are presented using the external mode solution as a stand–alone, two–dimensional model on a quarter annular test case and the North Sea/English Channel system. Part IV focuses on the internal mode solution. During the development of ADCIRC, a novel technique was discovered that replaces velocity with shear stress as the dependent variable in the internal mode equations. The resulting direct stress solution [DSS] allows physically realistic boundary layers to be included explicitly in a three–dimensional model. This formulation of the internal mode equations should be invaluable for modeling coastal and shelf circulation, in which the bottom and surface boundary layers comprise a significant portion of the water column, and for modeling processes that are critically dependent on boundary layer physics such as wave–current interaction, sediment transport, oil spill movement, ice floe movement, energy dissipation, physical–biological couplings, etc. Thorough descriptions of the DSS formulation and testing are presented in Part IV.

4. ADCIRC is being developed and implemented as a multi–level hierarchy of models. A 2DDI (two–dimensional, depth–integrated) option solves only the depth–integrated, external mode equations using parametric relationships for bottom friction and momentum dispersion. A 3DL (three–dimensional, local) option uses horizontally decoupled internal mode equations to solve for the vertical profile of horizontal velocity and to evaluate bottom friction and momentum dispersion terms for the depth–integrated external mode solution. A 3DLB (three–dimensional, local, baroclinic) option includes baroclinic terms as a diagnostic feature. Finally, the 3D and 3DB options solve the complete internal mode equations for nonstratified and

stratified flows, respectively. At present ADCIRC–2DDI is fully implemented and operational, ADCIRC–3DL is being tested, and other ADCIRC versions are under development.

5. ADCIRC achieves a high level of simultaneous regional/local modeling, accuracy, and efficiency. This performance is a consequence of the extreme grid flexibility, the optimized governing equation formulations, and the numerical algorithms used in ADCIRC. Together, these allow ADCIRC to run with order of magnitude reductions in the number of degrees of freedom and the computational costs of many presently existing circulation models.

PART II: GOVERNING EQUATIONS

Three–dimensional Equations for Nearly Horizontal Flow in Cartesian Coordinates

6. A survey of several recent review volumes (e.g., Heaps 1987; Nihoul and Jamart 1987; ASCE 1988a,b; Davies 1989) indicates that the turbulent incompressible Reynolds equations simplified using the Boussinesq approximation and the hydrostatic pressure approximation generally form the basis for state–of–the–art numerical models of coastal/shelf circulation. Although these equations describe fluid motion in three dimensions, because of the simplification of the vertical momentum equations, they are only correct for nearly horizontal flow (Koutitas 1987; Abbot 1990). Using a right–handed Cartesian coordinate system these equations can be written as

$$\frac{\partial u}{\partial x} + \frac{\partial v}{\partial y} + \frac{\partial w}{\partial z} = 0 \tag{1}$$

$$\frac{\partial u}{\partial t} + u\frac{\partial u}{\partial x} + v\frac{\partial u}{\partial y} + w\frac{\partial u}{\partial z} - fv = -\frac{\partial}{\partial x}\left[\frac{p}{\rho_o} - \Gamma\right] + \frac{1}{\rho_o}\left[\frac{\partial \tau_{xx}}{\partial x} + \frac{\partial \tau_{yx}}{\partial y} + \frac{\partial \tau_{zx}}{\partial z}\right] \tag{2}$$

$$\frac{\partial v}{\partial t} + u\frac{\partial v}{\partial x} + v\frac{\partial v}{\partial y} + w\frac{\partial v}{\partial z} + fu = -\frac{\partial}{\partial y}\left[\frac{p}{\rho_o} - \Gamma\right] + \frac{1}{\rho_o}\left[\frac{\partial \tau_{xy}}{\partial x} + \frac{\partial \tau_{yy}}{\partial y} + \frac{\partial \tau_{zy}}{\partial z}\right] \tag{3}$$

$$\frac{\partial p}{\partial z} = -\rho g \tag{4}$$

where

$f = 2\Omega\sin\phi$ = Coriolis parameter

g = acceleration of gravity

Γ = tide generating potential

ν = molecular viscosity

$p(x,y,z,t)$ = time–averaged pressure

$\rho(x,y,z,t)$ = density of water

ρ_o = reference density of water

t = time

T = integration time scale for separating turbulent and time–averaged quantities

$\tau_{xx}(x,y,z,t) = \nu\frac{\partial u}{\partial x} - \frac{1}{T}\int_0^T u'u'\,dt$ – combined viscous and turbulent Reynolds stress

$\tau_{yx}(x,y,z,t) = \nu\frac{\partial v}{\partial x} - \frac{1}{T}\int_0^T u'v'\,dt$ – combined viscous and turbulent Reynolds stress

$\tau_{zx}(x,y,z,t) = \nu \frac{\partial w}{\partial x} - \frac{1}{T}\int_0^T u'w'\,dt$ – combined viscous and turbulent Reynolds stress

$\tau_{xy}(x,y,z,t) = \nu \frac{\partial u}{\partial y} - \frac{1}{T}\int_0^T v'u'\,dt$ – combined viscous and turbulent Reynolds stress

$\tau_{yy}(x,y,z,t) = \nu \frac{\partial v}{\partial y} - \frac{1}{T}\int_0^T v'v'\,dt$ – combined viscous and turbulent Reynolds stress

$\tau_{zy}(x,y,z,t) = \nu \frac{\partial w}{\partial y} - \frac{1}{T}\int_0^T v'w'\,dt$ – combined viscous and turbulent Reynolds stress

ϕ = degrees latitude

$u(x,y,z,t)$, $v(x,y,z,t)$, $w(x,y,z,t)$ = time–averaged velocities in the x, y and z directions

$u'(x,y,z,t)$, $v'(x,y,z,t)$, $w'(x,y,z,t)$ = departures of the instantaneous turbulent velocities from the time–averaged velocities

x, y = horizontal coordinate directions

z = vertical coordinate direction

Ω = angular speed of the Earth (7.29212×10^{-5} rad/s)

7. Using the vertical momentum equation, pressure can be eliminated as a dependent variable from Equations 2 and 3, to give:

$$\frac{\partial u}{\partial t} + u\frac{\partial u}{\partial x} + v\frac{\partial u}{\partial y} + w\frac{\partial u}{\partial z} - fv = -\frac{\partial}{\partial x}\left[\frac{p_s}{\rho_o} + g\zeta - \Gamma\right] + \frac{\partial}{\partial z}\left(\frac{\tau_{zx}}{\rho_o}\right) - b_x + m_x \qquad (5)$$

$$\frac{\partial v}{\partial t} + u\frac{\partial v}{\partial x} + v\frac{\partial v}{\partial y} + w\frac{\partial v}{\partial z} + fu = -\frac{\partial}{\partial y}\left[\frac{p_s}{\rho_o} + g\zeta - \Gamma\right] + \frac{\partial}{\partial z}\left(\frac{\tau_{zy}}{\rho_o}\right) - b_y + m_y \qquad (6)$$

where

$b_x = \frac{g}{\rho_o}\frac{\partial}{\partial x}\int_z^\zeta (\rho - \rho_o)\,dz$ – baroclinic x – forcing

$b_y = \frac{g}{\rho_o}\frac{\partial}{\partial y}\int_z^\zeta (\rho - \rho_o)\,dz$ – baroclinic y – forcing

$\zeta(x,y,t)$ = free surface elevation relative to the geoid

$m_x = \frac{1}{\rho_o}\left[\frac{\partial \tau_{xx}}{\partial x} + \frac{\partial \tau_{yx}}{\partial y}\right]$ – horizontal momentum diffusion

$m_y = \frac{1}{\rho_o}\left[\frac{\partial \tau_{xy}}{\partial x} + \frac{\partial \tau_{yy}}{\partial y}\right]$ – horizontal momentum diffusion

$p_s(x,y,t)$ – atmospheric pressure at the free surface

8. The solution of Equations 1, 5, and 6 requires the following boundary conditions:

a. At the free surface,

$$w = \frac{\partial \zeta}{\partial t} + u \frac{\partial \zeta}{\partial x} + v \frac{\partial \zeta}{\partial y} \tag{7}$$

$$\tau_{zx} = \tau_{sx}, \ \tau_{zy} = \tau_{sy} \tag{8}$$

where $\tau_{sx}(x,y,t)$ and $\tau_{sy}(x,y,t)$ are wind stresses applied at the water surface.

b. At the bottom,

$$w = -\left[\frac{\partial h}{\partial t} + u \frac{\partial h}{\partial x} + v \frac{\partial h}{\partial y}\right] \tag{9}$$

$$\tau_{zx}/\rho_o = \tau_{bx}/\rho_o = k u_b, \ \tau_{zy}/\rho_o = \tau_{by}/\rho_o = k v_b \tag{10a}$$

or

$$u = 0, \ v = 0 \quad @ \quad z = -h + z_o \tag{10b}$$

where $\tau_{bx}(x,y,t)$ and $\tau_{by}(x,y,t)$ are bottom stresses, $u_b(x,y,t)$ and $v_b(x,y,t)$ are near bottom velocities, k is a slip coefficient and z_o is the effective bottom roughness height (e.g., $z_o = k_s/30$ where k_s is the physical bottom roughness). The physically correct no–slip condition, Equation 10b, is often replaced by the slip condition, Equation 10a, to avoid the need to numerically resolve the sharp vertical gradients of u and v that exist near the bottom. A quadratic slip condition is obtained by setting

$$k = C_d \ (u_b^2 + v_b^2)^{1/2} \tag{11}$$

If the velocity profile is logarithmic between the elevation where u_b and v_b are computed, $(-h+z_b)$, and the bottom, $(-h+z_o)$, C_d can be defined rigorously as

$$C_d = \left\{\frac{1}{\kappa} \ln[(z_b-h)/(z_o-h)]\right\}^{-2} \tag{12}$$

where κ is the von Kármán constant. Often the quadratic slip condition is replaced by a linear slip condition by setting k equal to a constant.

c. At land boundaries normal flux is specified. Typically, this is zero for a solid boundary or nonzero for a river boundary.

d. At open boundaries (either along the ocean or at rivers) the free surface elevation, $\zeta(x,y,t)$, is specified, a radiation boundary condition is used to allow waves to enter and propagate out of the domain (Davies and Furnes 1980; Reid 1990), or the discharge is specified.

Three–dimensional Equations for Nearly Horizontal Flow in σ Coordinates

9. It is often useful to transform Equations 1, 5 and 6 into a bottom and surface–following "σ" coordinate system. By this means, numerical solutions of the transformed equations maintain the same vertical resolution at each horizontal grid point, regardless of variations in depth (Davies 1985; Blumberg and Mellor 1987). In a general σ–coordinate system (where σ = a at the free surface and σ = b at the

bottom):

$$x_\sigma \equiv x \tag{13a}$$

$$y_\sigma \equiv y \tag{13b}$$

$$\sigma \equiv a + \frac{(a-b)(z-\zeta)}{H} \tag{13c}$$

$$t_\sigma \equiv t \tag{13d}$$

where

$H(x,y,t) \equiv \zeta + h$ – total water depth to the free surface

$h(x,y)$ – bathymetric depth relative to the geoid

(The σ subscript is used to denote variables in the new coordinate system.)

10. Derivatives are converted to the σ–coordinate system using the chain rule:

$$\frac{\partial}{\partial x} = \frac{\partial}{\partial x_\sigma} + \frac{\partial \sigma}{\partial x}\frac{\partial}{\partial \sigma} = \frac{\partial}{\partial x_\sigma} - \frac{(a-b)}{H}\left[\frac{\partial \zeta}{\partial x_\sigma} + \frac{(\sigma-a)}{(a-b)}\frac{\partial H}{\partial x_\sigma}\right]\frac{\partial}{\partial \sigma} \tag{14a}$$

$$\frac{\partial}{\partial y} = \frac{\partial}{\partial y_\sigma} + \frac{\partial \sigma}{\partial y}\frac{\partial}{\partial \sigma} = \frac{\partial}{\partial y_\sigma} - \frac{(a-b)}{H}\left[\frac{\partial \zeta}{\partial y_\sigma} + \frac{(\sigma-a)}{(a-b)}\frac{\partial H}{\partial y_\sigma}\right]\frac{\partial}{\partial \sigma} \tag{14b}$$

$$\frac{\partial}{\partial z} = \frac{(a-b)}{H}\frac{\partial}{\partial \sigma} \tag{14c}$$

$$\frac{\partial}{\partial t} = \frac{\partial}{\partial t_\sigma} + \frac{\partial \sigma}{\partial t}\frac{\partial}{\partial \sigma} = \frac{\partial}{\partial t_\sigma} - \frac{(a-b)}{H}\left[\frac{\partial \zeta}{\partial t_\sigma} + \frac{(\sigma-a)}{(a-b)}\frac{\partial H}{\partial t_\sigma}\right]\frac{\partial}{\partial \sigma} \tag{14d}$$

11. The velocity component aligned in the σ direction is defined as

$$w_\sigma \equiv \frac{d\sigma}{dt_\sigma} = \frac{(a-b)}{H}\left\{w - \left[\frac{\partial \zeta}{\partial t_\sigma} + \frac{(\sigma-a)}{(a-b)}\frac{\partial H}{\partial t_\sigma}\right] - u\left[\frac{\partial \zeta}{\partial x_\sigma} + \frac{(\sigma-a)}{(a-b)}\frac{\partial H}{\partial x_\sigma}\right] - v\left[\frac{\partial \zeta}{\partial y_\sigma} + \frac{(\sigma-a)}{(a-b)}\frac{\partial H}{\partial y_\sigma}\right]\right\} \tag{15}$$

12. The baroclinic forcings b_{x_σ}, b_{y_σ}, and the horizontal momentum diffusion m_{x_σ}, m_{y_σ} in the σ coordinate system become:

$$b_{x_\sigma} = \frac{g(\rho-\rho_0)}{\rho_0}\frac{\partial \zeta}{\partial x_\sigma} + \frac{g}{\rho_0(a-b)}\left\{\frac{\partial}{\partial x_\sigma}\left[H\int_\sigma^a (\rho-\rho_0)\, d\sigma\right] + (\sigma-a)\frac{\partial H}{\partial x_\sigma}(\rho-\rho_0)\right\} \tag{16a}$$

$$b_{y_\sigma} = \frac{g(\rho-\rho_0)}{\rho_0}\frac{\partial \zeta}{\partial y_\sigma} + \frac{g}{\rho_0(a-b)}\left\{\frac{\partial}{\partial y_\sigma}\left[H\int_\sigma^a (\rho-\rho_0)\, d\sigma\right] + (\sigma-a)\frac{\partial H}{\partial y_\sigma}(\rho-\rho_0)\right\} \tag{16b}$$

$$m_{x_\sigma} = \frac{1}{\rho_0}\left[\frac{\partial \tau_{xx}}{\partial x_\sigma} + \frac{\partial \tau_{yx}}{\partial y_\sigma}\right] - \frac{(a-b)}{H\rho_0}\left\{\left[\frac{\partial \zeta}{\partial x_\sigma} + \frac{(\sigma-a)}{(a-b)}\frac{\partial H}{\partial x_\sigma}\right]\frac{\partial \tau_{xx}}{\partial \sigma} + \left[\frac{\partial \zeta}{\partial y_\sigma} + \frac{(\sigma-a)}{(a-b)}\frac{\partial H}{\partial y_\sigma}\right]\frac{\partial \tau_{yx}}{\partial \sigma}\right\} \quad (17a)$$

$$m_{y_\sigma} = \frac{1}{\rho_0}\left[\frac{\partial \tau_{xy}}{\partial x_\sigma} + \frac{\partial \tau_{yy}}{\partial y_\sigma}\right] - \frac{(a-b)}{H\rho_0}\left\{\left[\frac{\partial \zeta}{\partial y_\sigma} + \frac{(\sigma-a)}{(a-b)}\frac{\partial H}{\partial y_\sigma}\right]\frac{\partial \tau_{yy}}{\partial \sigma} + \left[\frac{\partial \zeta}{\partial x_\sigma} + \frac{(\sigma-a)}{(a-b)}\frac{\partial H}{\partial x_\sigma}\right]\frac{\partial \tau_{xy}}{\partial \sigma}\right\} \quad (17b)$$

13. Substituting Equations 13 – 17 into Equations 1, and 4 – 6, and rearranging terms gives the three–dimensional governing equations in the σ–coordinate system. Dropping the σ subscripts for notational convenience, the transformed equations are

$$\frac{\partial \zeta}{\partial t} + \frac{\partial uH}{\partial x} + \frac{\partial vH}{\partial y} + \frac{\partial wH}{\partial \sigma} = 0 \quad (18)$$

$$\frac{\partial u}{\partial t} + u\frac{\partial u}{\partial x} + v\frac{\partial u}{\partial y} + w\frac{\partial u}{\partial \sigma} - fv = -\frac{\partial}{\partial x}\left[\frac{p_s}{\rho_0} + g\zeta - \Gamma\right] + \frac{(a-b)}{H}\frac{\partial}{\partial \sigma}\left(\frac{\tau_{zx}}{\rho_0}\right) - b_x + m_x \quad (19)$$

$$\frac{\partial v}{\partial t} + u\frac{\partial v}{\partial x} + v\frac{\partial v}{\partial y} + w\frac{\partial v}{\partial \sigma} + fu = -\frac{\partial}{\partial y}\left[\frac{p_s}{\rho_0} + g\zeta - \Gamma\right] + \frac{(a-b)}{H}\frac{\partial}{\partial \sigma}\left(\frac{\tau_{zy}}{\rho_0}\right) - b_y + m_y \quad (20)$$

$$\frac{\partial p}{\partial \sigma} = -\frac{\rho g H}{(a-b)} \quad (21)$$

14. The σ equations use the same boundary conditions as the original equations with the exception that $w_\sigma = 0$ at the free surface and at the bottom.

Vertically Integrated, Two–dimensional Equations for Nearly Horizontal Flow

15. The three–dimensional equations can be integrated over the vertical to yield a set of two–dimensional equations for free surface displacement and depth–averaged velocity. In conservative form these equations are:

$$\frac{\partial \zeta}{\partial t} + \frac{\partial UH}{\partial x} + \frac{\partial VH}{\partial y} = 0 \quad (22)$$

$$\frac{\partial UH}{\partial t} + \frac{\partial UUH}{\partial x} + \frac{\partial UVH}{\partial y} - fVH = -H\frac{\partial}{\partial x}\left[\frac{p_s}{\rho_0} + g(\zeta - \alpha\eta)\right]$$

$$+ M_x + D_x + B_x + \frac{\tau_{sx}}{\rho_o} - \frac{\tau_{bx}}{\rho_o} \qquad (23)$$

$$\frac{\partial VH}{\partial t} + \frac{\partial VUH}{\partial x} + \frac{\partial VVH}{\partial y} + fUH = - H \frac{\partial}{\partial y}\left[\frac{p_s}{\rho_o} + g(\zeta - \alpha\eta)\right]$$

$$+ M_y + D_y + B_y + \frac{\tau_{sy}}{\rho_o} - \frac{\tau_{by}}{\rho_o} \qquad (24)$$

where

α = effective Earth elasticity factor ($\alpha = 0.69$)

$B_x \equiv - \int_{-h}^{\zeta} b_x \, dz$ – depth–integrated baroclinic forcing

$B_y \equiv - \int_{-h}^{\zeta} b_y \, dz$ – depth–integrated baroclinic forcing

$D_x \equiv - \frac{\partial D_{uu}}{\partial x} - \frac{\partial D_{uv}}{\partial y}$ – momentum dispersion

$D_y \equiv - \frac{\partial D_{uv}}{\partial x} - \frac{\partial D_{vv}}{\partial y}$ – momentum dispersion

$D_{uu} \equiv \int_{-h}^{\zeta} \hat{u}\hat{u} \, dz, \qquad D_{uv} \equiv \int_{-h}^{\zeta} \hat{v}\hat{u} \, dz, \qquad D_{vv} \equiv \int_{-h}^{\zeta} \hat{v}\hat{v} \, dz$

$\eta(x,y,t)$ – Newtonian equilibrium tide potential

$M_x = \frac{\partial}{\partial x}\int_{-h}^{\zeta} \frac{\tau_{xx}}{\rho_o} \, dz + \frac{\partial}{\partial y}\int_{-h}^{\zeta} \frac{\tau_{yx}}{\rho_o} \, dz$ – depth–integrated, horizontal momentum diffusion

$M_y = \frac{\partial}{\partial x}\int_{-h}^{\zeta} \frac{\tau_{xy}}{\rho_o} \, dz + \frac{\partial}{\partial y}\int_{-h}^{\zeta} \frac{\tau_{yy}}{\rho_o} \, dz$ – depth–integrated, horizontal momentum diffusion

$U(x,y,t) \equiv \frac{1}{H}\int_{-h}^{\zeta} u \, dz$ – depth–averaged horizontal velocity

$V(x,y,t) \equiv \frac{1}{H}\int_{-h}^{\zeta} v \, dz$ – depth–averaged horizontal velocity

$\hat{u}(x,y,z,t) \equiv u - U$ – departure of horizontal velocity from depth–averaged velocity

$\hat{v}(x,y,z,t) \equiv v - V$ – departure of horizontal velocity from depth–averaged velocity

16. In non–conservative form, the vertically integrated momentum conservation equations are:

$$\frac{\partial U}{\partial t} + U\frac{\partial U}{\partial x} + V\frac{\partial U}{\partial y} - fV = - \frac{\partial}{\partial x}\left[\frac{p_s}{\rho_o} + g(\zeta - \alpha\eta)\right]$$

$$+ \frac{1}{H}\left[M_x + D_x + B_x + \frac{\tau_{sx}}{\rho_o} - \frac{\tau_{bx}}{\rho_o}\right] \qquad (25)$$

$$\frac{\partial V}{\partial t} + U\frac{\partial V}{\partial x} + V\frac{\partial V}{\partial y} + fU = -\frac{\partial}{\partial y}\left[\frac{p_s}{\rho_o} + g(\zeta - \alpha\eta)\right] + \frac{1}{H}\left[M_y + D_y + B_y + \frac{\tau_{sy}}{\rho_o} - \frac{\tau_{by}}{\rho_o}\right] \quad (26)$$

17. The derivation of the Newtonian equilibrium tide potential, η, is presented by Reid (1990). A practical expression for η given by Reid is

$$\eta(\lambda,\phi,t) = \sum_{n,j} C_{jn}\, f_{jn}(t_o)\, L_j(\phi)\, \cos[2\pi(t-t_o)/T_{jn} + j\lambda + \chi_{jn}(t_o)] \quad (27)$$

where

C_{jn} = constant characterizing the amplitude of constituent n of species j (Table 1)

$f_{jn}(t)$ = time–dependent nodal factor

j = 0, 1, 2 – tidal species (j=0 declinational, j=1 diurnal, j=2 semidiurnal)

$L_0 = 3\sin^2(\phi) - 1$

$L_1 = \sin(2\phi)$

$L_2 = \cos^2(\phi)$

λ, ϕ = degrees of longitude and latitude, respectively

t_o = reference time

T_{jn} = constant characterizing the period of constituent n of species j (Table 1)

$\chi_{jn}(t)$ – time–dependent astronomical argument

Values for f_{jn} and χ_{jn} can be computed from tables (e.g., Schureman 1941) or using available harmonic analysis packages (e.g., Foreman 1977).

18. The gradient of $\alpha\eta$ results in the effective tide–producing force. The factor α accounts for the reduction in the field of gravity due to the existence of small tidal deformations of the Earth's surface called Earth tides. The value $\alpha = 0.69$ is the ratio of the theoretical period of the Earth's wobble derived by Euler (assuming the Earth to be a perfectly rigid sphere) to the observed period of the Earth's wobble (Reid 1990). (Therefore α is a global measure of the rigidity of the Earth. For reference, $\alpha = 1$ would correspond to a perfectly rigid sphere.) $\alpha = 0.69$ has been used for modeling global ocean tides by investigators including Schwiderski (1980) and Hendershott (1981).

19. Due to their computational efficiency, models based on the vertically integrated equations have been widely used for modeling coastal, shelf, and even open ocean circulation (e.g., Leendertse 1967; Wang and Connor 1975; Spaulding 1984; Smith and Cheng 1987; Werner and Lynch 1987; Walters 1987; Vincent and Le Provost 1988; Westerink, Stolzenbach, and Connor 1989; Signell 1989). All of the physics contained in the original three–dimensional governing equations are embedded

Table 1

Constants for the Principal Tidal Constituents (from Reid 1990)

Species	Constituent	C m	T solar days or hrs*
0	M_f fortnightly lunar	0.041742	13.660791d
	M_m monthly lunar	0.022026	27.554553d
	S_{sa} semiannual solar	0.019446	182.6211d
	S_a annual solar	**	365.2597d
1	K_1 luni–solar	0.141565	23.9344696h
	O_1 principal lunar	0.100514	25.8193417h
	P_1 principal solar	0.046843	24.0658902h
	Q_1 elliptical lunar	0.019256	26.8683566h
2	M_2 principal lunar	0.242334	12.4206012h
	S_2 principal solar	0.112841	12.0000000h
	N_2 elliptical lunar	0.046398	12.6583482h
	K_2 luni–solar	0.030704	11.9672348h

*One lunar day = 1.035050 solar days or 24.8412 solar hours

**The annual solar tide is heavily dependent on seasonal heating and cooling of the ocean, as well as radiation pressure.

in the vertically integrated equations if the bottom stress and the momentum dispersion terms are specified correctly. Although more sophisticated approaches have been developed for specialized conditions (Lynch and Officer 1985; Nihoul and Djenidi 1987; Tee 1987; Poon 1988; Jenter and Madsen 1989), bottom stress is usually parameterized as a collinear function of the depth–averaged velocity, and momentum dispersion is either neglected or represented as a "diffusion–like" function of the depth–averaged velocity (Bedford 1984).

20. Parameterized bottom stress relationships are typically quadratic in the depth–averaged velocity and of the form

$$\frac{\tau_{bx}}{\rho_o} = C_f \left(U^2 + V^2\right)^{1/2} U \tag{28a}$$

$$\frac{\tau_{by}}{\rho_o} = C_f \left(U^2 + V^2\right)^{1/2} V \tag{28b}$$

where C_f is computed using one of the following relationships:

$$C_f = \frac{f_{DW}}{8} \tag{29a}$$

$$C_f = \frac{g}{C^2} \tag{29b}$$

$$C_f = \frac{n^2 g}{h^{1/3}} \tag{29c}$$

In Equation 29, f_{DW} is the Darcy–Weisbach friction factor, C is the Chezy friction coefficient, and n is the Manning friction factor.

21. The depth–integrated lateral momentum diffusion terms are typically lumped together with the momentum dispersion terms into a standard isotropic and homogeneous eddy diffusion/dispersion model (Blumberg and Mellor 1987)

$$M_x + D_x = E_{h1}^{MD} \left[2\frac{\partial^2 UH}{\partial x^2} + \frac{\partial^2 UH}{\partial y^2} + \frac{\partial^2 VH}{\partial x \partial y}\right] \tag{30a}$$

$$M_y + D_y = E_{h1}^{MD} \left[\frac{\partial^2 VH}{\partial x^2} + 2\frac{\partial^2 VH}{\partial y^2} + \frac{\partial^2 UH}{\partial x \partial y}\right] \tag{30b}$$

where E_{h1}^{MD} is a horizontal eddy diffusion/dispersion coefficient. Equation 30 is based directly on a molecular diffusion analogy as applied to depth–integrated flow. Kolar and Gray (1990) use a slightly simpler model that approximates Equation 30 as:

$$M_x + D_x = E_{h2}^{MD} \left[\frac{\partial^2 UH}{\partial x^2} + \frac{\partial^2 UH}{\partial y^2}\right] \tag{31a}$$

$$M_y + D_y = E_{h2}^{MD} \left[\frac{\partial^2 VH}{\partial x^2} + \frac{\partial^2 VH}{\partial y^2} \right] \quad (31b)$$

where E_{h2}^{MD} is an eddy diffusion/dispersion coefficient that will generally not be equal to E_{h1}^{MD}.

22. For flows with horizontal length scales that are large compared to the depth, M_x and M_y are negligible in the momentum balance in Equations 25 and 26 (Blumberg and Mellor 1987). D_x and D_y are similarly small when the velocity profile is nearly uniform over the vertical. In such flows E_{h1}^{MD} or E_{h2}^{MD} are either set to zero or kept at a relatively small value to provide stability to the numerical scheme. (The latter must be done with considerable caution to ensure that the contributions of these terms in the momentum equations remain small. Otherwise, the model solutions will be artificially altered.) Conversely, when the velocity profile varies strongly over the vertical, D_x and D_y may have a significant contribution to the momentum balance.

23. For tidal flows in relatively shallow, unstratified waters, depth–integrated computations that make use of the parameterizations given in Equations 28 – 31 appear to work reasonably well (although detailed studies of tidal constituent dynamics indicate that all of the flow physics are not captured in two–dimensional simulations due to the form of the bottom friction term (Westerink, Stolzenbach, and Connor 1989)). However, in wind–driven flows, stratified flows, Ekman layers, or when wave orbital velocities or suspended sediment gradients are significant near the bottom, the simple parameterizations for bottom friction and momentum dispersion given above become entirely inadequate. Also, since the depth–averaged velocity may be very different from the actual velocity at a specific elevation in the water column (particularly if flow reversal occurs over the depth), the use of the depth–averaged velocity in a transport model (e.g., for sediment transport) may cause considerable error in predicted transport patterns. Therefore, for many applications of practical interest, a model based solely on the vertically integrated governing equations is not adequate.

Mode Splitting

24. Unfortunately, numerical solutions of the three–dimensional governing equations require substantially increased computer time and storage in comparison to solutions of the vertically integrated equations. To help minimize this cost, most three–dimensional models use some type of mode–splitting scheme. Mode splitting is accomplished by solving the two–dimensional, vertically integrated, "external mode"

equations for the free surface displacement (and sometimes the depth–averaged velocity). The external mode solutions are then used to force "internal mode" equations that account for the vertical propagation of momentum. The internal mode equations are solved for the vertical profile of velocity and the results used to compute τ_{bx}, τ_{by}, D_x, and D_y for subsequent external mode calculations. Internal mode equations have been generated by integrating the three–dimensional equations over discrete layers in the vertical and then subtracting the equations for adjacent layers (Simmons 1974; Sheng and Lick 1980), by subtracting the external mode equations from the three–dimensional equations (Wang 1982; Sheng 1983; Davies 1985), by differentiating the three–dimensional equations in the vertical direction (Tee 1979), or by using the three–dimensional equations themselves (Blumberg and Mellor 1987; Lynch and Werner 1991). (The internal mode equations and their solution are discussed in detail in Part IV of this report.) Mode splitting allows the free surface elevation to be evaluated with the computational efficiency of a vertically integrated model. This can be quite important since the allowable time step for this computation is often severely constrained by accuracy requirements or a Courant stability criterion. Since the internal mode calculations are free from surface gravity waves, the vertical profile of velocity can often be computed using a significantly larger time step than the free surface elevation.

25. In effect, mode splitting replaces the parameterizations of bottom stress and momentum dispersion used in a purely two–dimensional model with values computed from the vertical profiles of velocity generated by the internal mode equations. Therefore, the vertically integrated, external mode computations do not require parameterizations of either bottom stress or momentum dispersion in terms of the depth–averaged velocity. The only parameterizations maintained in the external mode equations are for the horizontal momentum diffusion terms. These terms are usually insignificant in the momentum balance, although for small–scale computations horizontal momentum diffusion can be a physically important process. Most often the horizontal momentum diffusion terms are retained only to provide numerical stability and are parameterized with expressions identical to Equations 30 and 31, i.e.,

$$M_x = E_{h1}^M \left[2\frac{\partial^2 UH}{\partial x^2} + \frac{\partial^2 UH}{\partial y^2} + \frac{\partial^2 VH}{\partial x \partial y} \right] \tag{32a}$$

$$M_y = E_{h1}^M \left[\frac{\partial^2 VH}{\partial x^2} + 2\frac{\partial^2 VH}{\partial y^2} + \frac{\partial^2 UH}{\partial x \partial y} \right] \tag{32b}$$

or alternatively,

$$M_x = E_{h2}^M \left[\frac{\partial^2 UH}{\partial x^2} + \frac{\partial^2 UH}{\partial y^2} \right] \tag{33a}$$

$$M_y = E_{h2}^M \left[\frac{\partial^2 VH}{\partial x^2} + \frac{\partial^2 VH}{\partial y^2}\right] \tag{33b}$$

where E_{h1}^M and E_{h2}^M are eddy coefficients for horizontal momentum diffusion.

Vertical Turbulent Closure

26. The internal mode equations require the parameterization of the vertical turbulent momentum transport terms, τ_{zx} and τ_{zy}, (also called the vertical shear stresses). These terms can dominate the momentum balance in portions of the domain and it is therefore critical to find an adequate closure scheme. Turbulent closure has been and continues to be the subject of considerable research. Recent summaries of this work include Mellor and Yamada (1982); Rodi (1984, 1987); Ferziger (1987); Johns and Oguz (1987); and ASCE (1988a,b). The most general approach is to solve transport equations for the turbulent velocity correlations that make up the turbulent stresses (stress/flux models). However, this adds considerably to the computational burden of a three–dimensional model. Models based on this technique have had little testing and virtually no application to geophysical flows (ASCE 1988b). Also, it appears that these models offer no decisive advantage in shear flows (Launder 1984). Alternatively, the vertical shear stresses can be parameterized in terms of the mean velocity field using eddy viscosity relationships of the form

$$\frac{\tau_{zx}}{\rho_o} = E_v \frac{\partial u}{\partial z} \tag{34a}$$

$$\frac{\tau_{zy}}{\rho_o} = E_v \frac{\partial v}{\partial z} \tag{34b}$$

On dimensional grounds the vertical eddy viscosity E_v should be proportional to a velocity scale v multiplied by a length scale l, both of which are characteristic of the turbulent motion. Particularly simple expressions such as the Prandtl mixing length model can be found for v and l for boundary–layer type flows (Rodi 1987). In more complex flows, v has been related to the square root of the total turbulent kinetic energy, k. The terms k and l (or some combination of k and l such as $\varepsilon \sim k^{3/2}/l$) can be solved for using quasi–empirical transport equations or specified using empirical algebraic expressions. The primary limitations to the eddy viscosity approach are its inability to simulate counter gradient transport or to account for nonisotropic turbulence. A third choice for expressing the turbulent stresses lies between the stress/flux models and the eddy viscosity models in complexity and potential for

representing complex flows. In this approach algebraic expressions (approximations to the transport equations used in stress/flux models) relate the vertical stresses to k and l (or ϵ) without the use of an eddy viscosity hypothesis.

27. Eddy viscosity models are by far the most widely used method for representing vertical momentum transport in coastal flows. These models can be expected to work reasonably well in such applications, since the water column is typically dominated by the bottom and surface boundary layers.

PART III: EXTERNAL MODE SOLUTION

Selection Considerations for the External Mode Solution

28. A basic objective in the development of ADCIRC is to provide the ability to perform computations on very large domains. This requires selecting algorithms that satisfy interrelated requirements of a high level of grid flexibility, accuracy, and efficiency. To ensure a high degree of solution accuracy, the discretization scheme must have numerical amplitude and phase propagation characteristics that are nearly identical to the analytical characteristics even for relatively poorly resolved wavelengths (e.g., good correspondence down to at least $\lambda/\Delta x = 20$, where λ is the wavelength and Δx the grid spacing). Furthermore, solution accuracy requires that all wavelengths with significant energy, (e.g., as generated in regions of rapidly varying flow, geometry, and/or topography), be well–resolved. A high degree of solution efficiency requires that the algorithm minimizes both the number of degrees of freedom and the operations required per degree of freedom per time step. Minimization of the number of degrees of freedom is constrained by the need to provide resolution on a localized basis and is highly dependent on the accuracy and the grid flexibility of the numerical scheme.

29. Because grid flexibility is pivotal to solution accuracy and efficiency, various strategies have been devised to allow variations in grid size over a model domain. A nested grid approach offers one solution. However, unless the grids are coupled, this approach cannot properly account for flow interactions between the various grids. Stretched FD grids offer the possibility of providing local refinement within a single grid. However, cell aspect ratio requirements limit the degree of grid size variability. Furthermore, since cell size in the x direction is fixed for all y locations for a given x and vice versa, portions of the domain are often over–refined. Boundary–fitted FD schemes that utilize conformal mapping techniques allow the land boundaries to be well–represented in addition to offering local refinement possibilities. However, these techniques suffer from the same shortcomings as stretched FD approximations and often significant difficulties are encountered in finding a suitable transformation function for complex geographic regions. The FE algorithms based on triangular elements are highly flexible and can provide local refinement in a systematic and optimal fashion. In fact, circulation computations for tides and storm surge in the Gulf of Mexico (Westerink et al., in press) have been achieved with cell area ratios greater than 1 to 15,000.

30. Algorithm accuracy per degree of freedom is another critical issue in the selection of an external mode solution algorithm. FD schemes were successful fairly early in their development owing to the use of the staggered or C grid approach (Hansen 1956; Leendertse 1967). Early FE schemes were plagued with severe spurious modes that required the heavy–handed addition of non–physical dissipation and resulted in very poor accuracy characteristics (Gray 1982). It was not until the introduction of the wave–continuity equation (WCE) formulation that robust and highly accurate FE schemes emerged (Lynch and Gray 1979). The WCE formulation is based on the rearrangement of the continuum equations prior to any spatial discretization. Extensive numerical testing has demonstrated that FE–based WCE solutions produce very accurate results (Lynch and Gray 1979; Lynch 1981; Walters and Carey 1983; Walters 1983 and 1984). It has also been shown that the fundamental success of the WCE FE scheme lies in its ability to propagate $2\Delta x$ waves (Platzman 1981; Foreman 1983). (This is also the reason why the C grid FD solutions are successful.)

31. Finally, overall algorithm efficiency is essential in the selection of an external mode solution. In general, implicit methods are more useful in long wave computations than explicit methods, particularly when small cells or elements are used. However, the use of implicit methods typically results in time–dependent matrices that must be reassembled and re–solved at every time step. This increases the computational burden significantly. The FD methods overcome this problem by implementing an alternating direction implicit (ADI) type approach that reduces a two–dimensional problem to a sequence of one–dimensional problems, resulting in significant computational savings for large problems. It is not possible to apply the ADI approach to FE–based methods. However, a WCE FE–based solution has been formulated that decouples the solutions for elevation and velocity and allows the use of time–independent matrices for the elevation solution and diagonal matrices for the velocity solution. These features have produced a highly efficient WCE FE solution called the generalized wave–continuity equation (GWCE) formulation (Kinmark 1985).

32. Careful consideration of the requirements for grid flexibility and a high level of accuracy and efficiency led to the selection of the FE–based GWCE formulation for the external mode solution in ADCIRC. Extensive analysis, testing, and field applications of the GWCE during the past decade have demonstrated the unparalleled capabilities and robustness of the scheme.

Development of the Generalized Wave–Continuity Equation

33. The GWCE formulation is a specifically designed WCE formulation that yields a discrete system of equations with time–independent matrices. Time–independent system matrices are critical in minimizing the computational cost for finite–element–based solutions due to the expense of both the matrix assembly and decomposition steps. The GWCE is based on the primitive depth–integrated continuity equation, Equation 22, and the primitive depth–integrated conservation of momentum equations in conservative form, Equations 23 and 24. The primitive continuity equation is differentiated with respect to time to yield:

$$\frac{\partial^2 \zeta}{\partial t^2} + \frac{\partial^2 UH}{\partial t \partial x} + \frac{\partial^2 VH}{\partial t \partial y} = 0 \tag{35}$$

The primitive momentum equations are differentiated with respect to x and y, respectively, and rearranged as:

$$\frac{\partial^2 UH}{\partial t \partial x} = \frac{\partial}{\partial x}\left\{- \frac{\partial UUH}{\partial x} - \frac{\partial UVH}{\partial y} + fVH - H \frac{\partial}{\partial x}\left[\frac{p_s}{\rho_o} + g(\zeta - \alpha\eta)\right] + M_x + D_x + B_x + \frac{\tau_{sx}}{\rho_o} - \frac{\tau_{bx}}{\rho_o}\right\} \tag{36}$$

$$\frac{\partial^2 VH}{\partial t \partial y} = \frac{\partial}{\partial y}\left\{- \frac{\partial UVH}{\partial x} - \frac{\partial VVH}{\partial y} - fUH - H \frac{\partial}{\partial y}\left[\frac{p_s}{\rho_o} + g(\zeta - \alpha\eta)\right] + M_y + D_y + B_y + \frac{\tau_{sy}}{\rho_o} - \frac{\tau_{by}}{\rho_o}\right\} \tag{37}$$

Equations 36 and 37 are then substituted into Equation 35:

$$\frac{\partial^2 \zeta}{\partial t^2} + \frac{\partial}{\partial x}\left\{- \frac{\partial UUH}{\partial x} - \frac{\partial UVH}{\partial y} + fVH - H \frac{\partial}{\partial x}\left[\frac{p_s}{\rho_o} + g(\zeta - \alpha\eta)\right] + M_x + D_x + B_x + \frac{\tau_{sx}}{\rho_o} - \frac{\tau_{bx}}{\rho_o}\right\} + \frac{\partial}{\partial y}\left\{- \frac{\partial UVH}{\partial x} - \frac{\partial VVH}{\partial y} - fUH - H \frac{\partial}{\partial y}\left[\frac{p_s}{\rho_o} + g(\zeta - \alpha\eta)\right] + M_y + D_y + B_y + \frac{\tau_{sy}}{\rho_o} - \frac{\tau_{by}}{\rho_o}\right\} = 0 \tag{38}$$

Finally, the primitive continuity equation is multiplied by a constant, τ_o, and added to Equation 38:

$$\frac{\partial^2 \zeta}{\partial t^2} + \tau_o \frac{\partial \zeta}{\partial t} + \frac{\partial}{\partial x}\left\{- \frac{\partial UUH}{\partial x} - \frac{\partial UVH}{\partial y} + fVH - H \frac{\partial}{\partial x}\left[\frac{p_s}{\rho_o} + g(\zeta - \alpha\eta)\right] + M_x + D_x + B_x + \frac{\tau_{sx}}{\rho_o} - \frac{\tau_{bx}}{\rho_o} + \tau_o UH\right\} + \frac{\partial}{\partial y}\left\{- \frac{\partial UVH}{\partial x} - \frac{\partial VVH}{\partial y} - fUH\right.$$

$$- H \frac{\partial}{\partial y} [\frac{p_s}{\rho_o} + g(\zeta - \alpha\eta)] + M_y + D_y + B_y + \frac{\tau_{sy}}{\rho_o} - \frac{\tau_{by}}{\rho_o} + \tau_o VH\} = 0 \quad (39)$$

34. The advective terms in Equation 39 are in conservative form. Our experience indicates that if these terms are put into non–conservative form, improved numerical stability is obtained when advection is dominant in the global or local force balance. The advective terms in the GWCE are reformulated by expanding the derivatives and substituting in the primitive continuity equation, Equation 22.

$$\begin{aligned}\frac{\partial^2\zeta}{\partial t^2} + \tau_o \frac{\partial\zeta}{\partial t} + \frac{\partial}{\partial x}\{U \frac{\partial\zeta}{\partial t} - UH \frac{\partial U}{\partial x} - VH \frac{\partial U}{\partial y} + fVH - H \frac{\partial}{\partial x}[\frac{p_s}{\rho_o} + g(\zeta - \alpha\eta)] \\ + M_x + D_x + B_x + \frac{\tau_{sx}}{\rho_o} - \frac{\tau_{bx}}{\rho_o} + \tau_o UH\} + \frac{\partial}{\partial y}\{V \frac{\partial\zeta}{\partial t} - UH \frac{\partial V}{\partial x} \\ - VH \frac{\partial V}{\partial y} - fUH - H \frac{\partial}{\partial y}[\frac{p_s}{\rho_o} + g(\zeta - \alpha\eta)] + M_y + D_y + B_y \\ + \frac{\tau_{sy}}{\rho_o} - \frac{\tau_{by}}{\rho_o} + \tau_o VH\} = 0 \end{aligned} \quad (40)$$

35. The lateral closure model in ADCIRC is the simplified eddy viscosity model of Kolar and Gray (1990), Equation 33. Substituting this into Equation 40 gives:

$$\begin{aligned}\frac{\partial^2\zeta}{\partial t^2} + \tau_o\frac{\partial\zeta}{\partial t} + \frac{\partial}{\partial x}\{U \frac{\partial\zeta}{\partial t} - UH \frac{\partial U}{\partial x} - VH \frac{\partial U}{\partial y} + fVH - H \frac{\partial}{\partial x}[\frac{p_s}{\rho_o} + g(\zeta - \alpha\eta)] \\ + D_x + B_x + \frac{\tau_{sx}}{\rho_o} - \frac{\tau_{bx}}{\rho_o} + \tau_o UH\} + \frac{\partial}{\partial y}\{V \frac{\partial\zeta}{\partial t} - UH \frac{\partial V}{\partial x} - VH \frac{\partial V}{\partial y} - fUH \\ - H \frac{\partial}{\partial y}[\frac{p_s}{\rho_o} + g(\zeta - \alpha\eta)] + D_y + B_y + \frac{\tau_{sy}}{\rho_o} - \frac{\tau_{by}}{\rho_o} + \tau_o VH\} \\ + \frac{\partial}{\partial x}[E_{h2}(\frac{\partial^2 UH}{\partial x^2} + \frac{\partial^2 UH}{\partial y^2})] + \frac{\partial}{\partial y}[E_{h2}(\frac{\partial^2 VH}{\partial x^2} + \frac{\partial^2 VH}{\partial y^2})] = 0 \end{aligned} \quad (41)$$

where E_{h2} is the generalized lateral diffusion/dispersion coefficient. For the 2DDI option, E_{h2} represents the combined effects of both lateral diffusion and dispersion. Therefore $E_{h2} = E_{h2}^{MD}$ and D_x and D_y are both set to zero. For the three–dimensional ADCIRC options, E_{h2} represents only lateral diffusion. In these cases, $E_{h2} = E_{h2}^{M}$, and D_x and D_y are explicitly computed from the internal mode solution. It is assumed that E_{h2} is constant in time and space and that it has a value of zero on the boundaries of the domain.

36. The lateral diffusive/dispersive terms in Equation 41 can be conveniently rearranged to decrease the functional continuity requirements for the symmetrical weak

weighted residual formulation from C^1 back to C^0 as is the case for the GWCE formulation without any lateral closure model (Kolar and Gray 1990). Rearranging the spatial derivatives of the lateral diffusive/dispersive terms in Equation 41 gives:

$$\frac{\partial^2\zeta}{\partial t^2} + \tau_0\frac{\partial\zeta}{\partial t} + \frac{\partial}{\partial x}\{U\frac{\partial\zeta}{\partial t} - UH\frac{\partial U}{\partial x} - VH\frac{\partial U}{\partial y} + fVH - H\frac{\partial}{\partial x}[\frac{p_s}{\rho_o} + g(\zeta - \alpha\eta)]$$
$$+ D_x + B_x + \frac{\tau_{sx}}{\rho_o} - \frac{\tau_{bx}}{\rho_o} + \tau_0 UH\} + \frac{\partial}{\partial y}\{V\frac{\partial\zeta}{\partial t} - UH\frac{\partial V}{\partial x} - VH\frac{\partial V}{\partial y} - fUH$$
$$- H\frac{\partial}{\partial y}[\frac{p_s}{\rho_o} + g(\zeta - \alpha\eta)] + D_y + B_y + \frac{\tau_{sy}}{\rho_o} - \frac{\tau_{by}}{\rho_o} + \tau_0 VH\}$$
$$+ E_{h2}[\frac{\partial^2}{\partial x^2}(\frac{\partial UH}{\partial x} + \frac{\partial VH}{\partial y})] + E_{h2}[\frac{\partial^2}{\partial y^2}(\frac{\partial UH}{\partial x} + \frac{\partial VH}{\partial y})] = 0 \qquad (42)$$

The primitive continuity equation, Equation 22, can be used to substitute for the divergence of flux in the lateral diffusion/dispersion terms in Equation 42 to give:

$$\frac{\partial^2\zeta}{\partial t^2} + \tau_0\frac{\partial\zeta}{\partial t} + \frac{\partial}{\partial x}\{U\frac{\partial\zeta}{\partial t} - UH\frac{\partial U}{\partial x} - VH\frac{\partial U}{\partial y} + fVH - H\frac{\partial}{\partial x}[\frac{p_s}{\rho_o} + g(\zeta - \alpha\eta)]$$
$$- E_{h2}\frac{\partial^2\zeta}{\partial x\partial t} + D_x + B_x + \frac{\tau_{sx}}{\rho_o} - \frac{\tau_{bx}}{\rho_o} + \tau_0 UH\}$$
$$+ \frac{\partial}{\partial y}\{V\frac{\partial\zeta}{\partial t} - UH\frac{\partial V}{\partial x} - VH\frac{\partial V}{\partial y} - fUH - H\frac{\partial}{\partial y}[\frac{p_s}{\rho_o} + g(\zeta - \alpha\eta)]$$
$$- E_{h2}\frac{\partial^2\zeta}{\partial y\partial t} + D_y + B_y + \frac{\tau_{sy}}{\rho_o} - \frac{\tau_{by}}{\rho_o} + \tau_0 VH\} = 0 \qquad (43)$$

37. Equation 43 can be solved in conjunction with the primitive conservation of momentum equations in either conservative or non–conservative form. ADCIRC uses the non–conservative momentum equations, Equations 25 and 26. Incorporating the same simplified eddy viscosity model into the non–conservative momentum equations gives:

$$\frac{\partial U}{\partial t} + U\frac{\partial U}{\partial x} + V\frac{\partial U}{\partial y} - fV = -\frac{\partial}{\partial x}[\frac{p_s}{\rho_o} + g(\zeta - \alpha\eta)]$$
$$+ \frac{1}{H}E_{h2}[\frac{\partial^2 UH}{\partial x^2} + \frac{\partial^2 UH}{\partial y^2}] + \frac{D_x}{H} + \frac{B_x}{H} + \frac{\tau_{sx}}{\rho_o H} - \frac{\tau_{bx}}{\rho_o H} \qquad (44)$$

$$\frac{\partial V}{\partial t} + U\frac{\partial V}{\partial x} + V\frac{\partial V}{\partial y} + fU = -\frac{\partial}{\partial y}[\frac{p_s}{\rho_o} + g(\zeta - \alpha\eta)]$$
$$+ \frac{1}{H}E_{h2}[\frac{\partial^2 VH}{\partial x^2} + \frac{\partial^2 VH}{\partial y^2}] + \frac{D_y}{H} + \frac{B_y}{H} + \frac{\tau_{sy}}{\rho_o H} - \frac{\tau_{by}}{\rho_o H} \qquad (45)$$

Bottom Stress Formulation

38. The bottom stress in Equations 43 – 45 is expressed using a drag tensor similar to that proposed by Jenter and Madsen (1989):

$$\frac{1}{\rho_o}\begin{bmatrix}\tau_{bx}\\ \tau_{by}\end{bmatrix} = H\tau_*\begin{bmatrix}\cos(\gamma) & -\sin(\gamma)\\ \sin(\gamma) & \cos(\gamma)\end{bmatrix}\begin{bmatrix}U\\ V\end{bmatrix} \tag{46a}$$

where

$$\tau_* \equiv \frac{C_f\,(U^2 + V^2)^{1/2}}{H} \tag{46b}$$

and γ is the angle measured counter clockwise from the depth–averaged velocity vector to the bottom stress vector.

39. Defining

$$f' \equiv f + \tau_*\sin(\gamma) \tag{47a}$$

$$\tau'_* \equiv \tau_*\cos(\gamma) \tag{47b}$$

and substituting Equations 46 and 47 into Equations 43 – 45 gives the GWCE and momentum equations in final form:

$$\begin{aligned}&\frac{\partial^2\zeta}{\partial t^2} + \tau_o\frac{\partial\zeta}{\partial t} + \frac{\partial}{\partial x}\left\{U\frac{\partial\zeta}{\partial t} - UH\frac{\partial U}{\partial x} - VH\frac{\partial U}{\partial y} + f'VH - H\frac{\partial}{\partial x}\left[\frac{p_s}{\rho_o} + g(\zeta - \alpha\eta)\right]\right.\\ &\qquad \left. - E_{h2}\frac{\partial^2\zeta}{\partial x\partial t} + D_x + B_x + \frac{\tau_{sx}}{\rho_o} + (\tau_o - \tau'_*)UH\right\}\\ &\qquad + \frac{\partial}{\partial y}\left\{V\frac{\partial\zeta}{\partial t} - UH\frac{\partial V}{\partial x} - VH\frac{\partial V}{\partial y} - f'UH - H\frac{\partial}{\partial y}\left[\frac{p_s}{\rho_o} + g(\zeta - \alpha\eta)\right]\right.\\ &\qquad \left. - E_{h2}\frac{\partial^2\zeta}{\partial y\partial t} + D_y + B_y + \frac{\tau_{sy}}{\rho_o} + (\tau_o - \tau'_*)VH\right\} = 0\end{aligned} \tag{48}$$

$$\begin{aligned}&\frac{\partial U}{\partial t} + U\frac{\partial U}{\partial x} + V\frac{\partial U}{\partial y} - f'V = -\frac{\partial}{\partial x}\left[\frac{p_s}{\rho_o} + g(\zeta - \alpha\eta)\right]\\ &\qquad + \frac{1}{H}E_{h2}\left[\frac{\partial^2 UH}{\partial x^2} + \frac{\partial^2 UH}{\partial y^2}\right] + \frac{D_x}{H} + \frac{B_x}{H} + \frac{\tau_{sx}}{\rho_o H} - \tau'_* U\end{aligned} \tag{49}$$

$$\begin{aligned}&\frac{\partial V}{\partial t} + U\frac{\partial V}{\partial x} + V\frac{\partial V}{\partial y} + f'U = -\frac{\partial}{\partial y}\left[\frac{p_s}{\rho_o} + g(\zeta - \alpha\eta)\right]\\ &\qquad + \frac{1}{H}E_{h2}\left[\frac{\partial^2 VH}{\partial x^2} + \frac{\partial^2 VH}{\partial y^2}\right] + \frac{D_y}{H} + \frac{B_y}{H} + \frac{\tau_{sy}}{\rho_o H} - \tau'_* V\end{aligned} \tag{50}$$

40. In the 2DDI option, the bottom stress and depth–averaged velocity are assumed to be co–linear ($\gamma = 0$). C_f is specified directly as an input parameter or computed using one of the relationships given in Equation 29. In the three–

dimensional ADCIRC options, γ and C_f are computed using τ_{bx} and τ_{by} from the internal mode solution. As noted above, γ is the angle measured counterclockwise from the depth–averaged velocity vector to the bottom stress vector. C_f is determined as:

$$C_f = \frac{(\tau_{bx}^2 + \tau_{by}^2)^{1/2}}{\rho_o(U^2 + V^2)} \tag{51}$$

It is easily shown that Equations 46, 47, and 51 introduce the bottom stresses computed in the internal mode solution directly into the external mode equations.

Development of Weighted Residual Statements

41. To develop a Galerkin weighted residual statement for the GWCE, Equation 48 is weighted by the interpolating basis function, ϕ_i, and spatially integrated over the interior domain, Ω, giving:

$$<\frac{\partial^2\zeta}{\partial t^2}, \phi_i>_\Omega + <\tau_o\frac{\partial\zeta}{\partial t}, \phi_i>_\Omega + <\frac{\partial A_x}{\partial x}, \phi_i>_\Omega + <\frac{\partial A_y}{\partial y}, \phi_i>_\Omega = 0 \quad i=1, \ldots N \tag{52}$$

where

$$<a,b>_\Omega \equiv \iint_\Omega a\ b\ d\Omega$$

Ω = the global domain

N = number of nodes in the spatial discretization

$$A_x \equiv U\frac{\partial\zeta}{\partial t} - UH\frac{\partial U}{\partial x} - VH\frac{\partial U}{\partial y} + f'VH - H\frac{\partial}{\partial x}\left[\frac{p_s}{\rho_o} + g(\zeta - \alpha\eta)\right] - E_{h2}\frac{\partial^2\zeta}{\partial x\partial t} + D_x + B_x + \frac{\tau_{sx}}{\rho_o} + (\tau_o - \tau_*')UH \tag{53a}$$

$$A_y \equiv V\frac{\partial\zeta}{\partial t} - UH\frac{\partial V}{\partial x} - VH\frac{\partial V}{\partial y} - f'UH - H\frac{\partial}{\partial y}\left[\frac{p_s}{\rho_o} + g(\zeta - \alpha\eta)\right] - E_{h2}\frac{\partial^2\zeta}{\partial y\partial t} + D_y + B_y + \frac{\tau_{sy}}{\rho_o} + (\tau_o - \tau_*')VH \tag{53b}$$

Applying Gauss's theorem to the integrals in Equation 52 that contain spatial derivatives gives:

$$<\frac{\partial^2\zeta}{\partial t^2}, \phi_i>_\Omega + <\tau_o\frac{\partial\zeta}{\partial t}, \phi_i>_\Omega - <A_x, \frac{\partial\phi_i}{\partial x}>_\Omega - <A_y, \frac{\partial\phi_i}{\partial y}>_\Omega = -\int_\Gamma [A_x\alpha_{nx} + A_y\alpha_{ny}]\phi_i\, d\Gamma \quad i=1, \ldots N \tag{54}$$

where Γ is the boundary of the domain Ω. The direction cosines are defined as:

$$\alpha_{nx} \equiv \cos(\theta_x) \tag{55a}$$

$$\alpha_{ny} \equiv \cos(\theta_y) \tag{55b}$$

where θ_x and θ_y are the (spatially varying) angles measured to the outward normal at any point along the boundary from the positive x and y axes, respectively.

42. Using the conservative form of the momentum equations, Equations 23 and 24, recasting the advective terms in Equation 53 into conservative form, and using the simplified lateral diffusion model, Equation 33, A_x and A_y can be written as:

$$A_x = \frac{\partial UH}{\partial t} - E_{h2}\left(\frac{\partial^2 UH}{\partial x^2} + \frac{\partial^2 UH}{\partial y^2}\right) - E_{h2}\frac{\partial^2 \zeta}{\partial x \partial t} + \tau_o UH \tag{56a}$$

$$A_y = \frac{\partial VH}{\partial t} - E_{h2}\left(\frac{\partial^2 VH}{\partial x^2} + \frac{\partial^2 VH}{\partial y^2}\right) - E_{h2}\frac{\partial^2 \zeta}{\partial y \partial t} + \tau_o VH \tag{56b}$$

Substituting Equation 56 into the line integral in Equation 54 and assuming that E_{h2} is zero on the boundary, Equation 54 becomes:

$$\begin{aligned}
&\left\langle \frac{\partial^2 \zeta}{\partial t^2}, \phi_i \right\rangle_\Omega + \left\langle \tau_o \frac{\partial \zeta}{\partial t}, \phi_i \right\rangle_\Omega - \left\langle U\frac{\partial \zeta}{\partial t} - UH\frac{\partial U}{\partial x} - VH\frac{\partial U}{\partial y} + f'VH \right. \\
&\quad - H\frac{\partial}{\partial x}\left[\frac{p_s}{\rho_o} + g(\zeta - \alpha\eta)\right] - E_{h2}\frac{\partial^2 \zeta}{\partial x \partial t} + D_x + B_x + \frac{\tau_{sx}}{\rho_o} + (\tau_o - \tau_*')UH, \frac{\partial \phi_i}{\partial x} \Big\rangle_\Omega \\
&\quad - \left\langle V\frac{\partial \zeta}{\partial t} - UH\frac{\partial V}{\partial x} - VH\frac{\partial V}{\partial y} - f'UH - H\frac{\partial}{\partial y}\left[\frac{p_s}{\rho_o} + g(\zeta - \alpha\eta)\right] - E_{h2}\frac{\partial^2 \zeta}{\partial y \partial t} \right. \\
&\quad + D_y + B_y + \frac{\tau_{sy}}{\rho_o} + (\tau_o - \tau_*')VH, \frac{\partial \phi_i}{\partial y} \Big\rangle_\Omega = -\int_\Gamma \left[\frac{\partial}{\partial t}(UH\alpha_{nx} + VH\alpha_{ny})\right. \\
&\quad \left. + \tau_o(UH\alpha_{nx} + VH\alpha_{ny})\right]\phi_i \, d\Gamma \qquad i = 1, \ldots N
\end{aligned} \tag{57}$$

43. The terms that involve partial derivatives of the barometric pressure, surface elevation, and Newtonian equilibrium tidal potential can be written as:

$$H\frac{\partial}{\partial x}\left[\frac{p_s}{\rho_o} + g(\zeta - \alpha\eta)\right] = gh\frac{\partial \zeta}{\partial x} + \frac{g}{2}\frac{\partial \zeta^2}{\partial x} + gH\frac{\partial}{\partial x}\left(\frac{p_s}{\rho_o g} - \alpha\eta\right) \tag{58a}$$

$$H\frac{\partial}{\partial y}\left[\frac{p_s}{\rho_o} + g(\zeta - \alpha\eta)\right] = gh\frac{\partial \zeta}{\partial y} + \frac{g}{2}\frac{\partial \zeta^2}{\partial y} + gH\frac{\partial}{\partial y}\left(\frac{p_s}{\rho_o g} - \alpha\eta\right) \tag{58b}$$

44. The normal flux across the boundary is defined as:

$$Q_n \equiv UH\alpha_{nx} + VH\alpha_{ny} \tag{59}$$

45. The line integral in Equation 57 is non–zero only on flux–specified boundaries, Γ_Q. Using the specified normal flux Q_{n*} for Q_n, and substituting Equations 58 and 59 into Equation 57 gives the final symmetrical weak weighted

residual statement for the GWCE:

$$<\frac{\partial^2\zeta}{\partial t^2},\phi_i>_\Omega + <\tau_o\frac{\partial\zeta}{\partial t},\phi_i>_\Omega + <gh\frac{\partial\zeta}{\partial x}, \frac{\partial\phi_i}{\partial x}>_\Omega + <gh\frac{\partial\zeta}{\partial y}, \frac{\partial\phi_i}{\partial y}>_\Omega + E_{h2}<\frac{\partial^2\zeta}{\partial x\partial t}, \frac{\partial\phi_i}{\partial x}>_\Omega$$
$$+ E_{h2}<\frac{\partial^2\zeta}{\partial y\partial t}, \frac{\partial\phi_i}{\partial y}>_\Omega = <U\frac{\partial\zeta}{\partial t}, \frac{\partial\phi_i}{\partial x}>_\Omega + <V\frac{\partial\zeta}{\partial t}, \frac{\partial\phi_i}{\partial y}>_\Omega + <W_x, \frac{\partial\phi_i}{\partial x}>_\Omega$$
$$+ <W_y, \frac{\partial\phi_i}{\partial y}>_\Omega - \int_{\Gamma_Q} (\frac{\partial Q_{n*}}{\partial t} + \tau_o Q_{n*})\ \phi_i\ d\Gamma \qquad i = 1, \ldots N \qquad (60)$$

where

$$W_x \equiv - UH\frac{\partial U}{\partial x} - VH\frac{\partial U}{\partial y} + f'VH - \frac{g}{2}\frac{\partial\zeta^2}{\partial x} - gH\frac{\partial}{\partial x}(\frac{p_s}{\rho_o g} - \alpha\eta) + D_x + B_x$$
$$+ \frac{\tau_{sx}}{\rho_o} + (\tau_o - \tau_*')UH \qquad (61a)$$

$$W_y \equiv - UH\frac{\partial V}{\partial x} - VH\frac{\partial V}{\partial y} - f'UH - \frac{g}{2}\frac{\partial\zeta^2}{\partial y} - gH\frac{\partial}{\partial y}(\frac{p_s}{\rho_o g} - \alpha\eta) + D_y + B_y$$
$$+ \frac{\tau_{sy}}{\rho_o} + (\tau_o - \tau_*')VH \qquad (61b)$$

46. The weighted residual form of the conservation of momentum equations is obtained by weighting Equations 49 and 50 by ϕ_i and integrating over the domain Ω:

$$<\frac{\partial U}{\partial t} + U\frac{\partial U}{\partial x} + V\frac{\partial U}{\partial y} - f'V + \frac{\partial}{\partial x}[\frac{p_s}{\rho_o} + g(\zeta - \alpha\eta)]$$
$$- \frac{1}{H}E_{h2}[\frac{\partial^2 UH}{\partial x^2} + \frac{\partial^2 UH}{\partial y^2}] - \frac{D_x}{H} - \frac{B_x}{H} - \frac{\tau_{sx}}{\rho_o H} + \tau_*'U,\ \phi_i>_\Omega = 0 \qquad (62)$$

$$<\frac{\partial V}{\partial t} + U\frac{\partial V}{\partial x} + V\frac{\partial V}{\partial y} + f'U + \frac{\partial}{\partial y}[\frac{p_s}{\rho_o} + g(\zeta - \alpha\eta)]$$
$$- \frac{1}{H}E_{h2}[\frac{\partial^2 VH}{\partial x^2} + \frac{\partial^2 VH}{\partial y^2}] - \frac{D_y}{H} - \frac{B_y}{H} - \frac{\tau_{sy}}{\rho_o H} + \tau_*'V,\ \phi_i>_\Omega = 0 \qquad (63)$$

Applying Gauss's theorem to the lateral diffusive/dispersive terms in Equations 62 and 63, and recalling that E_{h2} equals zero on the boundary, gives the symmetrical weak weighted residual form of the momentum equations:

$$<\frac{\partial U}{\partial t},\ \phi_i>_\Omega - <f'V,\ \phi_i>_\Omega + E_{h2}<\frac{\partial UH}{\partial x}, \frac{\partial}{\partial x}(\frac{\phi_i}{H})>_\Omega + E_{h2}<\frac{\partial UH}{\partial y}, \frac{\partial}{\partial y}(\frac{\phi_i}{H})>_\Omega =$$
$$- <\frac{\partial}{\partial x}[\frac{p_s}{\rho_o} + g(\zeta - \alpha\eta)] - \frac{\tau_{sx}}{\rho_o H} + \tau_*'U,\ \phi_i>_\Omega$$
$$- <U\frac{\partial U}{\partial x} + V\frac{\partial U}{\partial y},\ \phi_i>_\Omega + <\frac{D_x}{H} + \frac{B_x}{H},\ \phi_i>_\Omega \qquad (64)$$

$$<\frac{\partial V}{\partial t},\ \phi_i>_\Omega + <f'U,\ \phi_i>_\Omega + E_{h2}<\frac{\partial VH}{\partial x}, \frac{\partial}{\partial x}(\frac{\phi_i}{H})>_\Omega + E_{h2}<\frac{\partial VH}{\partial y}, \frac{\partial}{\partial y}(\frac{\phi_i}{H})>_\Omega =$$

$$- <\frac{\partial}{\partial y}\left[\frac{p_s}{\rho_o} + g(\zeta - \alpha\eta)\right] - \frac{\tau_{sy}}{\rho_o H} + \tau_*' V,\ \phi_i>_\Omega$$

$$- <U\frac{\partial V}{\partial x} + V\frac{\partial V}{\partial y},\ \phi_i>_\Omega + <\frac{D_y}{H} + \frac{B_y}{H},\ \phi_i>_\Omega \qquad (65)$$

Time Discretization

47. The GWCE equation is discretized in time using a variably weighted, three–time–level, implicit scheme for the linear terms (i.e., those terms on the left side of Equation 60). W_x and W_y are treated explicitly. The time derivatives that appear on the right side of Equation 60 are evaluated at two known time levels. The time–discretized GWCE is:

$$<\frac{\zeta^{k+1} - 2\zeta^k + \zeta^{k-1}}{\Delta t^2},\ \phi_i>_\Omega + \tau_o<\frac{\zeta^{k+1} - \zeta^{k-1}}{2\Delta t},\ \phi_i>_\Omega$$

$$+ \alpha_1\left[<gh\frac{\partial\zeta^{k+1}}{\partial x},\ \frac{\partial\phi_i}{\partial x}>_\Omega + <gh\frac{\partial\zeta^{k+1}}{\partial y},\ \frac{\partial\phi_i}{\partial y}>_\Omega\right]$$

$$+ \alpha_2\left[<gh\frac{\partial\zeta^{k}}{\partial x},\ \frac{\partial\phi_i}{\partial x}>_\Omega + <gh\frac{\partial\zeta^{k}}{\partial y},\ \frac{\partial\phi_i}{\partial y}>_\Omega\right]$$

$$+ \alpha_3\left[<gh\frac{\partial\zeta^{k-1}}{\partial x},\ \frac{\partial\phi_i}{\partial x}>_\Omega + <gh\frac{\partial\zeta^{k-1}}{\partial y},\ \frac{\partial\phi_i}{\partial y}>_\Omega\right]$$

$$+ \frac{E_h}{2\Delta t}\left[<\left(\frac{\partial\zeta^{k+1}}{\partial x} - \frac{\partial\zeta^{k-1}}{\partial x}\right),\ \frac{\partial\phi_i}{\partial x}>_\Omega + <\left(\frac{\partial\zeta^{k+1}}{\partial y} - \frac{\partial\zeta^{k-1}}{\partial y}\right),\ \frac{\partial\phi_i}{\partial y}>_\Omega\right]$$

$$= <U^k\left(\frac{\zeta^k - \zeta^{k-1}}{\Delta t}\right),\ \frac{\partial\phi_i}{\partial x}>_\Omega + <V^k\left(\frac{\zeta^k - \zeta^{k-1}}{\Delta t}\right),\ \frac{\partial\phi_i}{\partial y}>_\Omega$$

$$+ <W_x^k,\ \frac{\partial\phi_i}{\partial x}>_\Omega + <W_y^k,\ \frac{\partial\phi_i}{\partial y}>_\Omega - \int_{\Gamma_Q}\left(\frac{Q_{n*}^{k+1} - Q_{n*}^{k-1}}{2\Delta t} + \tau_o\alpha_1 Q_{n*}^{k+1}\right.$$

$$\left. + \tau_o\alpha_2 Q_{n*}^{k} + \tau_o\alpha_3 Q_{n*}^{k-1}\right)\phi_i\, d\Gamma \qquad i = 1, \ldots N \qquad (66)$$

where

Δt = time step

k+1, k, k–1 = future, present, and past time levels

α_1, α_2, α_3 = time weighting factors

The time weighting factors are selected so that:

$\alpha_1 + \alpha_2 + \alpha_3 = 1$

$\alpha_1 = \alpha_3$

Rearranging Equation 66 gives:

$$
\begin{aligned}
&(1 + \frac{\tau_0 \Delta t}{2}) \, <\zeta^{k+1}, \, \phi_i>_\Omega \\
&\quad + \alpha_1 g \Delta t^2 [<h \frac{\partial \zeta^{k+1}}{\partial x}, \frac{\partial \phi_i}{\partial x}>_\Omega + <h \frac{\partial \zeta^{k+1}}{\partial y}, \frac{\partial \phi_i}{\partial y}>_\Omega] \\
&\quad + \frac{E_{h_2} \Delta t}{2} [<\frac{\partial \zeta^{k+1}}{\partial x}, \frac{\partial \phi_i}{\partial x}>_\Omega + <\frac{\partial \zeta^{k+1}}{\partial y}, \frac{\partial \phi_i}{\partial y}>_\Omega] \\
&\quad = 2 \, <\zeta^k, \, \phi_i>_\Omega + (\frac{\tau_0 \Delta t}{2} - 1) \, <\zeta^{k-1}, \, \phi_i>_\Omega \\
&\quad - \alpha_2 g \Delta t^2 [<h \frac{\partial \zeta^k}{\partial x}, \frac{\partial \phi_i}{\partial x}>_\Omega + <h \frac{\partial \zeta^k}{\partial y}, \frac{\partial \phi_i}{\partial y}>_\Omega] \\
&\quad - \alpha_3 g \Delta t^2 [<h \frac{\partial \zeta^{k-1}}{\partial x}, \frac{\partial \phi_i}{\partial x}>_\Omega + <h \frac{\partial \zeta^{k-1}}{\partial y}, \frac{\partial \phi_i}{\partial y}>_\Omega] \\
&\quad + \frac{E_{h_2} \Delta t}{2} [<\frac{\partial \zeta^{k-1}}{\partial x}, \frac{\partial \phi_i}{\partial x}>_\Omega + <\frac{\partial \zeta^{k-1}}{\partial y}, \frac{\partial \phi_i}{\partial y}>_\Omega] \\
&\quad + \Delta t <U^k (\zeta^k - \zeta^{k-1}), \frac{\partial \phi_i}{\partial x}>_\Omega + \Delta t <V^k (\zeta^k - \zeta^{k-1}), \frac{\partial \phi_i}{\partial y}>_\Omega \\
&\quad + \Delta t^2 <W_x^k, \frac{\partial \phi_i}{\partial x}>_\Omega + \Delta t^2 <W_y^k, \frac{\partial \phi_i}{\partial y}>_\Omega - \Delta t^2 F_i \qquad i=1, \ldots N
\end{aligned} \tag{67}
$$

where

$$
F_i \equiv \int_{\Gamma_Q} (\frac{Q_{n*}^{k+1} - Q_{n*}^{k-1}}{2\Delta t} + \tau_0 \alpha_1 Q_{n*}^{k+1} + \tau_0 \alpha_2 Q_{n*}^k + \tau_0 \alpha_3 Q_{n*}^{k-1}) \, \phi_i \, d\Gamma \tag{68}
$$

48. The symmetrical weak weighted residual form of the momentum equations are discretized in time using a two–time–level implicit Crank–Nicolson approximation for all terms except the diffusive terms, which are treated with a variably weighted, two–time–level implicit scheme and the advective, dispersive, and baroclinic terms, which are treated explicitly:

$$
\begin{aligned}
&<\frac{U^{k+1} - U^k}{\Delta t}, \, \phi_i>_\Omega + \frac{1}{2} <\tau_*'^k (U^{k+1} + U^k), \, \phi_i>_\Omega - <\frac{f'^k}{2} (V^{k+1} + V^k), \, \phi_i>_\Omega \\
&\quad + E_{h2} [\beta_1 <\frac{\partial (UH)^{k+1}}{\partial x}, \frac{\partial}{\partial x} (\frac{\phi_i}{H^{k+1}})>_\Omega + \beta_2 <\frac{\partial (UH)^k}{\partial x}, \frac{\partial}{\partial x} (\frac{\phi_i}{H^k})>_\Omega \\
&\quad + \beta_1 <\frac{\partial (UH)^{k+1}}{\partial y}, \frac{\partial}{\partial y} (\frac{\phi_i}{H^{k+1}})>_\Omega + \beta_2 <\frac{\partial (UH)^k}{\partial y}, \frac{\partial}{\partial y} (\frac{\phi_i}{H^k})>_\Omega] \\
&\quad = -\frac{1}{2} <\frac{\partial}{\partial x} [\frac{p_s^{k+1}}{\rho_o} + g(\zeta^{k+1} - \alpha \eta^{k+1})] - (\frac{\tau_{s\,x}}{\rho_o H})^{k+1}, \, \phi_i>_\Omega \\
&\quad - \frac{1}{2} <\frac{\partial}{\partial x} [\frac{p_s^k}{\rho_o} + g(\zeta^k - \alpha \eta^k)] - (\frac{\tau_{s\,x}}{\rho_o H})^k, \, \phi_i>_\Omega \\
&\quad - <U^k \frac{\partial U^k}{\partial x} + V^k \frac{\partial U^k}{\partial y}, \, \phi_i>_\Omega + <\frac{D_x^k}{H^k} + \frac{B_x^k}{H^k}, \, \phi_i>_\Omega \qquad i=1, \ldots N
\end{aligned} \tag{69}
$$

$$
<\frac{V^{k+1} - V^k}{\Delta t}, \, \phi_i>_\Omega + \frac{1}{2} <\tau_*'^k (V^{k+1} + V^k), \, \phi_i>_\Omega + <\frac{f'^k}{2} (U^{k+1} + U^k), \, \phi_i>_\Omega
$$

$$+ E_{h2} [\beta_1 <\frac{\partial(VH)^{k+1}}{\partial x}, \frac{\partial}{\partial x}(\frac{\phi_i}{H^{k+1}})>_\Omega + \beta_2 <\frac{\partial(VH)^k}{\partial x}, \frac{\partial}{\partial x}(\frac{\phi_i}{H^k})>_\Omega$$

$$+ \beta_1 <\frac{\partial(VH)^{k+1}}{\partial y}, \frac{\partial}{\partial y}(\frac{\phi_i}{H^{k+1}})>_\Omega + \beta_2 <\frac{\partial(VH)^k}{\partial y}, \frac{\partial}{\partial y}(\frac{\phi_i}{H^k})>_\Omega]$$

$$= -\frac{1}{2} <\frac{\partial}{\partial y}[\frac{p_s^{k+1}}{\rho_o} + g(\zeta^{k+1} - \alpha\eta^{k+1})] - (\frac{\tau_{s\,y}}{\rho_o H})^{k+1}, \phi_i>_\Omega$$

$$-\frac{1}{2} <\frac{\partial}{\partial y}[\frac{p_s^k}{\rho_o} + g(\zeta^k - \alpha\eta^k)] - (\frac{\tau_{s\,y}}{\rho_o H})^k, \phi_i>_\Omega$$

$$- <U^k \frac{\partial V^k}{\partial x} + V^k \frac{\partial V^k}{\partial y}, \phi_i>_\Omega + <\frac{D_y^k}{H^k} + \frac{B_y^k}{H^k}, \phi_i>_\Omega \qquad i=1, \ldots N \qquad (70)$$

where β_1 and β_2 are time–weighting factors at the future and present time levels. These factors are selected so that

$$\beta_1 + \beta_2 = 1$$

Rearranging Equations 69 and 70 gives:

$$<(1 + \frac{\Delta t}{2}\tau'^k_*)\, U^{k+1}, \phi_i>_\Omega - \frac{\Delta t}{2} <f'^k V^{k+1}, \phi_i>_\Omega$$

$$+ \beta_1 E_{h2}\Delta t\, [<\frac{\partial(UH)^{k+1}}{\partial x}, \frac{\partial}{\partial x}(\frac{\phi_i}{H^{k+1}})>_\Omega + <\frac{\partial(UH)^{k+1}}{\partial y}, \frac{\partial}{\partial y}(\frac{\phi_i}{H^{k+1}})>_\Omega]$$

$$= <(1 - \frac{\Delta t}{2}\tau'^k_*)\, U^k, \phi_i>_\Omega + \frac{\Delta t}{2} <f'^k V^k, \phi_i>_\Omega$$

$$- \beta_2 E_{h2}\Delta t\, [<\frac{\partial(UH)^k}{\partial x}, \frac{\partial}{\partial x}(\frac{\phi_i}{H^k})>_\Omega + <\frac{\partial(UH)^k}{\partial y}, \frac{\partial}{\partial y}(\frac{\phi_i}{H^k})>_\Omega]$$

$$- \frac{\Delta t}{2} <\frac{\partial}{\partial x}[\frac{p_s^{k+1}}{\rho_o} + g(\zeta^{k+1} - \alpha\eta^{k+1})] - (\frac{\tau_{s\,x}}{\rho_o H})^{k+1}, \phi_i>_\Omega$$

$$- \frac{\Delta t}{2} <\frac{\partial}{\partial x}[\frac{p_s^k}{\rho_o} + g(\zeta^k - \alpha\eta^k)] - (\frac{\tau_{s\,x}}{\rho_o H})^k, \phi_i>_\Omega$$

$$- \Delta t <U^k \frac{\partial U^k}{\partial x} + V^k \frac{\partial U^k}{\partial y}, \phi_i>_\Omega + \Delta t <\frac{D_x^k}{H^k} + \frac{B_x^k}{H^k}, \phi_i>_\Omega \qquad i=1, \ldots N \qquad (71)$$

$$<(1 + \frac{\Delta t}{2}\tau'^k_*)\, V^{k+1}, \phi_i>_\Omega + \frac{\Delta t}{2} <f'^k U^{k+1}, \phi_i>_\Omega$$

$$+ \beta_1 E_{h2}\Delta t\, [<\frac{\partial(VH)^{k+1}}{\partial x}, \frac{\partial}{\partial x}(\frac{\phi_i}{H^{k+1}})>_\Omega + <\frac{\partial(VH)^{k+1}}{\partial y}, \frac{\partial}{\partial y}(\frac{\phi_i}{H^{k+1}})>_\Omega]$$

$$= <(1 - \frac{\Delta t}{2}\tau'^k_*)\, V^k, \phi_i>_\Omega - \frac{\Delta t}{2} <f'^k U^k, \phi_i>_\Omega$$

$$- \beta_2 E_{h2}\Delta t\, [<\frac{\partial(VH)^k}{\partial x}, \frac{\partial}{\partial x}(\frac{\phi_i}{H^k})>_\Omega + <\frac{\partial(VH)^k}{\partial y}, \frac{\partial}{\partial y}(\frac{\phi_i}{H^k})>_\Omega]$$

$$- \frac{\Delta t}{2} <\frac{\partial}{\partial y}[\frac{p_s^{k+1}}{\rho_o} + g(\zeta^{k+1} - \alpha\eta^{k+1})] - (\frac{\tau_{s\,y}}{\rho_o H})^{k+1}, \phi_i>_\Omega$$

$$- \frac{\Delta t}{2} <\frac{\partial}{\partial y}[\frac{p_s^k}{\rho_o} + g(\zeta^k - \alpha\eta^k)] - (\frac{\tau_{s\,y}}{\rho_o H})^k, \phi_i>_\Omega$$

$$- \Delta t \left\langle U^k \frac{\partial V^k}{\partial x} + V^k \frac{\partial V^k}{\partial y}, \phi_i \right\rangle_\Omega + \Delta t \left\langle \frac{D_y^k}{H^k} + \frac{B_y^k}{H^k}, \phi_i \right\rangle_\Omega \quad i=1, \ldots N \qquad (72)$$

49. There are two differences in the solution of Equations 67, 71, and 72 in the 2DDI option and the three–dimensional options. In the 2DDI option, the friction parameter (C_f or one of the parameters in Equation 29) is specified in the model input. The dispersive terms are included with the lateral diffusive terms by eliminating D_x and D_y from Equations 67, 71, and 72 and setting $E_{2h} = E_{2h}^{MD}$. In the three–dimensional options, C_f, γ, D_x, and D_y are computed from the most recent internal mode solution. In flows where the velocity reverses direction over the depth, it is possible for the depth–averaged velocity to be zero while the bottom stress is nonzero. In this case the drag coefficient computed in Equation 51 becomes infinite. To prevent the numerical difficulties that this causes, an upper limit is set on the computed drag coefficient. If this limit is exceeded, γ and C_f are set to zero and the bottom stress computed in the most recent internal mode solution is passed directly to the external mode equations. In the GWCE, $\frac{\tau_{bx}^k}{\rho_o}$ and $\frac{\tau_{by}^k}{\rho_o}$ determined in the internal mode solution are subtracted from W_x and W_y, respectively. In the momentum equations, $\frac{\tau_{bx}^k}{\rho_o H^k}$ and $\frac{\tau_{by}^k}{\rho_o H^k}$ are subtracted from the right–hand side of the corresponding equation. This modifies the final terms in Equations 71 and 72 to $\Delta t \left\langle - \frac{\tau_{bx}^k}{\rho_o H^k} + \frac{D_x^k}{H^k} + \frac{B_x^k}{H^k}, \phi_i \right\rangle_\Omega$ and $\Delta t \left\langle - \frac{\tau_{by}^k}{\rho_o H^k} + \frac{D_y^k}{H^k} + \frac{B_y^k}{H^k}, \phi_i \right\rangle_\Omega$, respectively.

Spatial Discretization

50. In order to complete the conversion of the governing partial differential equations into systems of algebraic equations, the FE method is applied to the time–discretized form of the symmetrical weak weighted residual equations developed in the previous section. Specifically, elemental approximations to the variables are substituted into Equations 67, 71, and 72, the elemental equations are summed over the global domain, and the required degree of inter–element functional continuity is enforced. Interpolating basis with at least C^o functional continuity are required to discretize most of the dependent variables. Departures from this are noted below.

51. In all linear terms, surface elevation, velocities, and depth are approximated over each element as:

$$\zeta^k \cong \sum_{j=1}^{n_{el}} \zeta_j^k \, \phi_j \tag{73a}$$

$$U^k \cong \sum_{j=1}^{n_{el}} U_j^k \, \phi_j \tag{73b}$$

$$V^k \cong \sum_{j=1}^{n_{el}} V_j^k \, \phi_j \tag{73c}$$

$$h \cong \sum_{j=1}^{n_{el}} h_j \, \phi_j \tag{73d}$$

where n_{el} equals the number of nodes per element. In nonlinear terms and certain forcing terms, the entire term may be interpolated over the element as described below.

52. The nonlinear and forcing terms in the GWCE are approximated as follows.

a. The Coriolis parameter and the fluxes in the Coriolis term are approximated by:

$$f'^k (UH)^k \cong \sum_{j=1}^{n_{el}} (f'UH)_j^k \, \phi_j \tag{74a}$$

$$f'^k (VH)^k \cong \sum_{j=1}^{n_{el}} (f'VH)_j^k \, \phi_j \tag{74b}$$

b. The finite amplitude component of the free surface gradient is approximated by:

$$(\zeta^2)^k \cong \sum_{j=1}^{n_{el}} (\zeta^2)_j^k \, \phi_j \tag{75}$$

c. The combined barometric pressure and Newtonian tidal potential term is approximated by:

$$\left(\frac{p_s}{\rho_o g} - \alpha\eta\right)^k \cong \sum_{j=1}^{n_{el}} \left(\frac{p_s}{\rho_o g} - \alpha\eta\right)_j^k \, \phi_j \tag{76}$$

The total depth factor in this term is evaluated using an L_2 approximation:

$$H^k \cong H_{el}^k \equiv \frac{1}{n_{el}} \sum_{j=1}^{n_{el}} H_j^k \tag{77}$$

d. The surface stress terms are approximated by:

$$\left(\frac{\tau_{sx}}{\rho_o}\right)^k \cong \sum_{j=1}^{n_{el}} \left(\frac{\tau_{sx}}{\rho_o}\right)_j^k \, \phi_j \tag{78a}$$

$$\left(\frac{\tau_{sy}}{\rho_o}\right)^k \cong \sum_{j=1}^{n_{el}} \left(\frac{\tau_{sy}}{\rho_o}\right)_j^k \, \phi_j \tag{78b}$$

e. The bottom stress and τ_o terms are approximated by:

$$(\tau_*'^k - \tau_o)H^kU^k \cong \sum_{j=1}^{n_{el}} [(\tau_*' - \tau_o)HU]_j^k \ \phi_j \tag{79a}$$

$$(\tau_*'^k - \tau_o)H^kV^k \cong \sum_{j=1}^{n_{el}} [(\tau_*' - \tau_o)HV]_j^k \ \phi_j \tag{79b}$$

In the three–dimensional model options, if the computed friction coefficient exceeds the maximum allowable value, the bottom stress terms are approximated directly by:

$$\frac{\tau_{bx}}{\rho_o}^k \cong \sum_{j=1}^{n_{el}} \left(\frac{\tau_{bx}}{\rho_o}\right)_j^k \ \phi_j \tag{80a}$$

$$\frac{\tau_{by}}{\rho_o}^k \cong \sum_{j=1}^{n_{el}} \left(\frac{\tau_{by}}{\rho_o}\right)_j^k \ \phi_j \tag{80b}$$

f. The dispersive terms are broken up into their components D_{uu}, D_{uv} and D_{vv}, (defined in Part II), and discretized as:

$$\frac{\partial}{\partial x}(D_{uu})^k \cong \sum_{j=1}^{n_{el}} D_{uu_j}^k \ \frac{\partial \phi_i}{\partial x} \tag{81a}$$

$$\frac{\partial}{\partial y}(D_{uv})^k \cong \sum_{j=1}^{n_{el}} D_{uv_j}^k \ \frac{\partial \phi_i}{\partial y} \tag{81b}$$

$$\frac{\partial}{\partial x}(D_{uv})^k \cong \sum_{j=1}^{n_{el}} D_{uv_j}^k \ \frac{\partial \phi_i}{\partial x} \tag{81c}$$

$$\frac{\partial}{\partial y}(D_{vv})^k \cong \sum_{j=1}^{n_{el}} D_{vv_j}^k \ \frac{\partial \phi_i}{\partial y} \tag{81d}$$

g. The baroclinic terms are not included in either ADCIRC–2DDI or ADCIRC–3DL. Therefore the discretization of these terms is not considered here.

h. The velocities that multiply the time derivative components of the non–conservative advective terms are approximated using L_2 interpolation:

$$U^k \cong U_{el}^k \equiv \frac{1}{n_{el}} \sum_{j=1}^{n_{el}} U_j^k \tag{82a}$$

$$V^k \cong V_{el}^k \equiv \frac{1}{n_{el}} \sum_{j=1}^{n_{el}} V_j^k \tag{82b}$$

The free surface elevations that appear in these terms are approximated using the standard C^o approximation, Equation 73a. The spatially differentiated components of the non–conservative advective terms are approximated by

$$(UH \ \frac{\partial U}{\partial x})^k \cong (UH)_{el}^k \sum_{j=1}^{n_{el}} U_j^k \ \frac{\partial \phi_i}{\partial x} \tag{83a}$$

$$(VH\ \frac{\partial U}{\partial y})^k \cong (VH)^k_{el} \sum_{j=1}^{n_{el}} U^k_j\ \frac{\partial \phi_i}{\partial y} \tag{83b}$$

$$(UH\ \frac{\partial V}{\partial x})^k \cong (UH)^k_{el} \sum_{j=1}^{n_{el}} V^k_j\ \frac{\partial \phi_i}{\partial x} \tag{83c}$$

$$(VH\ \frac{\partial V}{\partial y})^k \cong (VH)^k_{el} \sum_{j=1}^{n_{el}} V^k_j\ \frac{\partial \phi_i}{\partial y} \tag{83d}$$

where

$$(UH)^k_{el} \equiv \frac{1}{n_{el}} \sum_{j=1}^{n_{el}} (UH)^k_j \tag{84a}$$

$$(VH)^k_{el} \equiv \frac{1}{n_{el}} \sum_{j=1}^{n_{el}} (VH)^k_j \tag{84b}$$

53. Substituting the approximations in Equations 73 – 84 into Equation 67 and summing over the elements gives:

$$\sum_{el=1}^{M} \Bigg\{ \sum_{j=1}^{n_{el}} \Big[(1 + \frac{\tau_0 \Delta t}{2}) <\zeta^{k+1}_j \phi_j,\ \phi_i>_{\Omega_{el}}$$

$$+ \alpha_1 g \Delta t^2 [< \sum_{m=1}^{n_{el}} h_m \phi_m \zeta^{k+1}_j \frac{\partial \phi_j}{\partial x},\ \frac{\partial \phi_i}{\partial x}>_{\Omega_{el}} + < \sum_{m=1}^{n_{el}} h_m \phi_m \zeta^{k+1}_j \frac{\partial \phi_j}{\partial y},\ \frac{\partial \phi_i}{\partial y}>_{\Omega_{el}}]$$

$$+ \frac{E_{h_2} \Delta t}{2} [<\zeta^{k+1}_j \frac{\partial \phi_j}{\partial x},\ \frac{\partial \phi_i}{\partial x}>_{\Omega_{el}} + <\zeta^{k+1}_j \frac{\partial \phi_j}{\partial y},\ \frac{\partial \phi_i}{\partial y}>_{\Omega_{el}}]$$

$$= 2 <\zeta^k_j \phi_j,\ \phi_i>_{\Omega_{el}} + (\frac{\tau_0 \Delta t}{2} - 1) <\zeta^{k-1}_j \phi_j,\ \phi_i>_{\Omega_{el}}$$

$$- \alpha_2 g \Delta t^2 [< \sum_{m=1}^{n_{el}} h_m \phi_m \zeta^k_j \frac{\partial \phi_j}{\partial x},\ \frac{\partial \phi_i}{\partial x}>_{\Omega_{el}} + < \sum_{m=1}^{n_{el}} h_m \phi_m \zeta^k_j \frac{\partial \phi_j}{\partial y},\ \frac{\partial \phi_i}{\partial y}>_{\Omega_{el}}]$$

$$- \alpha_3 g \Delta t^2 [< \sum_{m=1}^{n_{el}} h_m \phi_m \zeta^{k-1}_j \frac{\partial \phi_j}{\partial x},\ \frac{\partial \phi_i}{\partial x}>_{\Omega_{el}} + < \sum_{m=1}^{n_{el}} h_m \phi_m \zeta^{k-1}_j \frac{\partial \phi_j}{\partial y},\ \frac{\partial \phi_i}{\partial y}>_{\Omega_{el}}]$$

$$+ \frac{E_{h_2} \Delta t}{2} [<\zeta^{k-1}_j \frac{\partial \phi_j}{\partial x},\ \frac{\partial \phi_i}{\partial x}>_{\Omega_{el}} + <\zeta^{k-1}_j \frac{\partial \phi_j}{\partial y},\ \frac{\partial \phi_i}{\partial y}>_{\Omega_{el}}]$$

$$+ \Delta t\ [<U^k_{el}(\zeta^k_j - \zeta^{k-1}_j)\ \phi_j,\ \frac{\partial \phi_i}{\partial x}>_{\Omega_{el}} + <V^k_{el}(\zeta^k_j - \zeta^{k-1}_j)\ \phi_j,\ \frac{\partial \phi_i}{\partial y}>_{\Omega_{el}}]$$

$$- \Delta t^2 [<(UH)^k_{el} U^k_j \frac{\partial \phi_j}{\partial x},\ \frac{\partial \phi_i}{\partial x}>_{\Omega_{el}} + <(VH)^k_{el} U^k_j \frac{\partial \phi_j}{\partial y},\ \frac{\partial \phi_i}{\partial x}>_{\Omega_{el}}$$

$$+ <(UH)^k_{el} V^k_j \frac{\partial \phi_j}{\partial x},\ \frac{\partial \phi_i}{\partial y}>_{\Omega_{el}} + <(VH)^k_{el} V^k_j \frac{\partial \phi_j}{\partial y},\ \frac{\partial \phi_i}{\partial y}>_{\Omega_{el}}]$$

$$+ \Delta t^2 [<(f' VH)^k_j\ \phi_j,\ \frac{\partial \phi_i}{\partial x}>_{\Omega_{el}} - <(f' UH)^k_j\ \phi_j,\ \frac{\partial \phi_i}{\partial y}>_{\Omega_{el}}]$$

$$- \frac{g \Delta t^2}{2} [<(\zeta^2)^k_j \frac{\partial \phi_j}{\partial x},\ \frac{\partial \phi_i}{\partial x}>_{\Omega_{el}} + <(\zeta^2)^k_j \frac{\partial \phi_j}{\partial y},\ \frac{\partial \phi_i}{\partial y}>_{\Omega_{el}}]$$

$$- g \Delta t^2 H^k_{el} [<(\frac{p_s}{\rho_0 g} - \alpha\eta)^k_j \frac{\partial \phi_j}{\partial x},\ \frac{\partial \phi_i}{\partial x}>_{\Omega_{el}} + <(\frac{p_s}{\rho_0 g} - \alpha\eta)^k_j \frac{\partial \phi_j}{\partial y},\ \frac{\partial \phi_i}{\partial y}>_{\Omega_{el}}]$$

$$+ \Delta t^2[<(\frac{\tau_{sx}}{\rho_o})_j^k \phi_j, \frac{\partial \phi_i}{\partial x}>_{\Omega_{el}} + <(\frac{\tau_{sy}}{\rho_o})_j^k \phi_j, \frac{\partial \phi_i}{\partial y}>_{\Omega_{el}}]$$

$$- \Delta t^2\{<[(\tau_*' - \tau_o)HU]_j^k \phi_j, \frac{\partial \phi_i}{\partial x}>_{\Omega_{el}} + <[(\tau_*' - \tau_o)HV]_j^k \phi_j, \frac{\partial \phi_i}{\partial y}>_{\Omega_{el}}\}$$

$$- \Delta t^2[<D_{uu}{}_j^k \frac{\partial \phi_i}{\partial x}, \frac{\partial \phi_i}{\partial x}>_{\Omega_{el}} + <D_{uv}{}_j^k \frac{\partial \phi_i}{\partial y}, \frac{\partial \phi_i}{\partial x}>_{\Omega_{el}} + <D_{uv}{}_j^k \frac{\partial \phi_i}{\partial x}, \frac{\partial \phi_i}{\partial y}>_{\Omega_{el}}$$

$$+ <D_{vv}{}_j^k \frac{\partial \phi_i}{\partial y}, \frac{\partial \phi_i}{\partial y}>_{\Omega_{el}}]\Big\} - \Delta t^2 F_i \qquad i=1, \ldots N \tag{85}$$

where

M = the total number of elements

Ω_{el} = the elemental domain for the element, el.

Equation 85 can be rewritten as:

$$\sum_{el=1}^{M}\Bigg\{ \sum_{j=1}^{n_{el}} [(1 + \frac{\tau_o \Delta t}{2})M_{ji}^{(1)} + \alpha_1 g \Delta t^2 M_{ji}^{(2)} + \frac{E_{h_2} \Delta t}{2} M_{ji}^{(3)}]\zeta_j^{k+1}$$

$$= \sum_{j=1}^{n_{el}} \Big[2M_{ji}^{(1)}\zeta_j^k + (\frac{\tau_o \Delta t}{2} - 1)M_{ji}^{(1)}\zeta_j^{k-1} - \alpha_2 g \Delta t^2 M_{ji}^{(2)}\zeta_j^k$$

$$- \alpha_3 g \Delta t^2 M_{ji}^{(2)}\zeta_j^{k-1} + \frac{E_{h_2} \Delta t}{2} M_{ji}^{(3)}\zeta_j^{k-1}$$

$$+ \Delta t\ [M_{ij}^{(7)}U_{el}^k(\zeta_j^k - \zeta_j^{k-1}) + M_{ij}^{(8)}V_{el}^k(\zeta_j^k - \zeta_j^{k-1})]$$

$$- \Delta t^2[M_{ji}^{(4)}(UH)_{el}^k U_j^k + M_{ij}^{(5)}(VH)_{el}^k U_j^k + M_{ji}^{(5)}(UH)_{el}^k V_j^k + M_{ji}^{(6)}(VH)_{el}^k V_j^k]$$

$$+ \Delta t^2[M_{ij}^{(7)}(f'VH)_j^k - M_{ij}^{(8)}(f'UH)_j^k] - \frac{g\Delta t^2}{2} M_{ji}^{(3)}(\zeta^2)_j^k$$

$$- g\Delta t^2 M_{ji}^{(3)}(\frac{p_s}{\rho_o g} - \alpha\eta)_j^k H_{el}^k + \Delta t^2[M_{ij}^{(7)}(\frac{\tau_{sx}}{\rho_o})_j^k + M_{ij}^{(8)}(\frac{\tau_{sy}}{\rho_o})_j^k]$$

$$- \Delta t^2\{M_{ij}^{(7)}[(\tau_*' - \tau_o)HU]_j^k + M_{ij}^{(8)}[(\tau_*' - \tau_o)HV]_j^k\}$$

$$- \Delta t^2[M_{ji}^{(4)}D_{uu}{}_j^k + M_{ij}^{(5)}D_{uv}{}_j^k + M_{ji}^{(5)}D_{uv}{}_j^k + M_{ji}^{(6)}D_{vv}{}_j^k]\Big\} - \Delta t^2 F_i$$

$$i=1, \ldots N \tag{86}$$

where

$$M_{ij}^{(1)} \equiv <\phi_i, \phi_j>_{\Omega_{el}} \tag{87a}$$

$$M_{ij}^{(2)} \equiv <\sum_{m=1}^{n_{el}} h_m \phi_m \frac{\partial \phi_i}{\partial x}, \frac{\partial \phi_i}{\partial x}>_{\Omega_{el}} + <\sum_{m=1}^{n_{el}} h_m \phi_m \frac{\partial \phi_i}{\partial y}, \frac{\partial \phi_i}{\partial y}>_{\Omega_{el}} \tag{87b}$$

$$M_{ij}^{(3)} \equiv <\frac{\partial \phi_i}{\partial x}, \frac{\partial \phi_i}{\partial x}>_{\Omega_{el}} + <\frac{\partial \phi_i}{\partial y}, \frac{\partial \phi_i}{\partial y}>_{\Omega_{el}} \tag{87c}$$

$$M_{ij}^{(4)} \equiv <\frac{\partial \phi_i}{\partial x}, \frac{\partial \phi_i}{\partial x}>_{\Omega_{el}} \tag{87d}$$

$$M_{ij}^{(5)} \equiv <\frac{\partial \phi_i}{\partial y}, \frac{\partial \phi_i}{\partial x}>_{\Omega_{el}} \tag{87e}$$

$$M_{ij}^{(6)} \equiv <\frac{\partial \phi_i}{\partial y}, \frac{\partial \phi_i}{\partial y}>_{\Omega_{el}} \tag{87f}$$

$$M_{ij}^{(7)} \equiv <\phi_j, \frac{\partial \phi_i}{\partial x}>_{\Omega_{el}} \tag{87g}$$

$$M_{ij}^{(8)} \equiv <\phi_j, \frac{\partial \phi_i}{\partial y}>_{\Omega_{el}} \tag{87h}$$

Note that the elemental matrices, $M_{ij}^{(1)}$, $M_{ij}^{(2)}$, $M_{ij}^{(3)}$, $M_{ij}^{(4)}$, and $M_{ij}^{(6)}$ are symmetrical and that $M_{ij}^{(5)}$, $M_{ij}^{(7)}$, and $M_{ij}^{(8)}$ are non–symmetrical.

54. The fully discretized GWCE can be written in a compact form as:

$$\sum_{el=1}^{M} \sum_{j=1}^{n_{el}} [M_{ij}^{GWCE}] \{\zeta_j^{k+1}\} = \sum_{el=1}^{M} \{P_i^{GWCE}\} \qquad i=1, \ldots N \tag{88}$$

where

$$M_{ij}^{GWCE} \equiv (1 + \frac{\tau_0 \Delta t}{2}) M_{ji}^{(1)} + \alpha_1 g \Delta t^2 M_{ji}^{(2)} + \frac{E_{h2} \Delta t}{2} M_{ji}^{(3)} \tag{89}$$

$$\begin{aligned} P_i^{GWCE} = \sum_{j=1}^{n_{el}} \Big[& 2M_{ji}^{(1)} \zeta_j^k + (\frac{\tau_0 \Delta t}{2} - 1) M_{ji}^{(1)} \zeta_j^{k-1} - \alpha_2 g \Delta t^2 M_{ji}^{(2)} \zeta_j^k \\ & - \alpha_3 g \Delta t^2 M_{ji}^{(2)} \zeta_j^{k-1} + \frac{E_{h2} \Delta t}{2} M_{ji}^{(3)} \zeta_j^{k-1} \\ & + \Delta t \, [M_{ij}^{(7)} U_{el}^k (\zeta_j^k - \zeta_j^{k-1}) + M_{ij}^{(8)} V_{el}^k (\zeta_j^k - \zeta_j^{k-1})] \\ & - \Delta t^2 [M_{ji}^{(4)} (UH)_{el}^k U_j^k + M_{ij}^{(5)} (VH)_{el}^k U_j^k + M_{ji}^{(5)} (UH)_{el}^k V_j^k + M_{ji}^{(6)} (VH)_{el}^k V_j^k] \\ & + \Delta t^2 [M_{ij}^{(7)} (f' VH)_j^k - M_{ij}^{(8)} (f' UH)_j^k] - \frac{g \Delta t^2}{2} M_{ij}^{(3)} (\zeta^2)_j^k \\ & - g \Delta t^2 M_{ij}^{(3)} (\frac{p_s}{\rho_0 g} - \alpha \eta)_j^k H_{el}^k + \Delta t^2 [M_{ij}^{(7)} (\frac{\tau_{sx}}{\rho_0})_j^k + M_{ij}^{(8)} (\frac{\tau_{sy}}{\rho_0})_j^k] \\ & - \Delta t^2 \{M_{ij}^{(7)} [(\tau_*' - \tau_0) HU]_j^k + M_{ij}^{(8)} [(\tau_*' - \tau_0) HV]_j^k\} \\ & - \Delta t^2 [M_{ji}^{(4)} D_{uu_j}^k + M_{ij}^{(5)} D_{uv_j}^k + M_{ji}^{(5)} D_{uv_j}^k + M_{ji}^{(6)} D_{vv_j}^k] \Big] - \Delta t^2 F_i \end{aligned}$$

$$i=1, \ldots N \tag{90}$$

In the three–dimensional options, if the computed friction coefficient exceeds the maximum allowable value, the friction term in the right side load vector P_i^{GWCE} is slightly different:

$$P_i^{GWCE} = \sum_{j=1}^{n_{el}} \Big[2M_{ji}^{(1)}\zeta_j^k + (\frac{\tau_o \Delta t}{2} - 1)M_{ji}^{(1)}\zeta_j^{k-1} - \alpha_2 g\Delta t^2 M_{ji}^{(2)}\zeta_j^k$$

$$- \alpha_3 g\Delta t^2 M_{ji}^{(2)}\zeta_j^{k-1} + \frac{E_{h2}\Delta t}{2} M_{ji}^{(3)}\zeta_j^{k-1}$$

$$+ \Delta t \, [M_{ij}^{(7)}U_{el}^k(\zeta_j^k - \zeta_j^{k-1}) + M_{ij}^{(8)}V_{el}^k(\zeta_j^k - \zeta_j^{k-1})]$$

$$- \Delta t^2[M_{ji}^{(4)}(UH)_{el}^k U_j^k + M_{ij}^{(5)}(VH)_{el}^k U_j^k + M_{ji}^{(5)}(UH)_{el}^k V_j^k + M_{ji}^{(6)}(VH)_{el}^k V_j^k]$$

$$+ \Delta t^2[M_{ij}^{(7)}(fVH)_j^k - M_{ij}^{(8)}(fUH)_j^k] - \frac{g\Delta t^2}{2} M_{ij}^{(3)}(\zeta^2)_j^k$$

$$- g\Delta t^2 M_{ij}^{(3)}(\frac{p_s}{\rho_o g} - \alpha\eta)_j^k H_{el}^k + \Delta t^2[M_{ij}^{(7)}(\frac{\tau_{sx}}{\rho_o})_j^k + M_{ij}^{(8)}(\frac{\tau_{sy}}{\rho_o})_j^k]$$

$$- \Delta t^2\{M_{ij}^{(7)}[(\frac{\tau_{bx}}{\rho_o})_j^k - \tau_o(UH)_j^k] + M_{ij}^{(8)}[(\frac{\tau_{by}}{\rho_o})_j^k - \tau_o(VH)_j^k]\}$$

$$- \Delta t^2[M_{ji}^{(4)}D_{uu_j}^k + M_{ij}^{(5)}D_{uv_j}^k + M_{ji}^{(5)}D_{uv_j}^k + M_{ji}^{(6)}D_{vv_j}^k]\Big] - \Delta t^2 F_i$$

$$i=1, \ldots N \qquad (91)$$

55. Global assembly and enforcement of the C^o functional continuity requirement leads to the following global system of equations:

$$\sum_{j=1}^{N} [\, {}^gM_{ij}^{GWCE} \,] \{\, {}^g\zeta_j^{k+1} \,\} = \{\, {}^gP_i^{GWCE} \,\} \qquad i=1, \ldots N \qquad (92)$$

where

${}^gM_{ij}^{GWCE}$ = the global banded system matrix

${}^gP_i^{GWCE}$ = the global load vector

${}^g\zeta_j^{k+1}$ = the global nodal elevation vector

56. The fully discrete form of the momentum equations is obtained from the time–discretized symmetrical, weak weighted residual form of the momentum equations, Equations 71 and 72, as follows.

a. The local acceleration terms are interpolated using Equations 73b and 73c.

b. The friction terms are approximated by:

$$\tau_*'^k U^{k+1} \cong \sum_{j=1}^{n_{el}} \tau_{*j}'^k U_j^{k+1}\phi_j \qquad (93a)$$

$$\tau_*'^k V^{k+1} \cong \sum_{j=1}^{n_{el}} \tau_{*j}'^k V_j^{k+1}\phi_j \qquad (93b)$$

$$\tau'^{k}_{*} U^{k} \cong \sum_{j=1}^{n_{el}} \tau'^{k}_{*j} U^{k}_{j} \phi_j \tag{93c}$$

$$\tau'^{k}_{*} V^{k} \cong \sum_{j=1}^{n_{el}} \tau'^{k}_{*j} V^{k}_{j} \phi_j \tag{93d}$$

In the three–dimensional model options, if the computed friction coefficient exceeds the maximum allowable value, the bottom stress terms introduced on the right–hand side of the momentum equations are approximated by:

$$\left(\frac{\tau_{bx}}{\rho_o H}\right)^{k} \cong \sum_{j=1}^{n_{el}} \left(\frac{\tau_{bx}}{\rho_o H}\right)^{k}_{j} \phi_j \tag{94a}$$

$$\left(\frac{\tau_{by}}{\rho_o H}\right)^{k} \cong \sum_{j=1}^{n_{el}} \left(\frac{\tau_{by}}{\rho_o H}\right)^{k}_{j} \phi_j \tag{94b}$$

c. The Coriolis terms are approximated by:

$$f'^{k} U^{k+1} \cong \sum_{j=1}^{n_{el}} f'^{k}_{j} U^{k+1}_{j} \phi_j \tag{95a}$$

$$f'^{k} V^{k+1} \cong \sum_{j=1}^{n_{el}} f'^{k}_{j} V^{k+1}_{j} \phi_j \tag{95b}$$

$$f'^{k} U^{k} \cong \sum_{j=1}^{n_{el}} f'^{k}_{j} U^{k}_{j} \phi_j \tag{95c}$$

$$f'^{k} V^{k} \cong \sum_{j=1}^{n_{el}} f'^{k}_{j} V^{k}_{j} \phi_j \tag{95d}$$

d. The lateral diffusive/dispersive terms are approximated using Equations 73b and 73c for velocity and Equation 77 for total depth.

e. The barometric pressure and Newtonian tidal potential are interpolated using Equation 76.

f. The surface elevation is approximated using Equation 73a.

g. The surface stresses are evaluated as:

$$\left(\frac{\tau_{sx}}{\rho_o H}\right)^{k+1} \cong \sum_{j=1}^{n_{el}} \left(\frac{\tau_{sx}}{\rho_o H}\right)^{k+1}_{j} \phi_j \tag{96a}$$

$$\left(\frac{\tau_{sy}}{\rho_o H}\right)^{k+1} \cong \sum_{j=1}^{n_{el}} \left(\frac{\tau_{sy}}{\rho_o H}\right)^{k+1}_{j} \phi_j \tag{96b}$$

$$\left(\frac{\tau_{sx}}{\rho_o H}\right)^{k} \cong \sum_{j=1}^{n_{el}} \left(\frac{\tau_{sx}}{\rho_o H}\right)^{k}_{j} \phi_j \tag{96c}$$

$$\left(\frac{\tau_{sy}}{\rho_o H}\right)^{k} \cong \sum_{j=1}^{n_{el}} \left(\frac{\tau_{sy}}{\rho_o H}\right)^{k}_{j} \phi_j \tag{96d}$$

h. The advective terms are approximated by:

$$U^k \frac{\partial U^k}{\partial x} \cong U^k_{el} \sum_{j=1}^{n_{el}} U^k_j \frac{\partial \phi_j}{\partial x} \tag{97a}$$

$$V^k \frac{\partial U^k}{\partial x} \cong V^k_{el} \sum_{j=1}^{n_{el}} U^k_j \frac{\partial \phi_j}{\partial x} \tag{97b}$$

$$U^k \frac{\partial V^k}{\partial x} \cong U^k_{el} \sum_{j=1}^{n_{el}} V^k_j \frac{\partial \phi_j}{\partial x} \tag{97c}$$

$$V^k \frac{\partial V^k}{\partial x} \cong V^k_{el} \sum_{j=1}^{n_{el}} V^k_j \frac{\partial \phi_j}{\partial x} \tag{97d}$$

where U^k_{el} and V^k_{el} are defined in Equation 82.

i. The dispersive terms are broken up into their components D_{uu}, D_{uv}, and D_{vv}, (defined in Part II), and discretized as:

$$\left(\frac{1}{H} \frac{\partial D_{uu}}{\partial x}\right)^k \cong \left(\frac{1}{H_{el}}\right)^k \sum_{j=1}^{n_{el}} D_{uu}{}^k_j \frac{\partial \phi_i}{\partial x} \tag{98a}$$

$$\left(\frac{1}{H} \frac{\partial D_{uv}}{\partial y}\right)^k \cong \left(\frac{1}{H_{el}}\right)^k \sum_{j=1}^{n_{el}} D_{uv}{}^k_j \frac{\partial \phi_i}{\partial y} \tag{98b}$$

$$\left(\frac{1}{H} \frac{\partial D_{uv}}{\partial x}\right)^k \cong \left(\frac{1}{H_{el}}\right)^k \sum_{j=1}^{n_{el}} D_{uv}{}^k_j \frac{\partial \phi_i}{\partial x} \tag{98c}$$

$$\left(\frac{1}{H} \frac{\partial D_{vv}}{\partial y}\right)^k \cong \left(\frac{1}{H_{el}}\right)^k \sum_{j=1}^{n_{el}} D_{vv}{}^k_j \frac{\partial \phi_i}{\partial y} \tag{98d}$$

where H_{el} is defined in Equation 77.

j. The baroclinic terms are not included in either ADCIRC–2DDI or ADCIRC–3DL. Therefore the discretization of these terms is not considered here.

57. Substituting the approximations in Equations 93 – 98 into Equations 71 and 72 and summing over the elements gives the discrete system of equations:

$$\sum_{el=1}^{M} \sum_{j=1}^{n_{el}} \Big[\langle (1 + \frac{\Delta t}{2} \tau'^k_{*j})\, U^{k+1}_j \phi_j,\ \phi_i \rangle_{\Omega_{el}} - \frac{\Delta t}{2} \langle f'^k_j V^{k+1}_j \phi_j,\ \phi_i \rangle_{\Omega_{el}}$$

$$+ \beta_1 E_{h2} \Delta t \left[\langle U^{k+1}_j H^{k+1}_{el} \frac{\partial \phi_j}{\partial x},\ \frac{\partial}{\partial x}(\frac{\phi_i}{H^{k+1}_{el}}) \rangle_{\Omega_{el}} + \langle U^{k+1}_j H^{k+1}_{el} \frac{\partial \phi_j}{\partial y},\ \frac{\partial}{\partial y}(\frac{\phi_i}{H^{k+1}_{el}}) \rangle_{\Omega_{el}} \right]$$

$$= \langle (1 - \frac{\Delta t}{2} \tau'^k_{*j})\, U^k_j \phi_j,\ \phi_i \rangle_{\Omega_{el}} + \frac{\Delta t}{2} \langle f'^k_j V^k_j \phi_j,\ \phi_i \rangle_{\Omega_{el}}$$

$$- \beta_2 E_{h2} \Delta t \left[\langle U^k_j H^k_{el} \frac{\partial \phi_j}{\partial x},\ \frac{\partial}{\partial x}(\frac{\phi_i}{H^k_{el}}) \rangle_{\Omega_{el}} + \langle U^k_j H^k_{el} \frac{\partial \phi_j}{\partial y},\ \frac{\partial}{\partial y}(\frac{\phi_i}{H^k_{el}}) \rangle_{\Omega_{el}} \right]$$

$$- g \frac{\Delta t}{2} \langle \left[(\frac{p^{k+1}_{sj}}{\rho_o g} + \zeta^{k+1}_j - \alpha \eta^{k+1}_j) + (\frac{p^k_{sj}}{\rho_o g} + \zeta^k_j - \alpha \eta^k_j) \right] \frac{\partial \phi_j}{\partial x},\ \phi_i \rangle_{\Omega_{el}}$$

$$+ \frac{\Delta t}{2}<[(\frac{\tau_{sx}}{\rho_o H})_j^{k+1} + (\frac{\tau_{sx}}{\rho_o H})_j^k]\ \phi_j,\ \phi_i>_{\Omega_{el}}$$

$$- \Delta t[<U_{el}^k U_j^k \frac{\partial \phi_j}{\partial x},\ \phi_i>_{\Omega_{el}} + <V_{el}^k U_j^k \frac{\partial \phi_j}{\partial y},\ \phi_i>_{\Omega_{el}}]$$

$$- \Delta t[<(\frac{1}{H_{el}})^k D_{uu_j}^k \frac{\partial \phi_j}{\partial x},\ \phi_i>_{\Omega_{el}} + <(\frac{1}{H_{el}})^k D_{uv_j}^k \frac{\partial \phi_j}{\partial y},\ \phi_i>_{\Omega_{el}}]\Big]$$

$$i=1,\ \ldots N \qquad (99)$$

and

$$\sum_{el=1}^{M} \sum_{j=1}^{n_{el}} \Big[<(1 + \frac{\Delta t}{2}\tau'^k_{*j})\ V_j^{k+1}\phi_j,\ \phi_i>_{\Omega_{el}} - \frac{\Delta t}{2} <f'^k_j U_j^{k+1}\phi_j,\ \phi_i>_{\Omega_{el}}$$

$$+ \beta_1 E_{h_2}\Delta t\ [<V_j^{k+1}H_{el}^{k+1} \frac{\partial \phi_i}{\partial x},\ \frac{\partial}{\partial x}(\frac{\phi_i}{H_{el}^{k+1}})>_{\Omega_{el}} + <V_j^{k+1}H_{el}^{k+1} \frac{\partial \phi_i}{\partial y},\ \frac{\partial}{\partial y}(\frac{\phi_i}{H_{el}^{k+1}})>_{\Omega_{el}}]$$

$$= <(1 - \frac{\Delta t}{2}\tau'^k_{*j})\ V_j^k\phi_j,\ \phi_i>_{\Omega_{el}} + \frac{\Delta t}{2} <f'^k_j U_j^k\phi_j,\ \phi_i>_{\Omega_{el}}$$

$$- \beta_2 E_{h_2}\Delta t\ [<V_j^k H_{el}^k \frac{\partial \phi_i}{\partial x},\ \frac{\partial}{\partial x}(\frac{\phi_i}{H_{el}^k})>_{\Omega_{el}} + <V_j^k H_{el}^k \frac{\partial \phi_i}{\partial y},\ \frac{\partial}{\partial y}(\frac{\phi_i}{H_{el}^k})>_{\Omega_{el}}]$$

$$- g\frac{\Delta t}{2}<[(\frac{p_{sj}^{k+1}}{\rho_o g} + \zeta_j^{k+1} - \alpha\eta_j^{k+1}) + (\frac{p_{sj}^k}{\rho_o g} + \zeta_j^k - \alpha\eta_j^k)] \frac{\partial \phi_i}{\partial y},\ \phi_i>_{\Omega_{el}}$$

$$+ \frac{\Delta t}{2}<[(\frac{\tau_{sy}}{\rho_o H})_j^{k+1} + (\frac{\tau_{sy}}{\rho_o H})_j^k]\ \phi_j,\ \phi_i>_{\Omega_{el}}$$

$$- \Delta t[<U_{el}^k V_j^k \frac{\partial \phi_j}{\partial x},\ \phi_i>_{\Omega_{el}} + <V_{el}^k V_j^k \frac{\partial \phi_j}{\partial y},\ \phi_i>_{\Omega_{el}}]$$

$$- \Delta t[<(\frac{1}{H_{el}})^k D_{uv_j}^k \frac{\partial \phi_i}{\partial x},\ \phi_i>_{\Omega_{el}} + <(\frac{1}{H_{el}})^k D_{vv_j}^k \frac{\partial \phi_i}{\partial y},\ \phi_i>_{\Omega_{el}}]\Big]$$

$$i=1,\ \ldots N \qquad (100)$$

Equations 99 and 100 can be rewritten as:

$$\sum_{el=1}^{M} \sum_{j=1}^{n_{el}} \Big[(1 + \frac{\Delta t}{2}\tau'^k_{*j})M_{ij}^{(1)}U_j^{k+1} - \frac{\Delta t}{2}f'^k_j M_{ij}^{(1)}V_j^{k+1} + \beta_1 E_{h_2}\Delta t M_{ij}^{(3)}U_j^{k+1}$$

$$= (1 - \frac{\Delta t}{2}\tau'^k_{*j})M_{ij}^{(1)}U_j^k + \frac{\Delta t}{2}f'^k_j M_{ij}^{(1)}V_j^k - \beta_2 E_{h_2}\Delta t M_{ij}^{(3)}U_j^k$$

$$- g\frac{\Delta t}{2}M_{ji}^{(7)}[(\frac{p_{sj}^{k+1}}{\rho_o g} + \zeta_j^{k+1} - \alpha\eta_j^{k+1}) + (\frac{p_{sj}^k}{\rho_o g} + \zeta_j^k - \alpha\eta_j^k)]$$

$$+ \frac{\Delta t}{2}M_{ij}^{(1)}[(\frac{\tau_{sx}}{\rho_o H})_j^{k+1} + (\frac{\tau_{sx}}{\rho_o H})_j^k] - \Delta t(U_{el}^k M_{ji}^{(7)}U_j^k + V_{el}^k M_{ji}^{(8)}U_j^k)$$

$$- \Delta t(\frac{1}{H_{el}})^k[M_{ji}^{(7)}D_{uu_j}^k + M_{ji}^{(8)}D_{uv_j}^k]\Big] \qquad i=1,\ \ldots N \qquad (101)$$

and

$$\sum_{el=1}^{M} \sum_{j=1}^{n_{el}} \Big[(1 + \frac{\Delta t}{2}\tau'^k_{*j})M_{ij}^{(1)}V_j^{k+1} + \frac{\Delta t}{2}f'^k_j M_{ij}^{(1)}U_j^{k+1} + \beta_1 E_{h_2}\Delta t M_{ij}^{(3)}V_j^{k+1}$$

$$= (1 - \frac{\Delta t}{2}\tau'^{k}_{*j})M^{(1)}_{ij}V^{k}_{j} - \frac{\Delta t}{2}f'^{k}_{j}M^{(1)}_{ij}U^{k}_{j} - \beta_2 E_{h2}\Delta t M^{(3)}_{ij}V^{k}_{j}$$

$$- g\frac{\Delta t}{2}M^{(8)}_{ji}[(\frac{p^{k+1}_{sj}}{\rho_0 g} + \zeta^{k+1}_{j} - \alpha\eta^{k+1}_{j}) + (\frac{p^{k}_{sj}}{\rho_0 g} + \zeta^{k}_{j} - \alpha\eta^{k}_{j})]$$

$$+ \frac{\Delta t}{2}M^{(1)}_{ij}[(\frac{\tau_{sy}}{\rho_0 H})^{k+1}_{j} + (\frac{\tau_{sy}}{\rho_0 H})^{k}_{j}] - \Delta t(U^{k}_{el}M^{(7)}_{ji}V^{k}_{j} + V^{k}_{el}M^{(8)}_{ji}V^{k}_{j})$$

$$- \Delta t(\frac{1}{H_{el}})^{k}[M^{(7)}_{ji}D_{uvj}{}^{k} + M^{(8)}_{ji}D_{vvj}{}^{k}]\Big] \qquad i=1, \ldots N \qquad (102)$$

58. The $M^{(1)}_{ij}$ matrices on the left side of Equations 101 and 102 and in the first two terms on the right side of these equations are lumped so that all elements are added onto the diagonal. The $M^{(3)}_{ij}$ matrices on the left side of Equations 101 and 102 are decomposed into diagonal and non–diagonal matrices. The non–diagonal portion of $M^{(3)}_{ij}$ is moved to the right side of the equations. These operations give:

$$\sum_{el=1}^{M}\sum_{j=1}^{n_{el}}\Big[(1 + \frac{\Delta t}{2}\tau'^{k}_{*j})M^{(1L)}_{ij}U^{k+1}_{j} - \frac{\Delta t}{2}f'^{k}_{j}M^{(1L)}_{ij}V^{k+1}_{j} + \beta_1 E_{h2}\Delta t M^{(3D)}_{ij}U^{k+1}_{j}$$

$$= (1 - \frac{\Delta t}{2}\tau'^{k}_{*j})M^{(1L)}_{ij}U^{k}_{j} - \frac{\Delta t}{2}f'^{k}_{j}M^{(1L)}_{ij}V^{k}_{j} - E_{h2}\Delta t(\beta_1 M^{(3ND)}_{ij}U^{k+1}_{ij} + \beta_2 M^{(3)}_{ij}U^{k}_{j})$$

$$- g\frac{\Delta t}{2}M^{(7)}_{ji}[(\frac{p^{k+1}_{sj}}{\rho_0 g} + \zeta^{k+1}_{j} - \alpha\eta^{k+1}_{j}) + (\frac{p^{k}_{sj}}{\rho_0 g} + \zeta^{k}_{j} - \alpha\eta^{k}_{j})]$$

$$+ \frac{\Delta t}{2}M^{(1)}_{ij}[(\frac{\tau_{sx}}{\rho_0 H})^{k+1}_{j} + (\frac{\tau_{sx}}{\rho_0 H})^{k}_{j}] - \Delta t(U^{k}_{el}M^{(7)}_{ji}U^{k}_{j} + V^{k}_{el}M^{(8)}_{ji}U^{k}_{j})$$

$$- \Delta t(\frac{1}{H_{el}})^{k}[M^{(7)}_{ji}D_{uuj}{}^{k} + M^{(8)}_{ji}D_{uvj}{}^{k}]\Big] \qquad i=1, \ldots N \qquad (103)$$

and

$$\sum_{el=1}^{M}\sum_{j=1}^{n_{el}}\Big[(1 + \frac{\Delta t}{2}\tau'^{k}_{*j})M^{(1L)}_{ij}V^{k+1}_{j} + \frac{\Delta t}{2}f'^{k}_{j}M^{(1L)}_{ij}U^{k+1}_{j} + \beta_1 E_{h2}\Delta t M^{(3D)}_{ij}V^{k+1}_{j}$$

$$= (1 - \frac{\Delta t}{2}\tau'^{k}_{*j})M^{(1L)}_{ij}V^{k}_{j} - \frac{\Delta t}{2}f'^{k}_{j}M^{(1L)}_{ij}U^{k}_{j} - E_{h2}\Delta t(\beta_1 M^{(3ND)}_{ij}V^{k+1}_{j} + \beta_2 M^{(3)}_{ij}V^{k}_{j})$$

$$- g\frac{\Delta t}{2}M^{(8)}_{ji}[(\frac{p^{k+1}_{sj}}{\rho_0 g} + \zeta^{k+1}_{j} - \alpha\eta^{k+1}_{j}) + (\frac{p^{k}_{sj}}{\rho_0 g} + \zeta^{k}_{j} - \alpha\eta^{k}_{j})]$$

$$+ \frac{\Delta t}{2}M^{(1)}_{ij}[(\frac{\tau_{sy}}{\rho_0 H})^{k+1}_{j} + (\frac{\tau_{sy}}{\rho_0 H})^{k}_{j}] - \Delta t(U^{k}_{el}M^{(7)}_{ji}V^{k}_{j} + V^{k}_{el}M^{(8)}_{ji}V^{k}_{j})$$

$$- \Delta t(\frac{1}{H_{el}})^{k}[M^{(7)}_{ji}D_{uvj}{}^{k} + M^{(8)}_{ji}D_{vvj}{}^{k}]\Big] \qquad i=1, \ldots N \qquad (104)$$

where

$M^{(1L)}_{ij}$ = the diagonally lumped elemental matrix $M^{(1)}_{ij}$

$M^{(3D)}_{ij}$ = the diagonal portion of the elemental matrix $M^{(3)}_{ij}$

$M_{ij}^{(3ND)}$ = the non–diagonal portion of the elemental matrix $M_{ij}^{(3)}$

59. The fully discretized momentum equations can be written in compact form as:

$$\sum_{el=1}^{M} \sum_{j=1}^{n_{el}} [M_{ij}^{1ME}] \{U_j^{k+1}\} - [M_{ij}^{2ME}] \{V_j^{k+1}\} = \sum_{el=1}^{M} \{P_i^{XME}\} \qquad i=1, \ldots N \tag{105}$$

$$\sum_{el=1}^{M} \sum_{j=1}^{n_{el}} [M_{ij}^{2ME}] \{U_j^{k+1}\} + [M_{ij}^{1ME}] \{V_j^{k+1}\} = \sum_{el=1}^{M} \{P_i^{YME}\} \qquad i=1, \ldots N \tag{106}$$

where

$$M_{ij}^{1ME} \equiv (1 + \frac{\Delta t}{2}\tau'^{k}_{*j})M_{ij}^{(1L)} + \beta_1 E_{h2}\Delta t M_{ij}^{(3D)} \tag{107a}$$

$$M_{ij}^{2ME} \equiv \frac{\Delta t}{2} f'^{k}_{j} M_{ij}^{(1L)} \tag{107b}$$

$$\begin{aligned} P_i^{XME} \equiv \sum_{j=1}^{n_{el}} \Big[& (1 - \frac{\Delta t}{2}\tau'^{k}_{*j})M_{ij}^{(1L)}U_j^k + \frac{\Delta t}{2} f'^{k}_{j} M_{ij}^{(1L)} V_j^k \\ & - E_{h2}\Delta t(\beta_1 M_{ij}^{(3ND)}U_{ij}^{k+1} + \beta_2 M_{ij}^{(3)}U_j^k) \\ & - g\frac{\Delta t}{2}M_{ji}^{(7)}[(\frac{p_{sj}^{k+1}}{\rho_o g} + \zeta_j^{k+1} - \alpha\eta_j^{k+1}) + (\frac{p_{sj}^{k}}{\rho_o g} + \zeta_j^{k} - \alpha\eta_j^{k})] \\ & + \frac{\Delta t}{2}M_{ij}^{(1)}[(\frac{\tau_{sx}}{\rho_o H})_j^{k+1} + (\frac{\tau_{sx}}{\rho_o H})_j^{k}] - \Delta t(U_{el}^k M_{ji}^{(7)}U_j^k + V_{el}^k M_{ji}^{(8)}U_j^k) \\ & - \Delta t(\frac{1}{H_{el}})^k [M_{ji}^{(7)}D_{uu_j}^k + M_{ji}^{(8)}D_{uv_j}^k] \Big] \qquad i=1, \ldots N \end{aligned} \tag{107c}$$

$$\begin{aligned} P_i^{YME} \equiv \sum_{j=1}^{n_{el}} \Big[& (1 - \frac{\Delta t}{2}\tau'^{k}_{*j})M_{ij}^{(1L)}V_j^k - \frac{\Delta t}{2} f'^{k}_{j} M_{ij}^{(1L)} U_j^k \\ & - E_{h2}\Delta t(\beta_1 M_{ij}^{(3ND)}V_j^{k+1} + \beta_2 M_{ij}^{(3)}V_j^k) \\ & - g\frac{\Delta t}{2}M_{ji}^{(8)}[(\frac{p_{sj}^{k+1}}{\rho_o g} + \zeta_j^{k+1} - \alpha\eta_j^{k+1}) + (\frac{p_{sj}^{k}}{\rho_o g} + \zeta_j^{k} - \alpha\eta_j^{k})] \\ & + \frac{\Delta t}{2}M_{ij}^{(1)}[(\frac{\tau_{sy}}{\rho_o H})_j^{k+1} + (\frac{\tau_{sy}}{\rho_o H})_j^{k}] - \Delta t\ [U_{el}^k M_{ji}^{(7)}V_j^k + V_{el}^k M_{ji}^{(8)}V_j^k] \\ & - \Delta t(\frac{1}{H_{el}})^k [M_{ji}^{(7)}D_{uv_j}^k + M_{ji}^{(8)}D_{vv_j}^k] \Big] \qquad i=1, \ldots N \end{aligned} \tag{107d}$$

In the three–dimensional model options, if the computed friction coefficient exceeds the maximum allowable value, the bottom stress terms appear explicitly on the right side of the momentum equations and therefore are included in P_i^{XME} and P_i^{YME}:

$$P_i^{XME} \equiv \sum_{j=1}^{n_{el}} \Big[M_{ij}^{(1L)}U_j^k + \frac{\Delta t}{2} f_j^k M_{ij}^{(1L)} V_j^k$$

$$- E_{h2}\Delta t(\beta_1 M_{ij}^{(3ND)} U_{ij}^{k+1} + \beta_2 M_{ij}^{(3)} U_j^k)$$

$$- g\frac{\Delta t}{2} M_{ji}^{(7)}[(\frac{p_{sj}^{k+1}}{\rho_o g} + \zeta_j^{k+1} - \alpha\eta_j^{k+1}) + (\frac{p_{sj}^{k}}{\rho_o g} + \zeta_j^{k} - \alpha\eta_j^{k})]$$

$$+ \frac{\Delta t}{2} M_{ij}^{(1)}[(\frac{\tau_{sx}}{\rho_o H})_j^{k+1} + (\frac{\tau_{sx}}{\rho_o H})_j^{k}] - \Delta t(U_{el}^k M_{ji}^{(7)} U_j^k + V_{el}^k M_{ji}^{(8)} U_j^k)$$

$$- \Delta t(\frac{1}{H_{el}})^k [M_{ji}^{(7)} D_{uu_j}^k + M_{ji}^{(8)} D_{uv_j}^k] - \Delta t M_{ij}^{(1)} (\frac{\tau_{bx}}{\rho_o H})_j^k \Big] \qquad (108a)$$

$$P_i^{YME} \equiv \sum_{j=1}^{n_{el}} \Big[M_{ij}^{(1L)} V_j^k - \frac{\Delta t}{2} f_j^k M_{ij}^{(1L)} U_j^k$$

$$- E_{h2}\Delta t(\beta_1 M_{ij}^{(3ND)} V_j^{k+1} + \beta_2 M_{ij}^{(3)} V_j^k)$$

$$- g\frac{\Delta t}{2} M_{ji}^{(8)}[(\frac{p_{sj}^{k+1}}{\rho_o g} + \zeta_j^{k+1} - \alpha\eta_j^{k+1}) + (\frac{p_{sj}^{k}}{\rho_o g} + \zeta_j^{k} - \alpha\eta_j^{k})]$$

$$+ \frac{\Delta t}{2} M_{ij}^{(1)}[(\frac{\tau_{sy}}{\rho_o H})_j^{k+1} + (\frac{\tau_{sy}}{\rho_o H})_j^{k}] - \Delta t(U_{el}^k M_{ij}^{(7)} V_j^k + V_{el}^k M_{ji}^{(8)} V_j^k)$$

$$- \Delta t(\frac{1}{H_{el}})^k [M_{ji}^{(7)} D_{uv_j}^k + M_{ji}^{(8)} D_{vv_j}^k] - \Delta t M_{ij}^{(1)} (\frac{\tau_{by}}{\rho_o H})_j^k \Big] \qquad (108b)$$

60. Global assembly and enforcement of the C^o functional continuity requirement gives the following systems of equations:

$$\sum_{j=1}^{N} [{}^g M_{ij}^{1ME}] \{{}^g U_j^{k+1}\} - [{}^g M_{ij}^{2ME}] \{{}^g V_j^{k+1}\} = \{{}^g P_i^{XME}\} \qquad i=1, \ldots N \qquad (109)$$

$$\sum_{j=1}^{N} [{}^g M_{ij}^{2ME}] \{{}^g U_j^{k+1}\} + [{}^g M_{ij}^{1ME}] \{{}^g V_j^{k+1}\} = \{{}^g P_i^{YME}\} \qquad i=1, \ldots N \qquad (110)$$

where

${}^g M_{ij}^{1ME}$, ${}^g M_{ij}^{2ME}$ = global diagonal system matrices

${}^g P_i^{XME}$, ${}^g P_i^{YME}$ = global right–hand–side load vectors,

${}^g U_j^{k+1}$, ${}^g V_j^{k+1}$ = global velocity vectors in the x and y directions

Solution Strategy

61. The horizontal discretization for ADCIRC has been implemented with three–node linear triangles and four–node bilinear quadrilaterals. The triangle element provides a maximum degree of flexibility and is extremely cost–effective on a per–node basis for long wave computations. All elemental matrices $M_{ij}^{(1)}$ through $M_{ij}^{(8)}$ are integrated using a numerical quadrature rule that is specified with the input data. A

four–point Gaussian quadrature rule integrates the elemental matrices, Equation 87, exactly (Connor and Brebbia 1976). However, for most applications, a three–point Gaussian quadrature rule appears to be sufficient. The elemental matrices are computed once and then stored for use during the time–stepping operations.

62. The GWCE is solved first. The global system matrix for the GWCE, ${}^{g}M_{ij}^{GWCE}$, is time–independent and is therefore assembled and LU decomposed only once. ${}^{g}M_{ij}^{GWCE}$ has a banded structure with a band width that is dependent on the node numbering of the grid. Prior to running ADCIRC, the node numbering should be optimized to minimize the maximum difference in the global node numbers associated with each element in the grid. The right side load vector, ${}^{g}P_{i}^{GWCE}$, is efficiently updated every time step since all elemental matrices have been pre–computed. Flux–specified boundary conditions have been incorporated into the load vector by the model formulation and therefore require no additional equation manipulation. Elevation–specified boundary conditions are incorporated into the system matrix, ${}^{g}M_{ij}^{GWCE}$, by zeroing out rows corresponding to boundary nodes with specified elevations and placing a value of unity onto the diagonal. The boundary condition values are then stored into the appropriate location in ${}^{g}P_{i}^{GWCE}$. The equations associated with elevation–specified boundary conditions are multiplied through by a constant to ensure that the modified global matrix has a good condition number. The modified system of equations (i.e., Equation 92 modified to include the elevation–specified boundary conditions), is then solved for elevation at the new time level, k+1.

63. The momentum equations are solved second and use the elevation values at time level k+1 computed from the GWCE. The global system matrices for the momentum equations, (${}^{g}M_{ij}^{1ME}$ and ${}^{g}M_{ij}^{2ME}$), are time–dependent and therefore need to be reevaluated at every time step. However, since these matrices are diagonal, matrix evaluation and decomposition are very economical. Specified normal flux boundary conditions are incorporated into Equations 109 and 110 by reorienting the x and y equation pairs that correspond to the specified flux boundary nodes into a locally (for each node) normal/tangential coordinate system. The reoriented equations are then replaced by the corresponding specified normal flow boundary condition values (Wang and Connor 1975; Gray 1984).

64. The right sides of Equations 109 and 110 are dependent on ζ_j^{k+1}, ζ_j^k, U_j^k, and V_j^k, which are all known quantities, and on U_j^{k+1} and V_j^{k+1} (because of the lateral

closure model). Therefore, these equations must be solved iteratively for velocities at the new time level, k+1. ${}^{g}P_i^{XME}$ and ${}^{g}P_i^{YME}$ are updated each iteration with the new values of U_j^{k+1} and V_j^{k+1} until a specified convergence criteria has been reached. When E_{h2} is zero, no iteration takes place.

65. When a three–dimensional option is used, the external mode solution depends on the internal mode solution through D_{uu}, D_{uv}, D_{vv}, C_f and γ [or if the drag coefficients exceed the maximum allowable values on τ_{bx} and τ_{by}]. These quantities are computed at each internal mode time step and assumed to be constant in time for subsequent external mode time steps. If the external mode solution and the internal mode solution are evaluated at the same model time, the external mode solution is evaluated first. The updated surface elevations and depth–averaged velocities are then used in the internal mode solution. This solution sequence requires the specification of initial values for D_{uu}, D_{uv}, D_{vv}, C_f, and γ as input parameters for the external mode solution.

Fourier Properties of the External Mode Solution

66. Fourier analysis characterizes the damping and phase propagation properties of a numerical solution in relation to the corresponding analytical solution. Although it is typically applied to the one–dimensional form of the shallow–water equations and a constant bathymetric depth is usually assumed, the results give a good indication of how a circulation model will behave in a more general two–dimensional, nonlinear field application. They also allow inter–comparisons with other discretization strategies. Procedures for applying Fourier analysis to the shallow–water equations are described by Pinder and Gray (1977) and Lynch (1978).

67. The discrete form of the ADCIRC 2DDI governing equations has been Fourier analyzed. These results are presented below along with results from the Fourier analyses of several other numerical solution schemes for the shallow–water equations. All of the other numerical schemes that were considered use primitive formulations of the shallow–water equations (as opposed to the generalized wave–continuity formulation used in ADCIRC). The schemes include a finite element solution using linear elements (PEFE) (Wang and Connor 1975; Westerink, Connor and Stolzenbach 1987, 1988), a second order, non–staggered, finite difference solution (PENSFD), and a second order, staggered, finite difference solution (PESFD) (Hansen

1956; Leendertse 1967). A second order, Crank–Nicholson scheme was used to integrate the PEFE, PENSFD, and PESFD in time. As described previously, ADCIRC uses a three–time–level scheme for the GWCE ($\alpha_1 = 0.35$, $\alpha_2 = 0.30$ and $\alpha_3 = 0.35$), and a Crank–Nicholson scheme for the momentum equations. The bottom friction coefficient (Equation 46) in each model was specified as

$$\tau_* = 0.8\ \pi\ \sqrt{gh}\ /\lambda \tag{111}$$

where λ is the wavelength of the Fourier component.

68. The modulus of the propagation factor indicates the ratio of the numerical amplitude to the analytical amplitude during the propagation of one wavelength. The phase of the propagation factor indicates the phase lag or lead a given wavelength experiences during one period. Figure 1 presents the modulus and phase of the propagation factor for the PEFE and PENSFD schemes. Comparisons are shown for $\mathbb{C}_r = 0.1$, 0.5, 1.0, and 2.0 where $\mathbb{C}_r$ is the Courant number based on wave celerity,

$$\mathbb{C}_r \equiv \frac{\Delta t\ \sqrt{gh}}{\Delta x} \tag{112}$$

Δt is the time step, and Δx is the grid spacing. For increasing $\mathbb{C}_r$, both the PEFE and the PENSFD solutions have less damping than the analytical solution for low ratios of $\lambda/\Delta x$. Neither solution, regardless of $\mathbb{C}_r$, propagates energy at the shortest resolvable wavelength, $\lambda = 2\Delta x$. This characteristic of PEFE and PENSFD solutions accounts for the severe $2\Delta x$ numerical noise problems encountered using these schemes.

69. Figure 2 presents the modulus and phase of the propagation factor for the PESFD scheme and the generalized wave–continuity equation finite element (GWCEFE) scheme used in ADCIRC. For low ratios of $\lambda/\Delta x$, both schemes provide less damping than the analytical solution and show poorer phase propagation behavior as $\mathbb{C}_r$ increases. For a fixed $\mathbb{C}_r$ and $\lambda/\Delta x$, the PESFD scheme has slightly better damping characteristics, while the GWCEFE scheme has better phase propagation characteristics. At low $\mathbb{C}_r$, the GWCEFE solution leads the analytical solution. As $\mathbb{C}_r$ increases, the GWCEFE phase propagation factor swings through a zero value (corresponding to perfect phase behavior) and then develops a phase lag. This indicates that there will be a local minimum in the time convergence curve with optimal accuracy being achieved at $\mathbb{C}_r \approx 0.5$.

70. The primary difference between numerical solutions using PEFE and PENSFD schemes and numerical solutions using GWCEFE and PESFD schemes is that the latter schemes propagate energy at $\lambda = 2\Delta x$. Propagation of $2\Delta x$ waves corresponds to a non–folded dispersion relationship and prevents two responses from

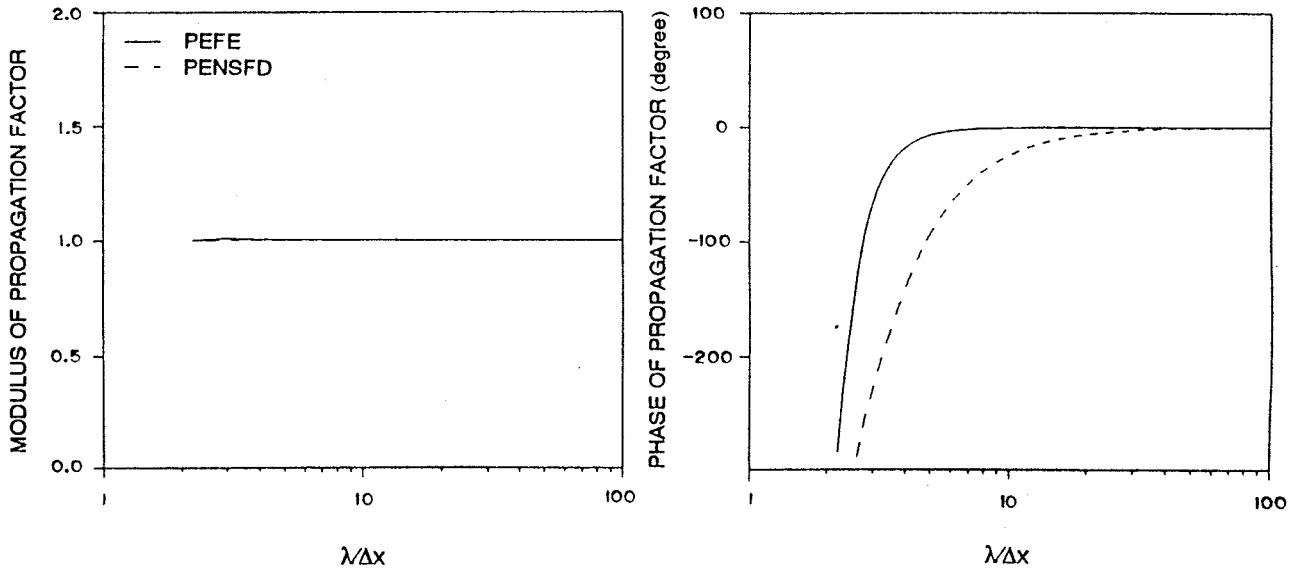

a. $\mathbb{C}_r = 0.1$

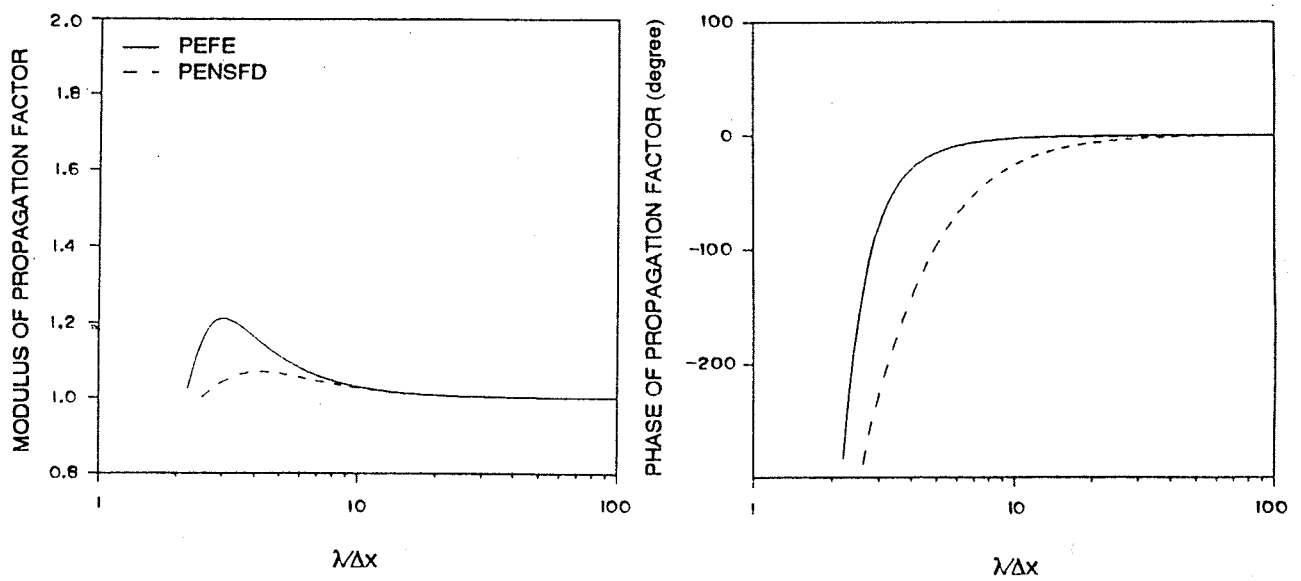

b. $\mathbb{C}_r = 0.5$

Figure 1. Modulus and phase of the propagation factor for PEFE and PENSFD solutions (Continued)

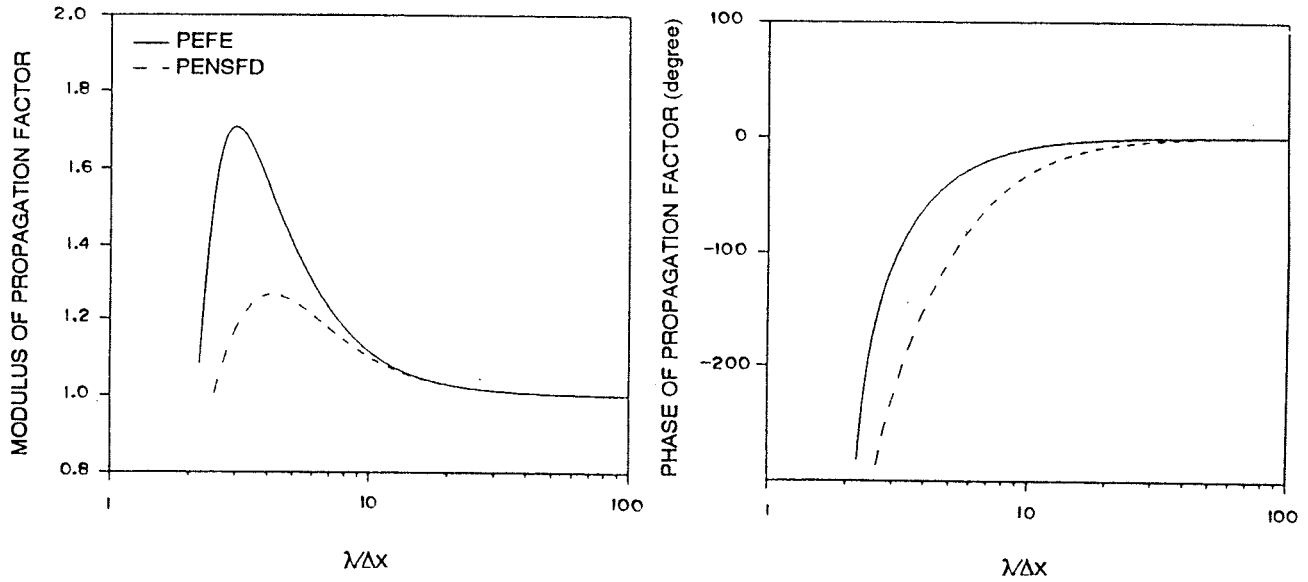

c. $\mathbb{C}_r = 1.0$

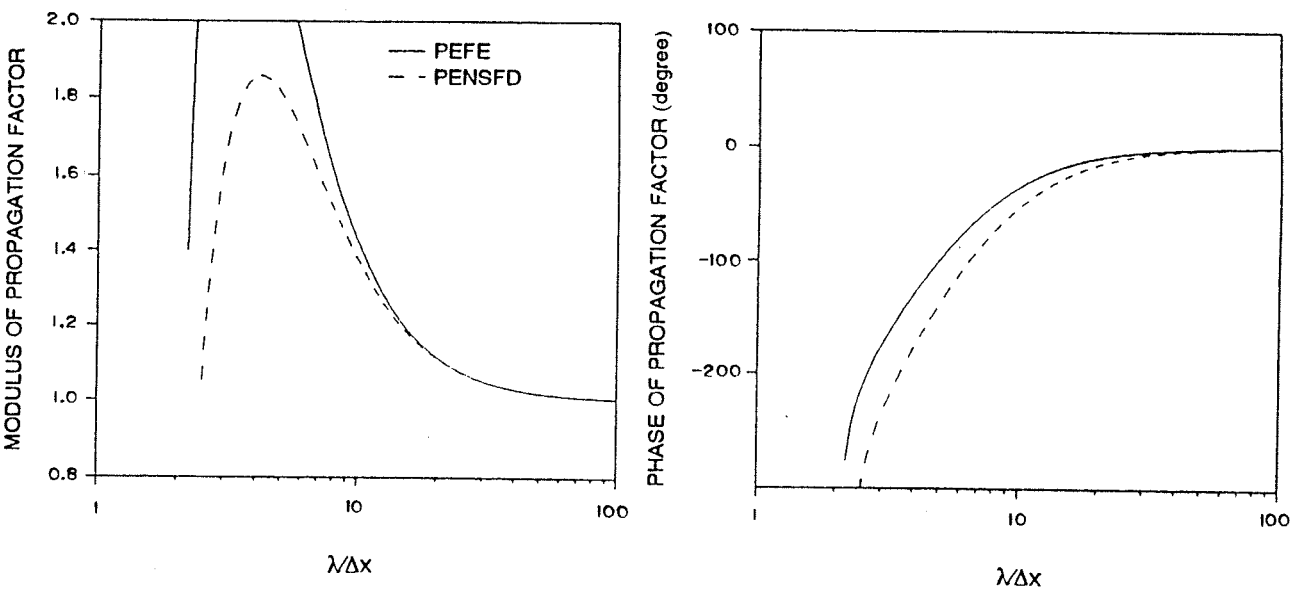

d. $\mathbb{C}_r = 2.0$

Figure 1. (Concluded)

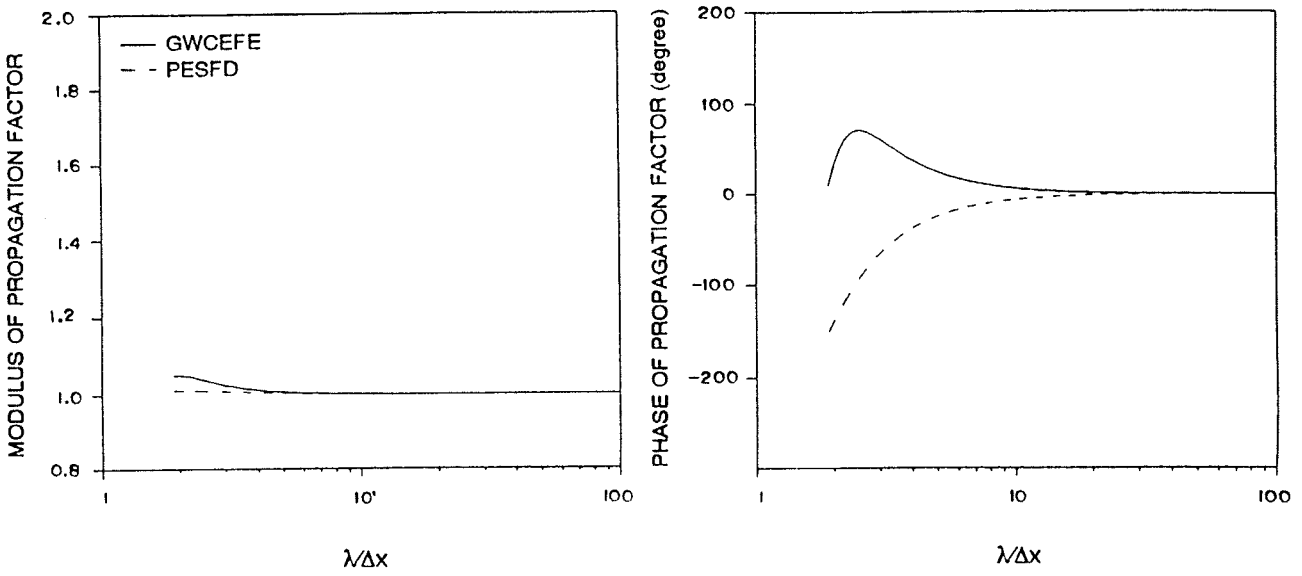

a. $\mathbb{C}_r = 0.1$

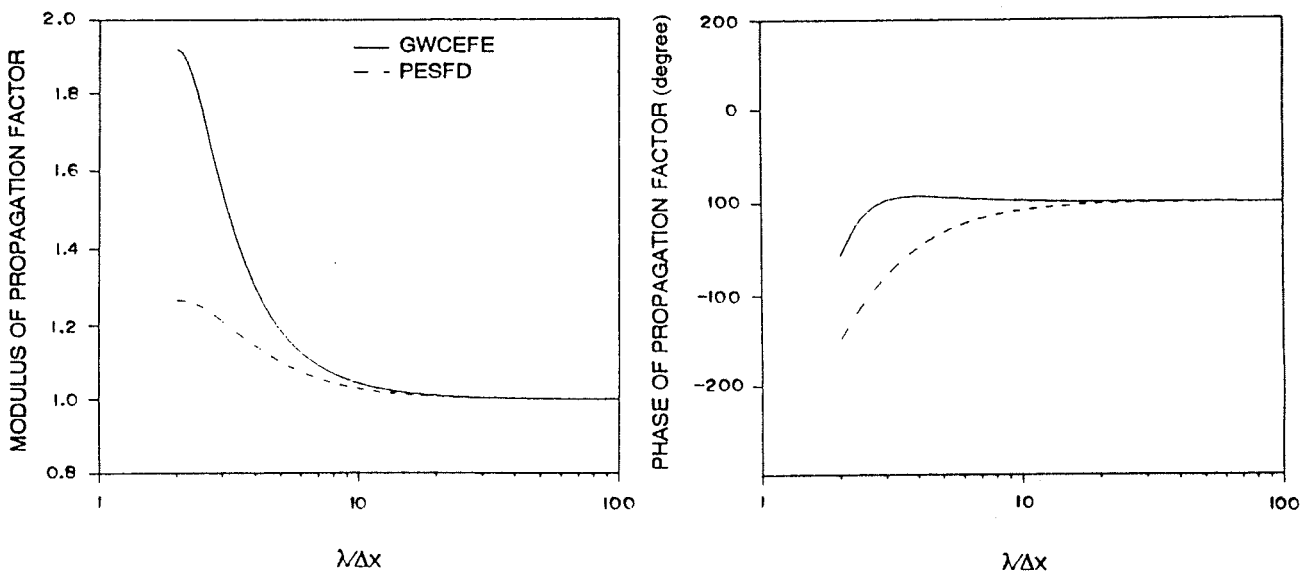

b. $\mathbb{C}_r = 0.5$

Figure 2. Modulus and phase of the propagation factor for GWCEFE and PESFD solutions (Continued)

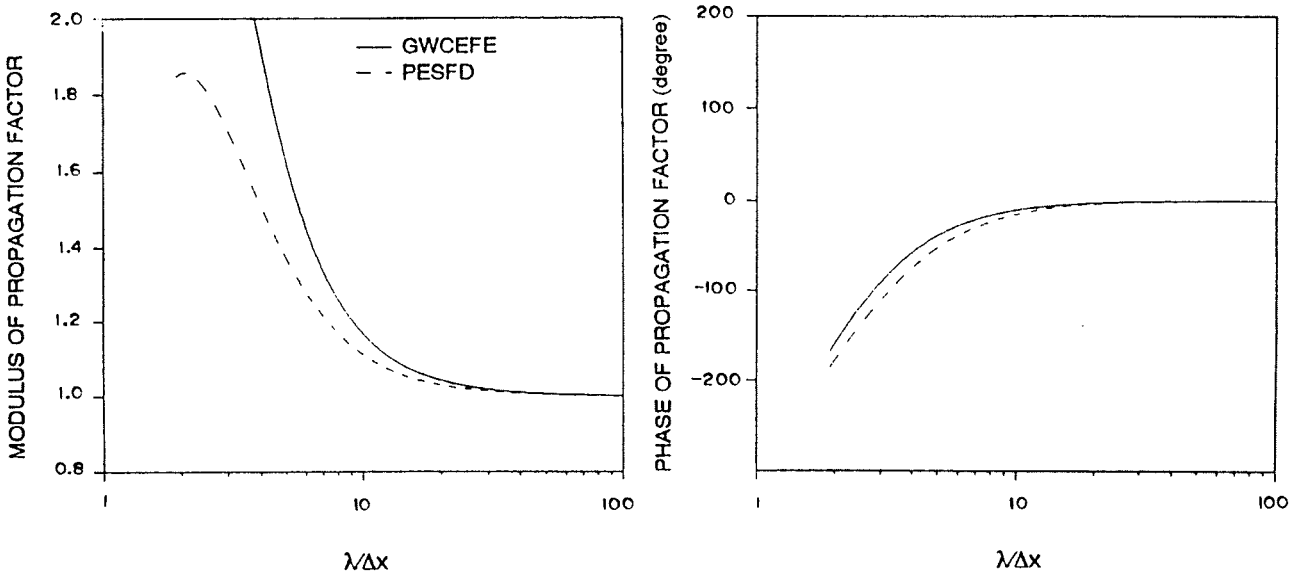

c. $\mathfrak{C}_r = 1.0$

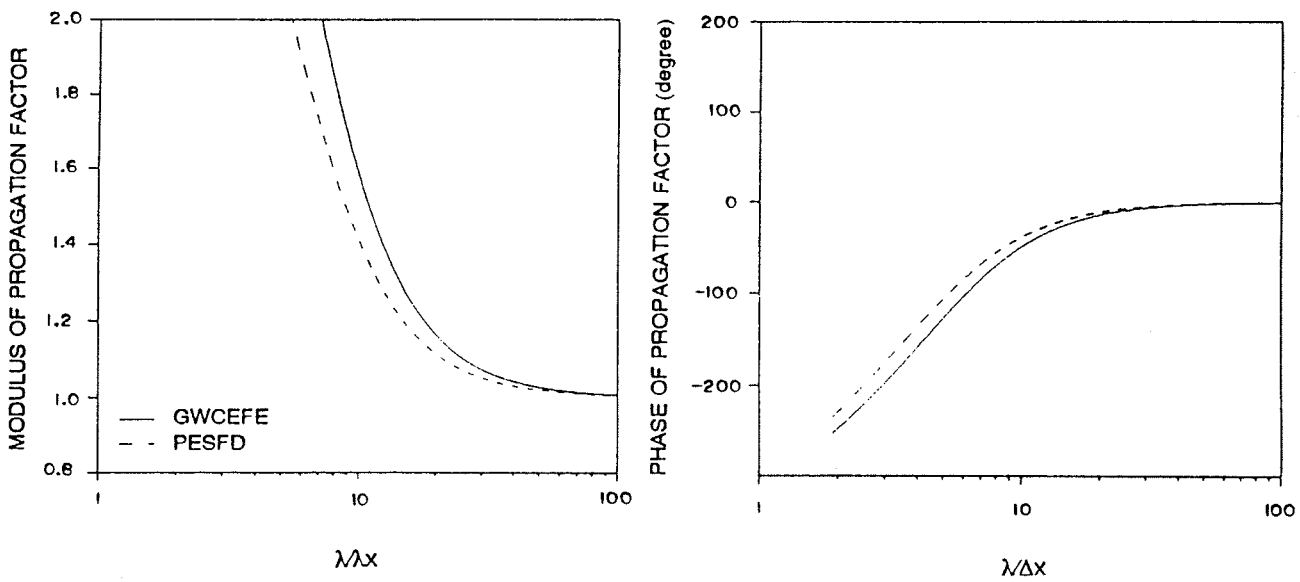

d. $\mathfrak{C}_r = 2.0$

Figure 2. (Concluded)

developing to a single forcing frequency, i.e., one physical response at the forcing wavelength and one numerical response at a wavelength near $2\Delta x$ (Platzman 1981). As a consequence, GWCEFE and PESFD schemes do not have the severe $2\Delta x$ noise problem of the PEFE and PENSFD schemes.

Convergence Properties of the External Mode Solution

71. In order to verify the accuracy of the external mode solution of ADCIRC and to establish convergence properties in space and time, ADCIRC–2DDI was applied to a modified form of the quarter annular test problems originally developed and applied by Lynch and Gray (1978, 1979) and Gray and Lynch (1979). These two–dimensional, variable–depth test problems were developed to give insight into a numerical scheme's $2\Delta x$ oscillations and its ability to propagate longer physical waves. The original geometry and bathymetry of Lynch and Gray (1978, 1979) were modified as follows. The arc of the annulus was increased to 135 deg*; the inner radius was decreased to 125,000 ft; the outer radius was increased to 650,000 ft. The resulting geometry, with three land boundaries and one open ocean boundary, is shown in Figure 3. A linearly varying bathymetry was used that increased from 50 ft at the inner radius to 260 ft at the outer radius and a quadratically varying bathymetry was used that increased from 50 ft at the inner radius to 1,352 ft at the outer radius. These modifications accomplish two things. First, the modified domains are more representative of a coastal region that extends to near or beyond the Continental Shelf break. (In fact, the geometry and bathymetry are idealized approximations to the New York Bight.) Second, the numerical difficulty of the test problems is increased.

72. A sequence of four discretizations was considered: a 6– by 8–node discretization (Δr = 105,000 ft), an 11– by 15–node discretization (Δr = 52,500 ft), a 21– by 29–node discretization (Δr = 26,250 ft), and a 41– by 57–node discretization (Δr = 13,125 ft). These are shown in Figure 4. Grids consisting of linear triangles and of bilinear quadrilaterals were tested and gave very similar results. Only the bilinear quadrilateral results are presented here. For each grid, five different time steps were applied: $\Delta t = T_{M_2}/8$, $\Delta t = T_{M_2}/16$, $\Delta t = T_{M_2}/32$, $\Delta t = T_{M_2}/64$, and $\Delta t = T_{M_2}/128$ where T_{M_2} is the M_2 tidal forcing period equal to 44,712 seconds. ADCIRC–2DDI was run in its linear mode with an M_2 forcing frequency. Therefore,

---

*A table of factors for converting non–SI units of measurement to SI (metric) units is presented on page 6.

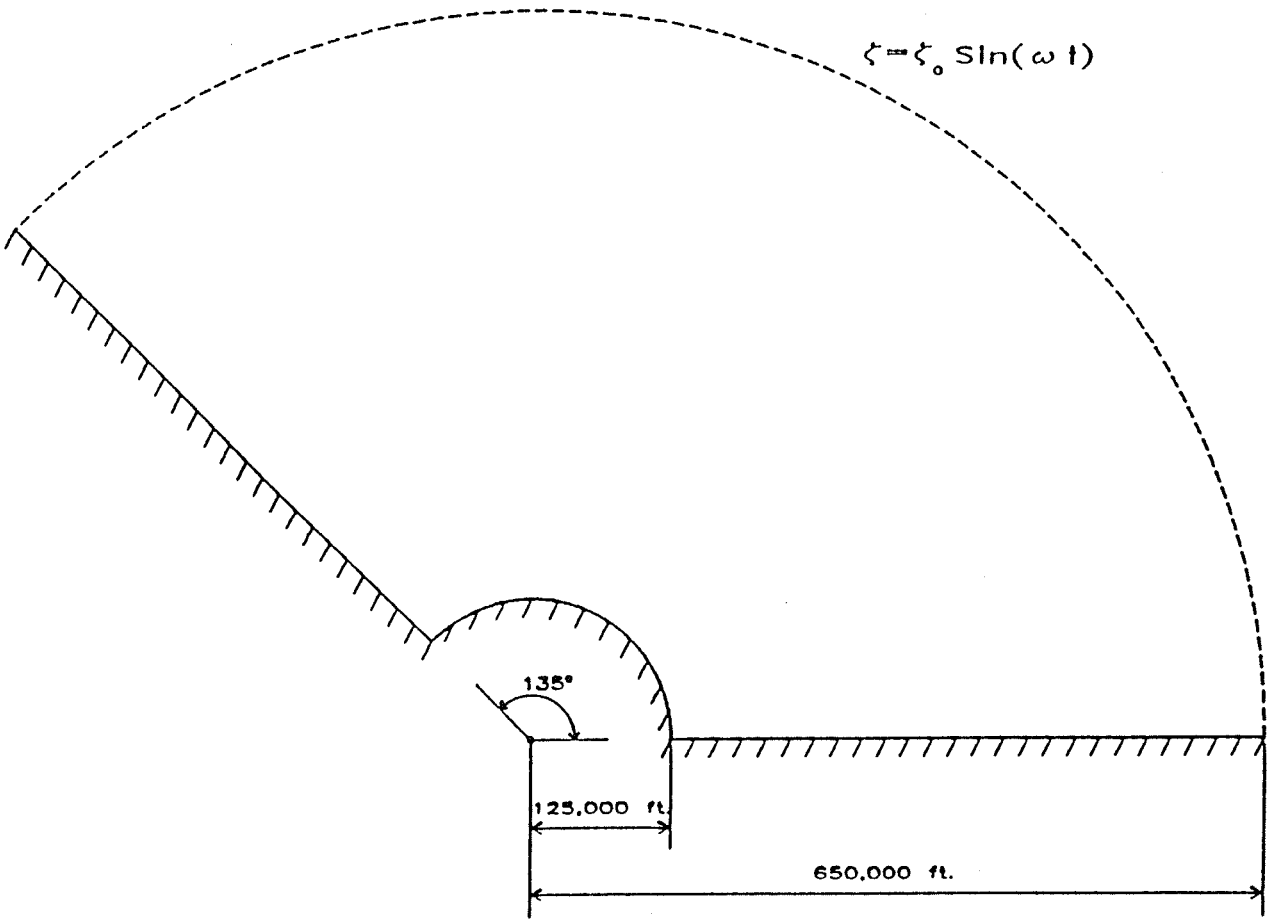

Figure 3. Test problem geometry

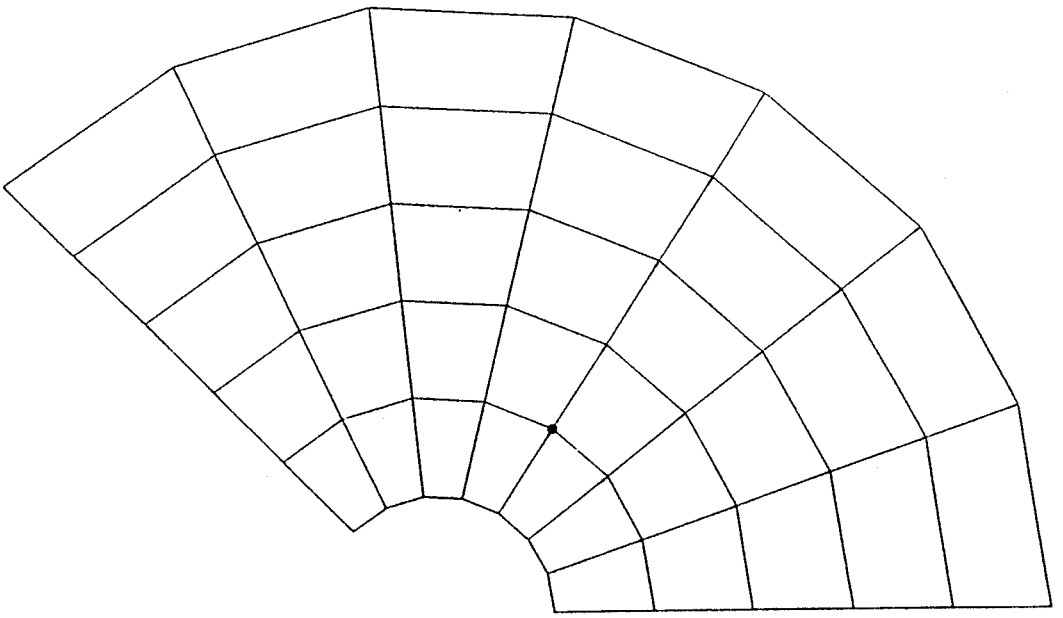

a. 6– by 8–node grid

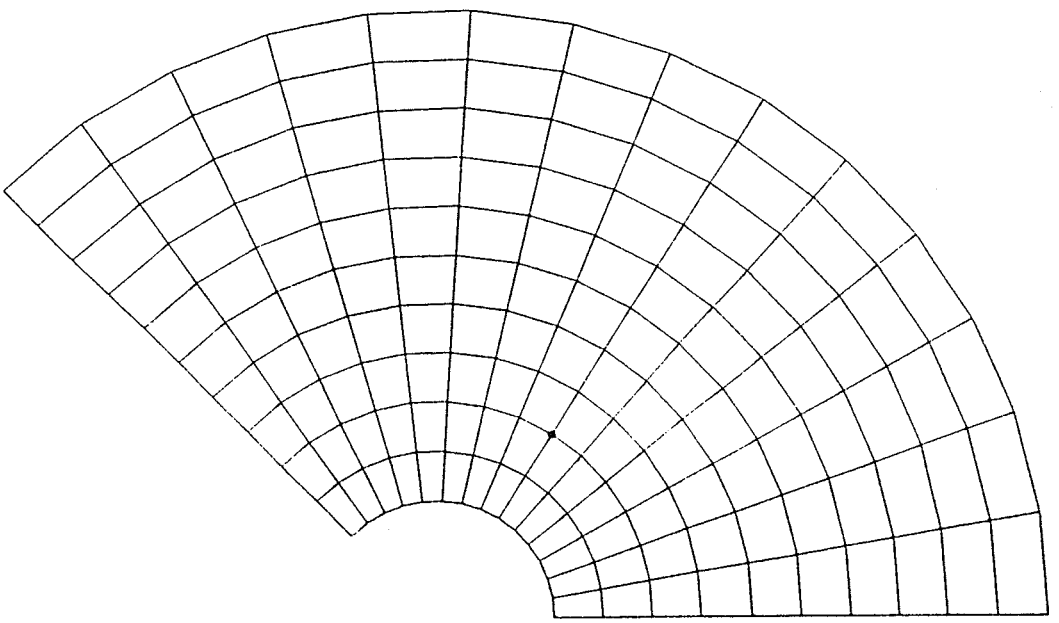

b. 11– by 15–node grid

Figure 4. Grids used for the test problem (Continued)

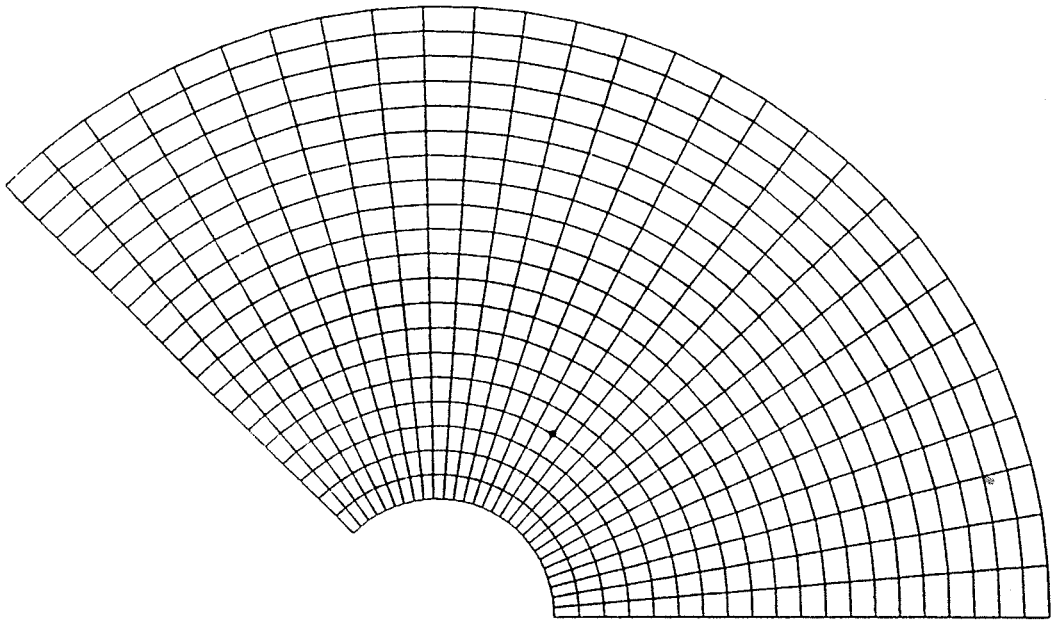

c. 21– by 29–node grid

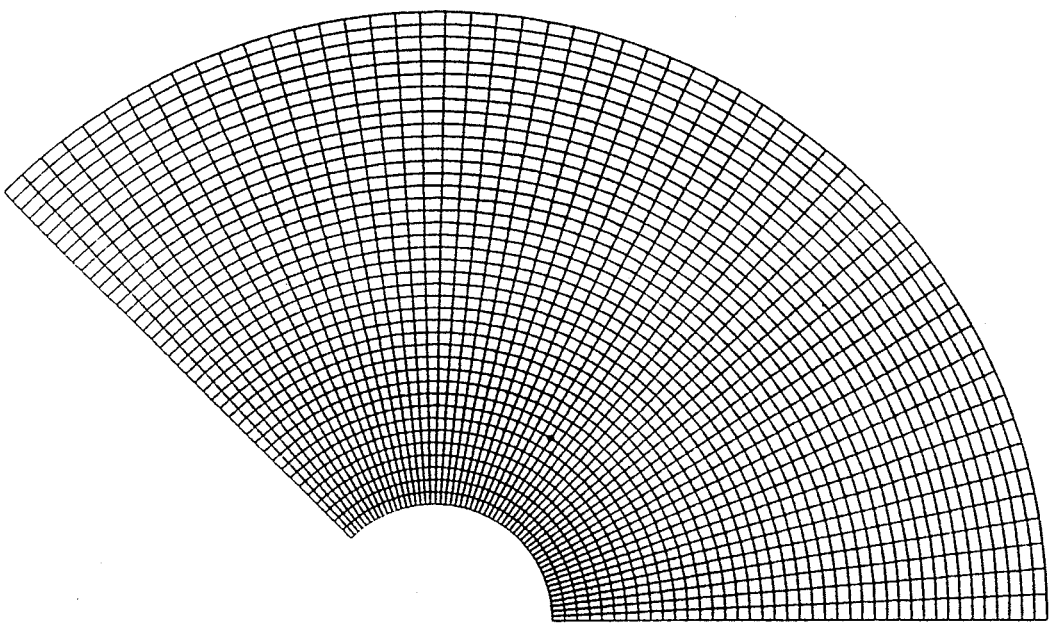

d. 41– by 57–node grid

Figure 4. (Concluded)

the theoretical model response should have included only an M_2 wave. The resolution of the M_2 wave provided by the sequence of grids varied between 17 and 312 nodes per wavelength for the linearly varying bathymetries and between 17 and 703 nodes per wavelength for the quadratically varying cases. Thus the M_2 wave was always well–resolved. $\mathbb{C}_r$ varied between 0.13 and 39 for the linearly varying bathymetries and between 0.13 and 88 for the quadratically varying cases. ADCIRC–2DDI is unconditionally stable in its linear mode and therefore permits the use of $\mathbb{C}_r > 1$.

73. All cases were forced at the open ocean boundary using $\zeta = 1.0 \sin(\omega_{M_2} t)$ where $\omega_{M_2} \equiv 2\pi/T_{M_2}$ is the M_2 forcing frequency. All other forcing mechanisms (i.e., tidal potential, free surface wind stress and atmospheric pressure gradients) were set to zero. The Coriolis and advective terms were also neglected. The bottom friction coefficient was set to $\tau_* = 0.0001$ and the value of $\tau_o = 0.0001$. All total depths were set equal to the depth to the geoid.

74. The computations were hot–started using the analytical solution for the specified geometry, bathymetry, and friction coefficient. The computations were then run for 10 tidal cycles to allow a dynamically steady–state numerical solution to develop. The elevation and radial velocity solutions at each node were recorded during the eleventh tidal cycle and were Fourier decomposed. Typical results are shown in Figure 5 for the sequence of runs using the coarsest grid and the linearly varying bathymetry. The figures compare the exact analytical solution to the maximum and minimum ADCIRC–2DDI solution for all nodes at the same radius. These plots indicate that there are no spurious $2\Delta x$ modes in either the radial or angular directions.

75. Error measures were calculated from comparisons between the harmonically decomposed numerical solutions and the analytical solutions. These were defined as:

$$E_1 \equiv \left\{ \frac{1}{N_p} \sum_{i=1}^{N_p} (a_{\zeta_i}^A - a_{\zeta_i}^N) \right\}^{1/2} \tag{113a}$$

$$E_2 \equiv \left\{ \frac{1}{N_p} \sum_{i=1}^{N_p} (b_{\zeta_i}^A - b_{\zeta_i}^N) \right\}^{1/2} \tag{113b}$$

$$E_3 \equiv \left\{ \frac{1}{N_p} \sum_{i=1}^{N_p} (a_{u_i}^A - a_{u_i}^N) \right\}^{1/2} \tag{113c}$$

$$E_4 \equiv \left\{ \frac{1}{N_p} \sum_{i=1}^{N_p} (b_{u_i}^A - b_{u_i}^N) \right\}^{1/2} \tag{113d}$$

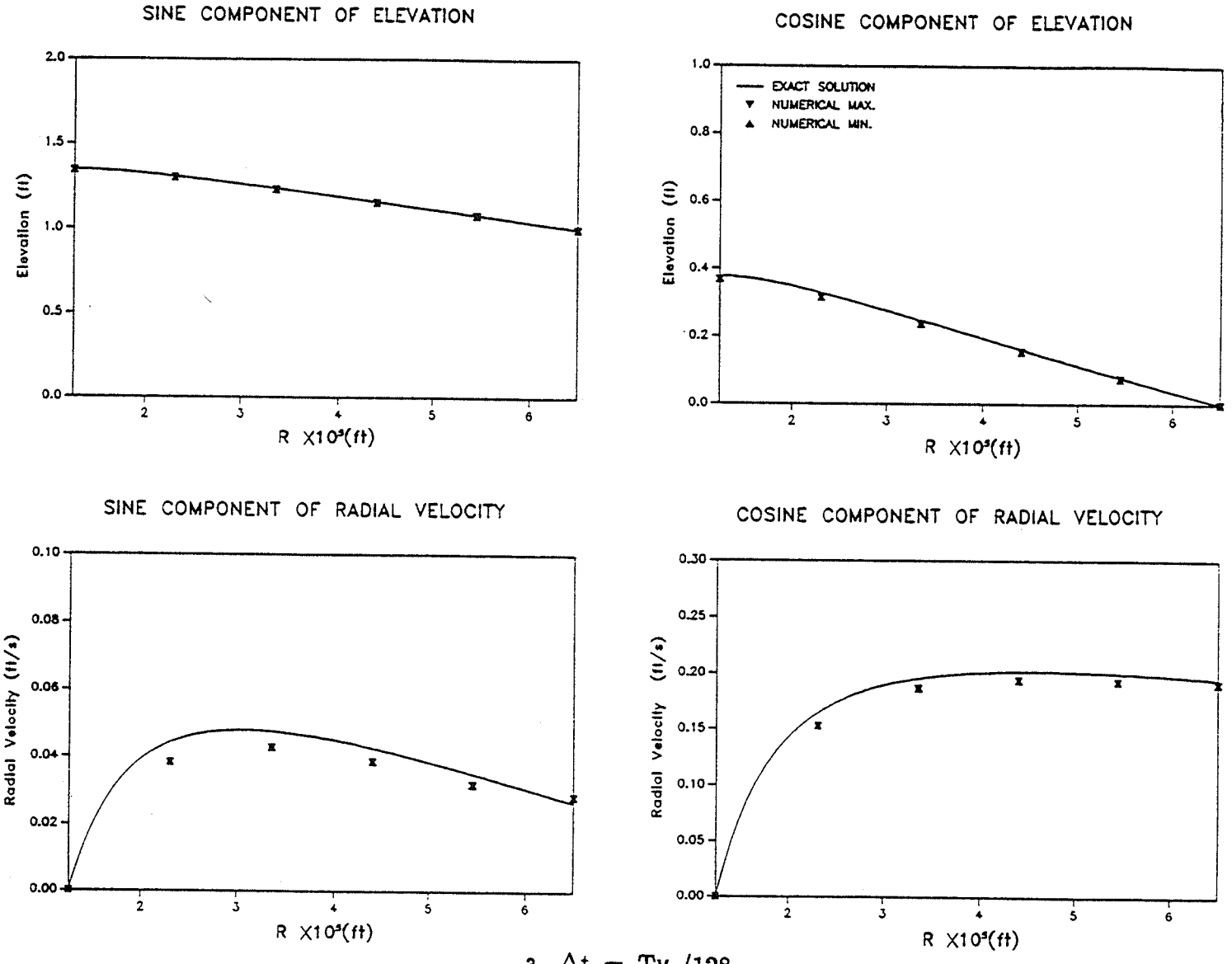

a. $\Delta t = T_{M_2}/128$

Figure 5. Elevation and radial velocity components on the 6– by 8– node grid with linear bathymetry (Sheet 1 of 5)

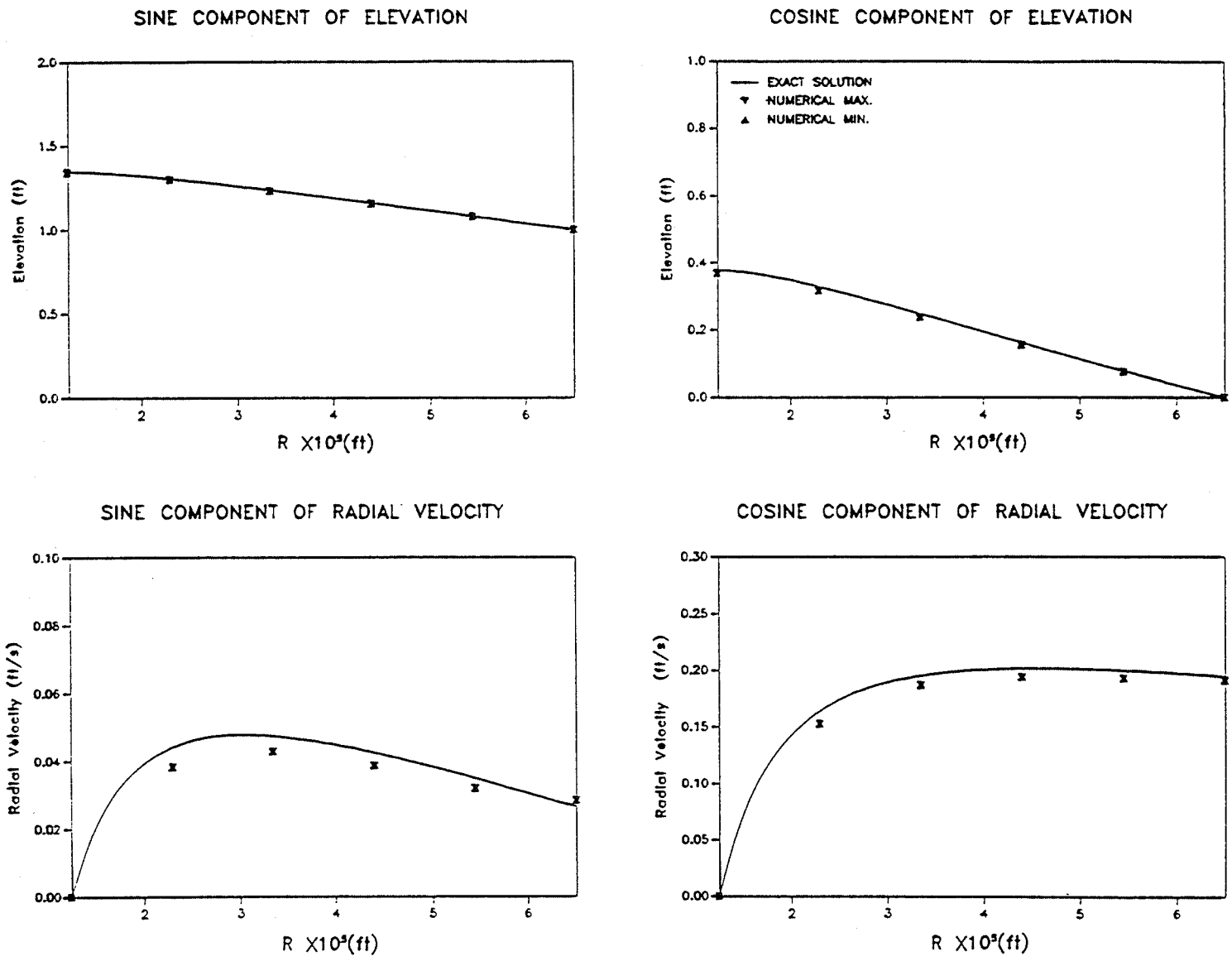

b. $\Delta t = T_{M_2}/64$

Figure 5. (Sheet 2 of 5)

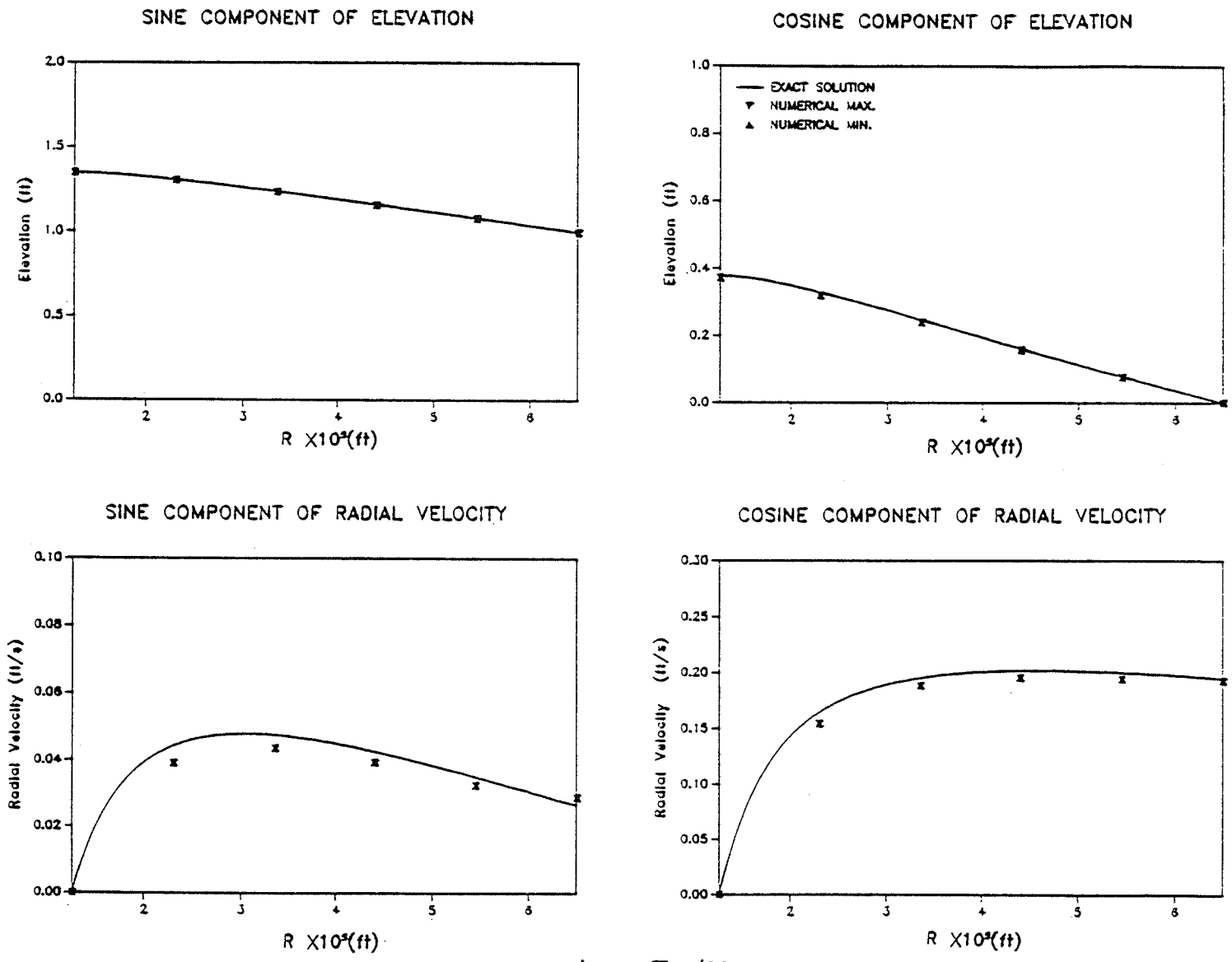

c. $\Delta t = T_{M_2}/32$

Figure 5. (Sheet 3 of 5)

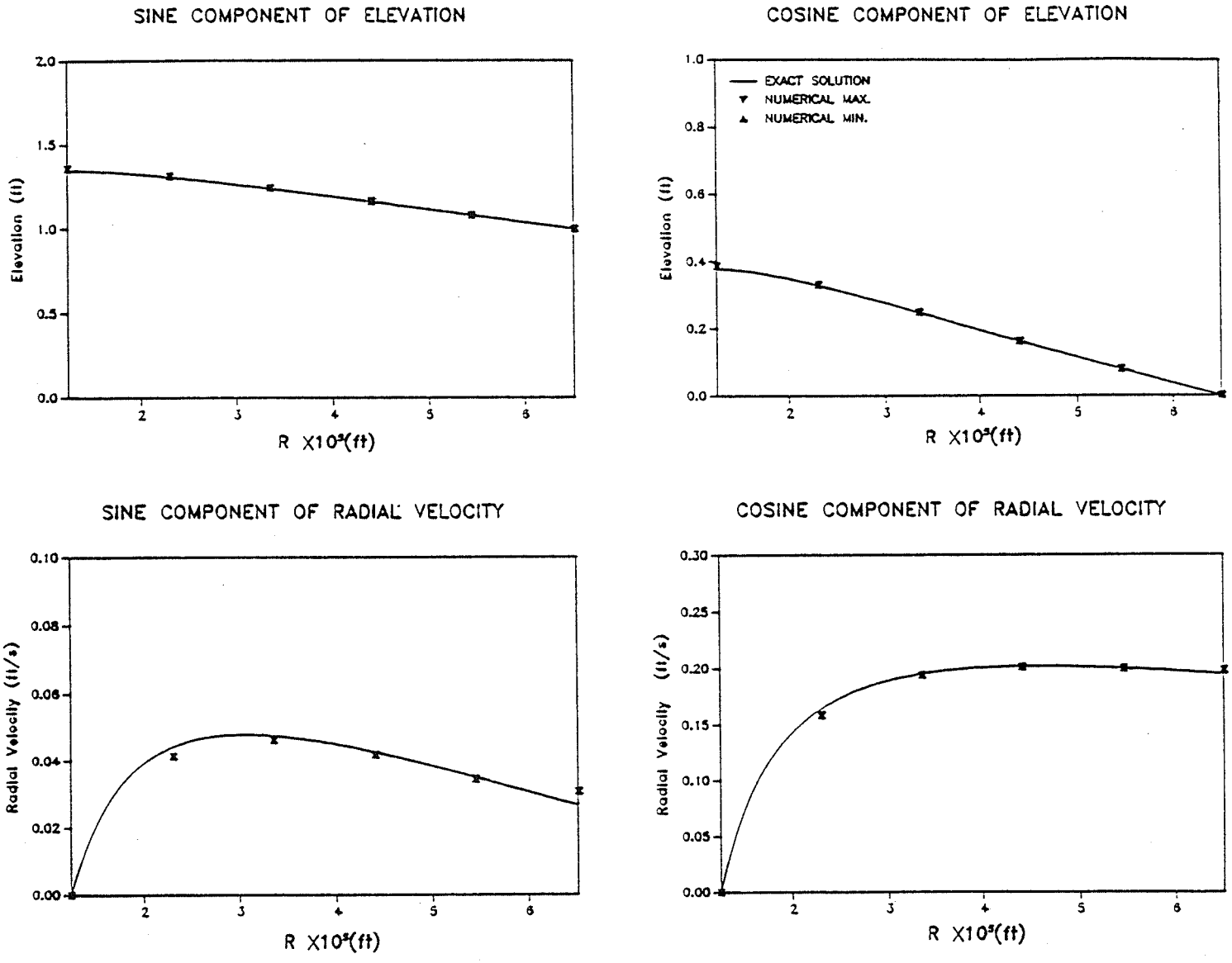

d. $\Delta t = T_{M_2}/16$

Figure 5. (Sheet 4 of 5)

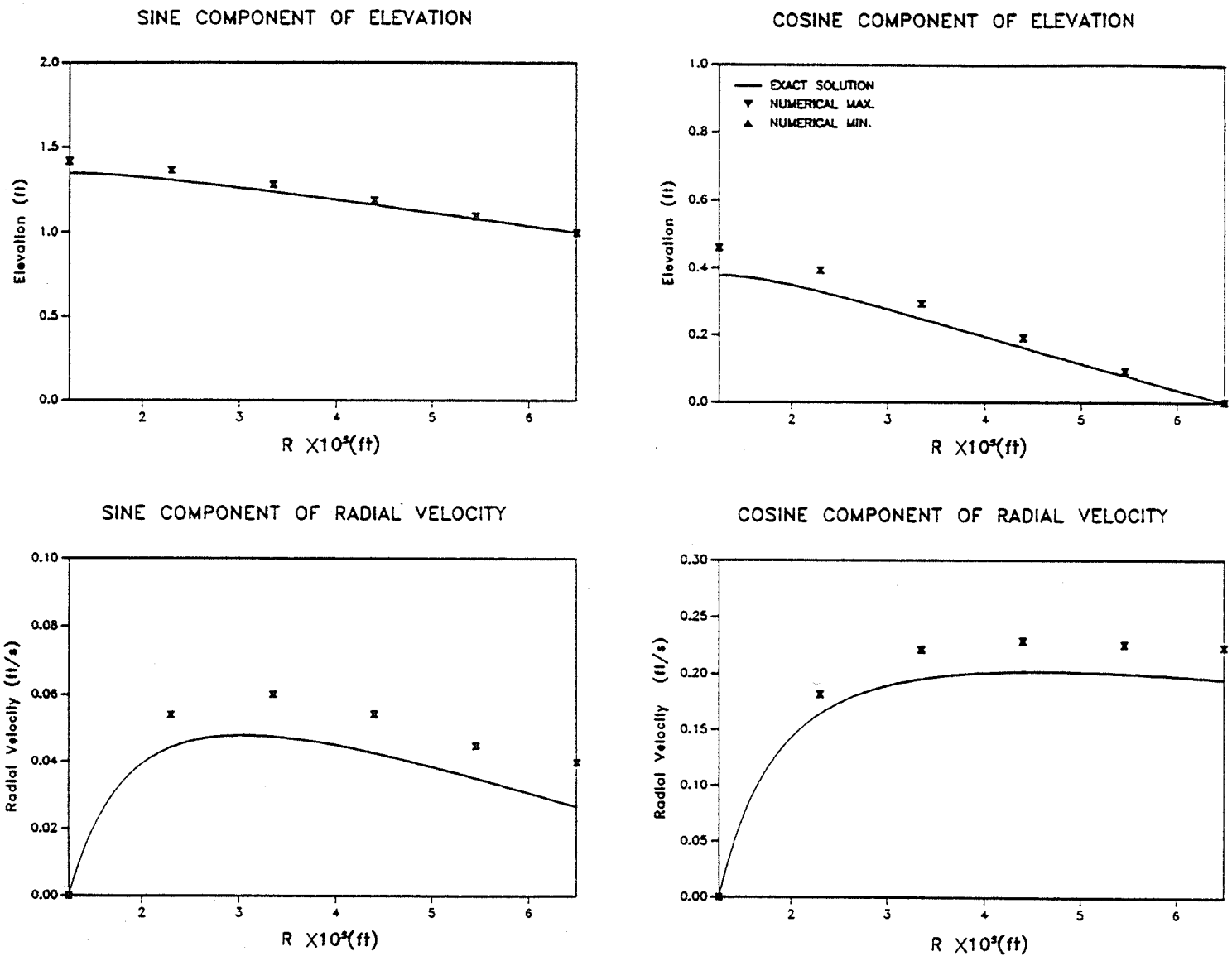

e. $\Delta t = T_{M_2}/8$

Figure 5. (Sheet 5 of 5)

where

N_p = the number of nodes within the grid

$a^A_{\zeta_i}$ = amplitude of the sine component of the analytical elevation solution at node i

$b^A_{\zeta_i}$ = amplitude of the cosine component of the analytical elevation solution at node i

$a^N_{\zeta_i}$ = amplitude of the sine component of the numerical elevation solution at node i

$b^N_{\zeta_i}$ = amplitude of the cosine component of the numerical elevation solution at node i

$a^A_{u_i}$ = amplitude of the sine component of the analytical radial velocity solution at node i

$b^A_{u_i}$ = amplitude of the cosine component of the analytical radial velocity solution at node i

$a^N_{u_i}$ = amplitude of the sine component of the numerical radial velocity solution at node i

$b^A_{u_i}$ = amplitude of the cosine component of the numerical radial velocity solution at node i

These error measures represent the absolute errors in the sine component of the elevation solution (E1), in the cosine component of the elevation solution (E2), in the sine component of the radial velocity solution (E3), and in the cosine component of the radial velocity solution (E4).

76. A summary of the error measures computed for all of the test runs is presented in Table 2. The error measures are plotted against $\mathbb{C}_r$ (the average value for a given grid) for the linear bathymetry test cases in Figures 6 and 7 (Figure 7 is a blow–up of the low $\mathbb{C}_r$ range in Figure 6), and for the quadratic bathymetry test cases in Figures 8 and 9 (Figure 9 is a blow–up of the low $\mathbb{C}_r$ range in Figure 8). All errors show good spatial convergence; i.e., the more refined the grid, the lower the error at any $\mathbb{C}_r$. In time, the errors decrease as $\mathbb{C}_r$ decreases, until $\mathbb{C}_r = 0.9 - 1.75$ for the linear bathymetries and $\mathbb{C}_r = 3.5 - 7$ for the quadratic bathymetries. A well–defined local error minimum exists for all grids within these Courant ranges for both the sine and cosine components of the elevation and radial velocity solutions. This local error minimum occurs because the phase of the propagation factor changes from a phase lead to a phase lag, passing through a region of almost perfect phase behavior, near $\mathbb{C}_r \approx 0.5$ (see Figure 2 and associated discussion). Figures 6 – 9 suggest that the optimal behavior occurs at somewhat higher values of $\mathbb{C}_r$. These figures were plotted using the average value of $\mathbb{C}_r$ for a given grid. However, the primary errors are generated in the shallow portions of the domain. If the $\mathbb{C}_r$ is

Table 2. Summary of Error Measures for All Convergence Runs

GRID	Δx (ft)	$1/\Delta x$	#time steps/ tidal cycle	Δt (hrs)	C_t	E1 (ft)	E2 (ft)	E3 (ft)	E4 (ft)
				LINEAR BATHYMETRY					
5x7	105,000	17.1-39.0	128	0.097	0.13-0.30	4.37E-3	8.44E-3	3.76E-3	7.42E-3
5x7	105,000	17.1-39.0	64	0.194	0.27-0.61	3.96E-3	7.94E-3	3.66E-3	7.16E-3
5x7	105,000	17.1-39.0	32	0.388	0.53-1.22	2.45E-3	5.93E-3	3.27E-3	6.08E-3
5x7	105,000	17.1-39.0	16	0.776	1.07-2.43	6.54E-3	4.03E-3	2.14E-3	2.61E-3
5x7	105,000	17.1-39.0	8	1.55	2.14-4.87	4.35E-2	4.82E-2	1.05E-2	2.30E-2
10x14	52,500	34.2-77.9	128	0.097	0.27-0.61	1.02E-3	2.08E-3	1.20E-3	2.27E-3
10x14	52,500	34.2-77.9	64	0.194	0.53-1.22	6.45E-4	1.57E-3	1.10E-3	2.02E-3
10x14	52,500	34.2-77.9	32	0.388	1.07-2.43	1.51E-3	8.61E-4	8.20E-4	1.28E-3
10x14	52,500	34.2-77.9	16	0.776	2.14-4.87	9.35E-3	9.82E-3	2.23E-3	5.00E-3
10x14	52,500	34.2-77.9	8	1.55	4.27-9.74	4.66E-2	5.58E-2	1.43E-2	2.99E-2
20x28	26,250	68.3-155.8	128	0.097	0.53-1.22	1.55E-4	4.02E-4	3.48E-4	6.27E-4
20x28	26,250	68.3-155.8	64	0.194	1.07-2.43	3.49E-4	1.84E-4	2.87E-4	4.77E-4
20x28	26,250	68.3-155.8	32	0.388	2.14-4.87	2.24E-3	2.32E-3	5.67E-4	1.25E-3
20x28	26,250	68.3-155.8	16	0.776	4.27-9.74	1.01E-2	1.15E-2	2.91E-3	6.50E-3
20x28	26,250	68.3-155.8	8	1.55	8.54-19.47	4.72E-2	5.76E-2	1.56E-2	3.20E-2
40x56	13,125	136.6-311.6	128	0.097	1.07-2.43	7.10E-5	3.27E-5	9.70E-5	1.49E-4
40x56	13,125	136.6-311.6	64	0.194	2.14-4.87	5.31E-4	5.63E-4	1.57E-4	3.12E-4
40x56	13,125	136.6-311.6	32	0.388	4.27-9.74	2.42E-3	2.73E-3	7.06E-4	1.57E-3
40x56	13,125	136.6-311.6	16	0.776	8.54-19.47	1.03E-2	1.19E-2	3.15E-3	6.92E-3
40x56	13,125	136.6-311.6	8	1.55	17.08-38.95	4.73E-2	5.79E-2	1.60E-2	3.27E-2
				QUADRATIC BATHYMETRY					
5x7	105,000	17.1-87.9	128	0.097	0.13-0.69	2.86E-3	2.68E-4	5.95E-4	5.21E-3
5x7	105,000	17.1-87.9	64	0.194	0.27-1.37	2.74E-3	2.60E-3	5.88E-4	5.16E-3
5x7	105,000	17.1-87.9	32	0.388	0.53-2.75	2.23E-3	2.27E-3	5.62E-4	4.95E-3
5x7	105,000	17.1-87.9	16	0.776	1.07-5.50	6.06E-4	1.02E-3	4.56E-4	4.16E-3
5x7	105,000	17.1-87.9	8	1.55	2.14-11.0	1.05E-2	5.80E-3	3.88E-4	4.06E-3
10x14	52,500	34.2-175.8	128	0.097	0.27-1.37	7.15E-4	6.82E-4	2.67E-4	2.42E-3
10x14	52,500	34.2-175.8	64	0.194	0.53-2.75	5.97E-4	6.04E-4	2.59E-4	2.37E-3
10x14	52,500	34.2-175.8	32	0.388	1.07-5.50	2.44E-4	3.10E-4	2.30E-4	2.18E-3
10x14	52,500	34.2-175.8	16	0.776	2.14-11.0	2.21E-3	1.14E-3	1.72E-4	1.77E-3
10x14	52,500	34.2-175.8	8	1.55	4.27-21.98	1.26E-2	7.81E-3	8.33E-4	6.19E-3
20x28	26,250	68.3-351.7	128	0.097	0.53-2.75	1.54E-4	1.59E-4	9.20E-5	8.86E-4
20x28	26,250	68.3-351.7	64	0.194	1.07-5.50	6.03E-5	8.43E-5	8.41E-5	8.46E-4
20x28	26,250	68.3-351.7	32	0.388	2.14-11.0	5.11E-4	2.68E-4	6.63E-5	7.42E-4
20x28	26,250	68.3-351.7	16	0.776	4.27-21.98	2.70E-3	1.64E-3	1.71E-4	1.42E-3
20x28	26,250	68.3-351.7	8	1.55	8.54-43.96	1.30E-2	8.24E-3	1.06E-3	7.51E-3
40x56	13,125	136.6-703.4	128	0.097	1.07-5.50	1.82E-5	2.83E-5	2.53E-5	2.67E-4
40x56	13,125	136.6-703.4	64	0.194	2.14-11.0	1.10E-4	6.16E-5	2.17E-5	2.42E-4
40x56	13,125	136.6-703.4	32	0.388	4.27-21.98	6.32E-4	3.94E-4	4.78E-5	3.72E-4
40x56	13,125	136.6-703.4	16	0.776	8.54-43.96	2.81E-3	1.77E-3	2.21E-4	1.65E-3
40x56	13,125	136.6-703.4	8	1.55	17.08-87.92	1.31E-2	8.33E-3	1.14E-3	8.00E-3

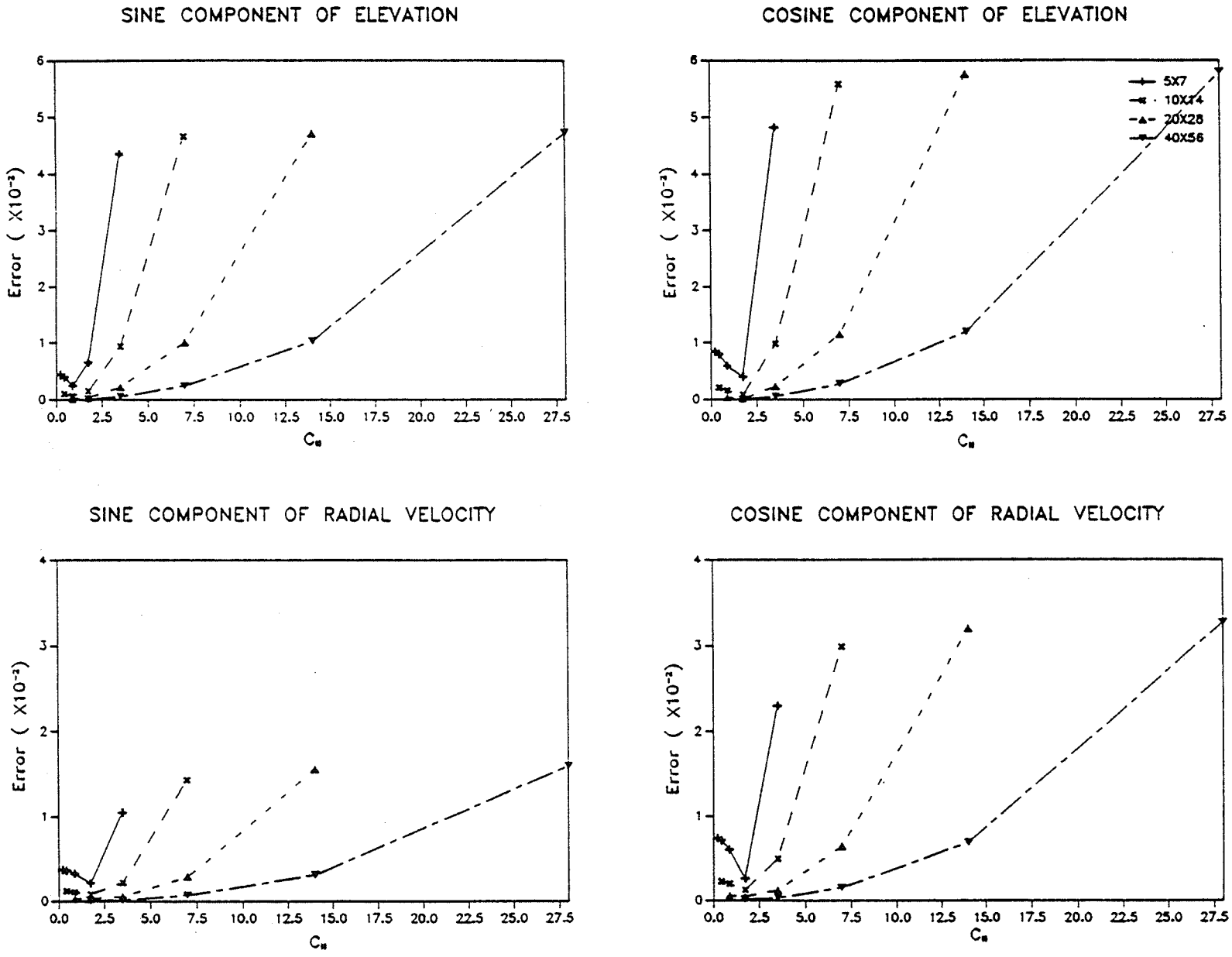

Figure 6. Convergence properties of the linear bathymetry test cases

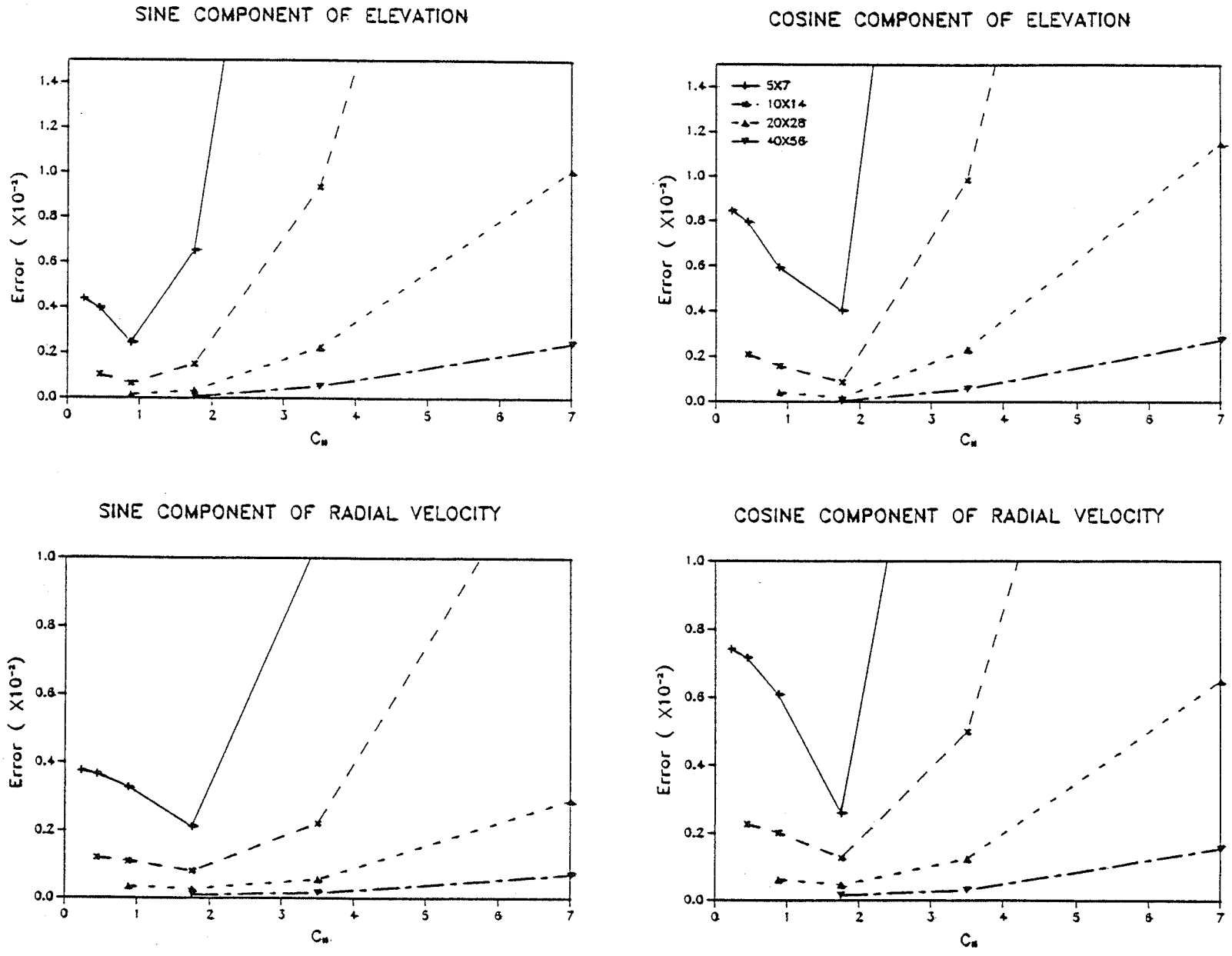

Figure 7. Detail of the convergence properties of the linear bathymetry test cases at low C_r

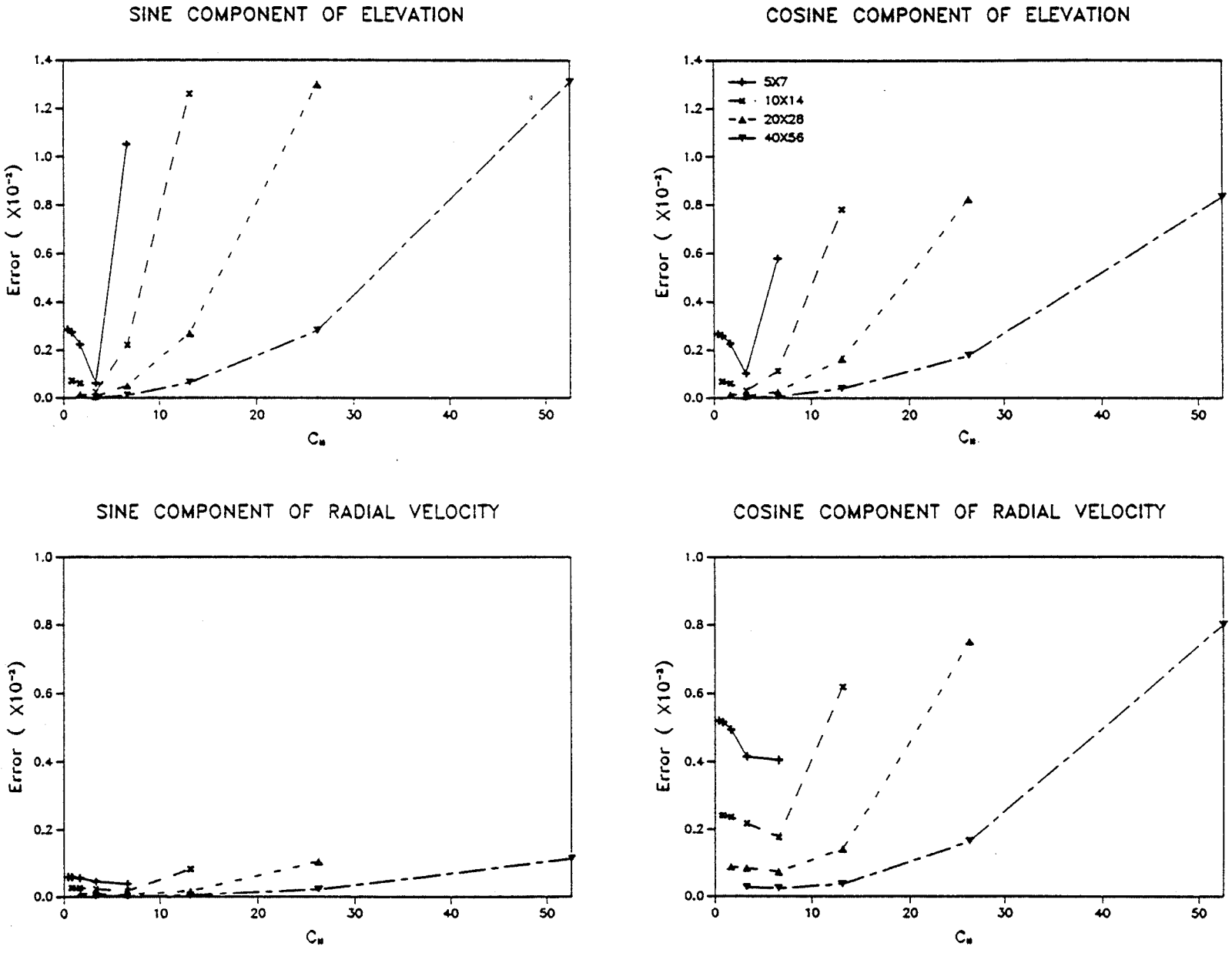

Figure 8. Convergence properties of the quadratic bathymetry test cases

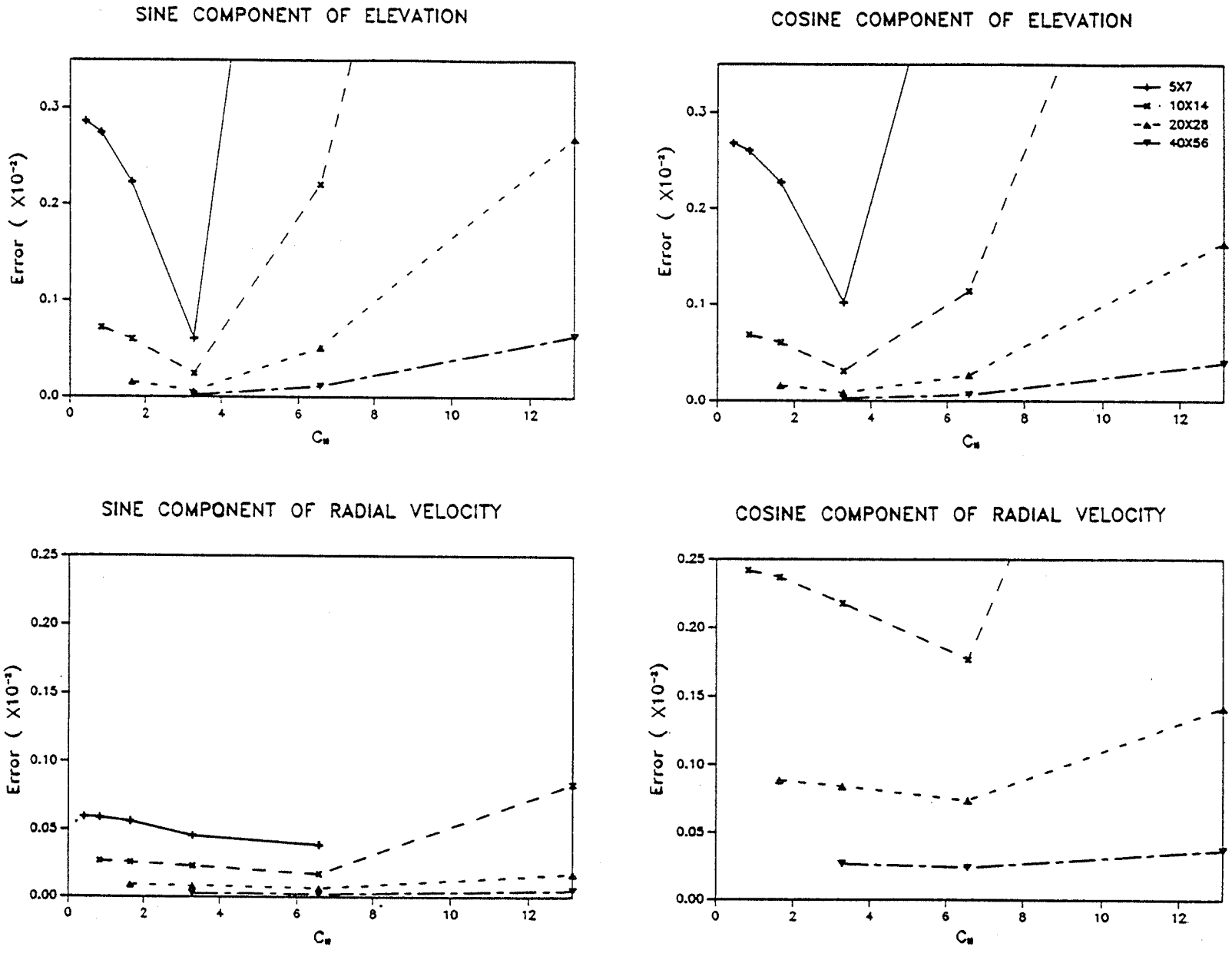

Figure 9. Detail of the convergence properties of the quadratic bathymetry test cases at low C_r

adjusted to account for this, the optimal range of values changes to $\mathbb{C}_r = 0.52 - 1.07$ for the linearly varying bathymetries and $\mathbb{C}_r = 1.07 - 2.14$ for the quadratically varying bathymetries.

77. It is concluded that the external mode solution used in ADCIRC has excellent numerical properties. There are no spurious $2\Delta x$ or $2\Delta t$ modes due to the ability of the GWCEFE scheme to propagate high wave number energy. Convergence properties in space and time are good with superconvergence occurring in the range $\mathbb{C}_r = 0.5 - 1.5$. In this range, more accurate solutions are obtained using larger time steps.

Application of ADCIRC–2DDI to the English Channel and Southern North Sea

78. The accuracy and behavioral characteristics of the external mode solution have been tested in field applications including (a) tidal and hurricane storm surge simulations in the Gulf of Mexico (Westerink et al., in review), (b) tidal simulations in the English Channel and Southern North Sea, (c) tidal simulations in a small coastal inlet (Luettich, Birkhahn, and Westerink 1991) and (d) tidal simulations in the New York Bight. The English Channel/Southern North Sea system is probably the best documented field site presently in existence for testing a long–wave, hydrodynamic model. Since the emphasis of this report is on the development and testing of the various components of ADCIRC, the results of applying ADCIRC–2DDI to the English Channel and Southern North Sea are presented below.

79. In the mid–1980's considerable effort was put forth to establish and make readily available a set of standard grids, boundary conditions, and verification data for model evaluation in the English Channel and Southern North Sea (Werner and Lynch 1988). This data has been used as the basis for modeling studies for the Tidal Flow Forum I at the Conference on Finite Elements in Water Resources, Lisbon, Portugal, in 1986 and for the Tidal Flow Forum II at the VII International Conference on Computational Methods in Water Resources, Cambridge, MA in 1988. Two collections of scientific papers have been published from this work and can be found in Advances in Water Resources, Vol. 10, No. 3 (1987) and Advances in Water Resources, Vol. 12, Nos. 3 and 4 (Dec 1989).

80. The fully nonlinear version of ADCIRC–2DDI was applied to the grid and bathymetry shown in Figure 10. The grid consists of 990 nodes and 1,762 linear triangular elements. The model was forced by specifying 11 harmonic constituents for elevation (O_1, K_1, M_2, N_2, S_2, K_2, MS_4, MN_4, M_4, M_6, $2MS_6$) along the two open

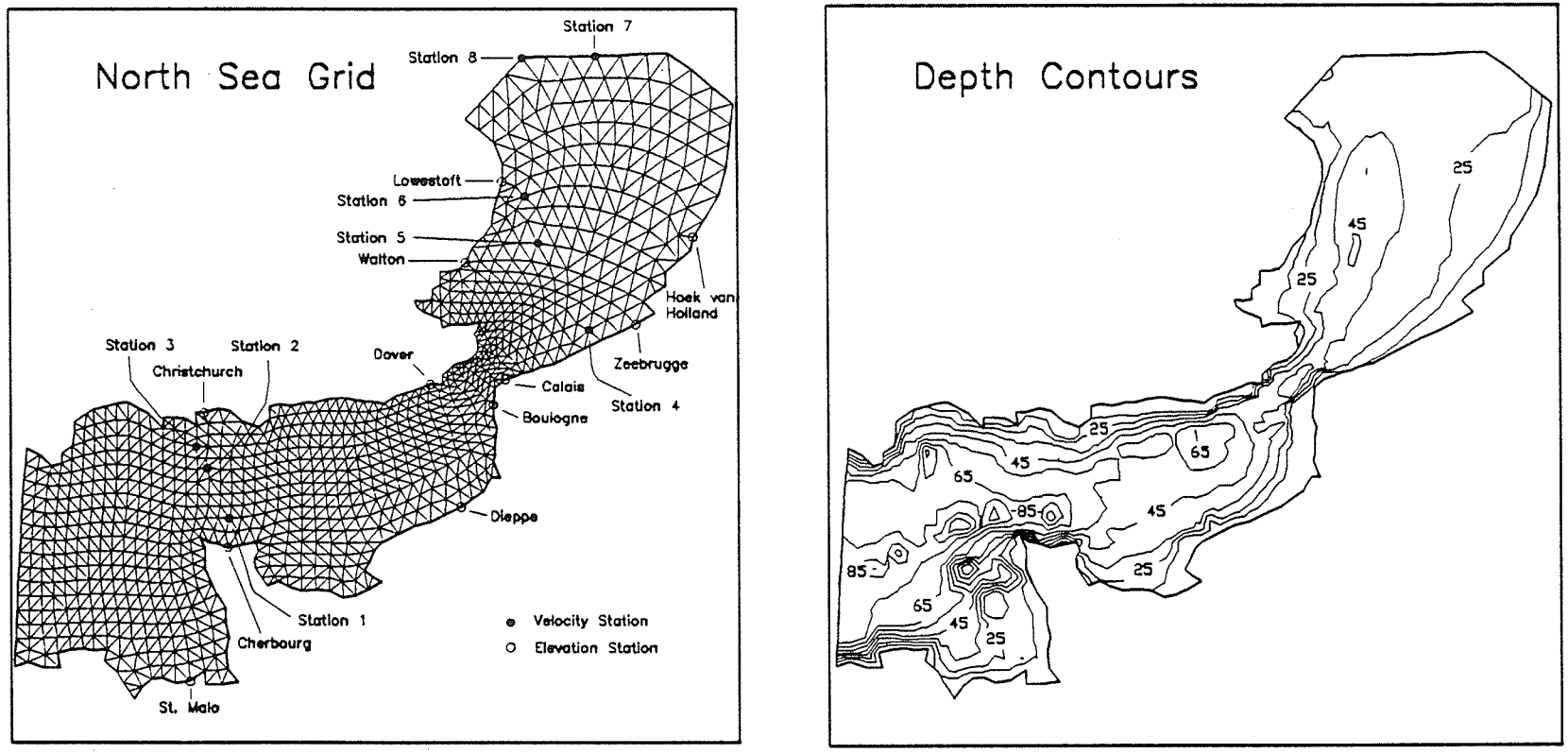

Figure 10. Finite element grid and bathymetry used in the ADCIRC–2DDI simulations of the English Channel and Southern North Sea

model boundaries. Wind stress and tidal potential forcings were not used in the model runs. Model parameters were selected to match those used by previous investigators to allow the direct comparison of model results with field data and with previously published model results. The following parameter values were used in the model: $\tau_0 = 0.0002s^{-1}$, $\Delta t = 360s$, $C_f = 0.002322$, $f = 0.000113341s^{-1}$, and $E_{h2} = 0.0$. The time integration coefficients in the GWCE were set to $\alpha_1 = 0.35$, $\alpha_2 = 0.30$, and $\alpha_3 = 0.35$.

81. ADCIRC–2DDI was run for the short–term test case suggested by Werner and Lynch (1988) covering the period from 0 hr on 15 March 1976 to 24 hr on 17 March 1976. Werner and Lynch (1987) found that it was necessary to use a minimum bathymetric depth of 15 m throughout the model domain to avoid generating negative water depths during their simulations. ADCIRC–2DDI ran successfully using a minimum bathymetric depth as small as 10 m, although the simulated results were highly insensitive to this change at the 19 locations where observational data were available (see Figures 11 and 12).

82. The first 47 hr 10 min of the simulation were used as a transient start–up period. Figures 11 and 12 present comparisons between modeled time series and observed time series of free surface elevation (at 11 stations) and depth–averaged current speed and direction (at 8 stations) for the final 24 hr 50 min of the simulation. (The locations of the elevation and velocity stations are shown in Figure 10. The observed time series were actually reconstructed from 11 primary tidal constituents at each station. The tidal constituents correspond to those used to force the model open boundaries and were extracted from raw time series at each observation station using harmonic analysis.) In general, the model does a good job of simulating the observed results. Some of the differences can be attributed to local topographic and bathymetric effects and to the inherent problems associated with representing bottom stress in a depth–integrated model. Also, Werner and Lynch (1989) point out that the model results contain harmonic constituents, generated by nonlinear interactions within the domain, that are not included in the reconstructed observed time series. By filtering this energy out of the model results, they were able to reduce the average difference between the simulated and observed surface elevations by approximately 40 percent. The worst comparison occurs at the tidal elevation station at Christchurch and is at least partially due to the neglect of the channel between the Isle of Wight and the mainland (located approximately 25 km east of Christchurch) in the model grid.

83. ADCIRC–2DDI was also run for the long–term test case suggested by

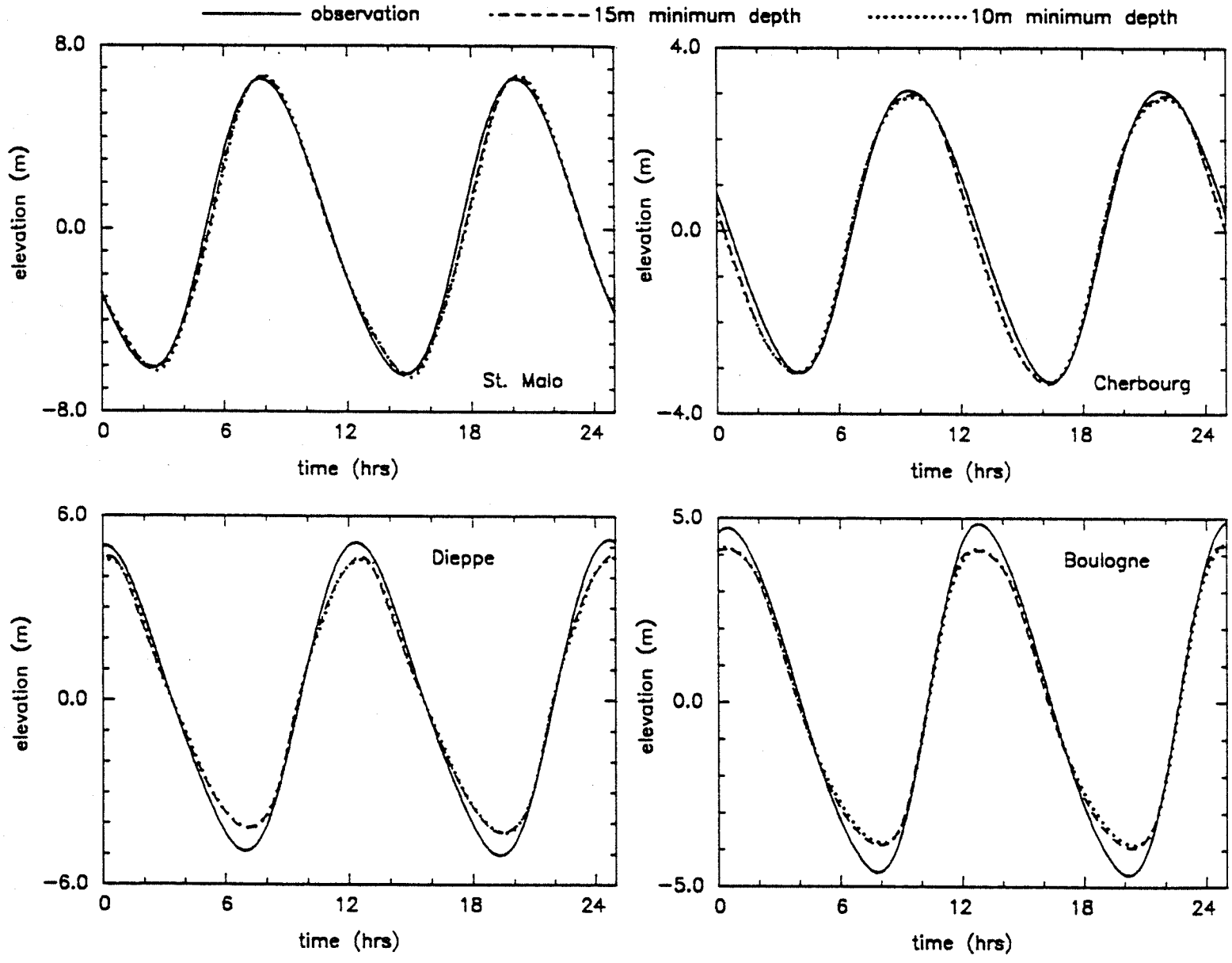

Figure 11. Time series of simulated and observed tidal elevations at various coastal stations (Sheet 1 of 3)

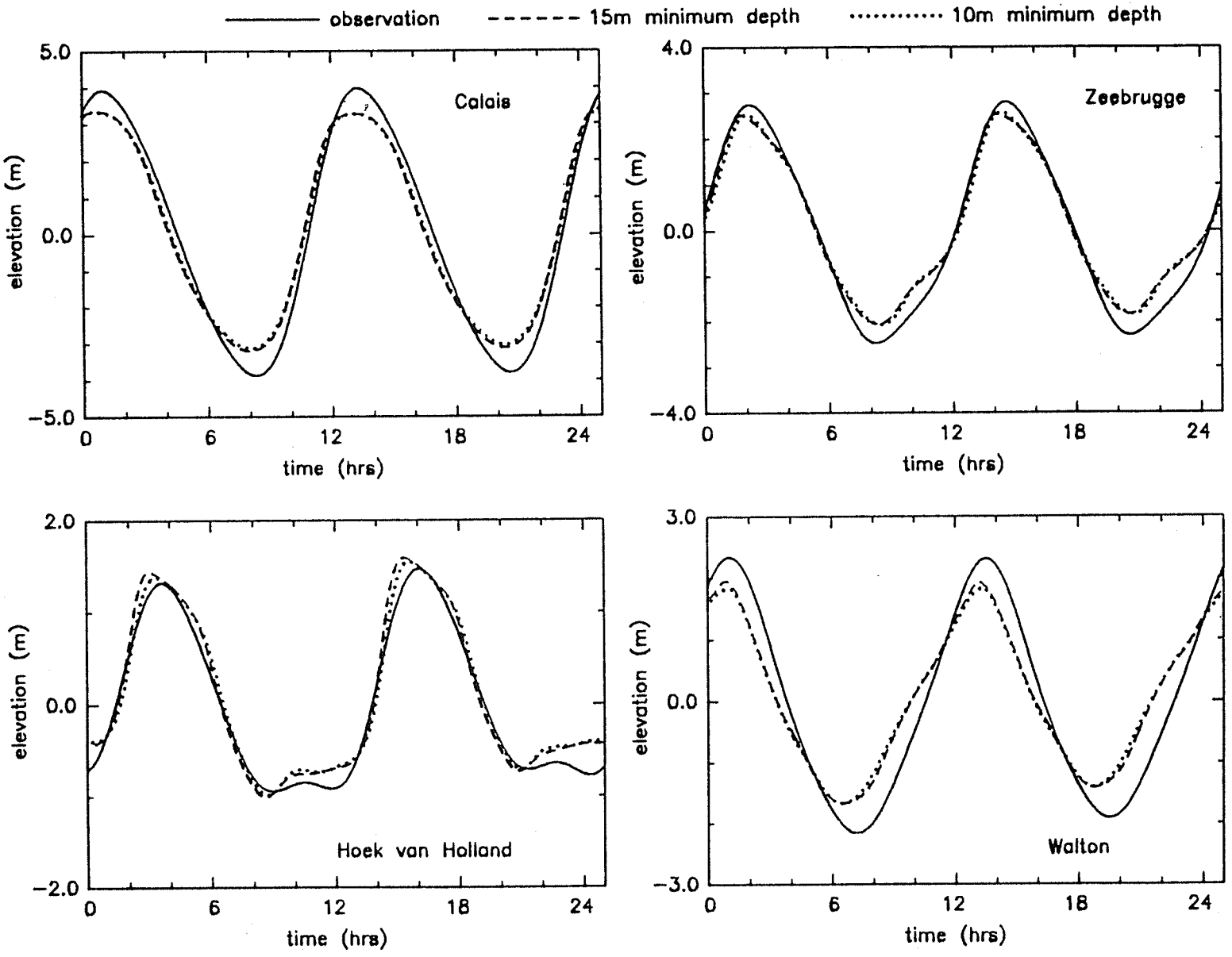

Figure 11. (Sheet 2 of 3)

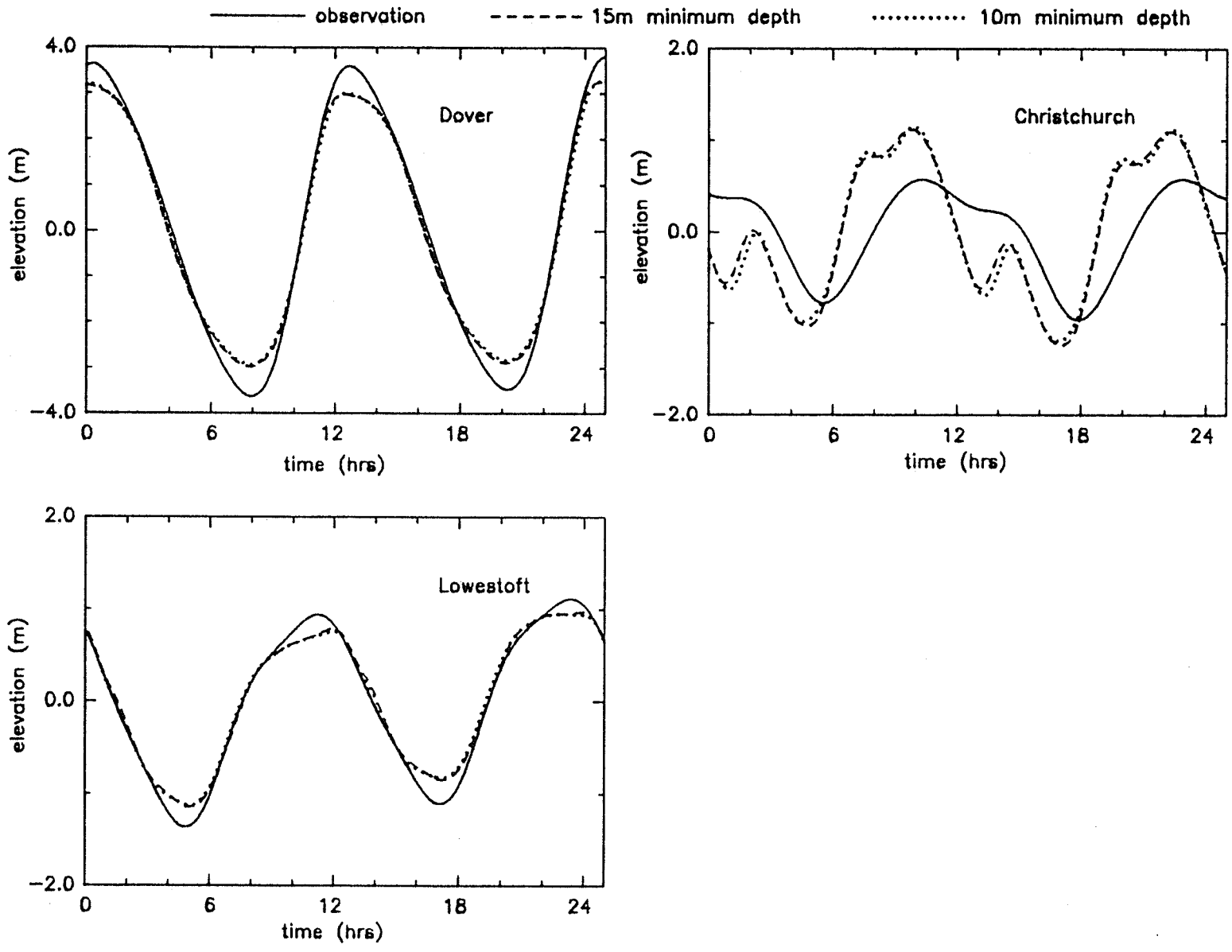

Figure 11. (Sheet 3 of 3)

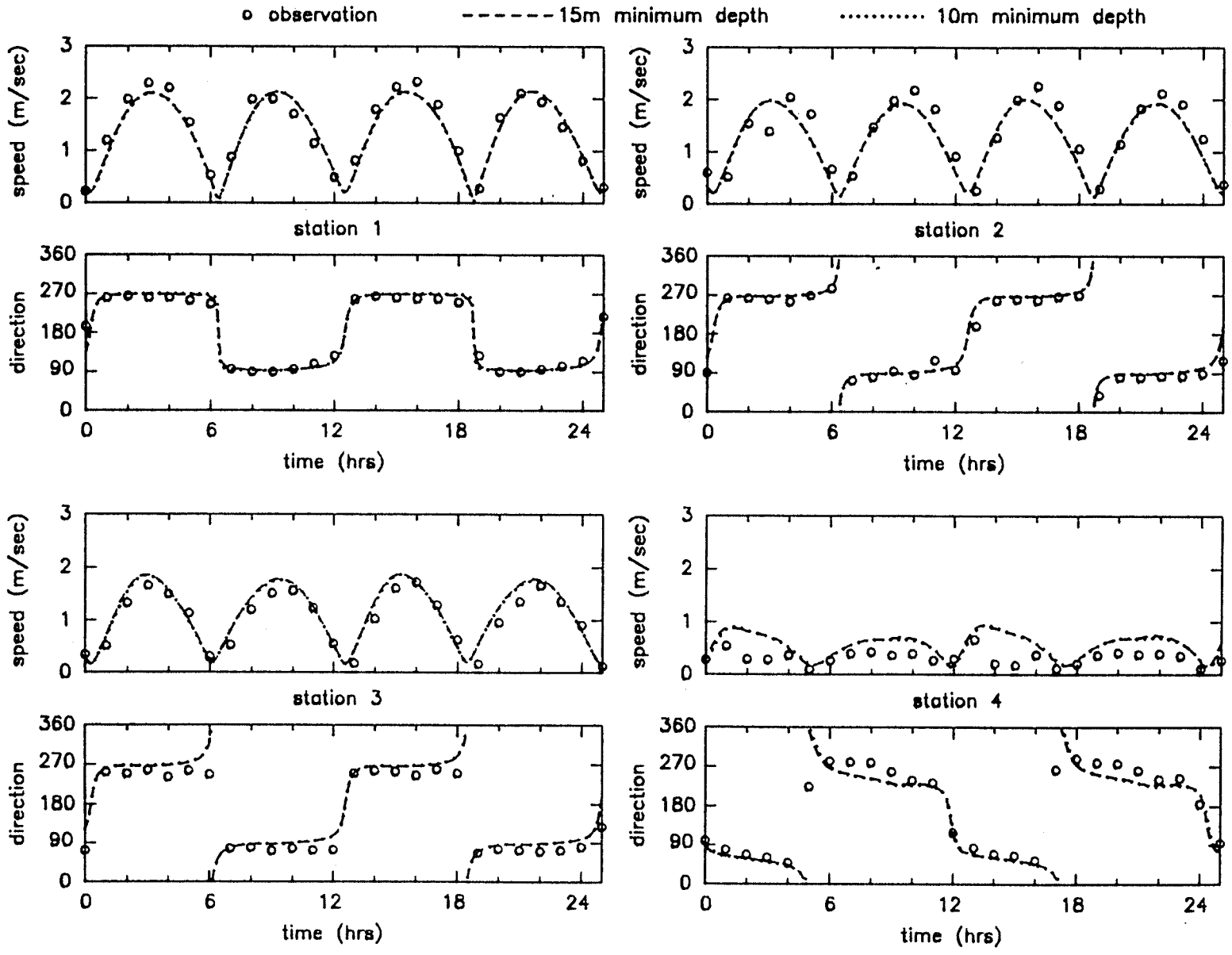

Figure 12. Time series of simulated and observed tidal speed and direction at various stations (Continued)

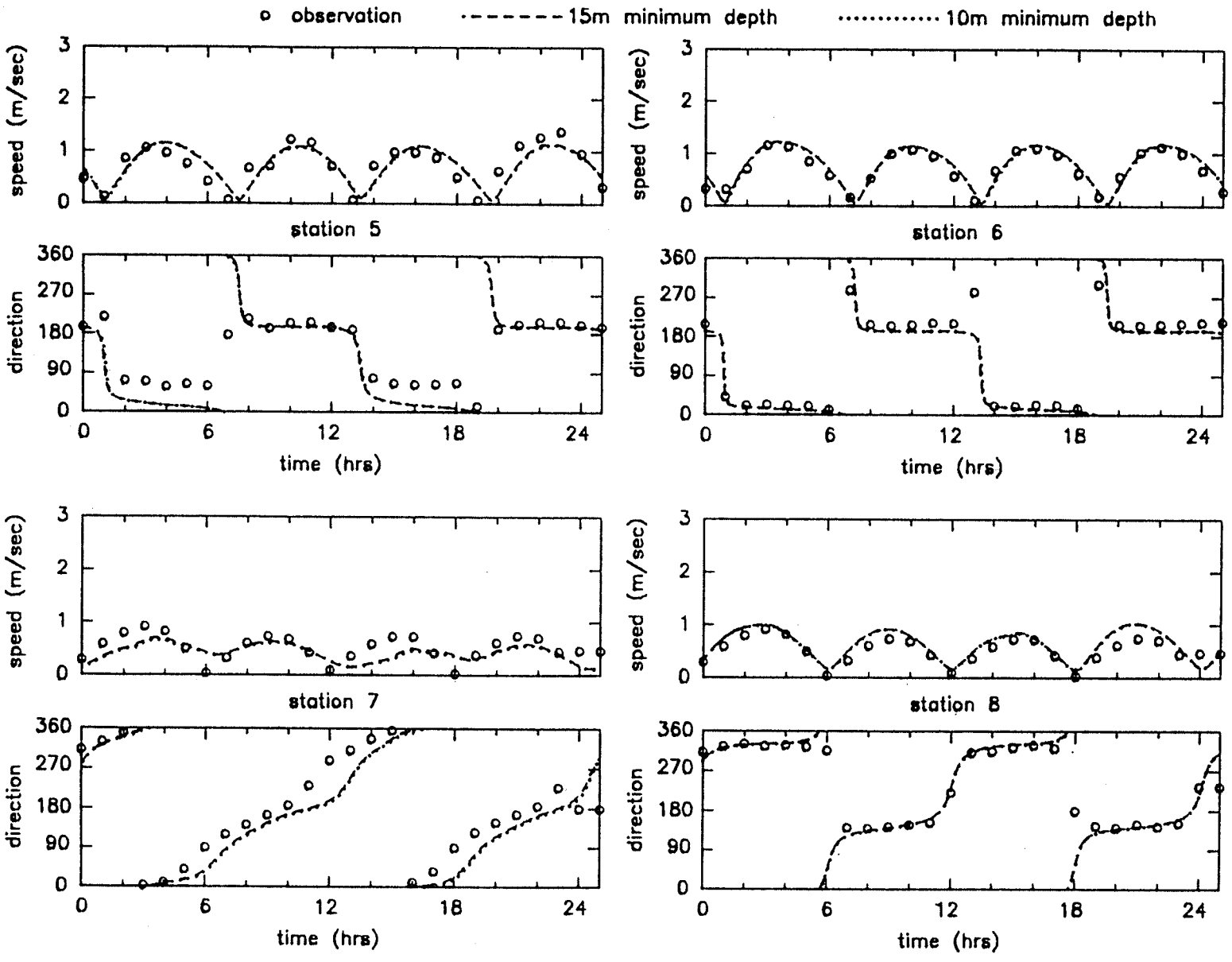

Figure 12. (Concluded)

Werner and Lynch (1988) covering the 190–day period starting at 0 hr on 15 March 1976. The first 5 days were discarded to allow for start–up transients and the remaining 185 days were harmonically analyzed using the least squares package of Foreman (1977). The amplitudes and phases of the primary surface elevation constituents from the ADCIRC simulation, from a simulation by Werner and Lynch (1989), and from the observed time series at the 11 elevation stations are compared in Table 3. The overall comparison between model results and observations is reasonable considering no effort has been made to calibrate the model by adjusting the bottom friction coefficient, as attempted by Baptista, Westerink, and Turner (1989). Some of the largest differences in phase occur at stations that are close to amphidromes. This is because a small displacement of an amphidrome's position can result in a large change in the nearby phase values. Some of the largest relative differences in amplitude (i.e., percent difference between the simulated and observed amplitude) occur in the M_6 constituents. Bottom friction is the primary nonlinear generating mechanism for this constituent, suggesting that this process is not captured very well by a depth–integrated model.

84. Figure 13 presents co–tidal charts for the entire domain for 14 tidal constituents. The ADCIRC–2DDI results presented in Figure 13 and Table 3 compare very closely with those of Werner and Lynch (1989). This is expected since Werner and Lynch (1989) used a depth–integrated, finite element, GWCE–based model that is similar to ADCIRC–2DDI. The minor deviations between the models are due to ADCIRC's use of a non–conservative formulation of the advective terms in the GWCE as well as slight differences in the discretizations of several of the terms. The close correspondence between the model results provides an excellent verification of the formulation and numerical discretization used in the external mode of ADCIRC.

Table 3. Amplitude (in Meters) and Phase Relative to Greenwich (Rounded to the Nearest Degree) for the Field Data, Model Results

	O_1		K_1		N_2		M_2		S_2		K_2		MN_4		M_4		MS_4		M_6		$2MS_6$	
	A	ph	A	ph	A	ph	A	ph	A	ph	A	ph	A	ph	A	ph	A	ph	A	ph	A	ph
ST MALO																						
Observed	0.079	344.	0.093	96.	0.740	162.	3.740	178.	1.470	229.	0.416	226.	0.111	267.	0.276	279.	0.207	335.	0.025	352.	0.029	39.
W-L Model	0.093	347.	0.110	96.	0.717	166.	3.877	177.	1.418	232.	0.405	229.	0.137	285.	0.271	295.	0.252	352.	0.008	291.	0.006	347.
ADCIRC	0.093	347.	0.110	96.	0.716	166.	3.875	176.	1.416	232.	0.405	229.	0.137	284.	0.270	294.	0.252	351.	0.010	305.	0.008	9.
CHERBOURG																						
Observed	0.064	354.	0.091	106.	0.365	210.	1.870	230.	0.690	273.	0.197	269.	0.045	334.	0.155	353.	0.078	49.	0.025	101.	0.027	135.
W-L Model	0.071	3.	0.104	110.	0.369	209.	1.974	226.	0.691	274.	0.192	272.	0.042	346.	0.128	4.	0.078	59.	0.028	94.	0.030	137.
ADCIRC	0.071	3.	0.105	110.	0.368	210.	1.973	226.	0.688	274.	0.192	273.	0.046	350.	0.139	7.	0.085	62.	0.034	89.	0.037	134.
DIEPPE																						
Observed	0.041	36.	0.075	123.	0.570	291.	3.080	311.	1.020	1.	0.297	359.	0.093	162.	0.262	185.	0.174	242.	0.029	299.	0.022	351.
W-L Model	0.049	45.	0.095	132.	0.511	293.	3.020	310.	0.933	4.	0.267	4.	0.088	172.	0.269	187.	0.171	246.	0.034	288.	0.038	338.
ADCIRC	0.049	45.	0.095	131.	0.517	293.	3.045	310.	0.942	4.	0.269	4.	0.089	172.	0.274	187.	0.174	246.	0.032	293.	0.036	340.
BOULOGNE																						
Observed	0.039	77.	0.046	131.	0.526	310.	2.930	331.	0.960	21.	0.273	21.	0.109	199.	0.325	223.	0.218	276.	0.064	93.	0.068	136.
W-L Model	0.045	85.	0.065	139.	0.483	311.	2.899	329.	0.883	23.	0.254	23.	0.111	209.	0.324	225.	0.206	281.	0.098	82.	0.097	135.
ADCIRC	0.045	85.	0.065	139.	0.488	311.	2.923	329.	0.892	23.	0.256	24.	0.114	209.	0.334	225.	0.211	281.	0.103	80.	0.101	134.
CALAIS																						
Observed	0.050	147.	0.030	68.	0.440	325.	2.460	345.	0.780	38.	0.200	38.	0.090	226.	0.250	249.	0.170	306.	0.050	146.	0.060	193.
W-L Model	0.056	140.	0.022	100.	0.394	317.	2.425	338.	0.719	31.	0.207	33.	0.079	228.	0.224	248.	0.131	299.	0.094	105.	0.091	157.
ADCIRC	0.055	139.	0.024	102.	0.398	318.	2.445	338.	0.725	31.	0.209	33.	0.083	226.	0.235	245.	0.137	297.	0.097	103.	0.094	154.
ZEEBRUGGE																						
Observed	0.110	174.	0.020	339.	0.370	355.	1.590	14.	0.430	72.	0.120	72.	0.060	2.	0.090	26.	0.080	98.	0.080	325.	0.090	13.
W-L Model	0.111	168.	0.057	350.	0.237	349.	1.622	15.	0.434	68.	0.127	71.	0.046	19.	0.159	35.	0.092	98.	0.067	328.	0.080	31.
ADCIRC	0.111	168.	0.057	351.	0.239	350.	1.633	15.	0.437	68.	0.129	71.	0.047	18.	0.161	33.	0.094	97.	0.071	321.	0.085	24.
HOEK VAN HOLLAND																						
Observed	0.100	180.	0.070	346.	0.110	29.	0.770	57.	0.190	116.	0.050	117.	0.060	79.	0.160	104.	0.100	161.	0.040	42.	0.04[illegible]	100.
W-L Model	0.119	175.	0.070	347.	0.118	29.	0.972	55.	0.224	112.	0.068	117.	0.078	90.	0.226	111.	0.116	168.	0.066	43.	0.068	113.
ADCIRC	0.120	175.	0.070	347.	0.120	28.	0.982	54.	0.227	112.	0.069	116.	0.080	86.	0.234	107.	0.121	164.	0.064	40.	0.067	108.
CHRISTCHURCH																						
Observed	0.040	347.	0.094	123.	0.062	256.	0.420	285.	0.125	312.	0.034	312.	0.033	19.	0.107	41.	0.083	102.	0.016	66.	0.023	122.
W-L Model	0.045	359.	0.093	119.	0.108	217.	0.387	226.	0.212	268.	0.058	261.	0.060	11.	0.184	25.	0.115	84.	0.095	57.	0.097	107.
ADCIRC	0.046	359.	0.094	118.	0.109	218.	0.393	227.	0.214	268.	0.058	262.	0.062	11.	0.189	25.	0.118	84.	0.096	56.	0.099	106.
DOVER																						
Observed	0.060	172.	0.060	46.	0.410	309.	2.230	332.	0.710	23.	0.180	25.	0.130	199.	0.270	220.	0.170	273.	0.070	104.	0.070	149.
W-L Model	0.054	169.	0.044	58.	0.366	310.	2.196	331.	0.660	24.	0.190	25.	0.082	215.	0.226	232.	0.142	282.	0.101	94.	0.100	147.
ADCIRC	0.055	170.	0.045	58.	0.369	311.	2.215	331.	0.665	24.	0.192	25.	0.085	214.	0.235	232.	0.146	282.	0.103	93.	0.102	146.
WALTON																						
Observed	0.120	183.	0.070	348.	0.290	311.	1.350	331.	0.360	25.	0.100	25.	0.040	299.	0.080	316.	0.050	24.	0.040	292.	0.050	339.
W-L Model	0.130	171.	0.101	351.	0.184	292.	1.178	320.	0.323	8.	0.092	12.	0.019	282.	0.084	311.	0.046	41.	0.058	267.	0.059	326.
ADCIRC	0.130	171.	0.102	351.	0.186	292.	1.190	320.	0.325	8.	0.093	13.	0.018	280.	0.080	309.	0.045	40.	0.056	268.	0.058	326.
LOWESTOFT																						
Observed	0.140	166.	0.080	321.	0.150	234.	0.680	257.	0.200	296.	0.050	296.	0.020	311.	0.040	334.	0.040	23.	0.040	116.	0.040	160.
W-L Model	0.135	160.	0.114	334.	0.116	232.	0.602	266.	0.195	302.	0.052	304.	0.015	324.	0.038	318.	0.044	21.	0.026	179.	0.049	257.
ADCIRC	0.136	160.	0.115	334.	0.116	233.	0.610	266.	0.196	302.	0.052	305.	0.016	329.	0.037	325.	0.044	23.	0.028	174.	0.053	252.

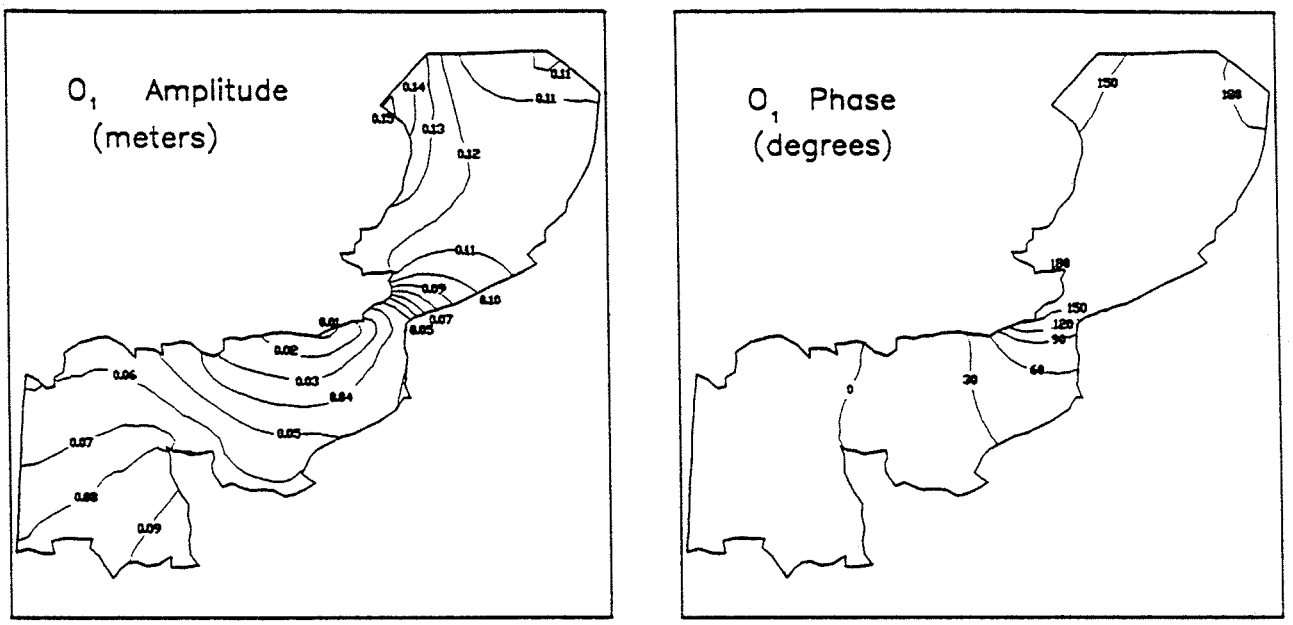

a. O_1 constituent

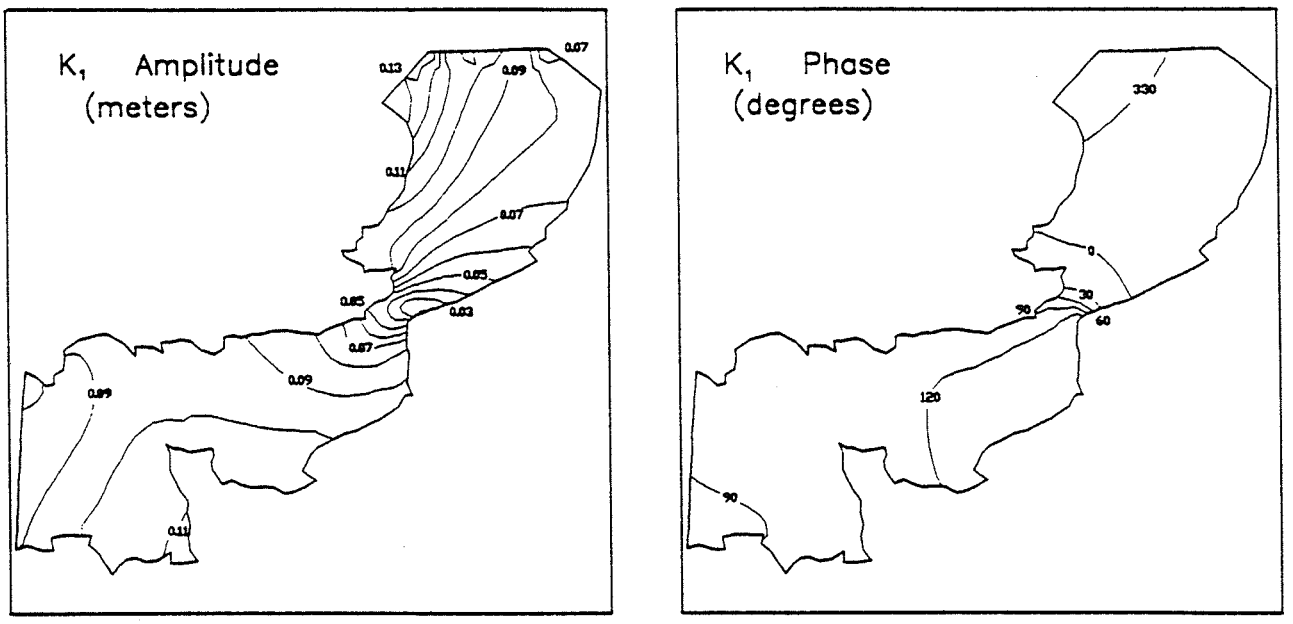

b. K_1 constituent

Figure 13. Co–tidal charts for simulated constituents (Sheet 1 of 7)

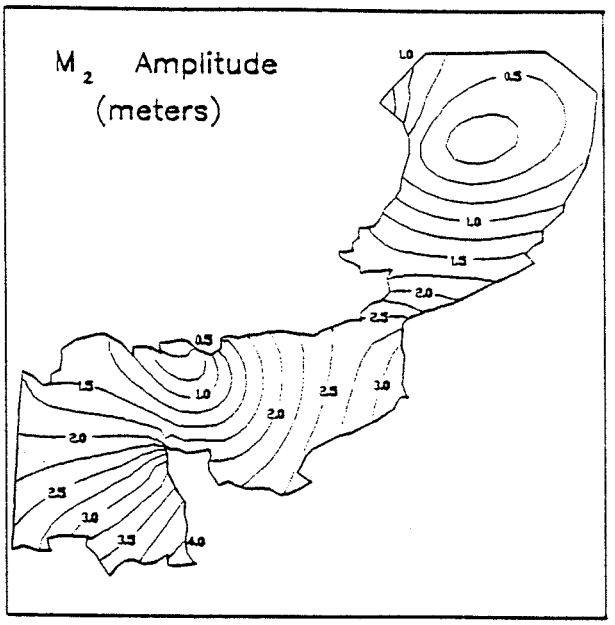

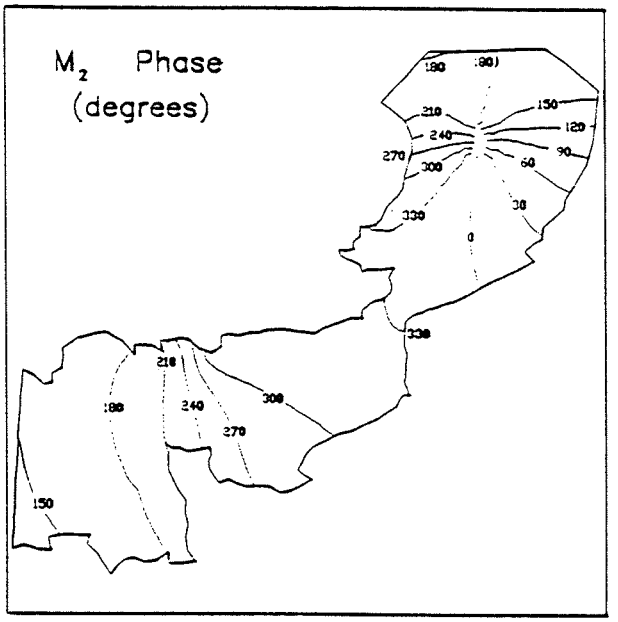

c. M_2 constituent

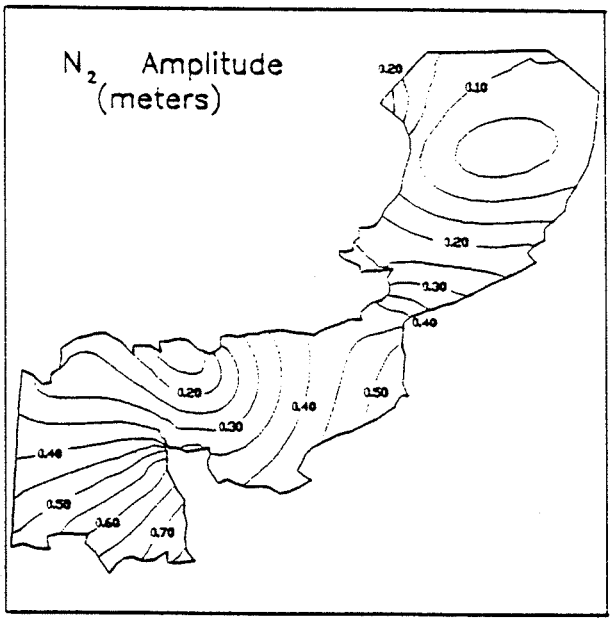

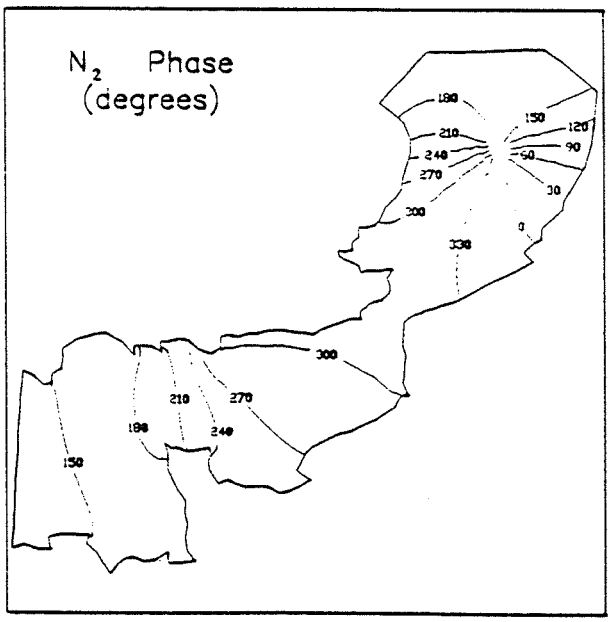

d. N_2 constituent

Figure 13. (Sheet 2 of 7)

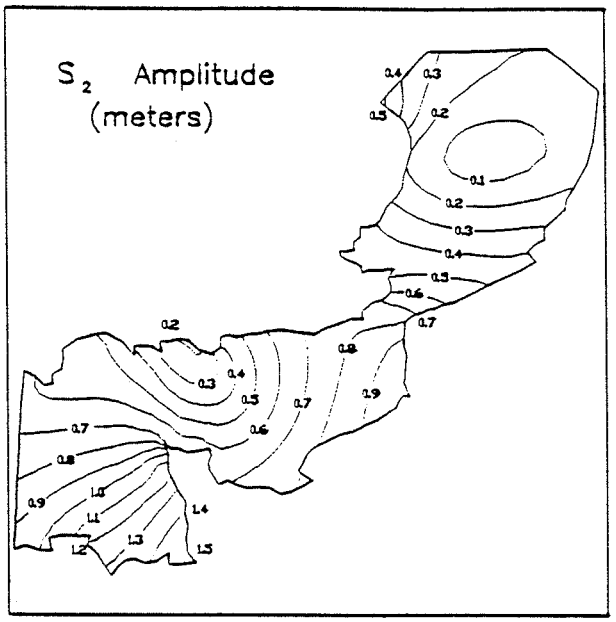

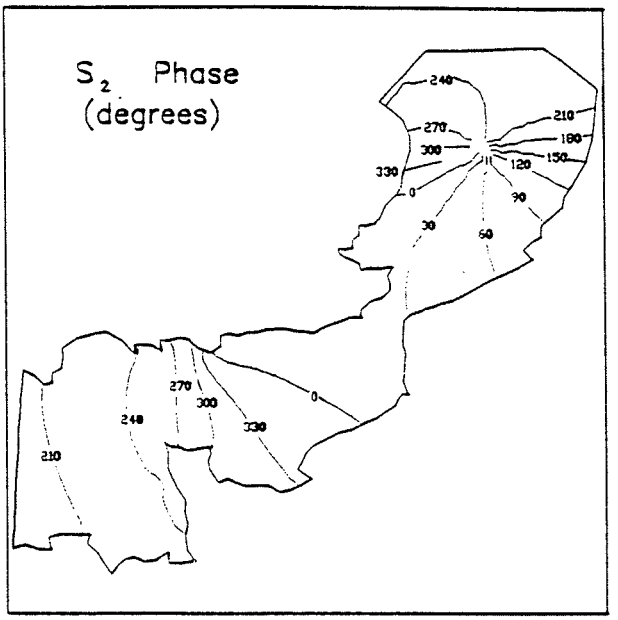

e. S_2 constituent

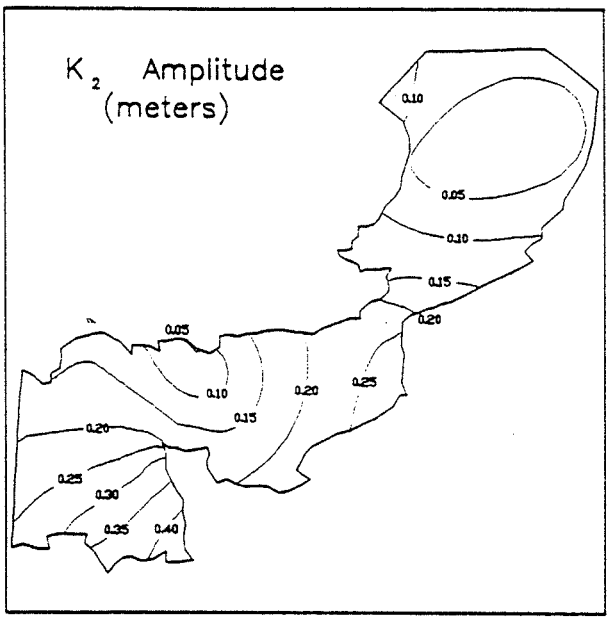

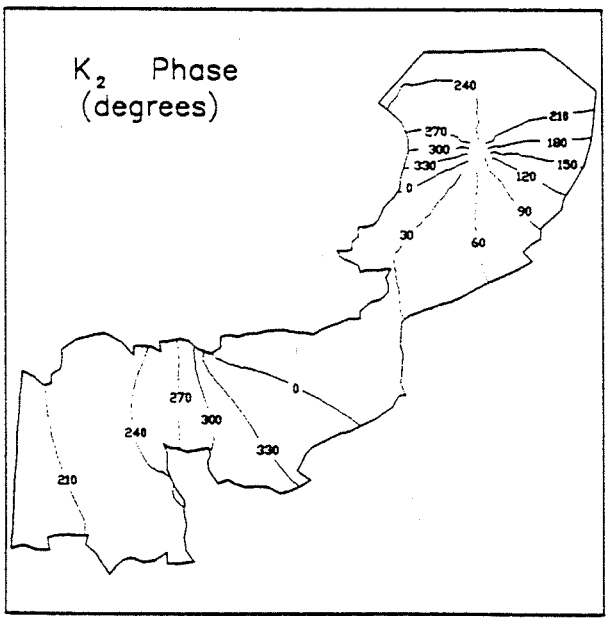

f. K_2 constituent

Figure 13. (Sheet 3 of 7)

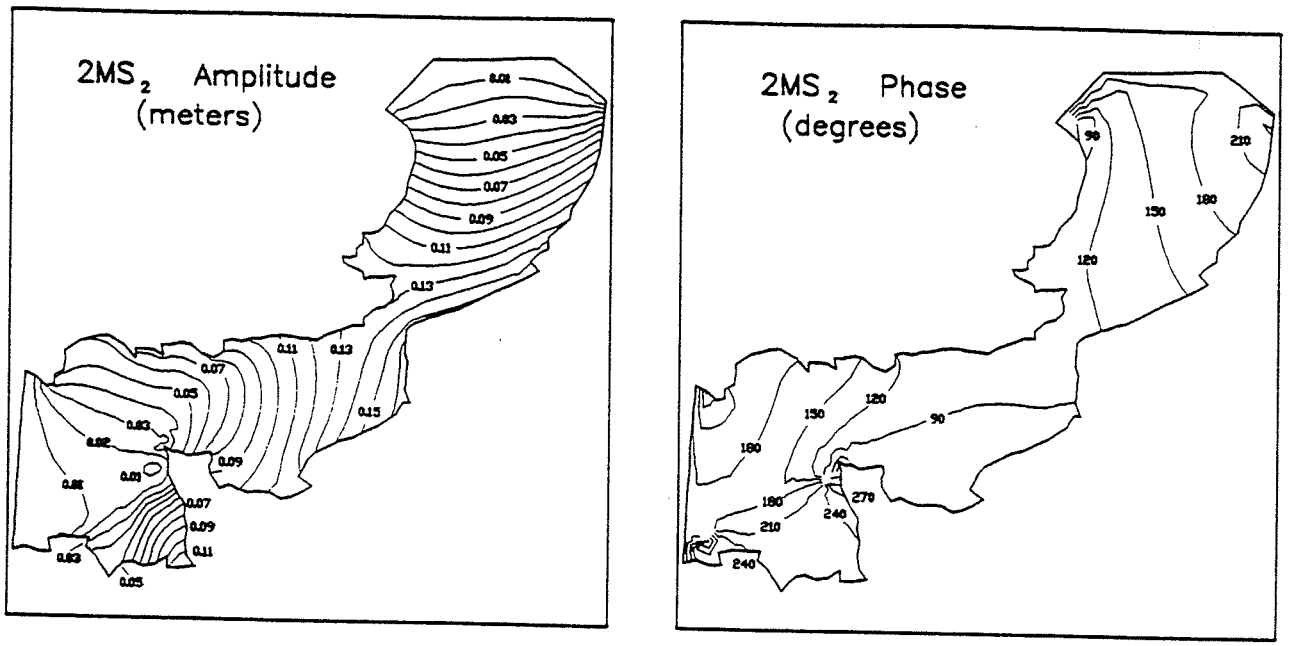

g. $2MS_2$ constituent

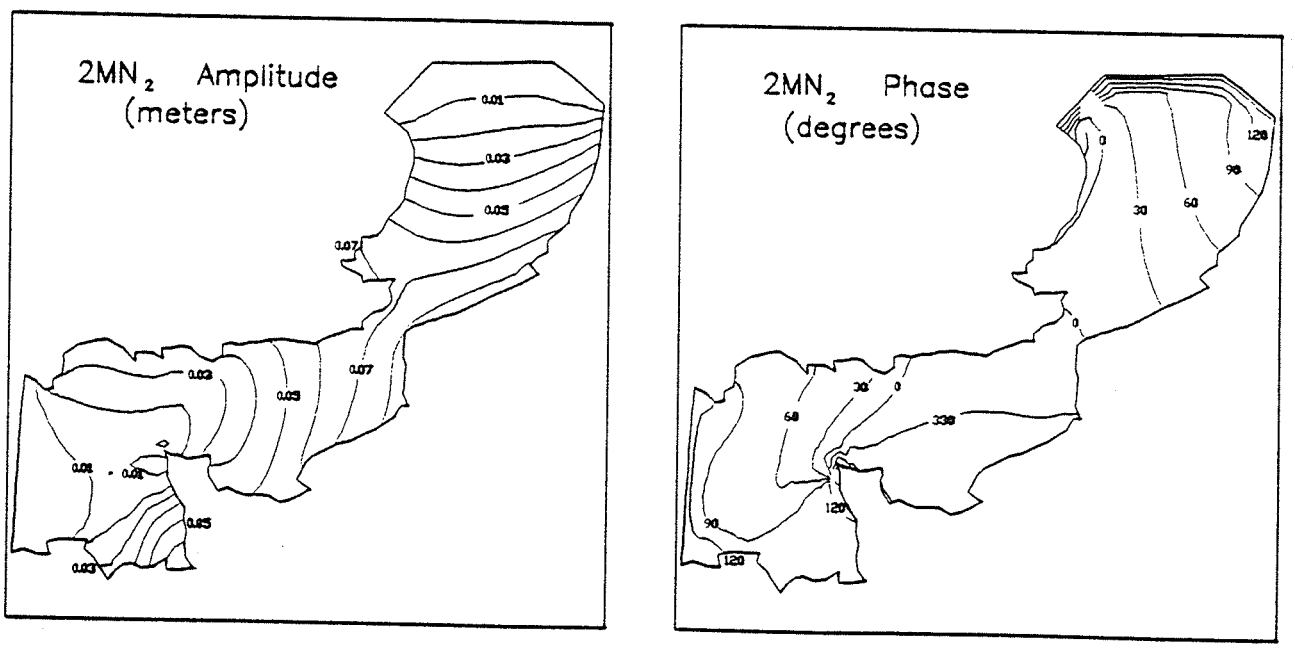

h. $2MN_2$ constituent

Figure 13. (Sheet 4 of 7)

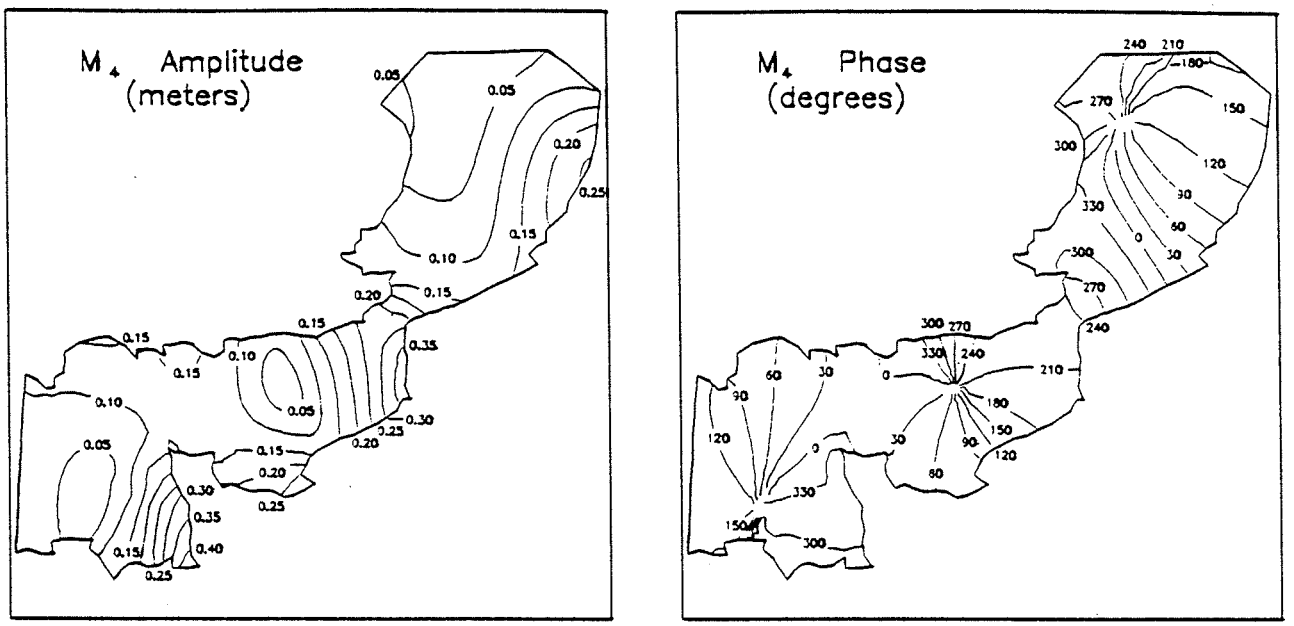

i. M_4 constituent

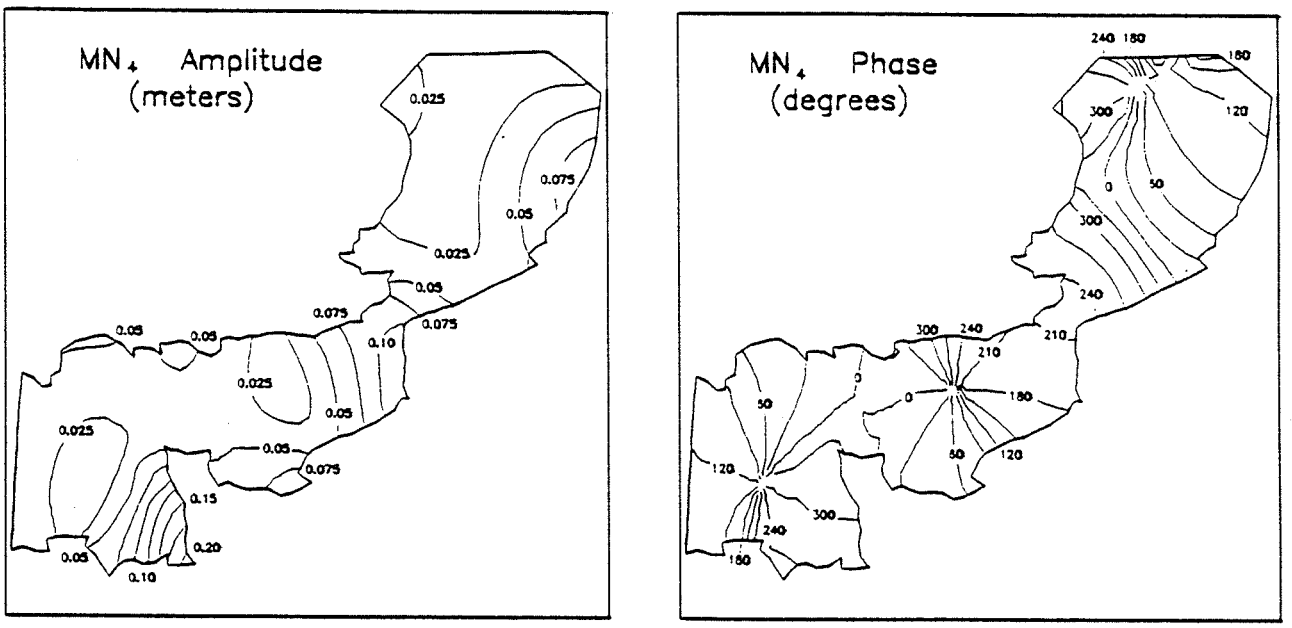

j. MN_4 constituent

Figure 13. (Sheet 5 of 7)

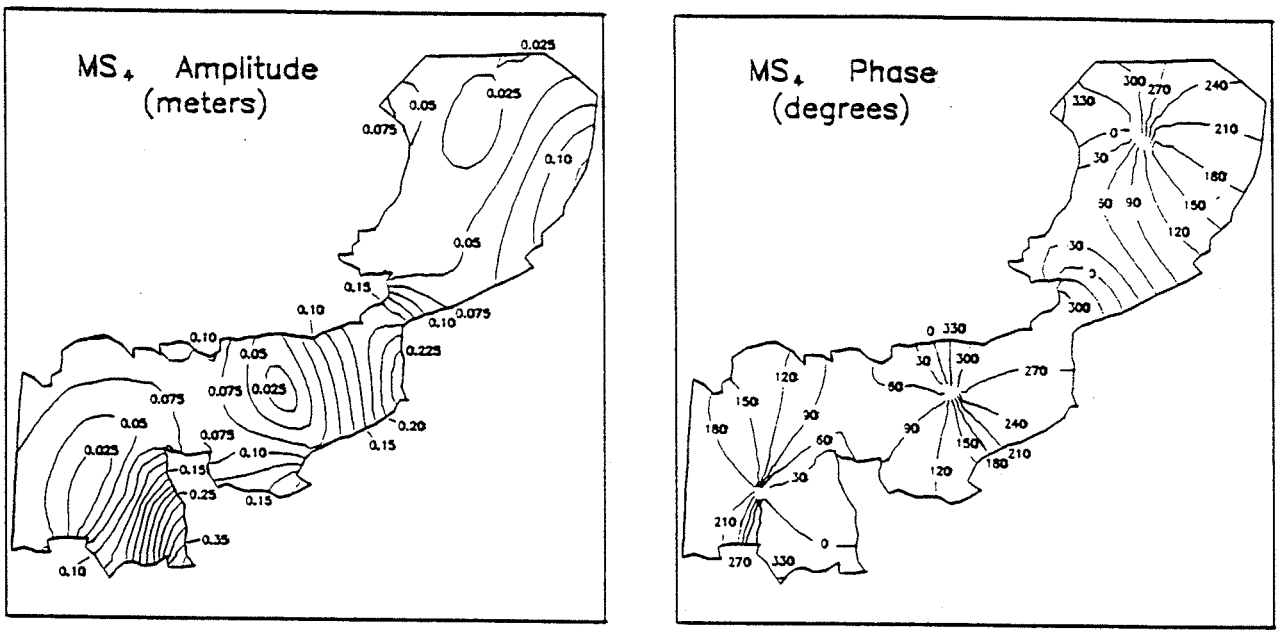

k. MS_4 constituent

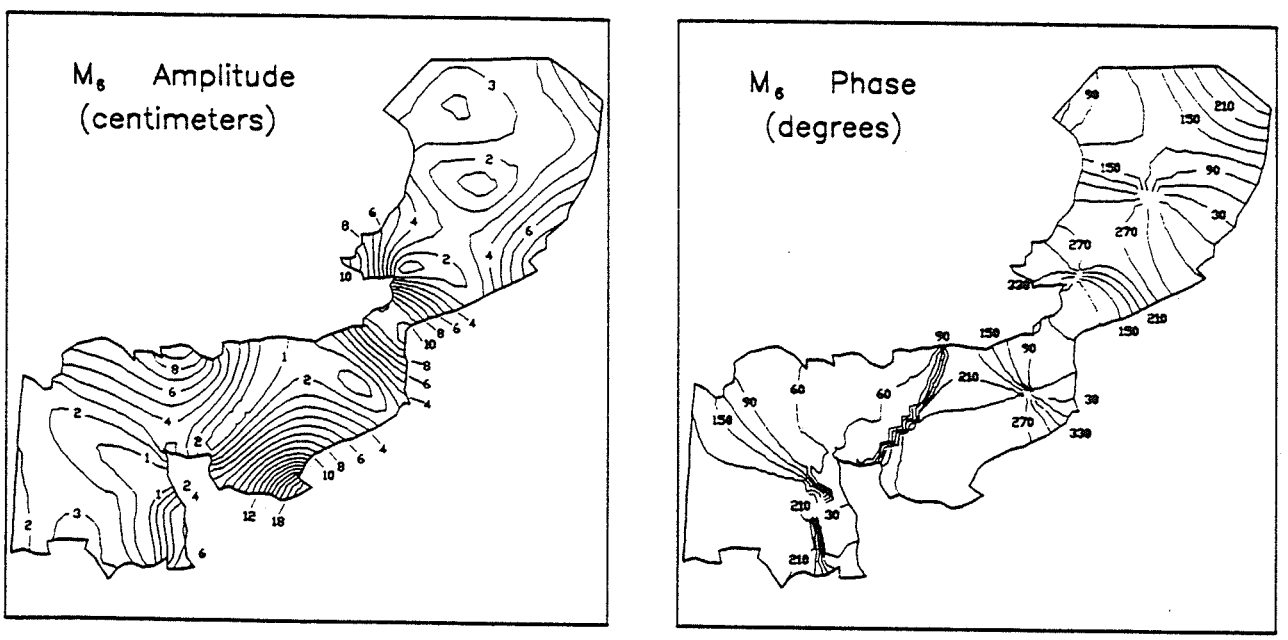

l. M_6 constituent

Figure 13. (Sheet 6 of 7)

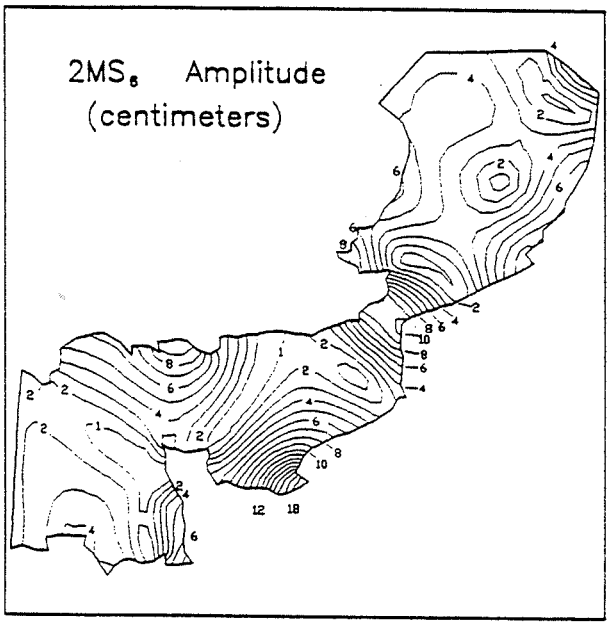

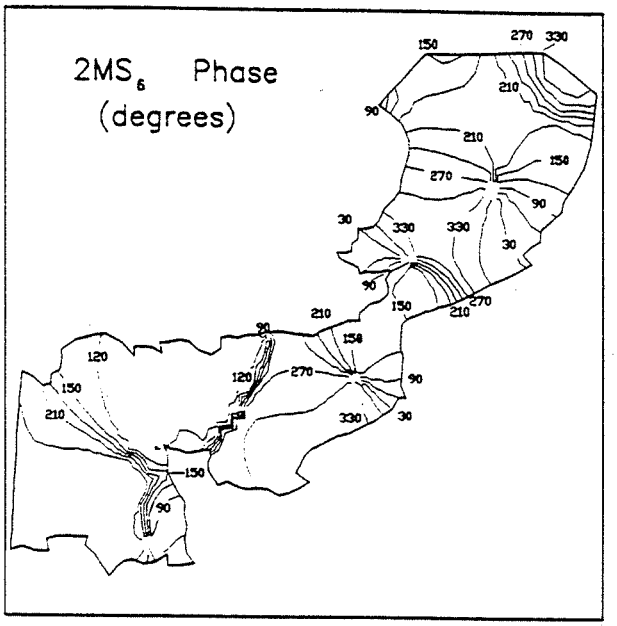

m. $2MS_6$ constituent

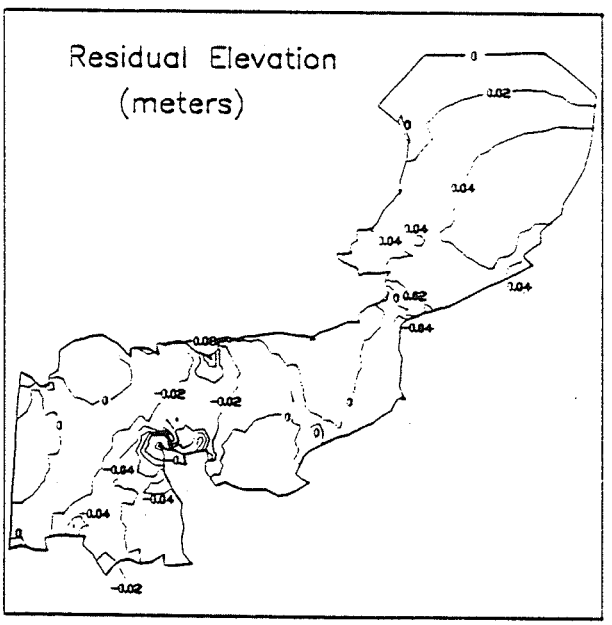

n. Residual constituent

Figure 13. (Sheet 7 of 7)

PART IV: INTERNAL MODE SOLUTION

Definition and Applicability of a 3DL Model

85. As discussed in Part II, mode splitting replaces the direct solution of the three–dimensional governing equations with an "external mode" computation for free surface elevation (using the vertically integrated governing equations) and an "internal mode" computation for the vertical profile of velocity. It was noted in Part II that all of the physics contained in the three–dimensional governing equations are included in the vertically integrated equations if the bottom stress and the momentum dispersion terms are specified correctly. The simple parameterizations of bottom stress and momentum dispersion in terms of depth–averaged velocity (Equations 28 – 31) are physically correct only for the simplest flows (e.g., a logarithmic velocity profile over depth). Mode splitting replaces these simple parameterizations with the internal mode equations. Therefore, when the complete internal mode equations are solved, the bottom stress and momentum dispersion used in the vertically integrated equations are (in theory) completely consistent with the three–dimensional equations.

86. While the external mode equations are two–dimensional, the internal mode equations retain the spatial variation of velocity in three dimensions. Considerable computational savings can be realized if the advective terms and the horizontal momentum diffusion terms are dropped in the internal mode computations (Nihoul and Djenidi 1987; Davies 1988). This simplification eliminates all horizontal gradients from the internal mode equations, thereby reducing them to one–dimensional equations in space (over the vertical). When simplified internal mode equations are solved, the bottom stress and momentum dispersion are no longer completely consistent with the three–dimensional equations. However, these approximations should be physically correct for flows in which the vertical distribution of momentum at each horizontal grid point is determined by a local balance between the surface and bottom stresses, vertical momentum diffusion, the Coriolis force, and the local inertia. (Clearly, this should encompass a much wider range of flows than parameterizations solely in terms of the depth–averaged velocity.) The required balance will exist when the rate of vertical momentum transport is much greater than the rate of horizontal momentum transport. Assuming horizontal momentum transport is dominated by advection, the rate of vertical momentum transport will be much greater than the rate of horizontal momentum transport in the three–dimensional governing equations if

$$\frac{\partial}{\partial z}\left[E_v \frac{\partial u}{\partial z}\right] >> u \frac{\partial u}{\partial x}$$

Scaling this yields

$$\frac{E_{vc} U_c}{h_c^2} >> \frac{U_c^2}{L_c} \qquad \text{or} \qquad \frac{L_c}{h_c} >> \frac{h_c U_c}{E_{vc}}$$

where E_{vc}, U_c, h_c, and L_c are a characteristic vertical eddy viscosity, horizontal velocity, water depth, and horizontal length scale, respectively. Dimensional arguments suggest $E_{vc} \approx \xi h_c U_c$ where ξ is a constant whose value for tidal and wind–driven flows typically ranges from 10^{-3} to 10^{-2} (Bowden, Fairmairn, and Huges 1959; Csanady 1976; Fischer et al. 1979; Davies 1985). Therefore, the simplified internal mode equations should be an accurate approximation to the full internal mode equations provided

$$\frac{L_c}{h_c} >> 100 - 1{,}000$$

Since coastal and shelf waters are usually characterized by large length–to–depth scales, a model based on the simplified internal mode equations should be widely applicable in these waters.

87. The model based on the simplified internal mode equations will be called a three–dimensional local (3DL) model. This name emphasizes the fact that the simplified internal mode equations give values of bottom stress and momentum dispersion for the two–dimensional (external mode) equations that are not fully consistent with three–dimensional equations, but rather are based on a local approximation of the three–dimensional equations.

Rationale for the DSS Technique

88. Despite the savings gained by simplifying the internal mode equations in the 3DL model, the internal mode equations are difficult to solve numerically because of the high velocity gradients that characterize the water column near the bottom and surface boundaries and across strong density changes. Existing state–of–the–art circulation models use velocity as a dependent variable and therefore require a fine numerical discretization to resolve regions of rapid velocity change. Davies (1991) and Davies and Jones (1991) have examined the computational effort required to resolve a bottom boundary layer using a one–dimensional model through the vertical solved with finite differences and several coordinate transformation/grid stretching schemes. For

tidal flows having an eddy viscosity that is constant over the upper 80 percent of the water column and that varies linearly with distance from the bed over the bottom 20 percent, Davies (1991) found that it was necessary to use a logarithmic or log–linear coordinate transformation and at least 20 grid cells to obtain convergence of the velocity solution. When the eddy viscosity was determined using a level 2–1/2 turbulent closure, the most efficient solution was found to require a log–linear coordinate transformation and 50 – 100 grid cells over the vertical for both a turbulent kinetic energy transport equation and the momentum equation.

89. Practical geophysical flows often have two or more regions containing sharp velocity gradients over the vertical. Because of the computational overhead in time and memory required to resolve these features, existing multi–dimensional circulation models almost always omit the near bottom region and use a slip boundary condition that expresses bottom stress as a quadratic function of near bottom velocity. This assumption is physically correct only when the velocity profile below the lowest grid point is logarithmic. An accurate treatment of surface and/or internal boundary layers requires a fine grid in the regions of these layers. In many cases the required computational overhead makes it impractical to resolve these features in multi–dimensional computations. A survey of the recent literature suggests that only rarely have more than ~ 20 grid cells been used over the vertical in three–dimensional engineering or geophysical model applications. For example, Oey, Mellor, and Hires (1985) used 11 grid cells over the vertical in their model of the Hudson–Raritan Estuary. Clearly, such models have limited ability to resolve even one significantly sheared velocity gradient region. (Note: Davies and Jones (1990) have recently published results from a three–dimensional model of the northern European continental shelf using 45 grid cells over the depth. However, this model uses a coarse horizontal grid and omits the advective terms in both the internal and the external mode–governing equations.)

90. It is well–established from laboratory and field experiments, theoretical arguments, and conventional one–dimensional models that the time–averaged vertical shear stress varies rather smoothly through the water column, particularly near boundaries. Therefore, it should be possible to use a relatively coarse vertical discretization to solve numerically for the vertical shear stress, even in boundary layers. A novel technique has been developed that allows the vertical shear stress to be used in place of velocity as the dependent variable in the internal mode equations. Applications of the DSS technique using linearized equations of motion (discussed in detail below) have shown that it provides a highly efficient means of solving the

internal mode equations. This technique promises to be invaluable for modeling coastal and shelf circulation in which the bottom and surface boundary layers comprise a significant portion of the water column and for modeling processes that are critically dependent on boundary layer physics such as wave–current interaction, sediment transport, oil spill movement, ice floe movement, energy dissipation, physical–biological couplings, etc.

Development and Testing of DSS Method No. 1

91. Internal mode equations can be generated by subtracting the vertically integrated equations from the three–dimensional equations (Wang 1982; Sheng 1983; Davies 1985). Using the three–dimensional equations in the σ coordinate system (Equations 19 – 21), the non–conservative vertically integrated momentum equations (Equations 25 and 26), assuming a constant density fluid, and neglecting advection and horizontal momentum diffusion terms, the resulting internal mode equations are

$$\frac{\partial \hat{u}}{\partial t} - f\hat{v} = \frac{1}{H\rho_o}\left[(a-b)\frac{\partial \tau_{zx}}{\partial \sigma} - \tau_{sx} + \tau_{bx}\right] \tag{114}$$

$$\frac{\partial \hat{v}}{\partial t} + f\hat{u} = \frac{1}{H\rho_o}\left[(a-b)\frac{\partial \tau_{zy}}{\partial \sigma} - \tau_{sy} + \tau_{by}\right] \tag{115}$$

92. Using the eddy viscosity relationships (Equation 34) to express τ_{zx} and τ_{zy} in terms of velocity and either the slip or the no–slip boundary condition (Equation 10) at the bottom, Equations 114 and 115 can be cast entirely in terms of velocity. Numerical solutions can then be sought for the dependent variables, $\hat{u}$ and $\hat{v}$. This is the standard velocity solution (VS) approach.

93. Alternatively, Equation 34 can be inverted to obtain expressions for velocity in terms of stress

$$\hat{u} = u_b - U + \frac{H}{(a-b)}\int_b^\sigma \frac{\tau_{zx}}{\rho_o E_v}\, d\sigma \tag{116a}$$

$$\hat{v} = v_b - V + \frac{H}{(a-b)}\int_b^\sigma \frac{\tau_{zy}}{\rho_o E_v}\, dz \tag{116b}$$

In Equation 116 the definitions of $\hat{u}$ and $\hat{v}$ have been used and nonzero slip velocities u_b and v_b have been included for generality. Relating u_b and v_b to the bottom stresses, τ_{bx} and τ_{by}, via the slip conditions

$$\tau_{bx}/\rho_o = k\ u_b = k(\hat{u}_b + U) \tag{117a}$$

$$\tau_{by}/\rho_o = k\ v_b = k(\hat{v}_b + V) \tag{117b}$$

Equation 116 can be written as

$$\hat{u} = \frac{\tau_{bx}}{\rho_o k} - U + \frac{H}{(a-b)} \int_b^\sigma \frac{\tau_{zx}}{\rho_o E_v}\, d\sigma \tag{118a}$$

$$\hat{v} = \frac{\tau_{by}}{\rho_o k} - V + \frac{H}{(a-b)} \int_b^\sigma \frac{\tau_{zy}}{\rho_o E_v}\, d\sigma \tag{118b}$$

(For a no–slip boundary condition, the terms $\frac{\tau_{bx}}{\rho_o k}$ and $\frac{\tau_{by}}{\rho_o k}$ do not appear in Equation 118. The no–slip condition is approached as $k \to \infty$.) Substituting Equation 118 into Equations 114 and 115 gives:

$$\frac{\partial}{\partial t}\left[\frac{H}{(a-b)} \int_b^\sigma \frac{\tau_{zx}}{\rho_o E_v}\, d\sigma + \frac{\tau_{bx}}{\rho_o k}\right] - f\left[\frac{H}{(a-b)} \int_b^\sigma \frac{\tau_{zy}}{\rho_o E_v}\, d\sigma + \frac{\tau_{by}}{\rho_o k}\right]$$

$$- \frac{1}{H\rho_o}\left[(a-b)\frac{\partial \tau_{zx}}{\partial \sigma} + \tau_{bx}\right] = \frac{\partial U}{\partial t} - fV - \frac{\tau_{sx}}{\rho_o H} \tag{119}$$

$$\frac{\partial}{\partial t}\left[\frac{H}{(a-b)} \int_b^\sigma \frac{\tau_{zy}}{\rho_o E_v}\, d\sigma + \frac{\tau_{by}}{\rho_o k}\right] + f\left[\frac{H}{(a-b)} \int_b^\sigma \frac{\tau_{zx}}{\rho_o E_v}\, d\sigma + \frac{\tau_{bx}}{\rho_o k}\right]$$

$$- \frac{1}{H\rho_o}\left[(a-b)\frac{\partial \tau_{zy}}{\partial \sigma} + \tau_{by}\right] = \frac{\partial V}{\partial t} + fU - \frac{\tau_{sy}}{\rho_o H} \tag{120}$$

Equations 119 and 120 have τ_{zx} and τ_{zy} as dependent variables and will be called the DSS[1] internal mode equations. (The superscript 1 is used to identify DSS method No. 1.) These equations are forced by the external mode solution (U, V, and H) and the applied surface stress.

94. Equations 119 and 120 contain both integral and differential terms; therefore, they are well–suited for a spatial discretization in which τ_{zx} and τ_{zy} are expressed in terms of assumed shape functions such as the spectral or finite element methods. Depending on the choice of the shape functions and the functional variation of E_v over the depth, the velocity profile can be recovered from the stress profile by solving Equation 118 in closed form. This is an important convenience because it avoids the troublesome operation of numerically integrating the near–logarithmic singularity that occurs in Equation 118 when E_v varies with distance from a boundary. The restrictions that a closed–form solution for Equation 118 impose on τ_{zx}, τ_{zy}, and E_v are not severe. For example, τ_{zx}, τ_{zy}, and E_v may be expressed in

terms of polynomials that span the vertical globally or in a piecewise manner. Polynomial variations of τ_{zx} and τ_{zy} are consistent with either the spectral method or the finite element method; for most practical problems, E_v can be approximated as piecewise linear over the vertical (Furnes 1983; Davies 1987; Chu, Liou, and Flenniken 1989; Jenter and Madsen 1989).

95. The effectiveness of the DSS[1] technique is evaluated using a simple test case consisting of flow generated by a specified surface stress aligned in the x–direction in a wide, straight channel of constant depth with no Coriolis force. An analytical solution can be found for the linear version of this problem and provides a benchmark for the numerical solutions. For convenience, the linear governing equations are repeated below:

$$\frac{\partial \eta}{\partial t} + h \frac{\partial U}{\partial x} = 0 \tag{121}$$

$$\frac{\partial U}{\partial t} = - g \frac{\partial \eta}{\partial x} + \frac{1}{h\rho_0}(\tau_s - \tau_b) \tag{122}$$

$$\frac{\partial \hat{u}}{\partial t} - \frac{(a-b)}{h} \frac{\partial}{\partial \sigma}\left(\frac{\tau_z}{\rho_0}\right) = \frac{1}{h\rho_0}[\tau_b - \tau_s] \tag{123}$$

$$\frac{h}{(a-b)} \frac{\partial}{\partial t}\int_b^\sigma \frac{\tau_z}{\rho_0 E_v}\, d\sigma + \frac{1}{k} \frac{\partial}{\partial t}\left(\frac{\tau_b}{\rho_0}\right) - \frac{1}{h\rho_0}\left[(a-b)\frac{\partial \tau_z}{\partial \sigma} + \tau_b\right] = \frac{\partial U}{\partial t} - \frac{\tau_s}{\rho_0 h} \tag{124}$$

Equations 121 and 122 are the depth–integrated (external mode) continuity and momentum equations; Equation 123 is the VS internal mode equation; Equation 124 is the DSS[1] internal mode equation. Since there is no motion in the y–direction, the y–direction equations and the subscript "x" in the stress terms have been dropped.

96. The Galerkin–spectral method, with shape functions consisting of Legendre polynomials (LPs) over the interval $-1 \leq \sigma \leq 1$ is used to discretize the VS and the DSS[1] internal mode equations. The m^{th} order LP is denoted L_m and can be computed from the recursion formulas

$L_0(\sigma) = 1$

$L_1(\sigma) = \sigma$

$L_{r+1}(\sigma) = \left[\frac{2r+1}{r+1}\right] \sigma L_r - \left[\frac{r}{r+1}\right] L_{r-1}$

The first eight LPs are shown in Figure 14. Other properties of LPs of note are

$L_{rs} \equiv L_r(1) = 1$

$L_{rb} \equiv L_r(-1) = (-1)^r$

$\int_{-1}^{1} L_0(\sigma)\, d\sigma = 2$

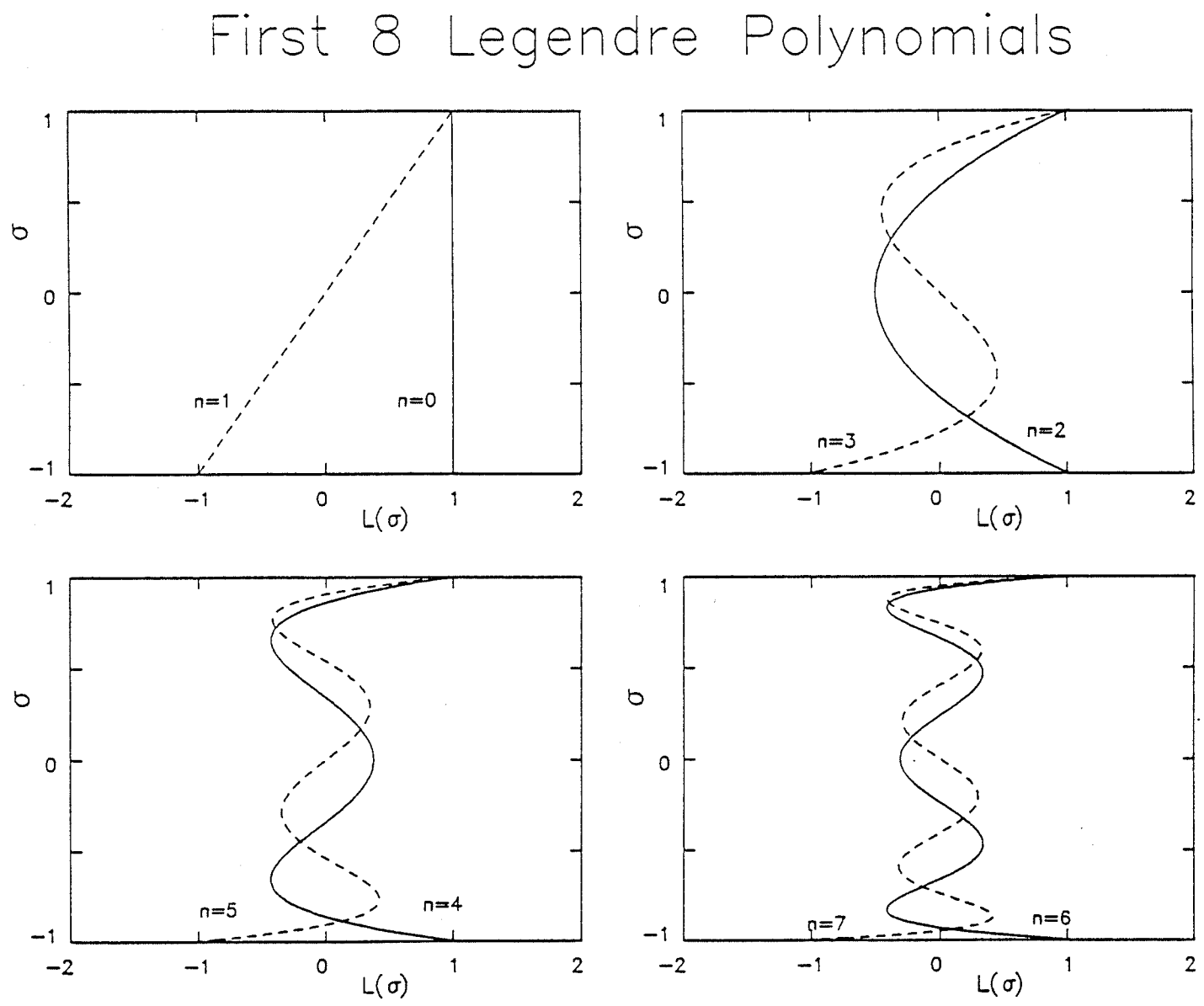

Figure 14. Drawings of the first eight Legendre polynomials in the range $-1 \leq \sigma \leq 1$

$$\int_{-1}^{1} L_r(\sigma)\, d\sigma = 0 \text{ for all } r \geq 1$$

It has been shown for wind–driven circulation that velocity solutions using Legendre and Chebyshev polynomials yield results of virtually identical accuracy, that these are highly superior to velocity solutions obtained using expansions of trigonometric functions, and that these are more accurate than velocity solutions computed with a second–order finite difference scheme having the same number of degrees of freedom (Davies and Owen 1979; Davies and Stephens 1983). For further information on the use of spectral methods in three–dimensional circulation models, the interested reader is referred to an excellent review by Davies (1987).

97. The Galerkin–spectral discretization for the VS internal mode equation is obtained by multiplying Equation 123 by the weighting function L_m and integrating from –1 to 1, i.e.,

$$\frac{\partial}{\partial t}\int_{-1}^{1} L_m\, \hat{u}\, d\sigma - \frac{2}{h}\int_{-1}^{1} L_m\, \frac{\partial}{\partial \sigma}\left(\frac{\tau_z}{\rho_o}\right) d\sigma = -\frac{1}{h}\left[\frac{\tau_s}{\rho_o} - \frac{\tau_b}{\rho_o}\right]\int_{-1}^{1} L_m\, d\sigma \tag{125}$$

Integrating the second term in Equation 125 by parts

$$\frac{2}{h}\int_{-1}^{1} L_m\, \frac{\partial}{\partial \sigma}\left(\frac{\tau_z}{\rho_o}\right) d\sigma = \frac{2}{h}\left[L_{ms}\, \frac{\tau_s}{\rho_o} - L_{mb}\, \frac{\tau_b}{\rho_o} - \int_{-1}^{1} \frac{\tau_z}{\rho_o}\, \frac{\partial L_m}{\partial \sigma}\, d\sigma\right] \tag{126}$$

and substituting this into Equation 125 yields:

$$\frac{\partial}{\partial t}\int_{-1}^{1} L_m\, \hat{u}\, d\sigma + \frac{2}{h}\int_{-1}^{1} \frac{\tau_z}{\rho_o}\, \frac{\partial L_m}{\partial \sigma}\, d\sigma = -\frac{1}{h}\left[\frac{\tau_s}{\rho} - \frac{\tau_b}{\rho}\right]\int_{-1}^{1} L_m\, d\sigma + \frac{2}{h}\left[L_{ms}\, \frac{\tau_s}{\rho_o} - L_{mb}\, \frac{\tau_b}{\rho_o}\right] \tag{127}$$

Using the definition of the LP, Equation 127 simplifies to

$$0 = 0 \qquad m = 0 \tag{128}$$

$$\frac{\partial}{\partial t}\int_{-1}^{1} L_m\, \hat{u}\, d\sigma + \frac{2}{h}\int_{-1}^{1} \frac{\tau_z}{\rho_o}\, \frac{\partial L_m}{\partial \sigma}\, d\sigma = \frac{2}{h}\left[\frac{\tau_s}{\rho_o} - L_{mb}\, \frac{\tau_b}{\rho_o}\right] \qquad m \geq 1 \tag{129}$$

Since $L_0(\sigma) = 1$, the operation that generates Equation 128 is equivalent to integrating Equation 123 over the depth when m = 0. The identity in Equation 128 occurs because Equation 123, by definition, has no depth–averaged component.

98. The final steps in applying the Galerkin–spectral discretization to the VS are to substitute Equation 34 for τ_z/ρ_o in Equation 129 (noting that $\frac{\partial u}{\partial \sigma} = \frac{\partial \hat{u}}{\partial \sigma}$) and to expand $\hat{u}$ as a series of LPs with time–varying coefficients, $\beta_n(t)$, i.e.,

$$\hat{u}(\sigma,t) \equiv \sum_{n=1}^{N} \beta_n(t)\ L_n(\sigma) \tag{130}$$

$$\frac{h^2}{4} \sum_{n=1}^{N} \frac{\partial \beta_n}{\partial t} \int_{-1}^{1} L_m L_n\ d\sigma + \sum_{n=1}^{N} \beta_n \int_{-1}^{1} E_v \frac{\partial L_n}{\partial \sigma} \frac{\partial L_m}{\partial \sigma}\ d\sigma = \frac{h}{2}\left[\frac{\tau_s}{\rho_o} - L_{mb} \frac{\tau_b}{\rho_o}\right] \qquad m \geq 1 \tag{131}$$

Because $\int_{-1}^{1} L_n\ d\sigma = 0$ for $n \geq 1$, the necessary condition $\int_{-1}^{1} \hat{u}\ d\sigma = 0$ is identically satisfied by the spectral solution by using only the $n \geq 1$ LP. The solution of Equation 131 requires a bottom boundary condition (Equation 117). After expanding $\hat{u}$, this becomes

$$\sum_{n=1}^{N} \beta_n\ L_{nb} = -\ U + \frac{\tau_b}{k\rho_o} \tag{132}$$

99. The Galerkin–spectral discretization for the DSS[1] is obtained by multiplying Equation 124 by the weighting function $L_m(\sigma)$ and integrating from –1 to 1, i.e.,

$$\frac{h}{2} \frac{\partial}{\partial t}\left[\int_{-1}^{1} L_m \int_{-1}^{\sigma} \frac{\tau_z}{\rho_o E_v}\ d\sigma d\sigma\right] + \left[\frac{1}{k} \frac{\partial}{\partial t}\left(\frac{\tau_b}{\rho_o}\right) - \frac{\tau_b}{h\rho_o}\right] \int_{-1}^{1} L_m\ d\sigma - \frac{2}{h} \int_{-1}^{1} L_m \frac{\partial}{\partial \sigma}\left(\frac{\tau_z}{\rho_o}\right)\ d\sigma =$$

$$\left[\frac{\partial U}{\partial t} - \frac{\tau_s}{h\rho_o}\right] \int_{-1}^{1} L_m\ d\sigma \tag{133}$$

Integrating the stress derivative by parts changes Equation 133 to

$$\frac{h}{2} \frac{\partial}{\partial t}\left[\int_{-1}^{1} L_m \int_{-1}^{\sigma} \frac{\tau_z}{\rho_o E_v}\ d\sigma d\sigma\right] + \left[\frac{1}{k} \frac{\partial}{\partial t}\left(\frac{\tau_b}{\rho_o}\right) - \frac{\tau_b}{h\rho_o}\right] \int_{-1}^{1} L_m\ d\sigma$$

$$- \frac{2}{h}\left[L_{ms} \frac{\tau_s}{\rho_o} - L_{mb} \frac{\tau_b}{\rho_o} - \int_{-1}^{1} \frac{\tau_z}{\rho_o} \frac{\partial L_m}{\partial \sigma}\ d\sigma\right] = \left[\frac{\partial U}{\partial t} - \frac{\tau_s}{h\rho_o}\right] \int_{-1}^{1} L_m\ d\sigma \tag{134}$$

Using the definition of the LP, Equation 134 simplifies to

$$0 = 0 \qquad m = 0 \tag{135}$$

$$\frac{h}{2}\frac{\partial}{\partial t}\left[\int_{-1}^{1} L_m \int_{-1}^{\sigma} \frac{\tau_z}{\rho_o E_v}\, d\sigma d\sigma\right] + \frac{2}{h}\left[L_{mb}\frac{\tau_b}{\rho_o} + \int_{-1}^{1}\frac{\tau_z}{\rho_o}\frac{\partial L_m}{\partial \sigma}\, d\sigma\right] = 2\frac{\tau_s}{h\rho_o} \qquad m \geq 1 \tag{136}$$

The identity in Equation 135 occurs because Equation 136 has no depth–averaged component.

100. The final step in applying the Galerkin–spectral method for the DSS[1] is to expand τ_z/ρ_o as a series of LPs with time–varying coefficients, $a_n(t)$, i.e.,

$$\frac{\tau_z(\sigma,t)}{\rho_o} \equiv \sum_{n=0}^{N} a_n(t)\, L_n(\sigma) \tag{137}$$

$$\frac{h^2}{4}\sum_{n=0}^{N}\frac{\partial a_n}{\partial t}\int_{-1}^{1} L_m \int_{-1}^{\sigma}\frac{L_n}{E_v}\, d\sigma d\sigma + \sum_{n=0}^{N} a_n\left[\int_{-1}^{1} L_n \frac{\partial L_m}{\partial \sigma}\, d\sigma + L_{nb}L_{ms}\right] = \frac{\tau_s}{\rho_o} \qquad m \geq 1 \tag{138}$$

101. The bottom boundary condition was introduced into Equation 118 and subsequently into Equation 138. Therefore it does not generate an extra equation, as was the case for the VS. However, the stress expansion, Equation 137, does not automatically satisfy the condition that $\int_{-1}^{1}\hat{u}\, d\sigma = 0$. Rather this must be enforced explicitly. Using Equation 118 and the definition of u, this requirement generates the additional equation

$$\int_{-1}^{1}\left[-U + \frac{\tau_b}{\rho_o k} + \frac{h}{2}\int_{-1}^{\sigma}\frac{\tau_z}{\rho_o E_v}\, d\sigma\right] d\sigma = 0 \tag{139}$$

Substituting the expansion for τ_z/ρ_o into Equation 139 yields

$$\sum_{n=0}^{N} a_n\left[\frac{L_{nb}}{kh} + \frac{1}{4}\int_{-1}^{1}\int_{-1}^{\sigma}\frac{L_n}{E_v}\, d\sigma d\sigma\right] = \frac{U}{h} \tag{140}$$

102. The relative merit of the DSS[1] versus the VS was evaluated by comparing solutions computed numerically with analytical solutions for the problem of wind–driven circulation in a closed, rectangular channel aligned with the x–axis and having a constant bathymetric depth. This was done for a steady–state case, for a periodically varying wind stress, and for an instantaneously imposed wind stress.

103. In each test case, E_v was assumed to be linear over the depth as expressed by

$$E_v(\sigma) = E_{zo}(\sigma+1+\sigma_o) \tag{141}$$

where $\sigma_0 \equiv 2z_0/h$ is the dimensionless roughness height. It is well known from theoretical, laboratory, and field experiments that an eddy viscosity that increases linearly with distance from a solid boundary realistically reproduces the physics of the boundary layer near the boundary (Monin and Yaglom 1971; Schlichting 1979; Grant and Madsen 1986). Despite the fact that this does not hold over the entire depth, (e.g., it has been suggested that E_v should also increase linearly with distance below the free surface (Jenter and Madsen 1989)), Equation 141 is used here because it generates a realistic bottom boundary layer and because it simplifies the analyses of model results by introducing only two parameters, E_{z0} and σ_0, into the problem. As is shown below, the presence of a velocity gradient region at the bottom is sufficient to illustrate the advantage of the DSS over the VS. In fact, the use of an eddy viscosity that does not also give a boundary layer at the free surface is a considerable advantage for the VS, since it eliminates the additional need to reproduce velocity gradients there.

104. Assuming reasonable ranges for z_0 of 0.1 to 10 cm, and for h of 1 to 100 m, suggests values of $\sigma_0 \sim 10^{-5}$ to 10^{-2}. (The combination of $z_0 = 10$ cm and $h = 1$ m, which gives $\sigma_0 \sim 10^{-1}$, is not considered realistic since z_0 is typically 3 to 10 percent of the physical roughness height. In this case the physical roughness would occupy the entire depth.) Assuming the slope of the variation of E_v with z scales with U_b^*, ($U_b^* \equiv \sqrt{\tau_b/\rho_0}$), then $E_{z0} \sim U_b^* h$. If U_b^* varies over the range 0.1 to 10 cm/s, $E_{z0} \sim 10^{-3}$ to 10^{1} m^2/s.

105. Equations 131, 132, 138, and 140 show that the VS and DSS[1] require the specification of τ_s/ρ_0 (which is the input forcing) and U. To eliminate the possibility that errors in the solution for U might affect the comparisons, U was obtained for each test case from an analytical solution of Equations 121 – 123. As a result, errors in the VS and DSS[1] over the vertical do not feed back into the solution for U as they would if the complete problem was solved numerically.

106. In all of the results presented below, bottom stresses are obtained from the VS by using computed bottom slip velocities and the linear slip boundary condition (Equation 117). Comparisons indicated that this method gave more accurate values of bottom stress than those obtained by evaluating Equation 34 at $\sigma = -1$. (A similar conclusion was reached by Gresho, Lee, and Sani (1987).) Velocities are obtained from the DSS[1] by solving Equation 118 analytically using the computed stress profiles.

107. At steady state, Equation 123 reduces to

$$\frac{\partial \tau_z}{\partial \sigma} = \frac{\tau_s - \tau_b}{2} \tag{142}$$

which has the analytical solution

$$\frac{\tau_z}{\tau_s} = \frac{\sigma+1}{2} + \frac{1-\sigma}{2}\left(\frac{\tau_b}{\tau_s}\right) \tag{143}$$

where

$$\frac{\tau_b}{\tau_s} = \frac{-1 + \sigma_o\left[\frac{2+\sigma_o}{2}\ln\left(\frac{2+\sigma_o}{\sigma_o}\right) - 1\right]}{\frac{4}{K} - 1 + (2+\sigma_o)\left[\frac{2+\sigma_o}{2}\ln\left(\frac{2+\sigma_o}{\sigma_o}\right) - 1\right]} \tag{144}$$

and $K \equiv kh/E_{zo}$ is the nondimensional slip coefficient. The nondimensional solutions for velocity are

$$\frac{UE_{zo}}{h\tau_s/\rho_o} = 0 \tag{145}$$

$$\frac{\hat{u}\,E_{zo}}{h\tau_s/\rho_o} = \frac{\tau_b}{\tau_s}\left[\frac{1}{K} - \frac{\sigma+1}{4} + \frac{2+\sigma_o}{4}\ln\left(\frac{\sigma+1+\sigma_o}{\sigma_o}\right)\right] + \frac{\sigma+1}{4} - \frac{\sigma_o}{4}\ln\left(\frac{\sigma+1+\sigma_o}{\sigma_o}\right) \tag{146}$$

108. The VS and DSS[1] are obtained from Equations 131, 132, 138, and 140 by dropping the time derivatives, setting U = 0, and considering all other terms to be constant in time.

109. Figure 15 presents a comparison of vertical profiles of horizontal velocity for several combinations of K and σ_o computed from the analytical solution, the DSS[1] using 2 LPs and the VS using various numbers of LPs. Equation 143 indicates that the analytical solution for stress varies linearly over the depth, regardless of the form of E_v. This solution can be represented exactly by the DSS[1] using only the n = 0 and n = 1 LP; therefore the DSS[1] and the analytical solution in Figure 15 are identical. Equation 146 indicates that the analytical solution for velocity has a logarithmic variation over the depth and consequently a potentially sharp gradient region near the bottom. In Figure 15a the combination of a small K (large amount of slip) and a large σ_o minimizes the gradient region. Over most of the depth the velocity profile is nearly linear and therefore closely reproduced using a VS with 2 LP. However, approximately 5 LPs are required to capture the mild velocity gradient near the bed. In Figure 15b, the same K is used with σ_o reduced by two orders of magnitude. This has the effect of pushing the gradient region closer to the bottom (i.e., it is equivalent to increasing the depth by a factor of 100 for the same roughness) and therefore steepening the velocity gradient. Because the velocity profile

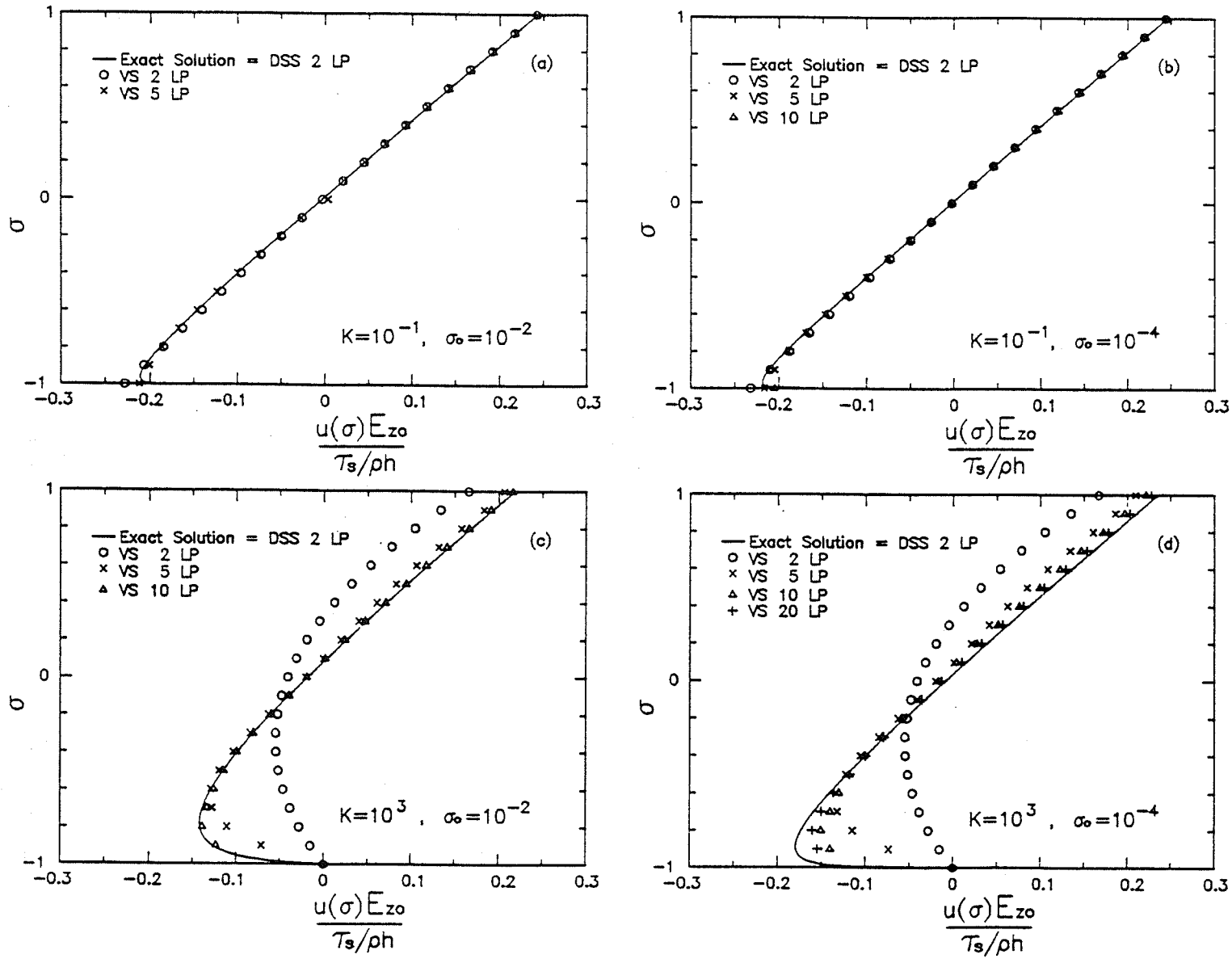

Figure 15. Vertical profiles of horizontal velocity for the steady state test case for the VS and DSS[1]

is nearly linear over much of the depth, it is reproduced well by the VS with 2 LPs. However, near the bed, approximately 10 LPs are required for the VS to capture the gradient region. As discussed below, this results in a poor prediction of bottom stress.

110. In Figures 15c and 15d, a high value of K is used, resulting in essentially no slip at the bottom. For large σ_0 (Figure 15c) a velocity expansion of 10 or more LPs is required to reproduce this profile. Reducing σ_0 by two orders of magnitude (Figure 15d) sharpens the profile further, and approximately 20 LPs are required to capture the velocity profile away from the boundary. Many more are required to represent the gradient region near the boundary.

111. As noted above, an important reason for using a three–dimensional model in place of a two–dimensional model is the former's improved representation of the bottom stress. However, since stress is proportional to the velocity gradient (Equation 34), or the bottom velocity (Equation 117), the bottom stress may still be represented poorly if the gradient region near the bottom is not resolved properly. To illustrate this problem, a comparison was made between the analytical bottom stress and computed bottom stresses from the DSS[1] and the VS over the practical range of K and σ_0. The DSS[1] reproduces bottom stress exactly using 2 LPs. On the other hand, Table 4 presents a summary of the number of LPs required for the computed bottom stress using the VS to come within 10 percent of the analytical bottom stress as a function of K and σ_0. Clearly, it is computationally practical to use the VS only for large roughnesses and large amounts of slip, both of which tend to minimize the velocity gradient at the bottom.

112. Although quite simple, the steady–state case demonstrates the relative ease with which a DSS can resolve a realistic boundary layer (i.e., no bottom slip and a linearly varying eddy viscosity) in a hydrodynamic model that explicitly includes the vertical dimension. In the following examples we evaluate how this highly desirable capability is affected by unsteady conditions. Only the no–slip case (K = 1,000) is considered.

113. If a periodic surface stress is assumed of the form $\tau_s(t)/\rho_0 = (\tau_s/\rho_0)e^{i\omega t}$ (where ω is the forcing frequency and $i \equiv \sqrt{-1}$), solutions can be sought to Equations 121 – 123 that have the form $U(t) = Ue^{i\omega t}$, $\hat{u}(\sigma,t) = \hat{u}(\sigma)e^{i\omega t}$, $\tau_b(t)/\rho_0 = (\tau_b/\rho_0)e^{i\omega t}$, and $\eta(t) = \eta e^{i\omega t}$. (Note: τ_s/ρ_0, U, $\hat{u}(\sigma)$, τ_b/ρ_0, and η are all complex variables; therefore they may be out of phase with each other.) Substituting these into Equations 121 – 123 transforms the linear hydrodynamic equations into

Table 4

Steady–State Bottom Stresses Computed Using Velocity Expansions

σ_o	K	#LP	$\left\lvert \frac{\tau_{b(anal)} - \tau_{b(comp)}}{\tau_{b(anal)}} \right\rvert$
10^{-2}	10^{-1}	3	0.100
10^{-2}	10^{0}	8	0.091
10^{-2}	10^{1}	9	0.099
10^{-2}	10^{2}	10	0.078
10^{-2}	10^{3}	10	0.078
10^{-3}	10^{-1}	8	0.096
10^{-3}	10^{0}	21	0.098
10^{-3}	10^{1}	24	0.095
10^{-3}	10^{2}	24	0.098
10^{-3}	10^{3}	24	0.099
10^{-4}	10^{-1}	22	0.100
10^{-4}	10^{0}	≤ 40	0.192*
10^{-4}	10^{1}	≤ 40	0.242*
10^{-4}	10^{2}	≤ 40	0.249*
10^{-4}	10^{3}	≤ 40	0.249*
10^{-5}	10^{-1}	≤ 40	0.174*
10^{-5}	10^{0}	≤ 40	0.476*
10^{-5}	10^{1}	≤ 40	0.602*
10^{-5}	10^{2}	≤ 40	0.619*
10^{-5}	10^{3}	≤ 40	0.620*

* This is the minimum difference obtained using no more than 40 Legendre polynomials.

$$i\omega\eta + h\frac{\partial U}{\partial x} = 0 \tag{147}$$

$$i\omega U = -g\frac{\partial \eta}{\partial x} + \frac{1}{h\rho_o}(\tau_s - \tau_b) \tag{148}$$

$$i\omega\hat{u} - \frac{(a-b)}{h}\frac{\partial}{\partial\sigma}\left[\frac{(a-b)E_v}{h}\frac{\partial\hat{u}}{\partial\sigma}\right] = \frac{1}{h\rho_o}(\tau_b - \tau_s) \tag{149}$$

114. The procedure used to solve Equations 147 – 149 analytically, together with the linear slip boundary condition, has been presented previously (Lynch and Officer 1985; Lynch and Werner 1987) and is not repeated here. Rather, the solutions are given without derivation in Table 5 (Equations 150 – 163).

115. Spectral approximations for the periodic case are generated by expressing $\beta_n(t) = \beta_n e^{i\omega t}$ and $\alpha_n(t) = \alpha_n e^{i\omega t}$ and substituting these as well as the periodic forms of u(t), $\tau_z(\sigma,t)/\rho_o$, $\tau_s(t)/\rho_o$, $\tau_b(t)/\rho_o$ and U(t) into Equations 130 – 132, 137, 138, and 140. The resulting equations for the VS are

$$\hat{u}(\sigma) \equiv \sum_{n=1}^{N} \beta_n L_n(\sigma) \tag{164}$$

$$\frac{h^2}{4}\sum_{n=1}^{N} i\omega\beta_n \int_{-1}^{1} L_m L_n \, d\sigma + \sum_{n=1}^{N}\beta_n \int_{-1}^{1} E_v \frac{\partial L_n}{\partial\sigma}\frac{\partial L_m}{\partial\sigma}\, d\sigma = \frac{h}{2}\left[\frac{\tau_s}{\rho_o} - \frac{\tau_b}{\rho_o} L_{mb}\right] \qquad m \geq 1 \tag{165}$$

$$\sum_{n=1}^{N} \beta_n L_{nb} = -U + \frac{\tau_b}{k\rho_o} \tag{166}$$

and for the DSS[1] are

$$\frac{\tau_z(\sigma)}{\rho_o} \equiv \sum_{n=0}^{N} a_n L_n(\sigma) \tag{167}$$

$$\frac{h^2}{4}\sum_{n=0}^{N} i\omega\alpha_n \int_{-1}^{1} L_m \int_{-1}^{\sigma}\frac{L_n}{E_v}\, d\sigma d\sigma + \sum_{n=0}^{N} a_n\left[\int_{-1}^{1} L_n \frac{\partial L_m}{\partial}\, d\sigma + L_{nb}L_{mb}\right] = \frac{\tau_s}{\rho_o} \qquad m \geq 1 \tag{168}$$

$$\sum_{n=0}^{N} a_n\left[\frac{L_{nb}}{kh} + \frac{1}{4}\int_{-1}^{1}\int_{-1}^{\sigma}\frac{L_n}{E_v}\, d\sigma d\sigma\right] = \frac{U}{h} \tag{169}$$

116. The periodic solution depends on the dimensionless parameters K and σ_o (as found for the steady–state solution), a dimensionless channel length L′, a dimensionless frequency Ω, and the dimensionless position in the channel x/L. L′ is the ratio of the channel length, L, to the wave length of a shallow–water wave having period ω (Equation 154). Ω is the ratio of the time scale for momentum to be

Table 5

Analytical Solution for the Periodic Test Case*

$$\frac{\hat{u}(\sigma)E_{zo}}{h\tau_s/\rho_o} = \frac{U_o E_{zo}}{h\tau_s/\rho_o}\left[\frac{A_1(\sigma) - \tilde{A}_1}{B}\right] + \frac{1}{2(2+\sigma_o)}\left[\frac{A_2(\sigma) - \tilde{A}_2}{B}\right] \tag{150}$$

$$\frac{UE_{zo}}{h\tau_s/\rho_o} = \frac{U_o E_{zo}}{h\tau_s/\rho_o}\left[1 + \frac{\tilde{A}_1}{B}\right] + \frac{1}{2(2+\sigma_o)}\frac{\tilde{A}_2}{B} \tag{151}$$

$$\frac{\tau(\sigma)}{\tau_s} = \left[2\,\frac{U_o E_{zo}}{h\tau_s/\rho_o}\frac{\dot{A}_1(\sigma)}{B} + \frac{1}{2+\sigma_o}\frac{\dot{A}_2(\sigma)}{B}\right](\sigma+1+\sigma_o) \tag{152}$$

$$\frac{U_o E_{zo}}{h\tau_s/\rho_o} = \frac{i(1+\gamma_2)}{\Omega}\left[\frac{(1-\exp(-\lambda L'))\exp(\lambda L'\frac{x}{L}) - (1-\exp(\lambda L'))\exp(-\lambda L'\frac{x}{L})}{\exp(\lambda L') - \exp(-\lambda L')}\right] \tag{153}$$

$$L' \equiv \frac{\omega L}{\sqrt{gh}} \tag{154}$$

$$\Omega \equiv \frac{\omega h^2}{E_{zo}} \tag{155}$$

$$\lambda \equiv \sqrt{i\gamma_1 - 1} \tag{156}$$

$$\gamma_1 \equiv \frac{2\dot{A}_1(-1)}{\Omega(\tilde{A}_1+B)}\,\sigma_o \tag{157}$$

$$\gamma_2 \equiv \left[\frac{\dot{A}_1(-1)\tilde{A}_2}{B(\tilde{A}_1+B)} - \frac{\dot{A}_2(-1)}{B}\right]\frac{\sigma_o}{2+\sigma_o} \tag{158}$$

$$A_1(\sigma) \equiv \mu_1(\sigma)\dot{\mu}_2(1) - \mu_2(\sigma)\dot{\mu}_1(1) \tag{159}$$

$$A_2(\sigma) \equiv \mu_1(\sigma)\left[\mu_2(-1) - \frac{2\sigma_o}{K}\dot{\mu}_2(-1)\right] - \mu_2(\sigma)\left[\mu_1(-1) - \frac{2\sigma_o}{K}\dot{\mu}_1(-1)\right] \tag{160}$$

$$B \equiv \dot{\mu}_1(1)\left[\mu_2(-1) - \frac{2\sigma_o}{K}\dot{\mu}_2(-1)\right] - \dot{\mu}_2(1)\left[\mu_1(-1) - \frac{2\sigma_o}{K}\dot{\mu}_1(-1)\right] \tag{161}$$

$$\mu_1(\sigma) = \mathrm{ber}\left[[\Omega(\sigma+1+\sigma_o)]^{1/2}\right] + i\,\mathrm{bei}\left[[\Omega(\sigma+1+\sigma_o)]^{1/2}\right] \tag{162}$$

$$\mu_2(\sigma) = \mathrm{ker}\left[[\Omega(\sigma+1+\sigma_o)]^{1/2}\right] + i\,\mathrm{kei}\left[[\Omega(\sigma+1+\sigma_o)]^{1/2}\right] \tag{163}$$

*ber, bei, ker, kei are zeroth order Kelvin functions, an overdot $(\dot{}) \equiv \partial/\partial\sigma$, an overbar $(\tilde{}) \equiv \frac{1}{2}\int_{-1}^{1} d\sigma$

transported through the water depth, h^2/E_{z0}, and the forcing time scale, $1/\omega$, Equation 155. Assuming ranges for ω of 10^{-3} sec^{-1} to 10^{-5} sec^{-1}, L of 1 km to 10^3 km, and h and U_b^* as given previously, suggests $L' \sim 10^{-5}$ to 10^2 and $\Omega \sim 10^{-4}$ to 10^2. In all cases results are presented for x/L = 0.5, as these are representative of the behavior throughout the rest of the channel.

117. Figures 16 and 17 present magnitude and phase portraits of the velocity structure for K = 1,000, $L' = 1$, and four combinations of σ_0 and Ω. For the case $\Omega = 10^{-1}$, momentum is transported through the depth in only a fraction of the forcing period. Figures 16a and 16b and 17a and 17b show that the velocity magnitude and phase obtained from the DSS[1] using 2 LPs are virtually identical to the analytical solution; therefore, the stress variation is very close to linear over the depth. This linear stress variation suggests that the momentum balance over the depth is nearly at steady state and is consistent with the low value of Ω. Since steady state is approached as $\Omega \to 0$, the DSS[1] using two LPs gives a highly accurate solution for $\Omega < 10^{-1}$ as well. The VS is able to capture the phase change through the water column with a comparable number of LP to the DSS[1]. However, as was the case at steady state, for $\sigma_0 = 10^{-2}$, approximately 10 LPs are required to reproduce the velocity magnitude with an accuracy comparable to the DSS[1] using 2 LPs. For $\sigma_0 = 10^{-4}$, more than 20 LPs are required.

118. For the case $\Omega = 10$, the vertical momentum balance is no longer near steady state; consequently the DSS[1] requires more than 2 LPs to capture the vertical stress variation. Figures 16c and 16d and 17c and 17d suggest that approximately 4 LPs may be needed by the DSS[1]. The VS, however, requires at least 10 LPs for $\sigma_0 = 10^{-2}$, and more than 20 LPs for $\sigma_0 = 10^{-4}$.

119. Figures 18 and 19 compare the amplitude and phase behavior of the analytical solution for bottom stress with solutions obtained using the DSS[1] and VS. These runs were made using a single value of $\sigma_0 = 10^{-3}$, but varying Ω and L'. The 10^4 change in L' has minimal effect in these pictures, indicating that the number of LPs required for the DSS[1] or the VS to converge to the analytical solution is only very weakly dependent on L'. For $\Omega \leq 1$, the DSS[1] with 2 LPs is nearly identical to the analytical solution, while for larger Ω the number of LPs required by the DSS[1] increases to as many as 7 for $\Omega = 10^2$. Considering the fact that comparable results using the VS require the use of more than 20 LPs, the DSS[1] is computationally quite superior to the VS for all Ω.

120. Although the Coriolis force was omitted from these test cases, the results can be used to infer whether a DSS will be equally effective when the Coriolis force is

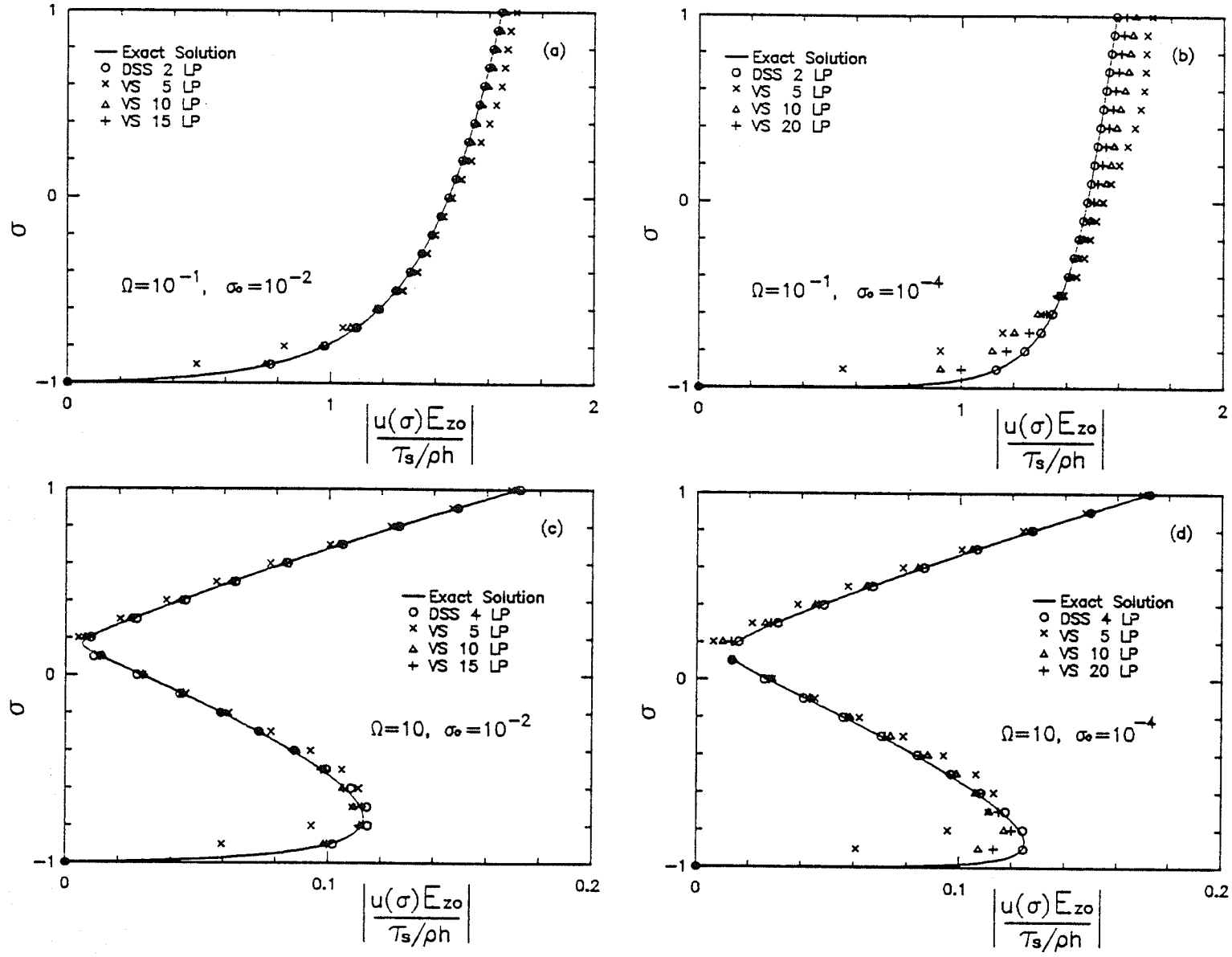

Figure 16. Vertical profiles of the horizontal velocity magnitude for the periodic test case for the VS and DSS[1]

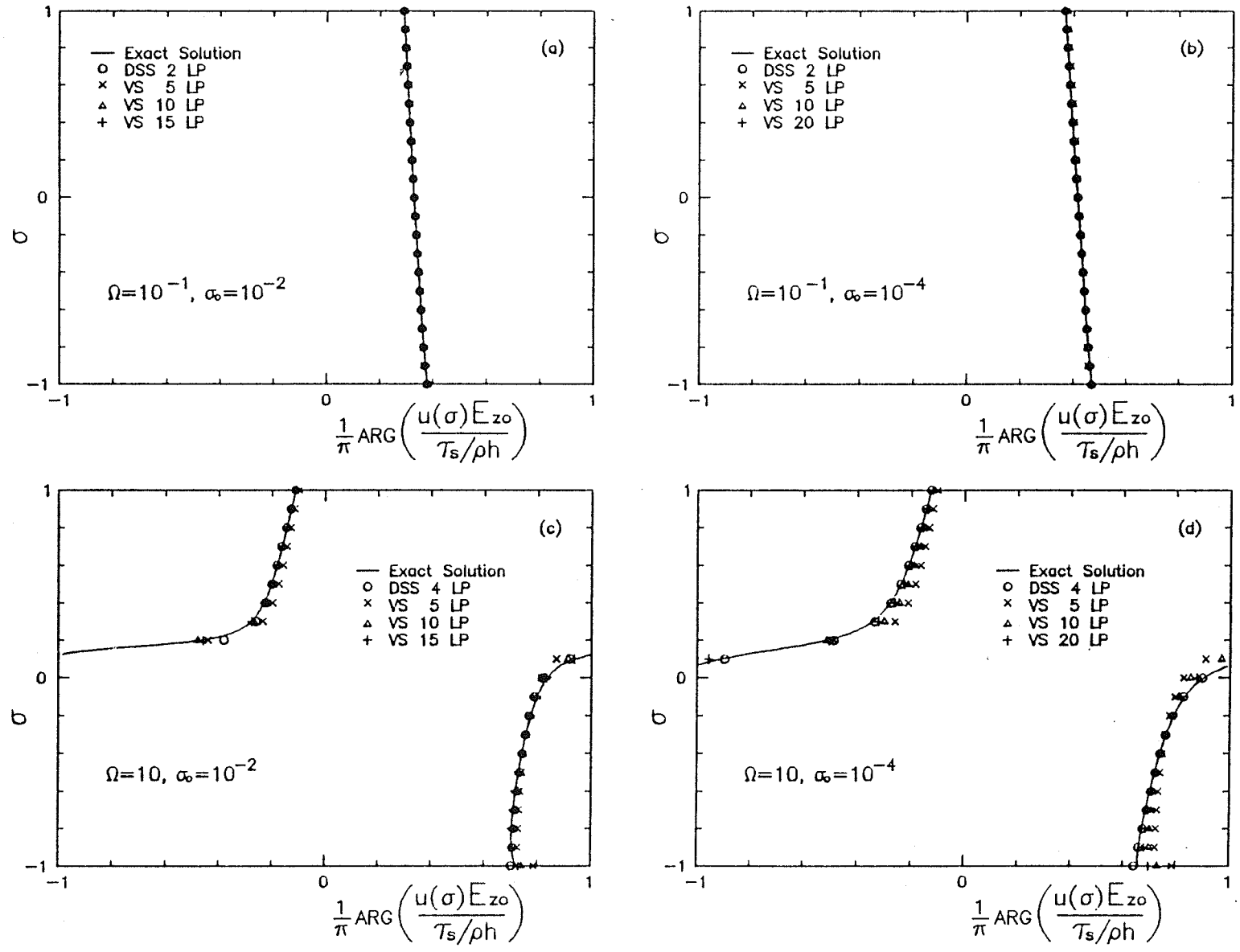

Figure 17. Vertical profiles of the horizontal velocity phase for the periodic test case for the VS and DSS[1]

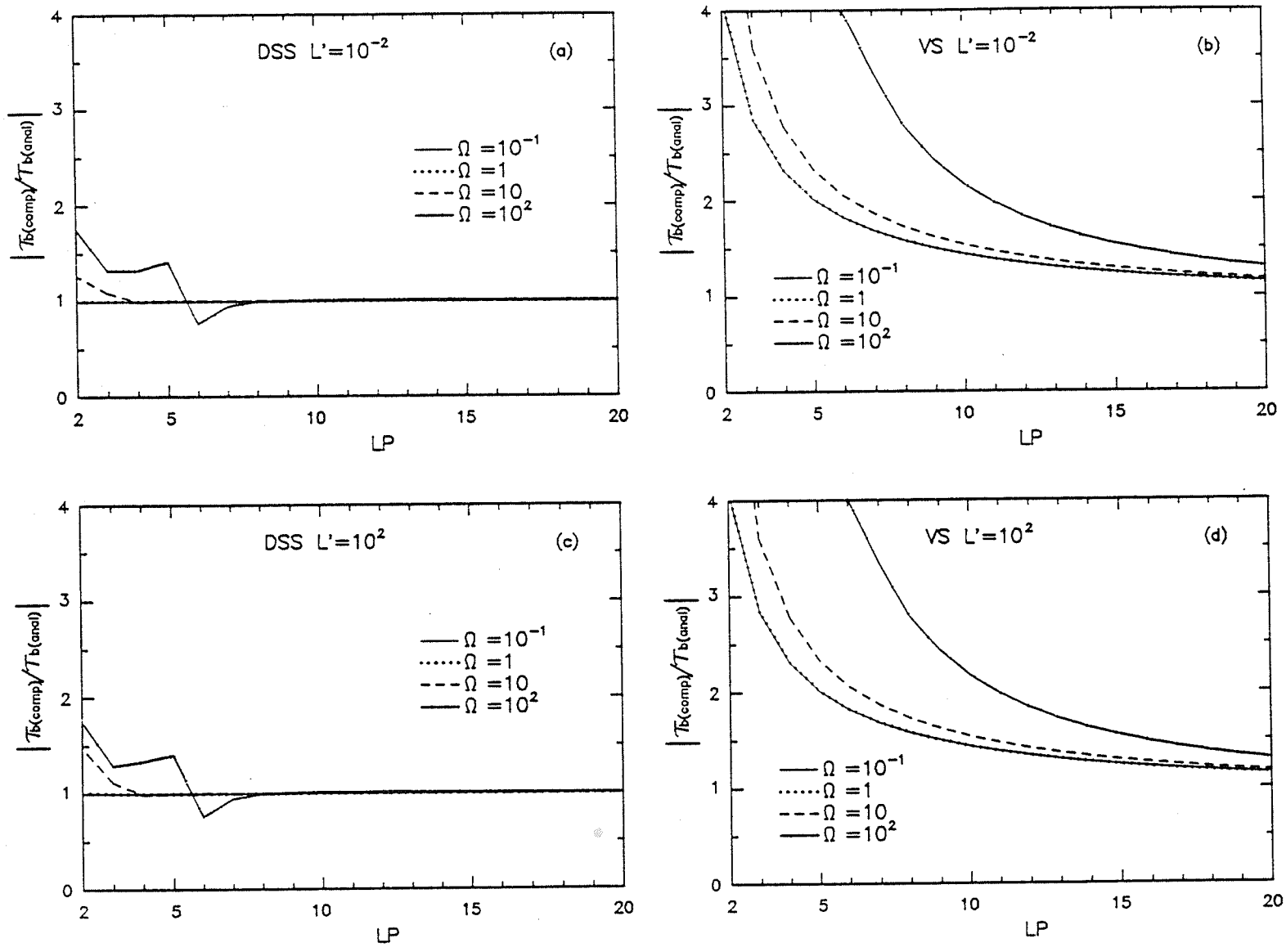

Figure 18. Ratio of the numerical and analytical bottom stress magnitudes for the periodic test case for VS and DSS[1]

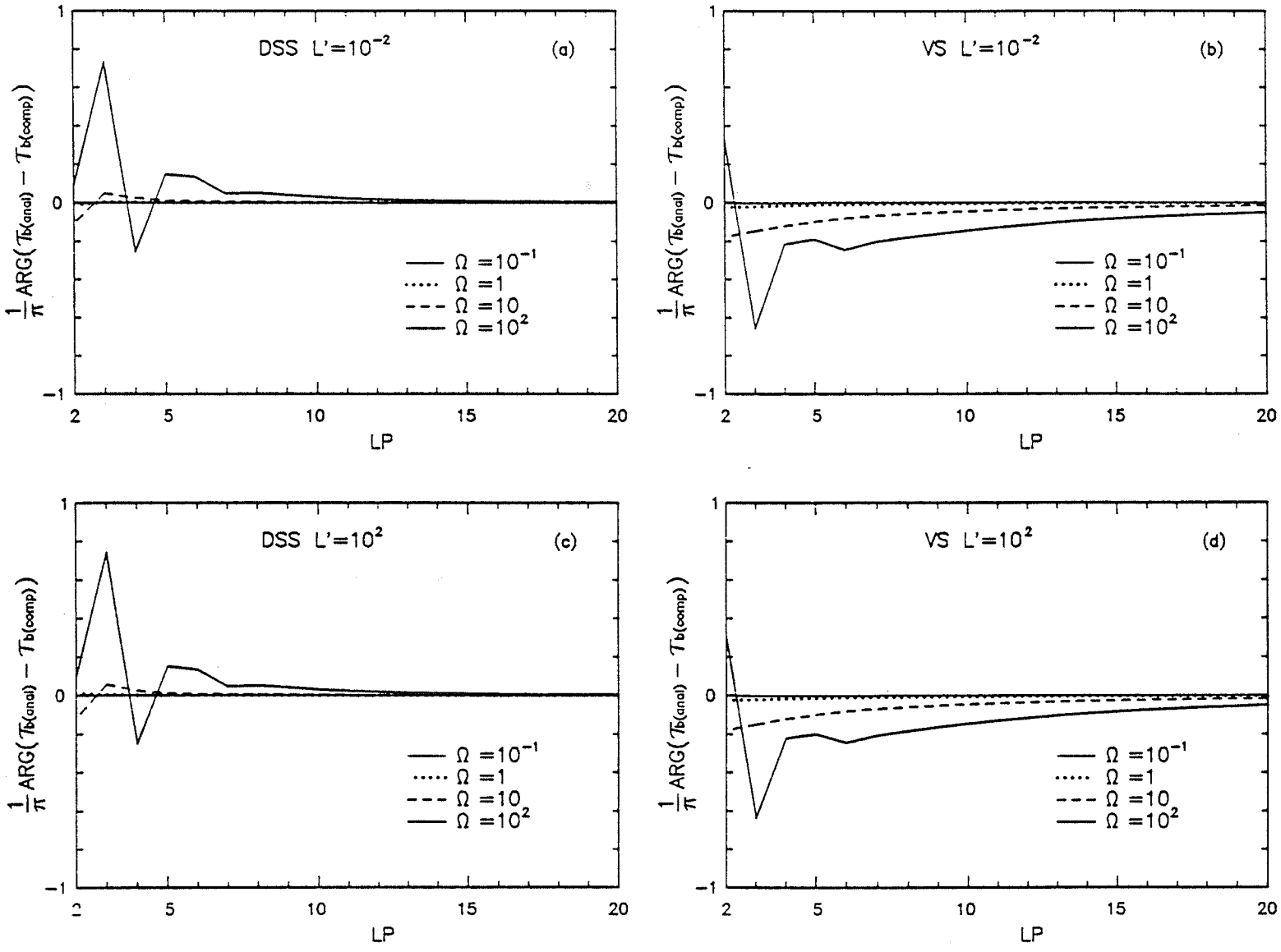

Figure 19. Ratio of the spectral to the analytical bottom stress phase for the periodic test case for the VS and DSS[1]

included. The counterparts to Equation 123 for the case in which Coriolis is included are

$$i\omega\hat{u} - f\hat{v} = \frac{(a-b)}{h}\frac{\partial}{\partial\sigma}\left(\frac{(a-b)E_v}{h}\frac{\partial\hat{u}}{\partial\sigma}\right) + \frac{1}{h\rho_o}(\tau_{bx} - \tau_{sx}) \tag{170}$$

$$i\omega\hat{v} + f\hat{u} = \frac{(a-b)}{h}\frac{\partial}{\partial\sigma}\left(\frac{(a-b)E_v}{h}\frac{\partial\hat{v}}{\partial\sigma}\right) + \frac{1}{h\rho_o}(\tau_{by} - \tau_{sy}) \tag{171}$$

It has been shown (Lynch and Officer 1985) that the linear combinations of $\hat{u}$ and $\hat{v}$

$$\hat{v}^+ \equiv \frac{\hat{u} + i\hat{v}}{2} \qquad \text{and} \qquad \hat{v}^- \equiv \frac{\hat{u} - i\hat{v}}{2}$$

transform Equations 170 and 171 into

$$i(\omega+f)\hat{v}^+ - \frac{(a-b)}{h}\frac{\partial}{\partial\sigma}\left(\frac{(a-b)E_v}{h}\frac{\partial\hat{v}^+}{\partial\sigma}\right) = \frac{1}{2h\rho_o}\left[(\tau_{bx} - \tau_{sx}) + i(\tau_{by} - \tau_{sy})\right] \tag{172}$$

$$i(\omega-f)\hat{v}^- - \frac{(a-b)}{h}\frac{\partial}{\partial\sigma}\left(\frac{(a-b)E_v}{h}\frac{\partial\hat{v}^-}{\partial\sigma}\right) = \frac{1}{2h\rho_o}\left[(\tau_{bx} - \tau_{sx}) - i(\tau_{by} - \tau_{sy})\right] \tag{173}$$

121. Equations 172 and 173 show that the vertical structures of $\hat{v}^+$ and $\hat{v}^-$ are uncoupled and that each is analogous to the structure of $\hat{u}$ in the absence of the Coriolis force, except that $\hat{v}^+$ is forced by the frequency $\omega + f$ and $\hat{v}^-$ is forced by the frequency $\omega - f$. Therefore the vertical structures of $\hat{v}^+$ and $\hat{v}^-$ will depend on the dimensionless frequencies $\Omega^+ \equiv \Omega + \mathcal{F}$ and $\Omega^- \equiv \Omega - \mathcal{F}$, respectively, where $\mathcal{F} \equiv f\,h^2/E_{zo}$. At mid-latitudes, $f \sim 10^{-4}$ sec^{-1}, giving the range of $\mathcal{F} \sim 10^{-3}$ to 10^{1}. This yields values for Ω^+ and Ω^- in the same range as Ω; consequently the results shown in Figures 16–19 are also indicative of the performance of the DSS[1] and the VS when the Coriolis force is included in the governing equations.

122. Analytical solutions can be obtained for the test problem for a transient forcing by decomposing the forcing into its Fourier components, using the periodic solutions presented above for each Fourier component and superimposing the resulting periodic solutions. In this section an illustrative set of results for bottom stress are presented for the often-used problem of an instantaneously imposed wind on an initially quiescent channel. Representative values of L = 100 km, h = 50 m, σ_o = 0.01, and E_{zo}= 0.5 m^2/s are used.

123. An instantaneously imposed forcing cannot be represented exactly by a finite Fourier series; however,

$$\frac{\tau_s(t)}{\tau_{s\text{-}steady}} = \frac{1}{2} + 2\sum_{n=1}^{N}\frac{\sin((2n-1)\pi t/T)}{\pi(2n-1)} \tag{174}$$

gives an approximation to a square wave of period T, as shown in Figure 20. By selecting T to be larger than the time required for the basin to reach steady state and considering only the period $0 \leq t/T < 1$, a reasonable representation of an instantaneously imposed wind can be obtained and used to develop an approximate analytical solution. Sensitivity analyses indicated that when 50 or more terms were used in Equation 174, minimal change occurred in the analytical solution of the basin response and any change that did occur was limited to times very close to zero (i.e., on the order of $t/T < 1$ percent). Seventy–five terms (N=74) were used in Equation 174 for the solution shown in Figure 20 and the runs presented below.

124. The VS and the DSS[1] for the transient test case were obtained by discretizing Equations 123 and 124 in time using a Crank–Nicholson scheme. As discussed above, the analytical solution for U was used to force these equations, thereby eliminating any feedback of error from the vertical representation into U. Figure 21 presents a comparison between bottom stresses obtained analytically and from the VS and the DSS[1]. The DSS[1] with 3 LPs is quite close to the analytical solution except very near $t = 0$ (due primarily to the overshoot in the forcing in Figure 20). Conversely, 15 or more LPs are required for the VS to attain comparable accuracy. We note that this test case uses σ_0 at the upper limit of the practical range and therefore is the easiest case for the VS to capture. For smaller values of σ_0, the transient performance of the VS becomes even poorer as suggested by the steady–state results in Table 4.

125. The results of this section suggest that shear stress can be a highly efficient substitute for velocity as the dependent variable in the internal mode equations. For this to be accomplished, it is only necessary that the shear stress and the vertical gradient of velocity be linked via an eddy viscosity relationship. Depending on the choice of shape functions and the functional variation of eddy viscosity over the depth, the velocity profile can be recovered from the stress profile in closed form. Under these conditions the difficulties associated with numerically integrating a near–logarithmic singularity are avoided. Most practical problems can be solved subject to this restriction by allowing a global or piecewise polynomial variation of τ_z and a piecewise linear variation of E_z.

126. One disadvantage with the DSS[1] is that it yields a fully populated matrix on the left side of the discretized equations that must be reformed, decomposed, and solved at every time step if a time–varying eddy viscosity is used. This requires $\sim N^3$ operations to solve for stress and $\sim N^2$ operations to extract velocity (using Equation 118), where N is the number of LPs that are used. Although often only a

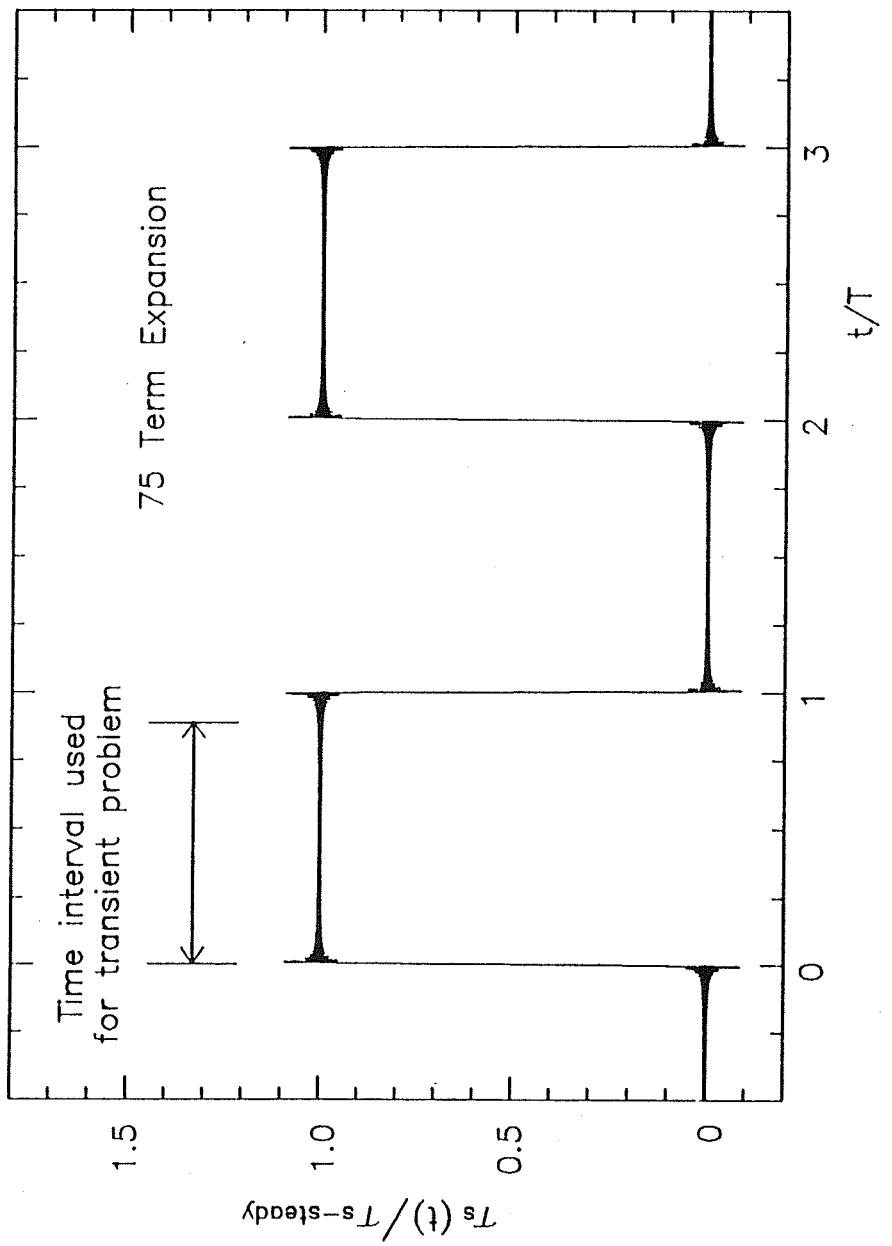

Figure 20. Fourier series approximation to a square wave used to represent an instantaneously applied wind for the transient test case

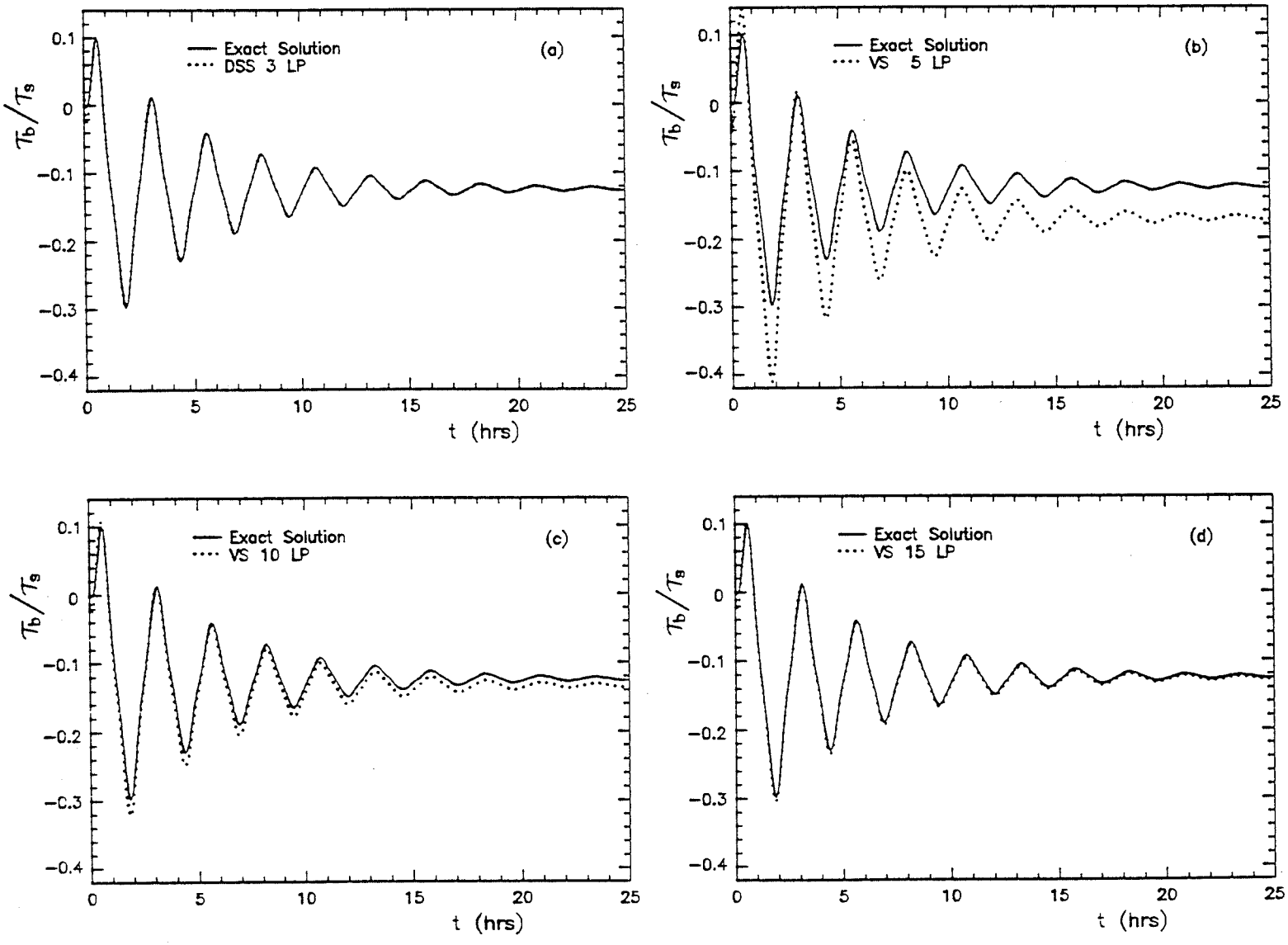

Figure 21. **Time histories of numerical and analytical bottom stress for the transient test case for the VS and DSS[1]**

few LPs are required for an accurate solution, as N reaches ~ 10, the computational attractiveness of the DSS[1] rapidly diminishes in comparison to a VS that only requires the solution of a banded matrix (e.g., Lynch and Werner 1991). Part of the reason for the fully populated matrix is due to the spectral method's use of globally, rather than locally, defined functions. If Equation 124 is discretized using the finite element method with linear elements, the left–side matrix is the sum of a triangular plus a tri–diagonal matrix. This requires ~ M^2 operations to solve, where M is the number of nodes used over the depth. It can be shown that the triangular part of the matrix arises because of the integral term in Equation 124.

Development and Testing of DSS Method No. 2

127. The solution of a fully populated or near–triangular matrix system can be avoided by reformulating the DSS internal mode equations to eliminate integral terms from the left side. This can be accomplished by generating internal mode equations by taking the vertical derivative of the three–dimensional momentum equations rather than by subtracting the vertically integrated equations from the three–dimensional equations. The use of internal mode equations derived by taking the vertical derivative of the three–dimensional equations has been reported by Tee (1979). Although this report focuses primarily on the simplified internal mode equations for a constant–density fluid, the derivation of the full internal mode equations is presented below for completeness.

128. Differentiating the σ–coordinate horizontal momentum equations (Equations 19 and 20) with respect to σ, and substituting Equation 21 for $\partial p/\partial\sigma$ gives

$$\frac{\partial}{\partial t}\left(\frac{\partial u}{\partial\sigma}\right) + u\frac{\partial}{\partial x}\left(\frac{\partial u}{\partial\sigma}\right) + \frac{\partial u}{\partial\sigma}\frac{\partial u}{\partial x} + v\frac{\partial}{\partial y}\left(\frac{\partial u}{\partial\sigma}\right) + \frac{\partial v}{\partial\sigma}\frac{\partial u}{\partial y} + \frac{\partial}{\partial\sigma}\left(w\frac{\partial u}{\partial\sigma}\right) - f\frac{\partial v}{\partial\sigma} = \frac{(a-b)}{H\rho_0}\frac{\partial^2\tau_{zx}}{\partial\sigma^2} - \frac{\partial b_x}{\partial\sigma} + \frac{\partial m_x}{\partial\sigma} \qquad (175)$$

(Note, this is illustrated for the x–momentum equation only. The y–momentum equation follows directly.)

Using the eddy viscosity relationship for τ_{zx} and τ_{zy} (Equation 34) the vertical gradient of velocity can be expressed in terms of the shear stress as

$$\frac{\partial u}{\partial\sigma} = \frac{H\tau_{zx}}{E_v(a-b)\rho_0} \qquad (176a)$$

$$\frac{\partial v}{\partial \sigma} = \frac{H\tau_{zy}}{E_v(a-b)\rho_o} \tag{176b}$$

Substituting Equation 176 and the expansions

$$u\,\frac{\partial}{\partial x}\left(\frac{\partial u}{\partial \sigma}\right) + \frac{\partial u}{\partial \sigma}\,\frac{\partial u}{\partial x} = \frac{\partial}{\partial x}\left(u\frac{\partial u}{\partial \sigma}\right)$$

$$v\,\frac{\partial}{\partial y}\left(\frac{\partial u}{\partial \sigma}\right) = \frac{\partial}{\partial y}\left(v\frac{\partial u}{\partial \sigma}\right) - \frac{\partial u}{\partial \sigma}\,\frac{\partial v}{\partial y}$$

into Equation 175 gives:

$$\frac{\partial}{\partial t}\left[\frac{H\tau_{zx}}{E_v(a-b)\rho_o}\right] - \frac{fH\tau_{zy}}{E_v(a-b)\rho_o} - \frac{(a-b)}{H\rho_o}\,\frac{\partial^2\tau_{zx}}{\partial\sigma^2} = -\frac{\partial}{\partial x}\left[\frac{uH\tau_{zx}}{E_v(a-b)\rho_o}\right] - \frac{\partial}{\partial y}\left[\frac{vH\tau_{zx}}{E_v(a-b)\rho_o}\right]$$

$$-\frac{\partial}{\partial \sigma}\left[\frac{wH\tau_{zx}}{E_v(a-b)\rho_o}\right] + \frac{H\tau_{zx}}{E_v(a-b)\rho_o}\,\frac{\partial v}{\partial y} - \frac{H\tau_{zy}}{E_v(a-b)\rho_o}\,\frac{\partial u}{\partial y} - \frac{\partial b_x}{\partial \sigma} + \frac{\partial m_x}{\partial \sigma} \tag{177}$$

Using the additional expansions

$$\frac{\partial}{\partial \sigma}\left[\frac{wH\tau_{zx}}{E_v(a-b)\rho_o}\right] = \frac{wH}{(a-b)\rho_o}\,\frac{\partial}{\partial \sigma}\left(\frac{\tau_{zx}}{E_v}\right) - \frac{\tau_{zx}}{E_v(a-b)\rho_o}\left[\frac{\partial H}{\partial t} + \frac{\partial uH}{\partial x} + \frac{\partial vH}{\partial y}\right]$$

$$\frac{\partial}{\partial t}\left[\frac{H\tau_{zx}}{E_v(a-b)\rho_o}\right] = \frac{H}{(a-b)\rho_o}\,\frac{\partial}{\partial t}\left(\frac{\tau_{zx}}{E_v}\right) + \frac{\tau_{zx}}{E_v(a-b)\rho_o}\,\frac{\partial H}{\partial t}$$

$$\frac{\partial}{\partial x}\left[\frac{uH\tau_{zx}}{E_v(a-b)\rho_o}\right] = \frac{uH}{(a-b)\rho_o}\,\frac{\partial}{\partial x}\left(\frac{\tau_{zx}}{E_v}\right) + \frac{\tau_{zx}}{E_v(a-b)\rho_o}\,\frac{\partial uH}{\partial x}$$

$$\frac{\partial}{\partial y}\left[\frac{vH\tau_{zx}}{E_v(a-b)\rho_o}\right] = \frac{vH}{(a-b)\rho_o}\,\frac{\partial}{\partial y}\left(\frac{\tau_{zx}}{E_v}\right) + \frac{\tau_{zx}}{E_v(a-b)\rho_o}\,\frac{\partial vH}{\partial y}$$

Equation 177 can be written in final form as

$$\frac{\partial}{\partial t}\left[\frac{\tau_{zx}}{E_v\rho_o}\right] - \frac{f\tau_{zy}}{E_v\rho_o} - \frac{(a-b)^2}{H^2\rho_o}\,\frac{\partial^2\tau_{zx}}{\partial\sigma^2} = c_x - \frac{(a-b)}{H}\left[\frac{\partial b_x}{\partial \sigma} - \frac{\partial m_x}{\partial \sigma}\right] \tag{178}$$

where c_x represents the contribution of the nonlinear advective terms

$$c_x = -u\frac{\partial}{\partial x}\left[\frac{\tau_{zx}}{E_v\rho_o}\right] - v\frac{\partial}{\partial y}\left[\frac{\tau_{zx}}{E_v\rho_o}\right] - w\frac{\partial}{\partial \sigma}\left[\frac{\tau_{zx}}{E_v\rho_o}\right] + \frac{\tau_{zx}}{E_v\rho_o}\,\frac{\partial v}{\partial y} - \frac{\tau_{zy}}{E_v\rho_o}\,\frac{\partial u}{\partial y} \tag{179}$$

Applying the same transformation to the y–momentum equation gives

$$\frac{\partial}{\partial t}\left[\frac{\tau_{zy}}{E_v\rho_o}\right] + \frac{f\tau_{zx}}{E_v\rho_o} - \frac{(a-b)^2}{H^2\rho_o}\,\frac{\partial^2\tau_{zy}}{\partial\sigma^2} = c_y - \frac{(a-b)}{H}\left[\frac{\partial b_y}{\partial \sigma} - \frac{\partial m_y}{\partial \sigma}\right] \tag{180}$$

where

$$c_y = -u\frac{\partial}{\partial x}\left[\frac{\tau_{zy}}{E_v\rho_o}\right] - v\frac{\partial}{\partial y}\left[\frac{\tau_{zy}}{E_v\rho_o}\right] - w\frac{\partial}{\partial \sigma}\left[\frac{\tau_{zy}}{E_v\rho_o}\right] + \frac{\tau_{zy}}{E_v\rho_o}\,\frac{\partial u}{\partial x} - \frac{\tau_{zx}}{E_v\rho_o}\,\frac{\partial v}{\partial x} \tag{181}$$

Introducing the complex shear stress $\tau_z \equiv \tau_{zx} + i\tau_{zy}$ (where $i \equiv \sqrt{-1}$),

Equations 178 and 180 can be combined into a single complex equation

$$\frac{\partial}{\partial t}\left[\frac{\tau_z}{E_v\rho_0}\right] + if\frac{\tau_z}{E_v\rho_0} - \frac{(a-b)^2}{H^2\rho_0}\frac{\partial^2\tau_z}{\partial\sigma^2} = c + b + m \tag{182}$$

where

$$c \equiv c_x + ic_y \tag{183a}$$

$$b \equiv -\frac{(a-b)}{H}\left[\frac{\partial b_x}{\partial\sigma} + i\frac{\partial b_y}{\partial\sigma}\right] \tag{183b}$$

$$m \equiv \frac{(a-b)}{H}\left[\frac{\partial m_x}{\partial\sigma} + i\frac{\partial m_y}{\partial\sigma}\right] \tag{183c}$$

Because both τ_z and E_v may vary in time, the discretization of Equation 182 in time may be facilitated by expanding the leading term as:

$$\frac{\partial}{\partial t}\left[\frac{\tau_z}{E_v\rho_0}\right] = \frac{1}{E_v}\frac{\partial}{\partial t}\left(\frac{\tau_z}{\rho_0}\right) - \frac{\tau_z}{\rho_0}\frac{1}{E_v^2}\frac{\partial E_v}{\partial t} \tag{184}$$

Substituting Equation 184 into Equation 182 and multiplying both sides by E_v gives

$$\frac{\partial}{\partial t}\left(\frac{\tau_z}{\rho_0}\right) - \frac{\tau_z}{\rho_0 E_v}\frac{\partial E_v}{\partial t} + if\frac{\tau_z}{\rho_0} - \frac{(a-b)^2E_v}{H^2\rho_0}\frac{\partial^2\tau_z}{\partial\sigma^2} = E_v[c + b + m] \tag{185}$$

129. For the 3DL model, the baroclinic, advective, and horizontal turbulent momentum terms are assumed to be equal to zero. This leaves

$$\frac{\partial}{\partial t}\left[\frac{\tau_z}{E_v\rho_0}\right] + if\frac{\tau_z}{E_v\rho_0} - \frac{(a-b)^2}{H^2\rho_0}\frac{\partial^2\tau_z}{\partial\sigma^2} = 0 \tag{186a}$$

or

$$\frac{\partial}{\partial t}\left(\frac{\tau_z}{\rho_0}\right) - \frac{\tau_z}{\rho_0 E_v}\frac{\partial E_v}{\partial t} + if\frac{\tau_z}{\rho_0} - \frac{(a-b)^2E_v}{H^2\rho_0}\frac{\partial^2\tau_z}{\partial\sigma^2} = 0 \tag{186b}$$

as simplified DSS[2] internal mode equations. (The superscript 2 is used to identify DSS method No. 2.) We note that for an eddy viscosity that is constant in time, Equations 186a and 186b have the form of complex diffusion equations for stress. This provides a physical interpretation for the internal mode equation; i.e, it describes the turbulent diffusion of stress through the water column.

130. Because of the second derivative term in stress in Equations 186a and 186b, two boundary conditions are needed to solve either equation over the vertical. The free surface boundary condition is

$$\tau_z/\rho_0 = \tau_s/\rho_0 \quad \text{at} \quad \sigma = a \tag{187}$$

where τ_s is the specified surface stress. A second boundary condition can be

generated by requiring the depth average of the internal mode velocity to match the external mode depth–averaged velocity. From Equation 118 this becomes

$$\frac{\tau_b}{\rho_0 k} + \frac{H}{(a-b)^2} \int_b^a \int_b^\sigma \frac{\tau_z}{\rho_0 E_v} \, d\sigma d\sigma = U + iV \tag{188}$$

131. To avoid the fully populated matrices generated by the Galerkin–spectral method, the DSS[2] uses the Galerkin–finite element method to discretize the internal mode equation over the vertical. τ_z/ρ_0 is expanded over M–1 depth intervals using depth–dependent, locally defined basis functions $F_r(\sigma)$ and complex coefficients $\gamma_r(x,y,t)$

$$\frac{\tau_z(x,y,\sigma,t)}{\rho_0} = \sum_{r=1}^{M} \gamma_r \, F_r(\sigma) \tag{189}$$

The Galerkin–finite element forms of Equations 186a and 186b are obtained by substituting Equation 189 for τ_z/ρ_0, multiplying each equation by $F_r(\sigma)$ and integrating with respect to σ over the interval from a to b:

$$\sum_{m=1}^{M} \left\{ \frac{\partial}{\partial t}\left[\gamma_m \int_b^a \frac{F_m F_n}{E_v} \, d\sigma \right] + if\gamma_m \int_b^a \frac{F_m F_n}{E_v} \, d\sigma - \gamma_m \frac{(a-b)^2}{H^2} \int_b^a F_n \frac{\partial^2 F_m}{\partial \sigma^2} \, d\sigma \right\} = 0$$

$$n = 1, \ldots M \tag{190a}$$

and

$$\sum_{m=1}^{M} \left\{ \left[\frac{\partial \gamma_m}{\partial t} + if\gamma_m \right] \int_b^a F_m F_n \, d\sigma - \gamma_m \int_b^a \frac{F_m F_n}{E_v} \frac{\partial E_v}{\partial t} \, d\sigma - \gamma_m \frac{(a-b)^2}{H^2} \int_b^a E_v F_n \frac{\partial^2 F_m}{\partial \sigma^2} \, d\sigma \right\} = 0$$

$$n = 1, \ldots M \tag{190b}$$

132. Linear chapeau functions will be used for $F_r(\sigma)$. The tendency observed in the DSS[1] results for stress to become linear over the depth for $\Omega \leq 1$ suggests that these functions should give a good representation of stress if the element size is selected so that $\Omega^e \sim 1$. (Ω^e is identical to Ω except it is defined using the element size rather than the total depth.) However, Equations 190a and 190b require a C^1 interpolating basis. To lower this requirement to C^0, we integrate by parts:

$$\int_b^a F_n \frac{\partial^2 F_m}{\partial \sigma^2} \, d\sigma = F_n(a)\frac{\partial F_m(a)}{\partial \sigma} - F_n(b)\frac{\partial F_m(b)}{\partial \sigma} - \int_b^a \frac{\partial F_n}{\partial \sigma} \frac{\partial F_m}{\partial \sigma} \, d\sigma \tag{191a}$$

$$\int_b^a E_v F_n \frac{\partial^2 F_m}{\partial \sigma^2}\, d\sigma = E_v(a)F_n(a)\frac{\partial F_m(a)}{\partial \sigma} - E_v(b)F_n(b)\frac{\partial F_m(b)}{\partial \sigma} - \int_b^a \frac{\partial}{\partial \sigma}(E_v F_n)\frac{\partial F_m}{\partial \sigma}\, d\sigma \tag{191b}$$

for Equations 190a and 190b, respectively.

133. Using linear basis functions, when n = 1 and n = M, the first two terms in Equations 191a and 191b exactly cancel the integral terms in these equations making the total diffusion terms equal to zero. However, when $2 \le n \le M-1$, the first two terms in Equations 191a and 191b are identically zero. Therefore, for $2 \le n \le M-1$, Equations 191a and 191b can be substituted into Equations 190a and 190b to give physically meaningful equations:

$$\sum_{m=1}^{M} \left\{ \frac{\partial}{\partial t}\left[\gamma_m \int_b^a \frac{F_m F_n}{E_v}\, d\sigma \right] + i f \gamma_m \int_b^a \frac{F_m F_n}{E_v}\, d\sigma + \gamma_m \frac{(a-b)^2}{H^2} \int_b^a \frac{\partial F_n}{\partial \sigma}\frac{\partial F_m}{\partial \sigma}\, d\sigma \right\} = 0$$

$$n = 2, \ldots M-1 \tag{192a}$$

and

$$\sum_{m=1}^{M} \left\{ \left[\frac{\partial \gamma_m}{\partial t} + i f \gamma_m \right] \int_b^a F_m F_n d\sigma - \gamma_m \frac{\partial}{\partial t} \int_b^a F_m F_n \ln(E_v)\, d\sigma + \gamma_m \frac{(a-b)^2}{H^2} \int_b^a \frac{\partial}{\partial \sigma}(E_v F_n)\frac{\partial F_m}{\partial \sigma}\, d\sigma \right\} = 0$$

$$n = 2, \ldots M-1 \tag{192b}$$

134. The boundary conditions are used to supplement Equations 192a and 192b when n = 1 or n = M. Equation 187 is used in place of the n = M equation:

$$R_e\{\gamma_M\} = \tau_{sx}/\rho_0 \qquad \text{and} \qquad I_m\{\gamma_M\} = \tau_{sy}/\rho_0 \tag{193}$$

In place of the n = 1 equation, Equation 188 gives

$$\sum_{m=1}^{M} \left\{ \frac{\gamma_m F_m(b)}{k} + \gamma_m \frac{H}{(a-b)^2} \int_b^a \int_b^\sigma \frac{F_m}{E_v}\, d\sigma\, d\sigma \right\} = U + iV \tag{194}$$

135. Velocity is recovered from stress by solving the discretized version of Equation 118

$$u + iv = \sum_{m=1}^{M} \left\{ \frac{\gamma_m F_m(b)}{k} + \gamma_m \frac{H}{(a-b)} \int_b^\sigma \frac{F_m}{E_v}\, d\sigma \right\} \tag{195}$$

136. Equations 192a or 192b and 193 form a tri-diagonal system; Equation 194 adds a fully populated bottom row to this system. However, only a few extra

computations are required to reduce the system to tri–diagonal. Therefore, the number of operations required to obtain a solution for stress at each time step scales with M. Since τ_z/ρ_o is piece wise linear over the depth, the integrals in Equation 195 can be evaluated analytically for many functional forms of E_v. For most practical model applications, it can be assumed that E_v has a piece wise linear variation with depth (Furnes 1983; Chu, Liou, and Flenniken 1989; Jenter and Madsen 1989). This is physically correct near boundaries and makes the analytical solution of the stress integrals particularly simple. Using this functional form for E_v, the number of operations required to analytically extract velocity from stress also scales with M.

137. An initial evaluation of the DSS[2] has been made using the same test problems solved for the DSS[1] and the VS. For these tests f = 0, τ_y= 0, and E_v is constant in time. Therefore, Equations 192 – 195 are simplified to:

$$\sum_{m=1}^{M} \left\{ \frac{\partial \gamma_m}{\partial t} \int_b^a \frac{F_m F_n}{E_v} \, d\sigma + \gamma_m \frac{(a-b)^2}{h^2} \int_b^a \frac{\partial F_n}{\partial \sigma} \frac{\partial F_m}{\partial \sigma} \, d\sigma \right\} = 0 \qquad n = 2, \ldots M-1 \qquad (196a)$$

$$\sum_{m=1}^{M} \left\{ \frac{\partial \gamma_m}{\partial t} \int_b^a F_m F_n d\sigma + \gamma_m \frac{(a-b)^2}{h^2} \int_b^a \frac{\partial}{\partial \sigma}(E_v F_n) \frac{\partial F_m}{\partial \sigma} \, d\sigma \right\} = 0 \qquad n = 2, \ldots M-1 \qquad (196b)$$

$$\gamma_M = \tau_{sx}/\rho_o \qquad n = M \qquad (197)$$

$$\sum_{m=1}^{M} \gamma_m \left\{ \frac{F_m(b)}{\rho_o k} + \frac{h}{(a-b)^2} \int_b^a \int_b^\sigma \frac{F_m}{E_v} \, d\sigma \, d\sigma \right\} = U \qquad n = 1 \qquad (198)$$

$$u = \sum_{m=1}^{M} \gamma_m \left\{ \frac{F_m(b)}{\rho_o k} + \frac{h}{(a-b)} \int_b^\sigma \frac{F_m}{E_v} \, d\sigma \right\} \qquad (199)$$

138. To distinguish between the two internal mode equations, results are designated as DSS_a^2 or DSS_b^2 depending on whether they are based on Equation 196a or Equation 196b, respectively. In all of the results, a specified number of equal–sized elements was used over the vertical. It may be possible to improve the efficiency of the DSS[2] further using elements that are not equally sized. However, this option has not yet been investigated completely.

139. In the steady–state test case, the stress distribution is linear over the depth (Equation 143); therefore, both the DSS_a^2 and the DSS_b^2 give the exact solution using one element over the vertical. The number of degrees of freedom (NDF) in the

finite element solution, (i.e., the number of simultaneous equations that must be solved) is equal to the number of nodes used in the discretization (number of nodes = 1 + number of elements). The NDF in the spectral solution is equal to the number of LPs used in the discretization. In both the DSS[1] method and the DSS[2] method, the exact steady–state solution is obtained using two degrees of freedom.

140. Results from the periodic test case are shown in Figures 22 – 26. When $\Omega \leq 1$, the DSS[2] is nearly exact using one finite element (two degrees of freedom) over the depth, Figures 22a and 22b, 23a and 23b, 24a and 24b, and 25a and 25b. For $\Omega > 1$, more than one finite element is required over the vertical for either DSS[2] to converge to the analytical solution (Figures 22c and 22d, 23c and 23d, 24c and 24d, and 25c and 25d). Comparing these results to the DSS[1] results indicates that both DSS[2] methods require more degrees of freedom than the DSS[1] method to reach the same level of convergence. The bottom stress plots presented in Figure 26 demonstrate the properties of the DSS[2] method further. In particular, they indicate that the DSS[2] is quite effective in the range $\Omega \sim 10$ or less. It may be possible to extend this range to higher values of Ω if an unequally spaced finite element grid is used over the depth.

141. A time history of bottom stress for the transient test case is shown in Figure 27. Comparing this to Figure 21a indicates that both DSS[2] methods require four degrees of freedom to give a solution that is approximately equivalent to the DSS[1] using three degrees of freedom.

142. In conclusion, new internal mode equations have been developed that allow shear stress to be used as the dependent variable in the internal mode solution and that yield a nearly tri–diagonal matrix system. While both DSS[2] require more degrees of freedom than the DSS[1] method to obtain comparable results for $\Omega > 1$, (due to the use of linear finite elements in the DSS[2] versus spectral functions in the DSS[1]), the matrix structure of the DSS[2] matrices makes this method much more efficient than the DSS[1].

Implementation of Wave–Current Interaction in a DSS Model

143. It is often observed in lakes, coastal waters, and shelf waters that near the bottom the orbital velocities associated with surface waves are as large as or larger than the mean current velocity. In such cases the surface waves have a significant effect on the bottom stress and the current profile. Several investigators have developed theoretical models to account for this wave–current interaction. To

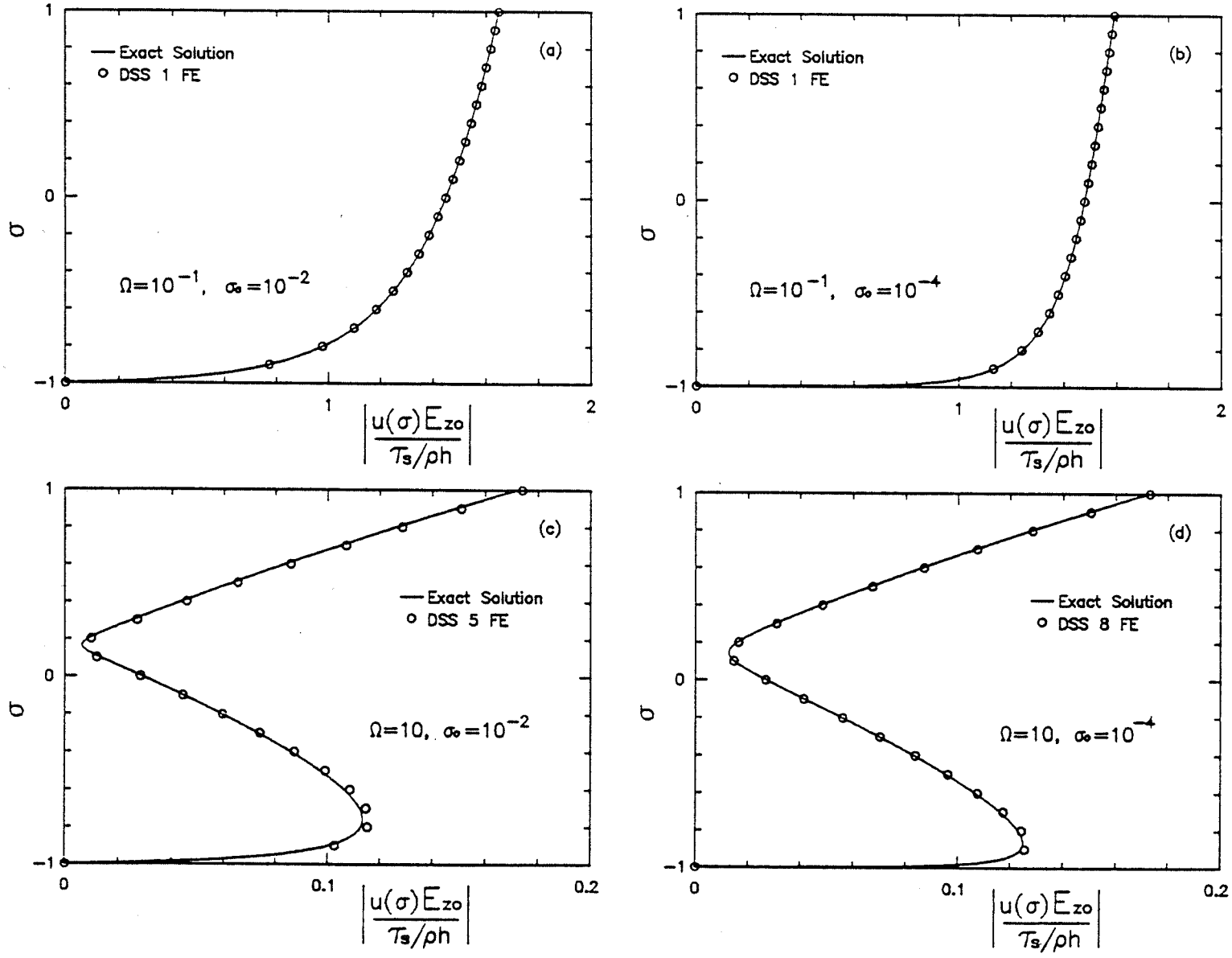

Figure 22. Vertical profiles of horizontal velocity magnitude for the periodic test case using the DSS_a^2

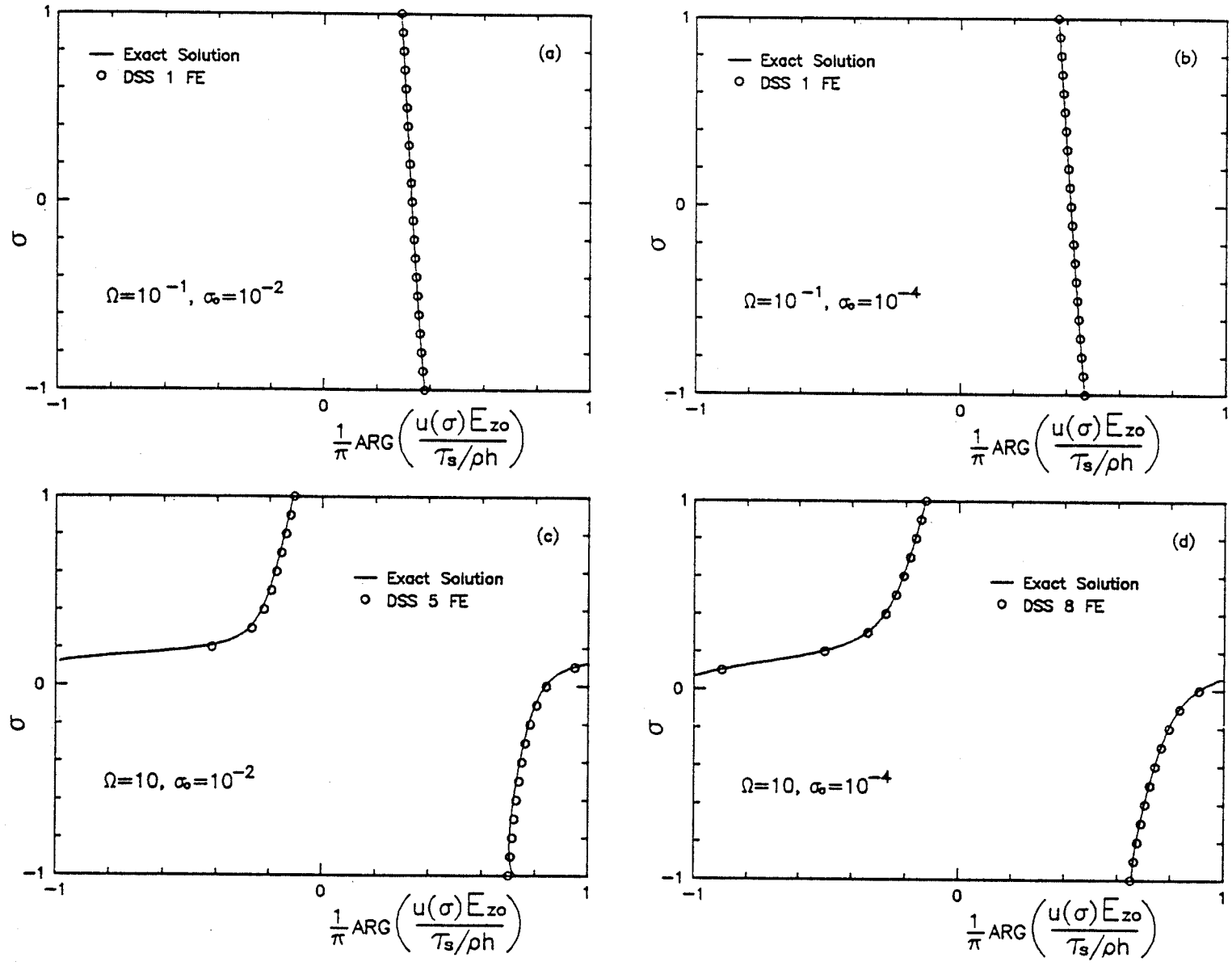

Figure 23. Vertical profiles of horizontal velocity phase for the periodic test case using the DSS_a^2

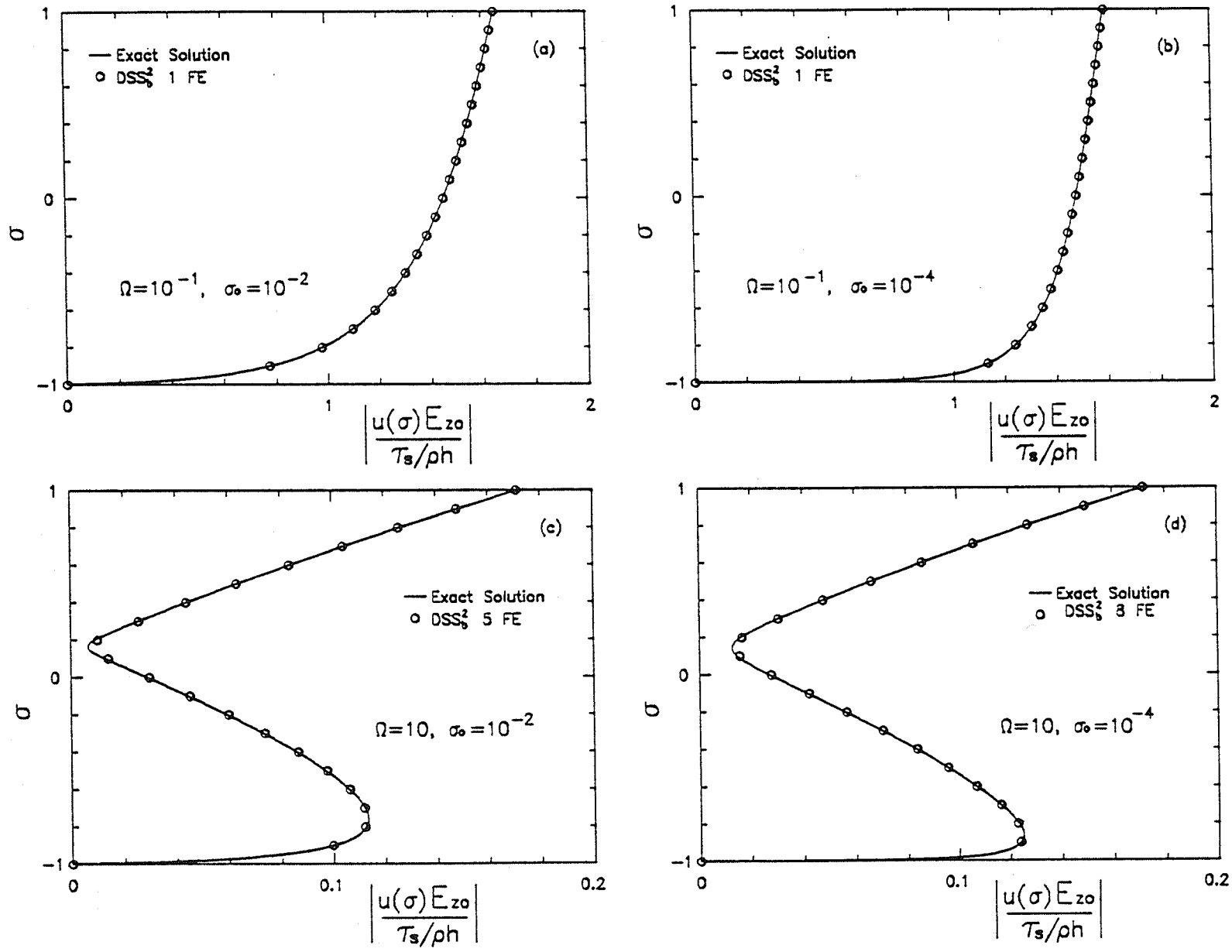

Figure 24. Vertical profiles of horizontal velocity magnitude for the periodic test case using the DSS$_b^2$

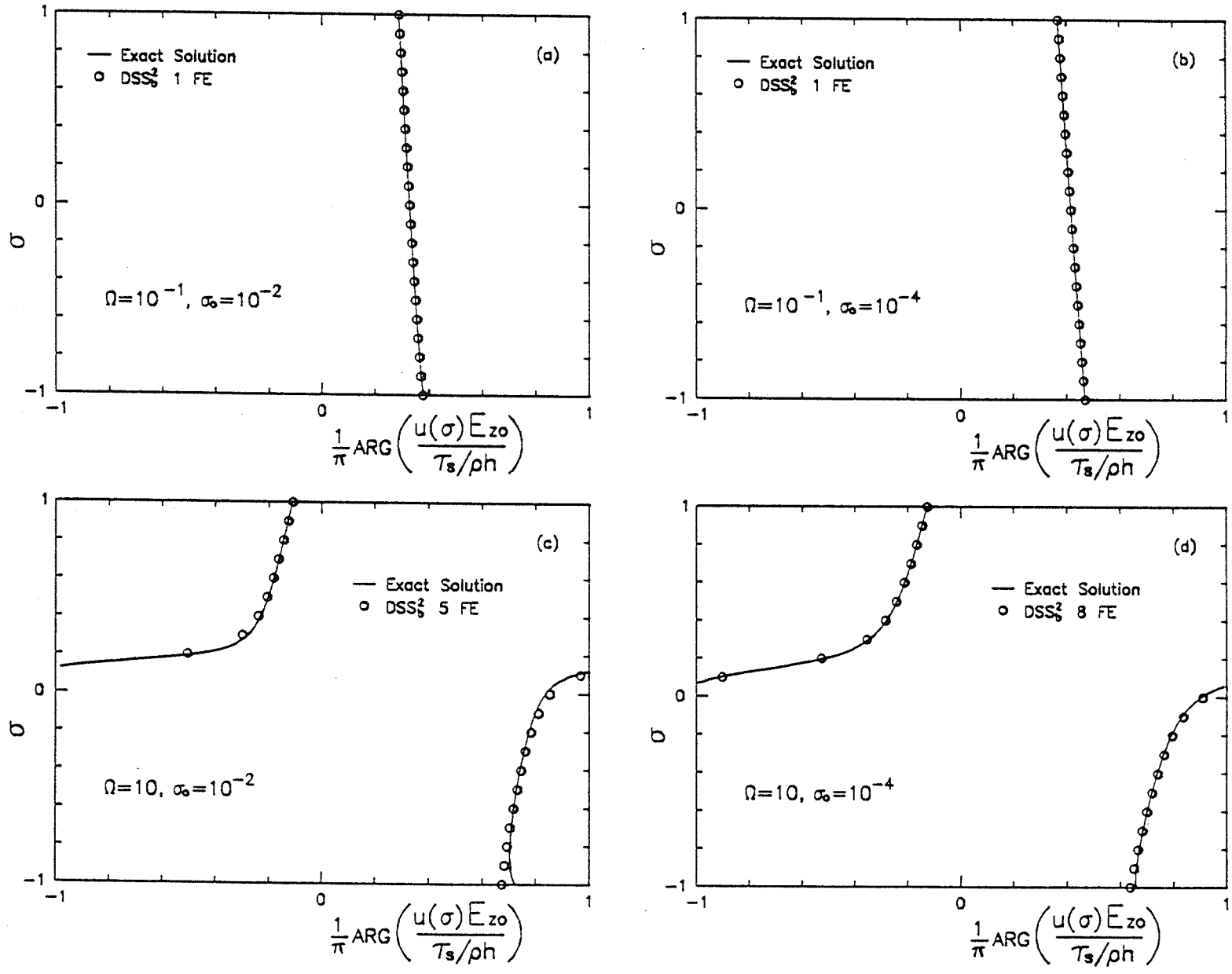

Figure 25. Vertical profiles of horizontal velocity phase for the periodic test case using the DSS$_0^2$

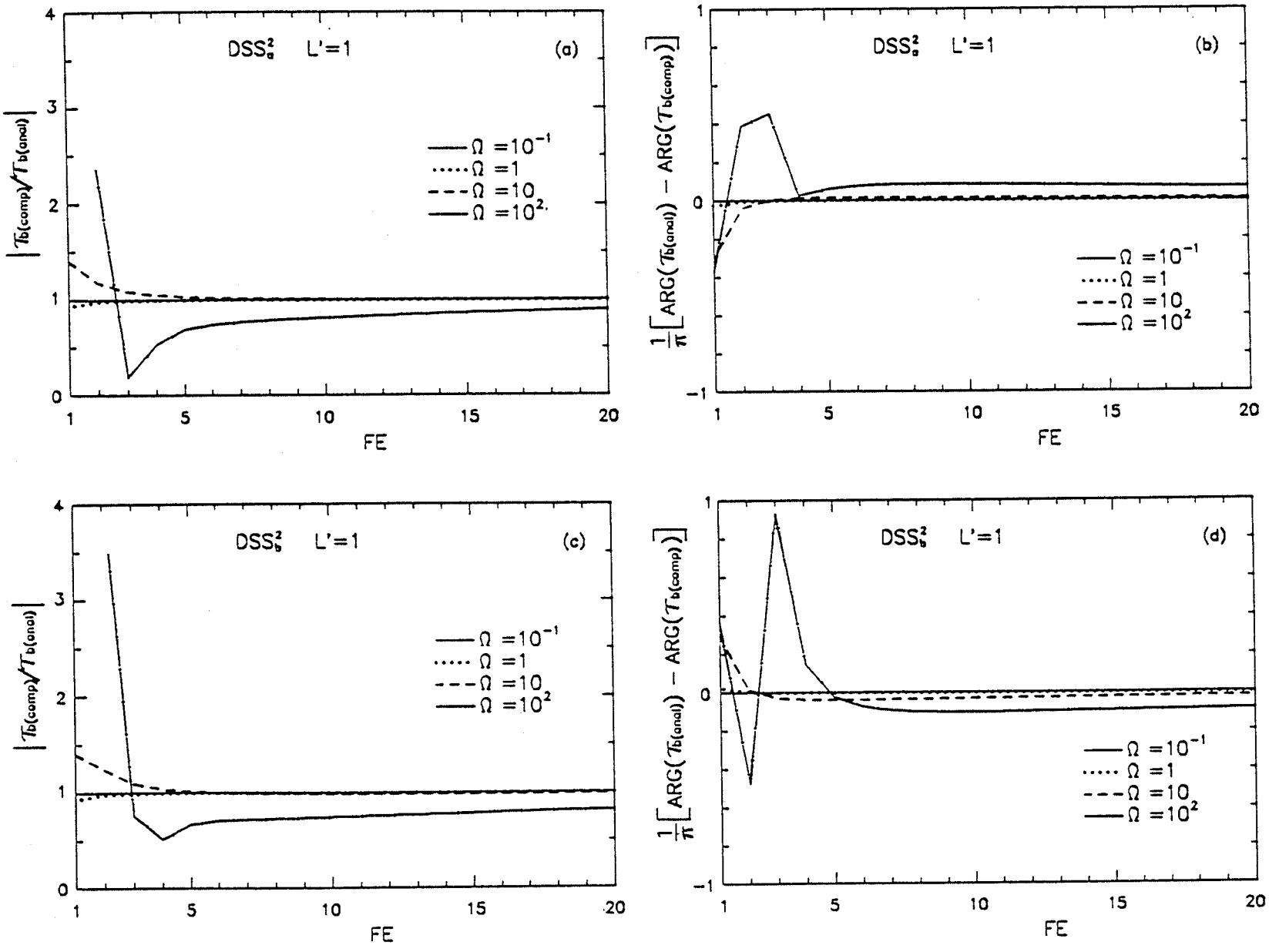

Figure 26. Comparison of the DSS_a^2 and DSS_b^2 bottom stresses and the analytical bottom stress for the periodic test case

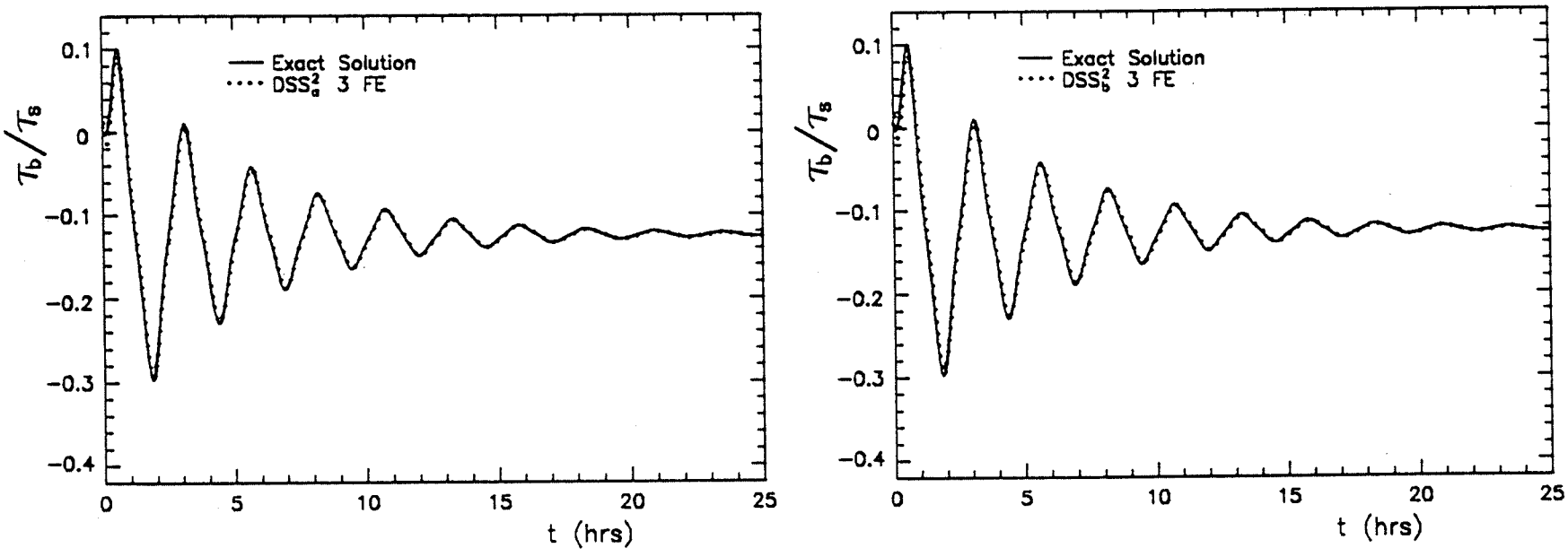

Figure 27. Time history of bottom stress using the DSS_a^2 and the DSS_b^2 for the transient test case

thoroughly assess the usefulness of the DSS approach, the effort required to implement the Grant and Madsen (1979) model (GM model) with a DSS of the internal mode equations has been considered. The GM model assumes that the mean current velocity can be determined as follows:

a. inside the wave boundary layer, $z < \delta_w$,

$$E_v = \kappa \, |U_{*cw}| \, z \tag{200}$$

$$|U_{*cw}| = \frac{1}{\rho_0} |\tau_c + \tau_w|^{1/2} \tag{201}$$

a no–slip boundary condition is applied at $z = z_o$, where z_o is the physical bottom roughness

b. outside the wave boundary layer, $z > \delta_w$

$$E_v = \kappa \, |U_{*c}| \, z \tag{202}$$

$$|U_{*c}| = \frac{1}{\rho_0} |\tau_c|^{1/2} \tag{203}$$

a no–slip boundary condition is applied at $z = z_{oa}$, where z_{oa} is an apparent bottom roughness experienced by the current due to the wave–current interaction.

In these relations, $\kappa = 0.4$ is the Von Kármán constant, τ_c is the bottom stress due to the current alone, τ_w is the maximum wave–induced bottom stress during a wave cycle, and δ_w is the thickness of the wave boundary layer.

144. The GM model can be included in a DSS of the internal mode equations as follows.

a. Estimate z_{oa} and $|U_{*c}|$ based on values at the previous time step.

b. Calculate E_v and use the DSS model to predict τ_c.

c. Solve Equation 201 for $|U_{*cw}|$ using τ_c from the previous step and τ_w from Equation 53 in Grant and Madsen (1979). Since τ_w is a function of U_{*cw}, Equation 201 must be solved iteratively.

d. Determine z_{oa} using Equations 46 and 49 in Grant and Madsen (1979).

e. Recalculate E_v using the new τ_c. Use this and the new value of z_{oa} in the DSS model to predict τ_c. Go to step c. and iterate until τ_c converges.

145. Because two levels of iterations are required to implement the wave–current interaction, it may be computationally infeasible to use this scheme in

practical model applications. It may be possible to simplify this procedure in two ways in the proposed model. First, rather than iterate as described in step e., z_{oa} can be calculated explicitly in time based only on results from the previous time step. This should introduce little error into the solution if the time step is small enough that changes in z_{oa} and τ_c are relatively small. Second, following the suggestion of Spaulding and Isaji (1987), τ_w can be determined by neglecting the effect of the current on the wave within the wave boundary layer. In this case

$$\tau_w/\rho = 0.5\ f_w\ |U_b|\ U_b \tag{204}$$

where f_w is the wave friction factor (Jonsson and Carlsen 1976) and U_b is the maximum bottom wave orbital velocity. For fully rough, turbulent flow, f_w can be determined from

$$\frac{1}{4\sqrt{f_w}} + \log_{10}\frac{1}{4\sqrt{f_w}} = \log_{10}\frac{A_b}{k_s} - 0.12 \tag{205}$$

where A_b is the bottom excursion amplitude of the wave and k_s is the Nikuradse equivalent sand roughness of the bottom (typically $z_o = k_s/30$).

146. The brief outline presented above suggests that the GM wave–current interaction can easily be included in the DSS model. In fact, if the implementation procedure outlined above for the DSS is compared with that described in Grant and Madsen (1979) for a standard VS, it is evident that the DSS simplifies the use of the GM model by eliminating the complications introduced by a quadratic slip bottom boundary condition.

PART V: SUMMARY AND CONCLUSIONS

147. This report documents the theory and methodology behind the ADCIRC (Advanced Circulation) model's 2DDI (2–dimensional, depth–integrated) option and the 3DL (3–dimensional, local internal mode equation) option. ADCIRC is based on the three–dimensional Reynold's equations simplified using the hydrostatic pressure and the Boussinesq approximations. Prior to their solution, the three–dimensional equations are separated into a set of external mode equations (the two–dimensional, vertically integrated equations) and a set of internal mode equations.

148. The external mode equations can be solved by themselves (the 2DDI option) for depth–averaged velocity and free–surface elevation by parameterizing bottom stress and momentum dispersion in terms of the depth–averaged velocity. Key features of the external mode solution are the use of a generalized wave–continuity equation (GWCE) formulation and the Galerkin–finite element (FE) method in space using triangular or quadrilateral elements. The FE method provides maximum grid flexibility and allows highly efficient numerical solutions to be obtained using model domains that include complicated bathymetries and shoreline geometries that also stretch considerable distances offshore to implement open–water boundary conditions. Detailed analyses and testing of ADCIRC–2DDI have shown that it has good stability characteristics, generates no spurious artificial modes, has minimal inherent numerical damping, and efficiently separates the external mode equations into small systems of algebraic equations with time–independent matrices. Applications of the ADCIRC–2DDI model to the English Channel and southern North Sea, the Gulf of Mexico, Masonboro Inlet, and the New York Bight have shown that it is capable of running month to year–long simulations while providing detailed intra–tidal computations.

149. In stratified flows, Ekman layers, wind–driven flows in enclosed or semi–enclosed basins, or flows affected by wave–current interaction in the boundary layer, it is generally impossible to parameterize bottom stress and momentum dispersion in terms of depth–averaged velocity. In such cases, it is necessary to solve the internal mode equations for the vertical variation of horizontal velocity and use this to evaluate the bottom stress and momentum dispersion terms in the external mode equation. Due to the shallow water depths that characterize coastal and shelf settings, the internal mode equations can often be simplified by dropping the horizontal gradient terms. This gives internal mode equations that express the vertical distribution of momentum at any horizontal position as a local balance between the

surface and bottom stresses, vertical momentum diffusion, the Coriolis force, and local inertia. The 3DL model option is formulated using the simplified, local internal mode equations. Existing numerical solutions of full or simplified internal mode equations use velocity as the dependent variable. Therefore, it is necessary to use a fine numerical discretization to resolve the sharp vertical gradients of velocity that occur near the bottom boundary and in wind–driven flows near the surface boundary. During the course of the ADCIRC–3DL model development, a novel technique was discovered that replaces velocity with shear stress as the dependent variable in the internal mode equations. The resulting direct stress solution (DSS) allows physically realistic boundary layers to be explicitly included in a three–dimensional model. Detailed testing of the DSS method has demonstrated its considerable advantage over standard velocity solutions and has led to an optimized DSS formulation. This treatment of the internal mode equations should be invaluable for modeling coastal and shelf circulation in which the bottom and surface boundary layers comprise a significant portion of the water column and for modeling processes that are critically dependent on boundary layer physics such as wave–current interaction, sediment transport, oil spill movement, ice floe movement, energy dissipation, physical–biological couplings, etc.

150. Considerable effort has gone into the development of ADCIRC to produce a model that has simultaneous regional/local capabilities, as well as very high levels of accuracy and efficiency. This has been achieved by combining extreme grid flexibility with optimized formulations of the governing equations and numerical algorithms. Together, these allow ADCIRC to run with improved physical realism and a significant reduction in the computational cost of most presently existing circulation models.

REFERENCES

Abbot, M. B. 1990. "Numerical Modeling for Coastal and Ocean Engineering," Handbook of Coastal and Ocean Engineering, J. Herbich, ed., Gulf Publishing.

ASCE. 1988a. "Turbulence Modeling of Surface Water Flow and Transport: Part I," J. Hydraulic Engineering, Vol 114, No. 9, pp 970–991.

_____. 1988b. "Turbulence Modeling of Surface Water Flow and Transport: Part II," J. Hydraulic Engineering, Vol 114, No. 9, pp 991–1014.

Baptista, A. M., Westerink, J. J., and Turner, P. J. 1989. "Tides in the English Channel and Southern North Sea. A Frequency Domain Analysis Using Model TEA–NL," Advances in Water Resources, Vol 12, No. 4, pp 166–183.

Bedford, K. W. 1984. "Selection of Turbulence and Mixing Parameterizations for Estuary Models," Report to the US Army Engineer Waterways Experiment Station, Environmental Impact Research Program, Vicksburg, MS.

Blumberg, A. F., and Mellor, G. L. 1987. "A Description of a Three–Dimensional Coastal Ocean Circulation Model," Three–Dimensional Coastal Ocean Models, N.S. Heaps, ed., AGU Press, Washington, DC, pp 1–16.

Bowden, K. F., Fairmairn, L. A., and Hughes, P. 1959. "The Distribution of Shearing Stresses in a Tidal Current," Geophysical Journal of the Royal Astronomical Society, Vol 2, pp 288–305.

Chu, W–S., Liou, J. –Y., and Flenniken, K. D. 1989. "Numerical Modeling of Tide and Current in Central Puget Sound: Comparison of a Three–Dimensional and a Depth–Averaged Model," Water Resources Research, Vol 25, No. 4, pp 721–734.

Connor, J. J, and Brebbia, C. A. 1976. Finite Element Techniques for Fluid Flow, Newnes–Butterworths, London.

Csanady, G. T. 1976. "Mean Circulation in Shallow Seas," J. Geophysical Research, Vol 81, No. 30, pp 5389–5399.

Davies, A. M. 1985. "Application of a Sigma Coordinate Sea Model to the Calculation of Wind–Induced Currents," Continental Shelf Research, Vol 4, pp 389–423.

_____. 1987. "Spectral Models in Continental Shelf Oceanography," Three–Dimensional Coastal Ocean Models, N.S. Heaps, ed., AGU Press, Washington, DC, pp 71–106.

_____. 1988. "On Formulating Two–Dimensional Vertically Integrated Hydrodynamic Numerical Models with Enhanced Representation of Bed Stress," J. Geophysical Research, Vol 93, No. C2, pp 1241–1263.

_____. 1989. Modeling Marine Systems, Vol 1, CRC Press, Boca Raton, FL.

_____. 1991. "On the Accuracy of Finite Difference and Modal Methods for Computing Tidal and Wind Wave Current Profiles," International J. Numerical Methods in Fluids, Vol 12, No. 2, pp 101–124.

Davies, A. M., and Furnes, G. 1980. "Observed and Computed M2 Tidal Currents in the North Sea," J. Physical Oceanography, Vol 10, pp 237–257.

Davies, A. M., and Jones, J. E. 1990. "Application of a Three–Dimensional Turbulence Energy Model to the Determination of Tidal Currents on the Northwest European Shelf," J. Geophysical Research, Vol 95, No. C10, pp 18,143–18,162.

Davies, A. M., and Jones, J. E. 1991. "On the Numerical Solution of the Turbulence Energy Equations for Wave and Tidal Flows," International J. Numerical Methods in Fluids, Vol 12, No. 1, pp 12–42.

Davies, A. M., and Owen, A. 1979. "Three–Dimensional Numerical Sea Model Using the Galerkin Method with a Polynomial Basis Set," Applied Mathematical Modelling, Vol 3, pp 421–428.

Davies, A. M., and Stephens, C. V. 1983. "Comparison of the Finite Difference and Galerkin Methods as Applied to the Solution of the Hydrodynamic Equations," Applied Mathematical Modelling, Vol 7, pp 226–240.

Ferziger, J. H. 1987. "Simulation of Incompressible Turbulent Flows," J. Computational Physics, Vol 69, pp 1–48.

Fischer, H. B., List, E. J., Koh, R. C. Y., Imberger, J., and Brooks, N. H. 1979. "Mixing in Inland and Coastal Waters", Academic Press, New York.

Foreman, M. G. G. 1977. Manual for Tidal Heights Analysis and Prediction, Pacific Marine Science Report 77–10, Institute of Ocean Sciences, Patricia Bay, Sidney, B.C.

_____. 1983. "An Analysis of the Wave Equation Model for Finite Element Tidal Computations," J. Computational Physics, Vol 52, pp 290–312.

Furnes, G. 1983. "A Three–Dimensional Numerical Sea Model with Eddy Viscosity Varying Piecewise Linearly in the Vertical," Continental Shelf Research, Vol 2, No. 4, pp 231–241.

Grant, W. D., and Madsen, O. S. 1979. "Combined Wave and Current Interaction with a Rough Bottom," J. Geophysical Research, Vol 84, No. C4, pp 1797–1808.

_____. 1986. "The Continental Shelf Bottom Boundary Layer," Annual Review of Fluid Mechanics, Vol 18, pp 265–305.

Gray, W. G. 1982. "Some Inadequacies of Finite Element Models as Simulators of Two–Dimensional Circulation," Advances in Water Resources, Vol 5, pp 171–177.

_____. 1984. "On Normal Flow Boundary Conditions in Finite Element Codes for Two–Dimensional Shallow Water Flow," International J. Numerical Methods in Fluids, Vol 4, pp 99–104.

Gray, W. G., and Lynch, D. R. 1979. "On the Control of Noise in Finite Element Tidal Computations: a Semi–Implicit Approach," Computers in Fluids, Vol 7, pp 47–67.

Gresho, P. M., Lee, R. L., and Sani, R. L. 1987. "The Consistent Method for Computing Derived Boundary Quantities When the Galerkin FEM is Used to Solve Thermal and/or Fluids Problems," International J. Numerical Methods in Fluids, Vol 7, pp 371–394.

Hansen, W. 1956. "Theorie zur Errechnung des Wasserstandes un der Stromungen in Randmeeren Nebst Anwendungen," Tellus, Vol 8.

Heaps, N. S. 1987. Three–Dimensional Coastal Ocean Models, AGU Press, Washington, DC.

Hendershott, M. C. 1981. "Long Waves and Ocean Tides," Evolution of Physical Oceanography, MIT Press, Cambridge, MA, pp 292–341.

Jenter, H. L., and Madsen, O. S. 1989. "Bottom Stress in Wind–Driven Depth–Averaged Coastal Flows," J. Physical Oceanography, Vol 19, No. 7, pp 962–974.

Johns, B., and Oguz, T. 1987. "Turbulent Energy Closure Schemes," Three–Dimensional Coastal Ocean Models, N.S. Heaps, ed., AGU Press, Washington, DC, pp 17–40.

Jonsson, I. G., and Carlsen, N. A. 1976. "Experimental and Theoretical Investigations in an Oscillatory Turbulent Boundary Layer," J. Hydraulic Research, Vol 14, No. 1, pp 45–60.

Kinmark, I. 1985. "The Shallow Water Wave Equations: Formulation, Analysis and Application," Lecture Notes in Engineering, Vol 15, C.A. Brebbia and S.A. Orszag, eds., Springer–Verlag, Berlin.

Kolar, R. L., and Gray, W. G. 1990. "Shallow Water Modeling in Small Water Bodies," Proceedings of the Eighth International Conference on Computational Methods in Water Resources, pp 39–44.

Koutitas, C. 1987. "Three–Dimensional Models of Coastal Circulation: An Engineering Viewpoint," Three–Dimensional Coastal Ocean Models, N.S. Heaps, ed., AGU Press, Washington, DC, pp 107–124.

Launder, B. E. 1984. "Second–Moment Closure: Methodology and Practice," Simulation of Turbulence Models and Their Applications, Vol 2, Collection de la Direction des Etudes et Recherches, Electricite de France, editions Eyrolles, Paris.

Leendertse, J. J. 1967. "Aspects of a Computational Model for Long–Period Water Wave Propagation," Memorandum RM5294–PR, Rand Corporation, Santa Monica, CA.

Luettich, R. A., Jr., and Westerink, J. J. 1991. "A Solution for the Vertical Variation of Stress, Rather Than Velocity, in a Three–Dimensional Circulation Model," International J. of Numerical Methods in Fluids, Vol 12, pp 911–928.

Lynch, D. R. 1978. "Finite Element Solution of the Shallow Water Equations," Ph.D. dissertation, Department of Civil Engineering, Princeton University, Princeton, N.J.

Lynch, D. R. 1981. "Comparison of Spectral and Time–Stepping Approaches for Finite Element Modeling of Tidal Circulation," Oceans 81 Conference Record, IEEE Publ. No. 81CH1685–7, Boston, MA.

Lynch, D. R., and Gray, W. G. 1978. "Analytical Solutions for Computer Flow Model Testing," J. of the Hydraulics Division, ASCE, No. HY10, pp 1409–1428.

_____. 1979. "A Wave Equation Model for Finite Element Tidal Computations," Computers and Fluids, Vol 7, pp 207–228.

Lynch, D. R., and Officer, C. B. 1985. "Analytic Test Cases for Three–Dimensional Hydrodynamic Models," International J. Numerical Methods in Fluids, Vol 5, pp 529–543.

Lynch, D. R., and Werner, F. E. 1987. "Three–Dimensional Hydrodynamics on Finite Elements. Part I: Linearized Harmonic Model," International J. Numerical Methods in Fluids, Vol 7, pp 871–909.

_____. 1991. "Three–Dimensional Hydrodynamics on Finite Elements. Part II: Nonlinear Time–Stepping Model," International J. Numerical Methods in Fluids, Vol 12, No. 6, pp 507–534.

Mellor, G. L., and Yamada, T. 1982. "Development of a Turbulence Closure Model for Geophysical Fluid Problems," Review of Geophysics and Space Physics, Vol 20, pp 851–875.

Monin, A., and Yaglom, A. 1971. Statistical Hydromechanics, Vol 1, MIT Press, Cambridge, MA.

Nihoul, J. C. J., and Jamart, B. M. 1987. Three–Dimensional Models of Marine and Estuarine Dynamics, Elsevier Science Publishing Co., Amsterdam.

Nihoul, J. C. J., and Djenidi, S. 1987. "Perspective in Three–Dimensional Modeling of the Marine System," Three–Dimensional Models of Marine and Estuarine Dynamics, J. J. Nihoul and B. M. Jamart, eds., Elsevier Science Publishing Co., Amsterdam, pp 1–19.

Oey, L. –Y., Mellor, G. L., and Hires, R. I. 1985. "A Three–Dimensional Simulation of the Hudson–Raritan Estuary. Part I: Description of the Model and Model Simulations," J. Physical Oceanography, Vol 15, No. 12, pp 1676–1692.

Pinder, G. F., and Gray, W. G. 1977. Finite Element Simulation in Surface and Subsurface Hydrology, Academic Press, New York.

Platzman, G. W. 1981. "Some Response Characteristics of Finite Element Tidal Models," J. of Computational Physics, Vol 40, pp 36–63.

Poon, Y. –K. 1988. "A Two–Layer Coupled Hydrodynamic and Ice Floe Movement Model", Sc.D. thesis, Department of Civil Engineering, Massachusetts Institute of Technology, Cambridge, MA.

Reid, R. O. 1990. "Water Level Changes – Tides and Storm Surges," Handbook of Coastal and Ocean Engineering, Gulf Publishing Co.

Rodi, W. 1984. Turbulence Models and Their Application in Hydraulics – a State of the Art Review, International Association for Hydraulic Research, Delft, Netherlands.

_____. 1987. "Examples of Calculation Methods for Flow and Mixing in Stratified Fluids," J. Geophysical Research, Vol 92, No. C5, pp 5305–5328.

Schlichting, H. 1979. Boundary Layer Theory, 7th ed., McGraw–Hill, New York.

Schureman, P. 1941. Manual of Harmonic Analysis and Prediction of Tides, Special Pub. No. 98, Coast and Geodetic Survey, US Dept. of Commerce, US Government Printing Office, Washington, DC.

Schwiderski, E. W. 1980. "On Charting Global Ocean Tides," Review of Geophysics and Space Physics, Vol 18, No. 1, pp 243–268.

Sheng, Y. P. 1983. "Mathematical Modeling of Three–Dimensional Coastal Currents and Sediment Dispersion: Model Development and Application," Technical Report CERC–83–2, US Army Engineer Waterways Experiment Station, Vicksburg, MS.

Sheng, Y. P., and Lick, W. 1980. "A Two–Mode Free–Surface Numerical Model for the Three–Dimensional Time–Dependent Currents in Large Lakes," EPA Project Report EPA–600/3–80–047.

Signell, R. P. 1989. "Tidal Dynamics and Dispersion Around Coastal Headlands," Report No. WHOI–89–38, WHOI–MIT Joint Program in Oceanography and Oceanographic Engineering.

Simmons, T. J. 1974. "Verification of Numerical Models of Lake Ontario: Part I. Circulation in Spring and Early Summer," J. Physical Oceanography, Vol 4, pp 507–523.

Smith, L. H., and Cheng, R. T. 1987. "Tidal and Tidally Averaged Circulation Characteristics of Suisan Bay, California," Water Resources Research, Vol 23, No. 1, pp 143–155.

Spaulding, M. L. 1984. "A Vertically Averaged Circulation Model Using Boundary Fitted Coordinates," J. Physical Oceanography, Vol 14, pp 973–982.

Spaulding, M. L., and Isaji, T. 1987. "Three Dimensional Continental Shelf Hydrodynamics Model Including Wave Current Interaction," Three–Dimensional Models of Marine and Estuarine Dynamics, J.J. Nihoul and B.M. Jamart, eds., Elsevier Science Publishing Co., Amsterdam, pp 405–426.

Tee, K. –T. 1979. "The Structure of Three–Dimensional Tide–Generating Currents. Part I: Oscillating Currents," J. Physical Oceanography, Vol 9, pp 930–944.

_____. 1987. "Simple Models to Simulate Three–Dimensional Tidal and Residual Currents," Three–Dimensional Coastal Ocean Models, N.S. Heaps, ed., AGU Press, Washington, DC, pp 125–148.

Vincent, P., and Le Provost, C. 1988. "Semidiurnal Tides in the Northeast Atlantic from a Finite Element Numerical Model," J. Geophysical Research, Vol 93, No. C1, pp 543–555.

Walters, R. A. 1983. "Numerically Induced Oscillations in Finite Element Approximations to the Shallow Water Equations," International J. of Numerical Methods in Fluids, Vol 3, pp 591–604.

_____. 1984. "Finite Element Solution Methods for Circulation in Estuaries," Proceedings of the Fifth International Conference on Computational Methods in Water Resources, J.P. Liable, et al., eds., Burlington, VT.

_____. 1987. "A Model for Tides and Currents in the English Channel and Southern North Sea," Advances in Water Resources, Vol 10, pp 138–148.

Walters, R. A., and Carey, G. F. 1983. "Analysis of Spurious Oscillation Modes for the Shallow Water and Navier–Stokes Equations," Computers and Fluids, Vol 11, pp 51–68.

Wang, D. –P. 1982. "Development of a Three–Dimensional, Limited–Area (Island) Shelf Circulation Model," J. Physical Oceanography, Vol 12, pp 605–617.

Wang, J. D., and Connor, J. J. 1975. "Mathematical Modeling of Near Coastal Circulation," R.M. Parsons Laboratory Tech. Rep. 200, Massachusetts Institute of Technology, Cambridge, MA.

Werner, F. E., and Lynch, D. R. 1987. "Field Verification of Wave Equation Tidal Dynamics in the English Channel and Southern North Sea," Advances in Water Resources, Vol 10, pp 184–193.

_____. 1988 (Feb). "Tides in the Southern North Sea/English Channel: Data Files and Procedure for Reference Computations," Dartmouth College Numerical Laboratory Report, Dartmouth, NH.

_____. 1989. "Harmonic Structure of English Channel/Sourhern Bight Tides from a Wave Equation Simulation," Advances in Water Resources, Vol 12, pp 121–142.

Westerink, J. J., Connor, J. J., and Stolzenbach, K. D. 1987. "A Primitive Pseudo Wave Equation Formulation for Solving the Harmonic Shallow Water Equations," Advances in Water Resources, Vol 10, pp 188–199.

_____. 1988. "A Frequency–Time Domain Finite Element Model for Tidal Circulation Based on the Least–Squares Harmonic Analysis Method," International J. of Numerical Methods in Fluids, Vol 8, pp 813–843.

Westerink, J. J., Stolzenbach, K. D., and Connor, J. J. 1989. "General Spectral Computations of the Nonlinear Shallow Water Tidal Interactions within the Bight of Abaco," J. Physical Oceanography, Vol 19, No. 9, pp 1348–1371.

Westerink, J. J., and Gray, W. G. 1991. "Progress in Surface Water Modeling," Reviews of Geophysics, Supplement, pp 210–219.

Westerink, J. J., Luettich, R. A., Jr., Baptista, A. M., Scheffner, N. W., and Farrar, P. "Tide and Storm Surge Predictions Using a Finite Element Model," J. Hydraulic Engineering, in press.

Waterways Experiment Station Cataloging-in-Publication Data

Luettich, Richard A.
ADCIRC : an advanced three-dimensional circulation model for shelves, coasts, and estuaries. Theory and methodology of ADCIRC-2DDI and ADCIRC-3DL / by R.A. Luettich, Jr., J.J. Westerink, Norman W. Scheffner ; prepared for Department of the Army, US Army Corps of Engineers.
141 p. : ill. ; 28 cm. — (Technical report ; DRP-92-6 rept. 1)
Includes bibliographical references.
1. Ocean circulation — Mathematical models. 2. Hydrodynamics — Mathematical models. 3. Ocean currents — Mathematical models. I. Westerink, J. J. II. Scheffner, Norman W. III. United States. Army. Corps of Engineers. IV. U.S. Army Engineer Waterways Experiment Station. V. Dredging Research Program. VI. Title. VII. Title: ADCIRC: an advanced three-dimensional circulation model for shelves, coasts, and estuaries. VIII. Title: Theory and methodology of ADCIRC-2DDI and ADCIRC-3DL. IX. Series: Technical report (U.S. Army Engineer Waterways Experiment Station) ; DRP-92-6 rept.1.
TA7 W34 no.DRP-92-6 rept.1